1-1-1995

Synthesis, characterization, and modelling of PBLG-PI rod-coil diblock copolymers :: microstructure in solution and at interfaces/

Diane E. Bennett
University of Massachusetts Amherst

SYNTHESIS, CHARACTERIZATION, AND MODELLING OF PBLG-PI ROD-COIL DIBLOCK COPOLYMERS

MICROSTRUCTURE IN SOLUTION AND AT INTERFACES

A Dissertation Presented

by

DIANE E. BENNETT

Submitted to the Graduate School of the
University of Massachusetts Amherst in partial fulfillment
of the requirements for the degree of

DOCTOR OF PHILOSOPHY

September 1995

Department of Polymer Science and Engineering

SYNTHESIS, CHARACTERIZATION, AND MODELLING OF PBLG-PI ROD-COIL DIBLOCK COPOLYMERS

MICROSTRUCTURE IN SOLUTION AND AT INTERFACES

A Dissertation Presented
by
DIANE E. BENNETT

Approved as to style and content by:

David A. Tirrell, Chair

Richard S. Stein, Member

Samuel P. Gido, Member

M. Muthukumar, Member

William J. MacKnight, Department Head
Polymer Science and Engineering

To my beloved husband, Gregg

ABSTRACT

SYNTHESIS, CHARACTERIZATION, AND MODELLING OF PBLG-PI ROD-COIL DIBLOCK COPOLYMERS

MICROSTRUCTURE IN SOLUTION AND AT INTERFACES

SEPTEMBER 1995

DIANE E. BENNETT, B.S., UNIVERSITY OF TEXAS AT AUSTIN

Ph.D., UNIVERSITY OF MASSACHUSETTS AMHERST

Directed by: Professor David A. Tirrell

In nature, the ability of DNA, enzymes, or membranes, for example, to perform a specific function is closely linked to architecture. One of the frontiers of polymer science is to more accurately mimic nature by controlling the supramolecular structure of polymeric assemblies. The design of the macromolecular building block set used for this work incorporated molecules with a persistent shape. The shape persistence acts as a constraint which has the effect of conferring order to the system. The goal of this work was to synthesize a rod-coil diblock copolymer, poly(isoprene-block-γ-benzyl-L-glutamate), and to investigate the novel structures which form in solution and at interfaces.

The goal for studying rod-coil diblock copolymers at solid surfaces was to form a well-ordered monolayer of rods. The diblock copolymers were adsorbed from a solution of N,N-dimethylformamide onto gold surfaces. Reflectance infrared spectroscopy and ellipsometry showed that the rods were only weakly tilted away from the surface, in agreement with published work with end-functionalized PBLG rods at surfaces. Modelling of the α-helix

dipole of PBLG showed that the dipole-dipole interaction energy between parallel helices was not responsible for the weak ordering.

Dynamic and total intensity light scattering measurements were used to characterize the structures formed by the diblock copolymers in three solvents: rod-selective, coil-selective, and non-selective. Compared with conventional flexible-coil block copolymers, fundamentally different microstructures and block length dependencies were observed. In the rod-selective solvent (N,N-dimethylformamide), large, star-like micelles were formed. Micelle formation in the coil-selective solvent (a mixed solvent of dichloromethane and heptane) was only observed for those diblocks possessing the longest coil blocks. This is in qualitative agreement with theoretical predictions. In the non-selective solvent, each block favors intimate contact with the solvent and non-aggregated or weakly aggregated diblocks were observed.

TABLE OF CONTENTS

LIST OF TABLES

LIST OF FIGURES

CHAPTER I

INTRODUCTION

One of the frontiers of polymer science is the control of supramolecular structure in which the cornerstone to success is the availability of unique polymeric building blocks. [1] Useful polymeric building blocks possess well-defined and persistent sizes and shapes. [2-4] In order for macromolecules to self-assemble into building blocks they must be encoded with molecular recognition sites which direct their assembly. Recognition sites on the surfaces of the building blocks are required to assemble into supramolecular architectures and to serve as active sites to perform the designed function. One goal of supramolecular assembly is to more accurately mimic nature where structural control is intimately linked with function, as in lipid bilayers, tubules, DNA, enzymes, etc. Liquid crystals, [5, 6] dendrimers, [7, 8] rotaxanes, [9-12] macrocyclics, [13, 14] well-defined crystals, [15] polymerized self-assembled monolayers and bilayers, [16] and block and graft copolymers [17, 18] are all potential avenues leading toward useful building blocks. This work will focus on novel structures in rod-coil diblock copolymers.

A. Block Copolymers

Block copolymers differ from statistical copolymers in that the repeat units of each type are isolated in blocks. Essentially, the copolymer is formed by linking two or more homopolymers in series. Polymers in general are immiscible with other polymers, but linking two polymers together forces the polymers to interact intimately with each other. This interaction is the origin of the structural development in block copolymer systems.

Block copolymers can vary from one another in many respects. Variables such as, the number of blocks, [19, 20] length of each block, [21] the repeating units comprising the blocks, [22] and the rigidity of the blocks, [23-31] all influence the resulting structure and properties. The effect of rigidity in polyisoprene-block-poly(γ-benzyl-L-glutamate) (PI-b-PBLG) copolymers is the focus of this work. Conceptually, three distinct types of block copolymers can be characterized by chain rigidity: coil-coil, rod-rod, and rod-coil. Coupling of rigid and flexible blocks in rod-coil diblock copolymers offers a unique opportunity to produce novel structures. Each of the different block copolymer architectures is briefly summarized below.

1. Coil-Coil

Flexible coil block copolymers have been studied extensively. [32, 33] It has been found that a myriad of tethered structures develop as the blocks attempt to minimize their interactions. Micelles, [32, 34] lamellae, [35-41] and adsorbed block copolymers [33, 42] are examples of tethered structures which form in solution, in the bulk, and at surfaces, respectively as a means for the system to achieve the most favorable environment for each block and thereby reduce the total energy of the system. [33]

a. Background

Solution properties are predominantly determined by the nature of the solvent. In a selective solvent, one for which the solvent "goodness" is not the same for one block compared to the other, micelles are known to form. Micelles reduce unfavorable osmotic interactions through the formation of typically spherical aggregates comprised of a core of the less soluble block

surrounded by a corona of the more soluble block. [32] Flexible coil block copolymer micelles are typically spherical in shape although non-spherical (ellipsoidal) micelles, common shapes for surfactant micelles, have been reported. [43-45] Solvent selectivity does not change the geometry of the micelle but only the composition of the core and corona. Micelle growth is limited by the stretching imposed in the core and the coronal regions. Knowledge of the block lengths and solvent is sufficient for completely specifying the micelle in terms of radius (both core and corona radii) and aggregation number. [33]

If this selective solvent solution is brought into contact with a solid surface, the block copolymer will adsorb onto the surface. Tethering coils to an interface leads to unique behavior because the chains are forced to adopt configurations different than in free solution. The poorly solvated block will form a solvent excluded layer on the surface and thereby anchor the well-solvated block onto the surface. If the average distance between grafting points is greater than the radius of gyration of the coils then the coils will be relatively unperturbed by the interface and will assume approximately free solution dimensions, $Rg \propto N^{3/5}$. If the grafting density is increased so that the spacing between anchored chains is much less than the radius of gyration of the coils then the chains will crowd one another. [33] Chain overlap is an energetically costly situation since it creates unfavorable polymer-polymer contacts at the expense of favorable polymer-solvent interactions. Therefore, the chains stretch away from the interface to improve this osmotic balance. The degree of chain stretching is limited by the associated increase in the stretching energy. The equilibrium surface density is that which minimizes the system free energy. The result is that the chains stretch to the point at which the radius of gyration, and thus the layer thickness, is proportional to the degree of polymerization. [33]

In the bulk and in concentrated solution, a range of morphologies, such as spheres, cylinders, ordered bicontinuous double diamonds, and lamellae, have been explored. [37-41]

b. Uses

Block copolymers have been used extensively in the area of thermoplastic elastomers, [46] pressure sensitive adhesives, [47] and toughened plastics (i.e. ABS rubber). [48] Other material applications include compatibilized or stabilized homopolymer blends. [49] In addition, microstructural diversity allows for the tailoring of material properties. [50, 51]

Adsorption of block copolymers to interfaces, such as solid surfaces, has been used to modify interactions with the environment. Surface modification can be aimed at imparting biocompatibility to implants; inhibiting corrosion; modifying adhesion, [47, 52] lubrication, [53] or flow in pipes; or stabilizing colloidal dispersions in motor oils, inks, and paints (especially pigment particles). [54-56]

The solution behavior of block copolymers leads to yet another host of applications. Micelles are useful for viscosity modification as well as emerging drug delivery systems. [57]

Unfortunately, the types of structures which form with flexible coil-coil block copolymers are severely limited. Chemical incompatibility is the major contributor to phase separation and the resulting structure. However, the structures which form are not intimately connected with the specific environment because of the geometrical symmetry of the two blocks. For example, coil-coil micelles are almost universally spherical, independent of the choice of solvent. Another example of the lack of structural diversity lies

in the symmetry of the flexible coil block copolymer phase diagram. In addition, the conformational freedom of the flexible polymer brush precludes the formation of thin surface layers of well-defined thickness and surface functionality.

2. Rod-Rod

A block copolymer composed of two or more rigid sequences, rigid-rod block copolymers, would possess the conformational specificity which is lacking in flexible coil-coil diblocks. In general, there are two basic methods of incorporating rod-like blocks into a block copolymer. The first method is to use a block with a rigid primary structure in the backbone (or the side-chains). In this case, the rigidity of the block is a result of hindered rotation about the chain backbone through the incorporation of rings and double bonds. On the other hand, a block may have a flexible backbone but possess a rigid secondary structure. A classical example of such a molecule is the α-helix of poly(γ-benzyl-L-glutamate) (PBLG).

Research in this area is limited. PBLG blocks connected by short spacers were studied in a solution of N,N-dimethylformamide (DMF). [58] Polymeric (PMMA [58] and PEO [59]) spacers were also employed (technically rod-coil-rod triblock copolymers). These studies were mostly concerned with the effect of rigidity "defects" imposed by the spacers. Studies involving the linking of chemically different rods are not known. While more interesting behavior is expected to result from linking chemically different rods, the structural diversity and ultimate usefulness of these rod-rod systems as building blocks are nevertheless expected to be limited. As in the case of coil-coil block

copolymers, rod-rod block copolymers are limited by the lack of geometrical diversity.

3. Rod-Coil

Rod-coil diblocks are the only family of block copolymer which has geometrical diversity as a tool to control its resulting structure. It is well known that the driving force for phase separation increases with the incompatibility of the blocks. In terms of generating interesting and novel microstructures and building blocks, rod-coil diblock copolymers could be considered "ideal" block copolymers because rods and coils are not only chemically incompatible, but also *spatially* incompatible. [60-62] Blends of rods and coils will macrophase separate into isotropic and anisotropic phases. [63, 64] The exclusion from each phase is mutual; the rods are incompatible with the isotropic phase and the random coils are even more incompatible with the anisotropic phase. [65] The selectivity in each phase increases with the length and the concentration of the chains. [66]

a. Prior Work

The field of rod-coil block copolymers has only recently emerged and research to date has been devoted almost exclusively to studying the phase and scaling behavior of these materials in the bulk and in concentrated solution. [23, 26-28]

One line of investigation has been to employ rod-coil block copolymers as potential single-component molecular composites. [24, 25, 29-31, 67, 68] The goal for these systems is to inhibit macroscopic phase separation, typical of blends of rods and coils, while embedding a molecular fiber (rod) into a matrix (coil).

High rod axial ratios result in the best reinforcing characteristics and for this reason the microstructure formation resulting from rod aggregation is also undesirable. Graft copolymers, both main-chain rigid with flexible side-chains, [67] and side-chain rigid with rigid side-chains, [25, 29] have been investigated for their potential in inhibiting rod aggregation.

Other research efforts are aimed at studying the microstructural diversity in these highly segregated materials. The key to these systems is the rigidity of the rod block which imposes a spatial constraint from which arises a degree of order typical of liquid crystalline polymers. The result is a superposition of liquid crystal structure onto flexible-coil block copolymer microstructures.

Duoy and Gallot initiated the research efforts in this area with work on polypeptide α-helical rods attached to a variety of coil blocks, such as polybutadiene, polystyrene, and random-coil polypeptides. [26-28] Their interests in this field were focused on the potential biological applications of these materials. The predominance of the lamellar morphology in bulk and concentrated solutions was established with TEM and X-ray investigations. Tilting and α-helix folding were proposed to rationalize the measured lamellar spacings. Furthermore, increasing fractions of a coil-selective solvent resulted in larger coil domains and smaller rod domains. This result was consistent with a subsequent theoretical prediction of a rod tilting transition imposed by the surface area requirements of the coils. [69] The extent of folding and/or tilting were dependent on both the rod and coil blocks and are likely interconnected mechanisms within these systems.

Recently, Stupp et al. [23] have been investigating a nearly monodisperse rod-coil diblock system composed of polyisoprene and an main-chain rigid rod molecule. This work has involved TEM and electron diffraction studies

of bulk films for several coil blocks attached to a single 6 nm rod. The results indicate that the lamellar microstructure is only stable for the shortest coil (3K). Relatively small increases in coil molecular weight (3K to 8K) have a dramatic effect on the resulting bulk morphology. Longer coils appear to result in the formation of smaller domains, consistent with theoretical predictions of the relative stability of lamellae and "hockey puck" structures. [70]

Another approach which is currently being explored is the synthesis of rigid-rod star-block copolymers possessing a fixed number of rigid-rod arms. [7] These are synthetic analogues of the self-assembled solution structures discussed in Chapter V.

There are no published research efforts into the adsorption behavior of rod-coil diblock copolymers. Chemisorption studies of end-functionalized PBLG indicate modified adsorption compared with the unfunctionalized PBLG, which adsorbs parallel to the substrate. The end-functionalization served to align the chains more with the normal, although the alignment was not complete. [71-73]

b. Theory of Structure Formation

i. Surface A change in grafting density in tethered coils is associated with a conformational change due to stretching away from the surface. For rigid rods, the conformation is fixed and an ordering normal to the surface results. Tethered, non-interacting rigid rods are predicted to order continuously as the surface density increases. [74, 75] However, if the rods are sufficiently attracted to one another, a first-order orientational ordering transition is predicted to occur. [75] The transition will occur for lower

interaction energies if the rods are also attracted to the surface. [75] At low surface densities the rods lie flat on the surface. As the surface density increases, the rods gradually orient more normal to the surface. If the interaction and adsorption energies are sufficient, the theory anticipates that the rods will jump from a "lying down" configuration to a "standing-up" configuration at a critical surface density. These predictions are summarized in Figure 1.1.

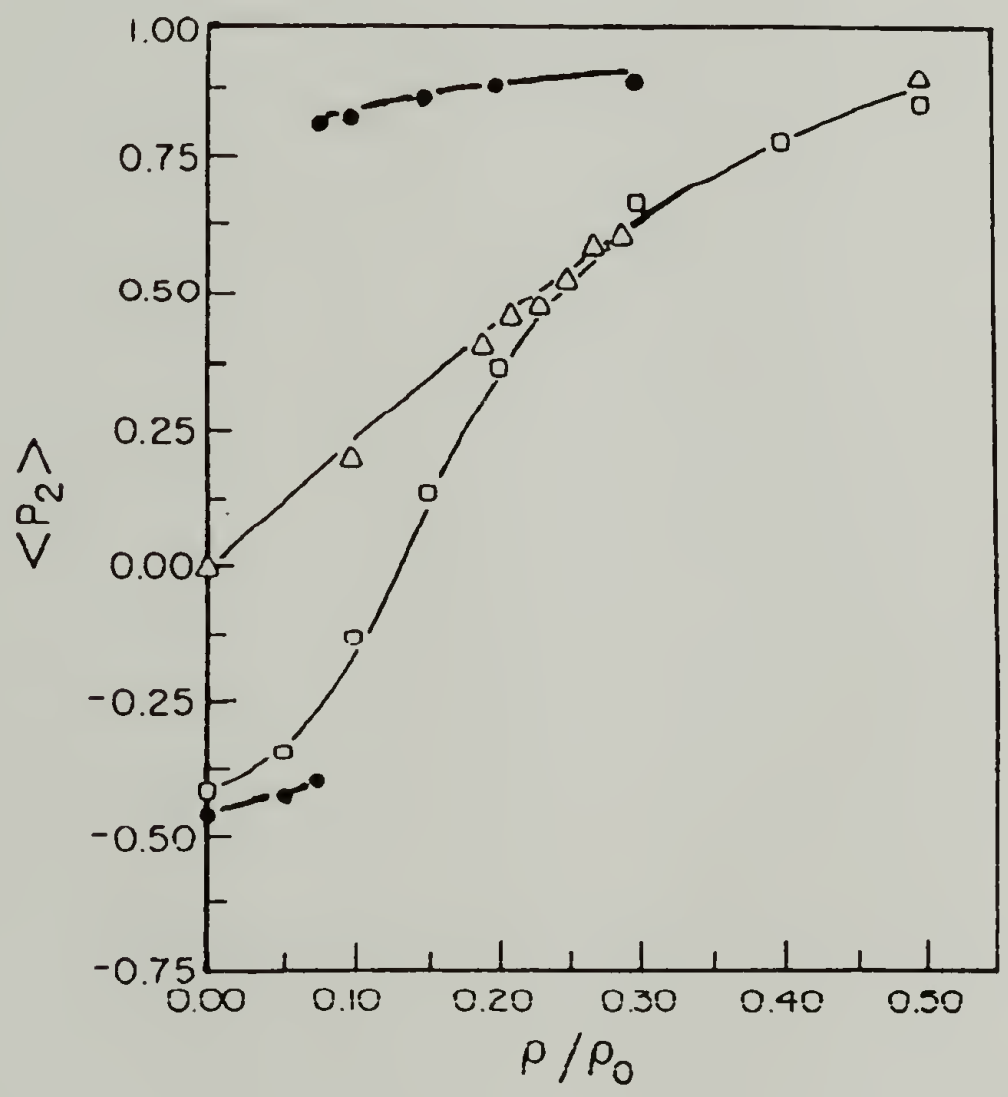

Figure 1.1. Monte Carlo predictions for the orientational ordering parameter as a function of surface density. Attraction between the surface and the rods and intermolecular attraction between the rods is increased above that for the pure hard core case, shown as triangles. Orientational order increases smoothly for low attractions. A first-order phase transition between lying down and standing-up configurations results for larger interaction energies (circles). Surface density is measured relative to that of closest packing. All curves are for an axial ratio of 4. Reprinted from Chen, et al., 1988. [75]

ii. Bulk Intuitively, one would expect the phase diagram of rod-coil diblock copolymers to be substantially different from that of flexible coil-coil diblocks because rods fill space much differently than coils. Lamellae are still expected, but microstructures such as spheres and cylinders would require the radial packing of rods. These microstructures are not expected because of the inability of rods to efficiently fill space radially.

Semenov and Vasilenko have proposed a theoretical phase diagram for melts of rod-coil diblocks which includes monolayer lamellae and bilayer lamellae phases. [76] The important parameters are the relative sizes of the rod and coil blocks and the incompatibility between the two blocks (χ_S). This phase diagram was later modified by Williams and Fredrickson [70] to include both monolayer and bilayer "hockey pucks". Hockey pucks are "cylindrical" micelles which have a core of axially packed rods and a hemispherical corona of coils. The Williams and Fredrickson phase diagram for rod-coil diblock copolymers is shown in Figure 1.2.

Monolayer lamellae are predicted for shorter coils. Lamellae require the greatest degree of coil stretching but achieve the greatest compartmentalization of rods and coils. For moderate χ_S and longer coils, monolayer hockey pucks are more stable than lamellae because of the additional volume available to the coils. Compared with monolayer structures, bilayer structures allow less interaction between the rods and coils but require more coil stretching. Therefore, bilayer hockey pucks are expected for higher χ_S, and for extremely incompatible rods and coils, bilayer lamellae are predicted for all coil lengths.

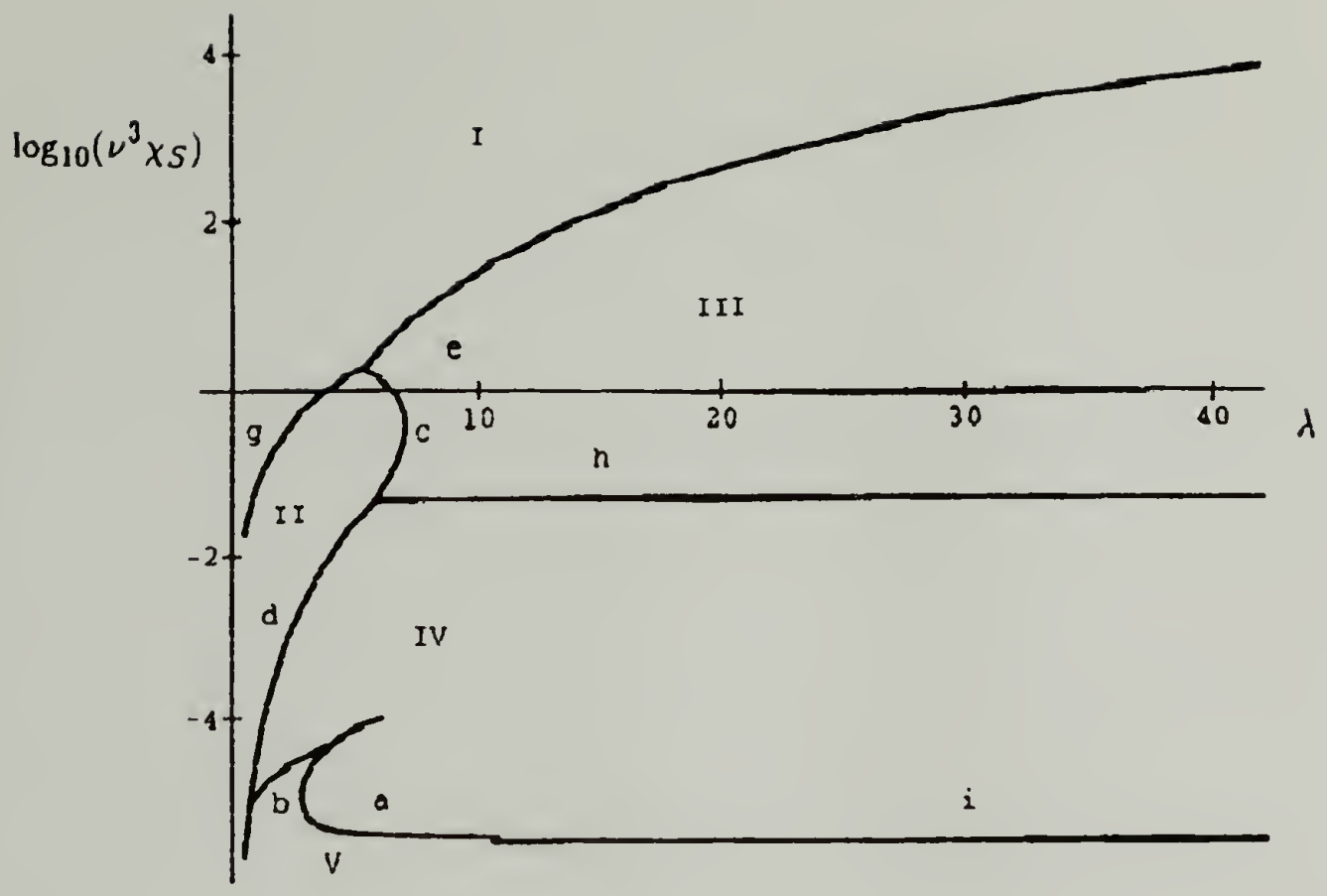

Figure 1.2. Theoretical phase diagram for rod-coil diblock copolymers in the bulk. The phases are (I) bilayer lamellae, (II) monolayer lamellae, (III) bilayer hockey pucks, (IV) monolayer hockey pucks, and (V) incomplete monolayer lamellae. Reprinted from Williams and Fredrickson, 1992. [70]

Tilting of the rod layers in the lamellae and/or the hockey pucks may also provide additional volume for the densely tethered coils. [69] Lamellae of rod-coil diblock copolymers have been predicted to undergo a first-order phase transition between Smectic-A (untilted) and Smectic-C (tilted) rods in a selective solvent, as shown in Figure 1.3. [69, 77] The selective solvent is good for the coil block and poor for the rod block. The tilting transition results from a balance of the stretching energy of the coil blocks ($F_{deformation}$) and the osmotic energy of the rod blocks ($F_{interface}$):

$$F = F_{deformation} + F_{interface} \qquad (1.1)$$

Tilting of the rods in the lamellae causes the surface density in the layer to decrease by a factor of $\cos^2\theta$ where θ is the angle which the rod axis makes with the surface normal. The tilting affects both the rod and coil blocks, Figure 1.3.

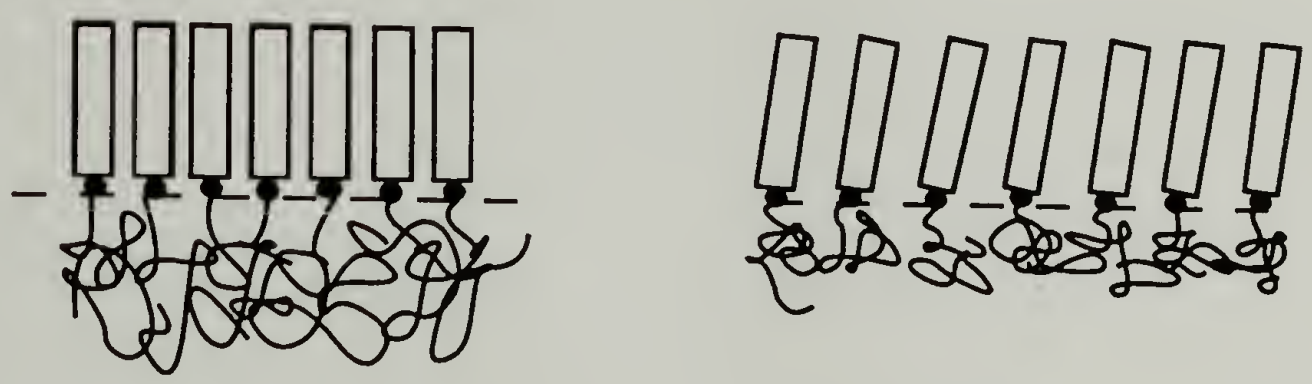

a. Smectic-A b. Smectic-C

Figure 1.3. The rod-coil diblock copolymer first-order tilting transition.

Tilting decreases the stretching of the coils by decreasing the surface density of tethered chains. This lowers the deformation free energy of the system so the coil blocks favor large tilt. The tilt also increases the surface area of the rods in contact with the poor solvent which increases the interface free energy. The rod blocks favor zero tilt because this limits the interaction with the poor solvent. These competing effects can be described in terms of the ratio of the magnitudes of the deformation and interface free energies, δ, for an untilted layer:

$$\delta = F_{interface}(\theta=0) \;/\; F_{deformation}(\theta=0) \qquad (1.2)$$

When the interface free energy term dominates (δ large), the stable structure for lamellae is untilted. A first-order tilting transition occurs at $\delta < \delta_{trans}$ where $\delta_{trans} = 0.26$. The result is a sharp decrease in the lamellar thickness as the rods tilt to an equilibrium angle of 53°. The equilibrium tilt angle increases for values of δ less than 0.26 where the relationship is given as follows:

$$\delta = (5/6) \cos^{11/6}\theta \sin\theta \qquad (1.3)$$

or approximately

$$\theta \approx 1.57 - 1.23\, \delta^{0.58} - 12.1\, \delta^{3.73} \qquad (1.4)$$

The parameter δ may be controlled by changing temperature, solvent quality, or the coil block length. For example, increasing the coil length results in a decrease in δ and therefore an increase in the equilibrium tilt angle in the layer. This has been experimentally observed for rod-coil diblocks in the melt and concentrated solution. [28]

iii. Solution Compared with flexible coil block copolymers, rod-coil diblocks are expected to behave very differently because of the geometric and space filling constraints imposed by the rigid block. As a result, simple spherical micelles are not likely to form and, moreover, the structures in coil-selective solvents are expected to be dramatically different from those in rod-selective solvents. [70] There has been no theoretical work concerning rod-coil block copolymers in rod-selective solvents.

In a selective solvent for the *coil*, each aggregate is predicted to form a cylindrical core of axially-packed rods and two semi-spherical caps of coils. [70, 77] The core can either be formed by interpenetrating rods ("monolayer pucks") or by rods packed end-to-end ("bilayer pucks") as depicted schematically in Figure 1.4. The aggregation number is predicted to scale linearly with the length of the rod block. [77] The equilibrium aggregate structure is expected to be a function of both the rod and coil lengths. Lamellae and "needles" have been proposed for coil-rod-coil triblocks in a selective solvent for the coils. These microstructures are only expected to occur if the concentration is greater than a critical concentration. The microstructure depends on the relative lengths of the blocks. Large rods favor lamellae and shorter rods favor large needles. [78]

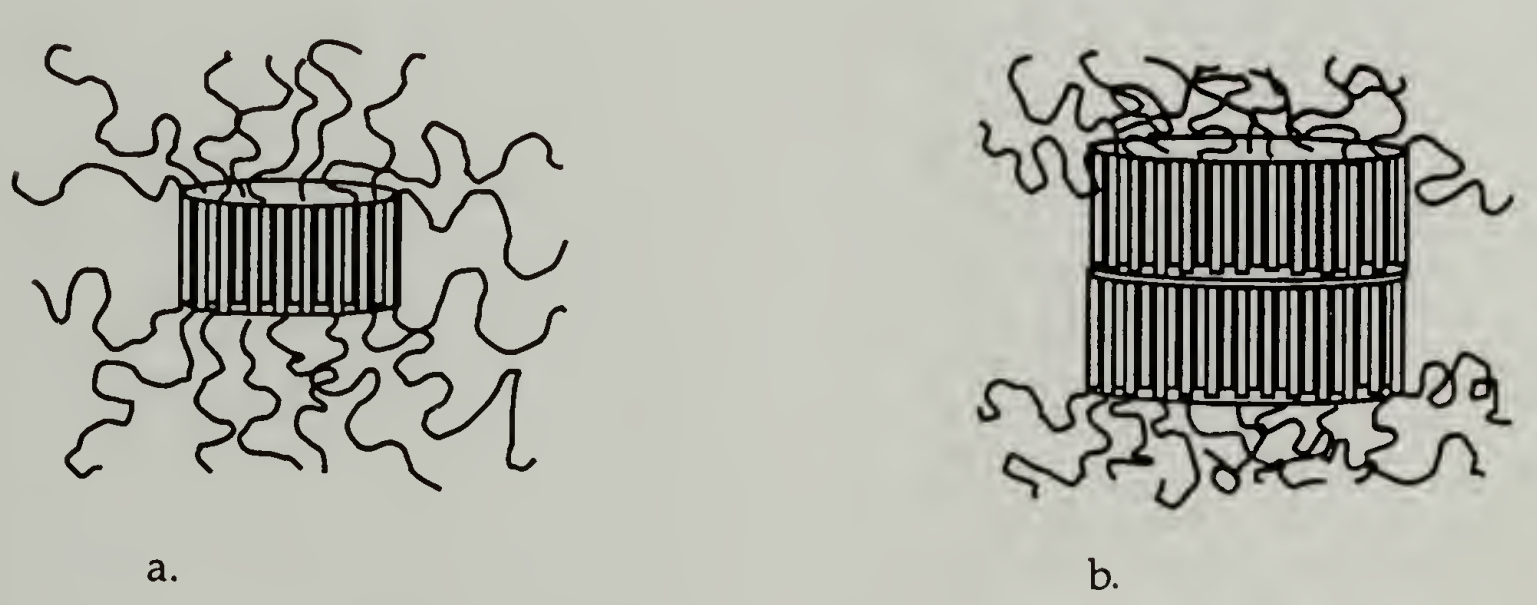

Figure 1.4. Predicted structures for rod-coil diblock copolymers in a coil-selective solvent: (a) monolayer "hockey puck", (b) bilayer "hockey puck".

c. Potential for Rod-Coil Diblocks

Novel structures emanate from the geometric diversity of rod-coil diblocks. This work focuses on the diverse nanoscale polymeric building

blocks which self-assemble from rod-coil diblocks in selective solvents. These building blocks may then serve as components in a complex supramolecular structure, such as a synthetic enzyme. The structure of rod-coil diblock and triblock copolymers in selective solvents may also lead to modified storage and display devices. [79] For example, micellar aggregates may be useful as fast-working ferroelectric and paraelectric media for electrooptic devices. [69, 77] If the proposed structure of "hockey puck" micelles proves to be the correct structure for rod-coil block copolymers in coil-selective solvents, then the dipoles of the highly-ordered cores of these micelles could be aligned with electric or magnetic fields. Compared with liquid crystalline melts, the alignment of the dipoles would be fast because of the lower viscosity of the micellar solutions.

This work also investigates the organization of a model rod-coil diblock at an impenetrable surface. Tethered rod structures are potentially useful for imparting surface biocompatibility [28] and as model systems for biological membranes and surfactant monolayers. [80] Molecularly thin, surface layers with a precise thickness and an exact placement of functionalities are possible. In addition, adsorbed rods are expected to result in dramatically different colloidal stabilization. Rods may tilt or interpenetrate to alleviate the compressive stresses. Both tilting and interpenetration are basically prohibited effects in adsorbed coils because the chains will simply retreat from their stretched state and become more coiled as the surfaces are compressed. [33]

Other motivations for studying rod-coil diblock copolymers derive from the commercial importance of coil-coil diblock copolymers, the desire to test the theoretical predictions developed for rod-coil diblocks, [37-41, 69, 70, 77, 78] and the potential for new ways to exploit the liquid crystallinity of rod-like

polymers. For example, liquid crystals are important reinforcing components, [65, 81] but their usefulness suffers from the incompatibility of the rods in the (coil) matrix. Rod-coil diblocks lead to single-component molecular composites which are molecularly mixed. [30, 31, 67, 68] In addition, rod-coil diblocks and coil-rod-coil triblocks may also find applications as novel thermoplastic elastomers [78] and adhesives.

The potential of rod-coil block copolymers notwithstanding, theoretical and experimental developments in the field of rod-coil block copolymers are extremely limited. Experimental investigations have highlighted the influence of chain rigidity on the bulk and concentrated solution microstructures. [23, 26-28] The goal of this dissertation was to study the previously unexplored area of rod-coil diblock copolymers in dilute solution and at interfaces and the interesting and useful structures which develop.

B. Dissertation Objectives and Overview

This doctoral thesis probes a relatively unexplored area: rod-coil diblock copolymers. Rods have a *single* 3-dimensional structure. Order in the molecules leads to order in macromolecular aggregates and eventually order in supramolecular structures. This work focuses on the formation of macromolecular structure in solution and at interfaces. Polyisoprene-poly(γ-benzyl-L-glutamate) (PI-PBLG) rod-coil diblock copolymers have been studied in environments which force the chains to "self-assemble" into a variety of energetically favored structures. Appropriate cross-linking steps are expected to result in useful macromolecular building blocks.

The rod imparts much of the unique character associated with rod-coil diblocks. The α-helix rod chosen in this study has a dipole oriented along the

helix axis. Chapter II discusses the effect of the α-helix dipole on the energetics of assembly of various structures: parallel, anti-parallel, head-to-head, and head-to-tail. A mathematical model was developed to predict the coulombic energy as a function of separation, chain tilt, and molecular weight for a pair of parallel helices. A Biosym computer simulation was used to corroborate these results, to extend the analysis to other arrangements, and also to predict the van der Waals energy profile.

A prerequisite to certain rod-coil structures is the *parallel*, side-to-side arrangement of α-helices. This arrangement was expected for rods adsorbed onto a solid surface by one end and for monolayer hockey-puck micelles. The ability of these structures to form depends on the relative magnitudes of the van der Waals and the coulombic energies which are attractive and repulsive, respectively.

In addition, the modeling was extended to include the energetics of end-to-end associations. This was essentially a simulation of a surface forces experiment on adsorbed α-helices. The range of interactions and the onset of repulsive interactions have implications for colloidal stabilization.

Chapter II highlights many of the unique properties a-helix rods can impart to a system. Rod-coil diblock copolymers are the subject of the experimental work of this thesis. Chapter III describes the synthesis of a series of ten poly(γ-benzyl-L-glutamate)-polyisoprene rod-coil diblock copolymers. The unique characteristics of rod-coil diblock copolymers preclude most conventional purification techniques. A novel purification strategy for rod-coil diblock copolymers is described.

Chapter IV details the relevant theory, procedures, and data analysis employed for the experimental techniques used in this work: dynamic and

total intensity light scattering, differential refractometry, transmission and reflectance infrared spectroscopy, and ellipsometry.

Chapter V discusses the characterization of PI-PBLG diblocks copolymers in solution using light scattering methods. The hydrodynamic radius and radius of gyration are presented as functions of block length for three solvent systems: rod-selective, coil-selective, and non-selective. Predictions of structure in solution are made based on empirical predictions of the hydrodynamic radii, the ratio of radii of gyration to the hydrodynamic radii, and differential refractive index measurements. Comparisons to theory are made.

Chapter VI discusses the surface microstructures of these highly segregating rod-coil diblock copolymers. The goal was to organize a surface layer of rigid rods through selective adsorption of a rod-coil diblock copolymer. The experimental conditions were chosen to enhance the incompatibility of the blocks by using a solvent which was a non-solvent for the coil block and a good solvent for the rod block. Selective adsorption of the anchor block (coil) onto the substrate and the tethering of the rods normal to the surface was expected.

Chapter VII summarizes the solution and surface structures which were studied in this work. The final chapter proposes future experimental and theoretical work which could shed light on other aspects of rod-coil block copolymer structure.

CHAPTER II

MODELLING

Rod-coil diblock copolymers attain much of their unique structure because of the geometric dissimilarity between the rod and the coil. The rod block used in this work is PBLG which in addition to its structural rigidity derived from its rod-like α-helical structure also possesses a large dipole moment. This characteristic will be useful in attaining unique solution and surface modified structures.

α-Helical polypeptides are known to posses large dipole moments parallel to the helical axis. [82, 83] The objective of this chapter is to ascertain the effect of this dipole moment on the ability of the α-helices to arrange in various orientations. Section A describes an analytical model which has been developed to calculate the effect of the helix dipole on the packing of a monolayer of parallel, unidirectional helices. This is accomplished by calculating the energy of such an assembly. The contributions from surface adsorption energy and dipole-dipole interactions were evaluated. Section B describes the results of a simulation which models the energy profiles of various orientations of two model α-helices, poly(alanine) and poly(methyl glutamate). The van der Waals and coulombic energy contributions as functions of separation were calculated for four α-helix orientations: antiparallel, parallel, head-to-head, and head-to-tail.

A. Analytical Modelling

1. Introduction

An analytical model was developed to calculate the dipole-dipole interaction energy between α-helices self-assembling into a monolayer. This

model was based on the adsorption of a cysteine-terminated poly(γ-benzyl-L-glutamate) (PBLG) onto a gold surface. The glutamic acid precursor to this end-functionalized polypeptide has been synthesized using recombinant DNA techniques; a subsequent benzylation reaction yields the ester. This biosynthetic pathway is unique in that the polypeptide is monodisperse in molecular weight, specific in primary structure, and stereospecific for the L-amino acid isomers. [84]

The single cysteine amino acid residue is at the amino terminus (or N-terminus) of the polypeptide, and it supplies a surface active sulfhydryl group. The sulfhydryl group has been shown to direct the assembly of molecules onto gold surfaces. [85-87] The helices are expected to assemble onto a surface with the functionalized end adsorbed onto the surface and the chains perpendicular or nearly perpendicular to the surface.

The helix dipole is directed from the C-terminus (negative pole) to the N-terminus (positive pole). The restriction of the cysteine residue to the amino terminus of the helix is expected to create a monolayer with a unidirectional alignment of the dipoles, as shown in Figure 2.1.

The model allows the calculation of the energy between two parallel helices modeled as a *line* of dipoles. The energy of the monolayer assembly is based only on the dipole-dipole interaction energy and the substrate binding energy; van der Waals contributions are not considered. A substrate binding energy of 35 kcal/mol is used to represent a cysteine-terminated helix adsorbing onto a gold substrate. [88, 89] The dipole-dipole energy calculation should be valid for any poly(amino acid) which possesses α-helical secondary structure.

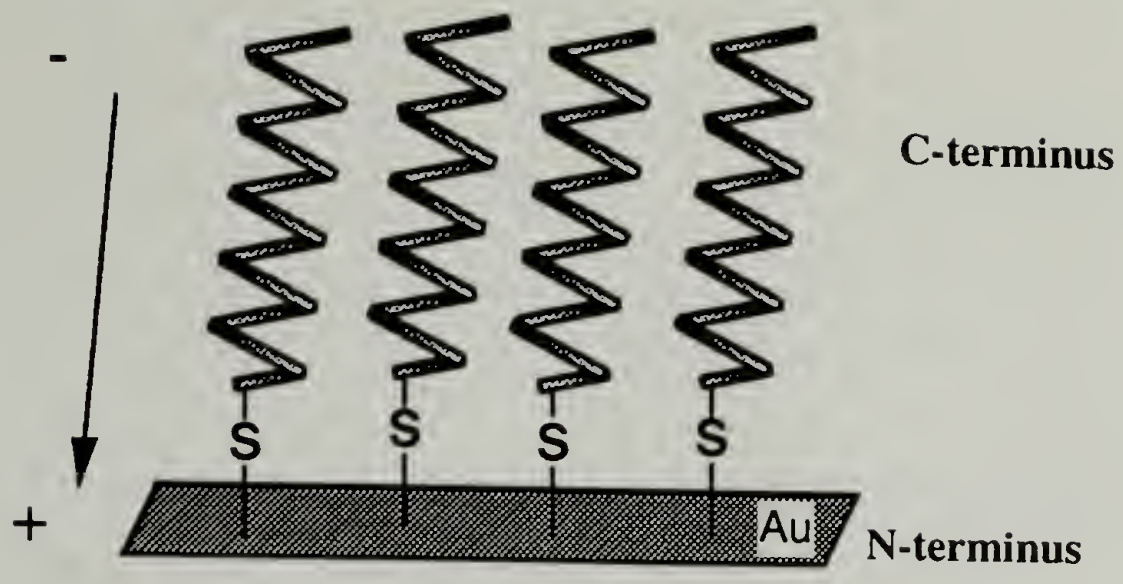

Figure 2.1. Predicted arrangement of the cysteine-terminated helices on a gold surface.

The calculations presented in this section can be extended to the adsorption of PBLG possessing any other "sticky foot." A flexible-coil anchor block in a PBLG diblock copolymer can also serve as a sticky foot. In this case, the adsorption energy would be proportional to the coil molecular weight because the anchor chain fully wets the surface under the action of Van der Waals attraction. [42, 90]

2. Properties of the α-Helix

There are two main types of secondary structure found in biological macromolecules: the α-helix and the β-pleated sheet. [91] These structures are similar in several ways: (1) the atoms of the amide linkage -C-CO-NH-C- lie in a plane (Figure 2.2), (2) the N,H, and O atoms involved in a hydrogen bond lie in a straight line, and (3) all of the amide groups are hydrogen bonded. [91] These structures differ, however, in how the hydrogen bonds are formed. The hydrogen bonding in α-helices is local. β-sheets form non-local hydrogen bonds. [92]

The α-helix is a well-defined spring-like secondary structure in which neighboring amino acid residues are separated by a rise of 1.5 Å and a rotation of 100°. The helix is right-handed and there are approximately 3.6 amino acid residues per turn of the helix. The α-helix structure is stabilized by intramolecular hydrogen bonding between every fourth peptide linkage in the chain.

An α-helix possesses an electric field due to the orientation of the polar amide linkages. This electric field is directed from the C-terminal to the N-terminal of the polypeptide chain. The strict regularity of the α-helix secondary structure aligns the net dipole moment nearly parallel to the helical axis. Wada [93] has calculated the axial component of the dipole moment to be approximately 3.5 Debye per 1.5 Å. The axial component is approximately 98% of the total dipole moment, μ_o, shown in Figure 2.2.

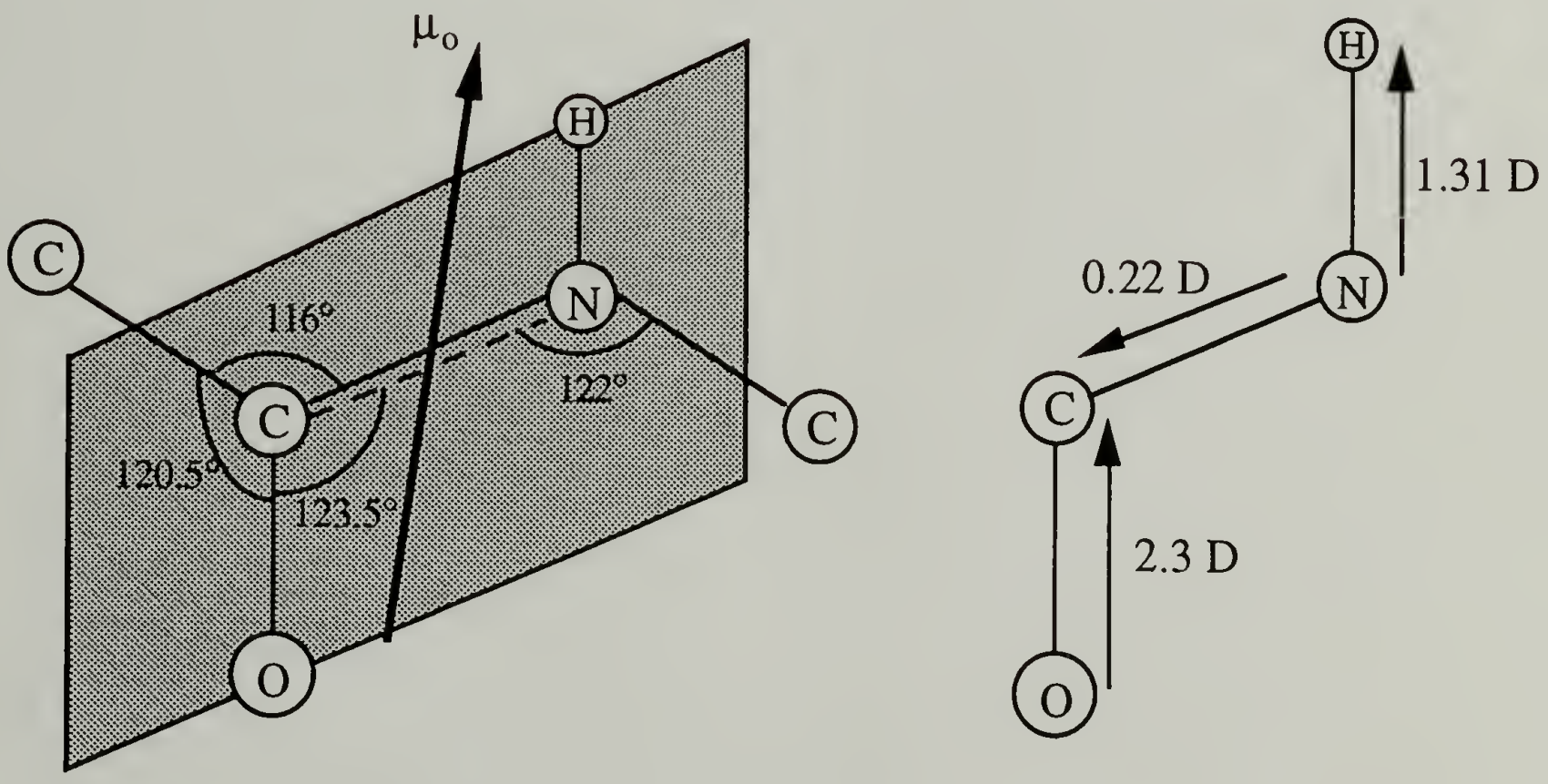

Figure 2.2. The planar peptide linkage of polypeptides and the associated dipole moment, μ_o. As shown at the right, the overall amide dipole moment is due to the bond dipole moments of the C=O, C-N, and the N-H bonds. [92]

3. Dipole-Dipole Interaction Energy

Dipoles are two equal and opposite charges separated by a distance, and dipole moments are the vector representation. The first step in calculating the energy between two helices is to take the simplest case of two isolated point dipoles where a point dipole is one in which the separation between the charges is small. [94] This forms the basis for the calculation of the energy between two helices. If the helices are represented by *lines* of dipoles, then the sum of the interaction energies for all of the dipole pairs is the helix dipole-dipole interaction energy. Appendix 1 schematically explains the modelling of the peptide dipoles as lines of dipoles located at the helical axis.

a. Two Point Dipoles

The general equation for the interaction energy, E, between two point dipoles is shown below in Equation 2.1. [95]

$$E = - \frac{\mu_1 \mu_2}{4\pi \varepsilon_0 \varepsilon_r r^3} [\, 2 \cos\theta_1 \cos\theta_2 - \sin\theta_1 \sin\theta_2 \cos\phi \,] \qquad (2.1)$$

where μ = dipole moment
ε_0 = vacuum permittivity, 8.854×10^{-12} C^2 / J m
ε_r = dielectric constant of the medium
r = separation between dipoles
θ = tilt angle with respect to the substrate
ϕ = splay angle

The orientation angles are represented schematically in Figure 2.3. Equation 2.1 is valid only at separations, r, greater than approximately three times the actual dipole length. [95]

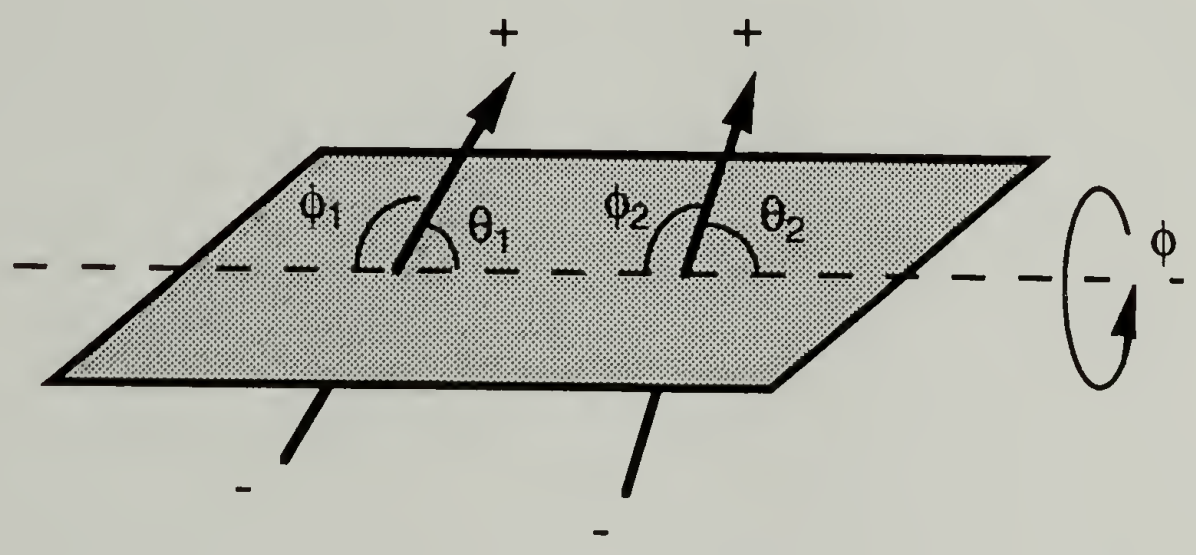

Figure 2.3. Orientation of two dipoles.

Equation 2.1 predicts the greatest repulsive energy when the dipoles are perpendicular to the substrate ($\theta_1 = \theta_2 = 90°$) and at $\phi = 0°$. The like-charges of each dipole are aligned as closely as possible. Equation 2.1 reduces to Equation 2.2 showing that the interaction is repulsive for all values of the separation.

$$E = \frac{\mu_1 \mu_2}{4\pi \varepsilon_o \varepsilon_r r^3} \qquad (2.2)$$

The anti-parallel arrangement ($\theta_1 = \theta_2 = 90°$ and $\phi = 180°$) and the in-line case ($\theta_1 = \theta_2 = 0°$) are the most favorable arrangements. Solving for the anti-parallel case results in Equation 2.3, and solving for the in-line case gives Equation 2.4.

$$E = - \frac{\mu_1 \mu_2}{4\pi \varepsilon_o \varepsilon_r r^3} \tag{2.3}$$

$$E = - \frac{2\mu_1 \mu_2}{4\pi \varepsilon_o \varepsilon_r r^3} \tag{2.4}$$

Equations 2.3 and 2.4 show that for a fixed separation, r, the maximum attractive energy is for dipoles which are in-line. However, if the size and shape of the molecule are such that the anti-parallel arrangement allows the dipole centers to approach more closely, the antiparallel geometry will be preferred.

The situation may be simplified by constraining the dipoles to be parallel and coplanar. These restrictions are accomplished by setting the angle each makes with the substrate to be equal ($\theta_1 = \theta_2$) and allowing no splay between the dipoles ($\phi = 0°$). Since the dipoles are identical to one another, the equation can be further simplified by setting $\mu_1 = \mu_2$. The equation now reduces to the following:

$$E = \frac{\mu^2}{4\pi \varepsilon_o \varepsilon_r r^3} (1 - 3 \cos^2 \theta) \tag{2.5}$$

Equation 2.5 shows that at a tilt angle of 54.7°, the attractive and repulsive contributions to the energy are equal and the net energy is zero for all separations. Tilt angles greater than 54.7° result in a net repulsive interaction; tilt below this angle results in a net attractive interaction.

b. α-Helix as a Line of Dipoles

Equation 2.5 is valid for two *single* point dipoles under the given conditions. In order to evaluate the dipole-dipole energy between two *lines* of dipoles, equation 2.5 must be expressed as a sum of the energies for all of the dipole pairs. Equation 2.6 defines the energy, E, between two lines of dipoles.

$$E = \frac{\mu^2}{4\pi \varepsilon_o \varepsilon_r} \sum_{i=0}^{m} \sum_{j=0}^{m} \frac{1}{r_{ij}^3} \left(1 - 3 \cos^2 \theta_{ij} \right) \tag{2.6}$$

The dipoles on each chain (i, j) are numbered from 0 to m where there are *m+1* dipoles per chain. The term θ_{ij} is the angle between each dipole pair (i,j), and is no longer equal to the overall chain tilt angle, now referred to as Θ.

Equation 2.6 was solved by separating the summation of *i* into three regimes: $i = j$, $i > j$, and $i < j$. This separation of terms was necessary because in each regime the equations for the distance and angle between the dipoles were different. This is shown in Appendix 2. Equation 2.6 is solved in detail in Appendix 4, and the solution for the energy between two lines of dipoles is shown as Equation 2.7.

$$E = \frac{\mu^2}{4\pi \varepsilon_o \varepsilon_r} \left[\frac{(L+a)(l^2 - 2z^2)}{a(z^2 + l^2)^{5/2}} + \frac{2}{a^2} \frac{1}{(z^2 + l^2)^{1/2}} - \frac{1}{a^2} \left[\frac{1}{((L-z)^2 + l^2)^{1/2}} + \frac{1}{((L+z)^2 + l^2)^{1/2}} \right] \right] \tag{2.7}$$

The axial distance between dipole centers is *a* so that the chain length, L, is equal to *ma*. The new parameter, l, is the perpendicular spacing between the helices. A register shift term, z, is used to define the angle which the chain makes with the substrate, as shown in Appendix 3.

4. Model Assumptions

The model assumes that the dipoles are located at the helical axis. This is considered to be a realistic assumption for helices at large separations. However, the peptide dipoles are actually located at the surface of a 6Å cylinder, not at the center. Some of the dipoles will be at zero separation when the separation between axes is 6Å. It will no longer be justified to assume that the dipoles reside at some average location. Ignoring the exact location of each dipole results in a significant error in the calculation. The energy between two dipoles is inversely proportional to the cube of the distance between them. As the separation approaches the diameter of the helix backbone some of the dipoles approach zero separation and the repulsive energy should diverge toward infinity. Equation 2.7 cannot predict this result.

The excluded volume effect must also be considered. The chains cannot pack closer than the helix diameter or they occupy the same space at a given time. This problem is resolved by arbitrarily prohibiting the perpendicular distance between helical axes to be less than 15 Å. Helices restricted in this way are termed "constrained helices". Likewise, helices which can acquire any separation, even if it is beyond the hard-core limit, are termed "unconstrained helices". The separation value of 15 Å is based on the geometric diameter (as opposed to the larger hydrodynamic diameter) of an α-

helical molecule of poly(γ-benzyl-L-glutamate) [96-100] and assumes no side-chain interpenetration.

Another assumption of the model is that the dipoles can be approximated as point dipoles. This approximation is necessary for two reasons. Equation 2.1 is valid only for point dipoles, and the helix dipole calculation was based on this equation. Second, the solution of Equation 2.6 relied on approximating the sums as integrals. This is valid only if the dipoles are very small in comparison to the length of the helix; point dipoles satisfy this requirement.

5. Graphical Analysis of the Dipole-Dipole Interaction Energy

Equation 2.7 is represented graphically in Figures 2.4 through 2.9. The values in Table 2.1 were used in the solutions. The choice of these parameters affects the magnitude of the energies calculated, but does not affect the general trends that are seen.

Table 2.1. Parameters used for the graphical analysis of Eqn. 2.7.

L	Helix length	300 Å
l	Perpendicular distance between chains	
	constrained helices	> 15 Å [96-100]
	unconstrained helices	---
a	Intrachain distance between dipoles	1.5 Å [101]
ε_r	Dielectric constant of medium	
	dichloromethane	9.08 [102]
E_{surf}	Surface interaction energy	
	thiol-gold	35 kcal/mol [88, 89]

It has been assumed that the dielectric constant of the medium is equal to the dielectric constant of the solvent from which the helices adsorb. This assumption neglects the dielectric contribution of the helices, however the solvent-induced dipole effects are taken into account by using experimental values for the dipole moment.

In addition, hexagonal packing of the helices was assumed because this type of packing has been observed for small molecule thiols adsorbing onto gold surfaces. [88, 89] The area per chain for hexagonal packing is related to the surface spacing, s, as shown in Equation 2.8:

$$\text{Area / Chain} = \frac{\sqrt{3}}{2} s^2 \tag{2.8}$$

The assumption of hexagonal packing affects the magnitude of the monolayer energy. Equation 2.7 gives the energy between a single pair of helices. Each chain has 6 nearest neighbors, each of which will contribute to the dipole-dipole interaction energy. The total monolayer energy per chain is 3 times the energy of an isolated helix pair. It is not 6 times the energy of a pair or each helix pair (i, j) would be counted twice. The pair would be counted once when considering the energy due to helix i and counting helix j as one of its 6 neighbors and again when considering the energy due to helix j and counting helix i as its neighbor.

a. Unconstrained Helices

The dipole-dipole interaction energy as a function of the area per chain is plotted in Figure 2.4 for various chain tilts. The helices were unconstrained meaning that a helix occupies no volume and a zero separation between axes

is allowed. This plot shows the general behavior of the dipole-dipole interaction between two lines of dipoles. At large spacings between helices the energy is approximately zero for all tilt angles. As the area per chain is decreased, the energy becomes non-zero and the magnitude and sign of the energy become strong functions of chain tilt. The most strongly repulsive interaction is at $\Theta = 90°$ or when the helices are perpendicular to the surface. Decreasing the tilt angle decreases the energy. This condition is similar to that of two point dipoles, given by equation 2.2, where the maximum repulsive energy is a result of the like-charges of the dipoles being in their closest arrangement.

b. Constrained Helices

Figure 2.5 shows the dipole-dipole energy as a function of area per chain for constrained helices; the spacing between axes is constrained to be greater than or equal to 15 Å. This plot reveals information about the packing of *real* helices. The helices cannot overlap so certain packing arrangements are no longer accessible. Each of the allowed arrangements results in a net repulsive interaction. Increased chain tilt requires an increased minimum surface spacing between chains.

Figure 2.6 shows the dipole-dipole energy, surface interaction energy, and the system energy for a tilt angle of 90°. This plot compares the magnitude of the dipole energy to the surface energy. It would seem that the lowest energy configuration is at the highest area per chain, implying that the chains would never pack into a dense monolayer. Plotting energy *per unit area* constrains the system so that it does not tend toward the situation of two

chains adsorbed infinitely far from one another. This situation does have the minimum energy per chain, but does not minimize the energy per unit area.

The system energy per unit area decreases with chain spacing as shown in Figure 2.7. Closest packing maximizes the number of *attractive* surface interactions per unit area and also maximizes the *repulsive* dipole-dipole energy. The latter is a significantly smaller contribution so it is energetically most favorable for chains to pack as closely as possible.

The system energy per unit area for constrained helices at various tilt angles is plotted as Figure 2.8. The lowest energy arrangement is for helices 15 Å apart and perpendicular to the substrate. At this spacing, only the tilt angle of 90° is allowed. Increasing the spacing allows progressively smaller tilt angles. The lowest energy arrangement at a given spacing is that of the lowest accessible tilt angle. The arrangement which the helices assume will be dictated by the spacing between binding sites of the substrate. For example, if the substrate binding sites are 6 Å apart, the minimum spacing at which the 15 Å helices can assemble is 18 Å. The substrate will determine the surface spacing, and the dipole-dipole interaction will determine the tilt. In this example, at a spacing of 18 Å (area per chain equal to 280 $Å^2$), the chians would tilt at 50° based on Figure 2.5.

Figure 2.9 shows the dependence of the system energy on the surface interaction energy. This plot shows that the surface interaction energy is the stronger contributor to the system energy. As the surface interaction energy decreases, it is less energetically favorable for a close-packed monolayer to form. The system energy at small chain separations is repulsive when the chain-end/substrate interaction energy is less than -5 kcal/mol. There is an energy minimum at -10 kcal/mol which is not seen in the other curves. This suggests that for surface energies near this value the packing arrangement of

the monolayer is energetically driven. A surface energy of -5 kcal/mol is predicted to be the limiting value for forming the proposed monolayer.

6. Conclusions

Dipole-dipole interactions are repulsive for all of the excluded volume configurations (l_{min} = 15 Å) of an α-helix modeled as a line of dipoles. Chains will tilt as far as allowed by hard-core repulsions because this results in the lowest dipole-dipole energy. The dipole-dipole interaction will determine the tilt angle for a given surface spacing. However, the configuration of the layer (s and Θ) will ultimately be directed by the substrate because the substrate will determine the surface spacing.

A surface interaction energy of greater than -5 kcal/mol is sufficient to overcome the repulsive dipole-dipole interaction energy. The helices are predicted to form a close-packed monolayer of parallel helices because this maximizes the surface density and the number of substrate/chain-end interactions. From this model, it is predicted that end-functionalized helices will self-assemble onto appropriate substrates.

B. Molecular Dynamics Modelling

1. Introduction

A Biosym molecular modelling software package (INSIGHT) was used to analyze the van der Waals and Coulombic energies between pairs of α-helices. This simulation served three purposes: (1) to compare the results with the analytical model presented in the previous section, (2) to account for the three-dimensional location of the atoms and bonds in the helices, (3) to include the van der Waals contribution. The energies (in vacuum) between

pairs of α-helices as a function of separation, orientation, and residues per chain were calculated. Polyalanine chains were used to represent the backbone dipole moment of PBLG and poly(methyl glutamate) (PMG) was used to represent the dipole moment of both the side-chains and the backbone of PBLG.

The simpler PMG polypeptide was substituted for PBLG because the structure minimization was more straightforward; the tilt angle of the phenyl rings was not an issue. The PMG model polypeptide should have a coulombic energy profile similar to PBLG because both possess the two major α-helix dipole components: the main-chain moment due to the peptide linkage and the side-chain moment due to the ester linkage. The van der Waals contribution will be slightly affected by the methyl/benzyl substitution. First, the diameter of PMG is approximately 5Å smaller than PBLG. Second, the phenyl rings will contribute significantly to the van der Waals energy, especially if the rings in the side-chains are stacked.

Four orientations of α-helix pairs in vacuum were modeled. Two side-to-side orientations (parallel and anti-parallel) model the energy required to assemble a monolayer of helices at a surface. The end-to-end orientations (head-to-tail and head-to-head) model the energy *between* two adsorbed layers of helices. Energetics of side-to-side and end-to-end associations are also important in the solution behavior of these molecules; i.e. liquid crystallinity and gelation.

2. Theory and Methodology

The PMG helices were constructed by bonding the desired number of residues of glutamic acid. Methyl groups were bonded to the side-chains, and

the potential types on the side-chain carboxylic acid were modified to those for an ester. [103] The formal charge was set to 0.00, and the torsion angles were manually assigned as 140, 180, and 115° for N-Cα-C-N, Cα-C-N-Cα, and C-N-Cα-C. The backbone structure was minimized by using 250 steps of steepest descents followed by 250 steps of quasi-Newton-Raphson. Next, the entire molecule was minimized with 250 steps of steepest descents. A copy of the molecule was made and pseudo-atoms were defined by using four carbonyl carbons. A distance monitor was set to measure the distance between the pseudo-atoms. A docking algorithm was used to measure the non-bonded intermolecular energy.

Polyalanine was constructed and analyzed similarly. Alanine residues were directly available in the residue library.

3. Side-to-Side Orientation

a. Polyalanine

Polyalanine was used to model the backbone contribution to the dipole moment of α-helical polypeptides. The simulation was performed using a pair of helices possessing 18 repeat units; this corresponds to five complete turns of an 18/5 helix. As expected, the coulombic energy is always repulsive (positive) for the parallel orientation and attractive (negative) for the anti-parallel case, as shown in Figure 2.10. This plot also shows the effect of helix length on the coulombic energy for both parallel and anti-parallel orientations. Results are shown for 10, 15, and 18 repeat units of polyalanine, corresponding to helix lengths of 15, 23, and 27Å. The helix length dependence is weak.

Figures 2.11 and 2.12 show how the coulombic and van der Waals energies vary with separation for polyalanine helices oriented anti-parallel and parallel, respectively. The coulombic energy is always attractive for the anti-parallel orientation. The van der Waals contribution dominates at small separations, and therefore controls the predicted separation. For the parallel orientation, the coulombic energy dominates at large separations, but the van der Waals energy begins to dominate strongly at small separations (approx. <11Å) such that the minimum total energy is near the van der Waals hard core limit. The parallel orientation is only allowed in a range of separation from 9 to 11 Å, although the maximum barrier to association at larger separations is only about 2 kcal/mol.

A surface interaction energy of -35 kcal/mol is included in the analysis of the association energy of polyalanine helices. This is included to model the energetics of adsorption of a thiol-terminated helix onto a gold substrate. Figure 2.13 shows that adsorption will be energetically possible at all surface densities, as opposed to the situation in Fig. 2.12 in which the surface adsorption energy was zero and adsorption was only predicted for a 2 Å window of separations. The surface energy provides the energetic "bridge" for organization at larger separations, i.e. before the van der Waals energy becomes important. Furthermore, helices will assemble into a close-packed monolayer because the surface energy benefit increases as the packing density increases; the van der Waals contribution stabilizes the close-packed arrangement.

b. Poly(Methyl Glutamate)

Both the backbone and the side-chain contributions to the dipole moment of PBLG are modeled with poly(methyl glutamate). While the

orientation of the side-chain dipole moment has been a subject of debate, [82, 83, 104, 105] infrared spectroscopy of oriented PBLG films and NMR investigations of the spin-lattice relaxation times of side-chain atoms suggest a random orientation of side-chain carbonyls. [104-108] An analysis of PMG which parallels that for polyalanine is presented in this section.

The coulombic energy as a function of separation and chain repeats is shown in Figure 2.14 for PMG helices oriented side-to-side. The parallel and anti-parallel orientations have approximately equal and opposite coulombic energy profiles. The total energy (coulombic energy and van der Waals) for the anti-parallel and parallel side-to-side orientations of PMG (18-mer) helices are shown in Figures 2.15 and 2.16, respectively. The anti-parallel case is allowed at all packing densities. As for polyalanine, the coulombic energy dominates at large separations and the van der Waals dominates at small separations so that there is a very small region of energetic stability at close-packing for the *parallel* case. The predicted lowest energy separations for both orientations are approximately the same, 17Å. This is because the van der Waals energy is dominating at close separations. Parallel, side-to-side association of PMG is predicted to be stable for separations between the hard-core limit (center-to-center separation of 16Å) and 18Å, although the barrier to association at larger separations is less than 1 kcal/mol.

Comparison of PMG and polyalanine energies can be made by comparing Figs. 2.16 and 2.12. The van der Waals energy at the hard-core limit is approximately -20 kcal/mol for polyalanine, but only approximately -3.5 kcal/mol for PMG. This difference is likely due to the larger helix diameter of PMG caused by the relatively long side-chains. The coulombic energies for the two cases are also quite different: 6 kcal/mol for polyalanine and 2.5 kcal/mol for PMG. This is also consistent with the greater separation

between the helix centers which decreases the dipole-dipole interaction energy.

A surface energy contribution of -35 kcal/mol is included in the analysis of PMG shown in Figure 2.17. This situation models the adsorption of thiol-terminated PBLG helices onto gold surfaces. The surface energy controls the magnitude of the total energy; the coulombic and van der Waals energies are weak in comparison. Dense-packing is predicted.

Figure 2.18 shows the effect of solvent on screening the dipole-dipole interaction. The coulombic energy was scaled by the dielectric constant of N,N-dimethylformamide (36.7) to approximate the behavior in this solvent. Inclusion of the dielectric constant causes the coulombic energy to be negligibly small compared with the van der Waals energy.

Figure 2.19 graphically demonstrates the accuracy of the determinations of the van der Waals and coulombic energies. Two parallel, 18-mer PMG chains were measured at three center-to-center separations: 25.1, 17.1, and 16.7 Å. The smallest separation is within 1Å of the hard core separation limit. The differences between the maximum and minimum separations were 0.1Å, and were apparently due to a slight tilt angle between the helices. The fluctuations in the energies increase as the separation between helices decreases. This trend is not unexpected if the discrete locations of the long side-chains are considered as well as the steeper slopes in the energy profiles at small separations, especially for the van der Waals energy. The 0.1Å oscillation in the separation becomes more important as the separation decreases. The effect of rotation on the energies were to affect errors of 0.05, 0.4 to 0.6, and 0.6 to 0.8 kcal/mol for the three separations.

c. Summary

This section has focused on understanding the relative magnitudes of the van der Waals and coulombic energies for parallel and anti-parallel orientations of α-helices. The reults are trivial for the anti-parallel case because the van der Waals and coulombic energies are both attractive; the most favorable separation is at the van der Waals hard-core limit. The parallel cases showed extremely narrow energetically accessible separation windows: 9-11Å center-to-center separation for polyalanine and 16-18 Å for poly(methyl glutamate). The adsorption energy (-35 kcal/mol) more than compensates for the repulsive dipole-dipole interaction and all separations are energetically available. Close-packing is most favorable. Similarly, inclusion of the solvent dielectric constant (36.7 for DMF) in the magnitude of the coulombic energy results in negligibly small dipole-dipole interaction energies at all separations. Therefore, α-helices are predicted to be able to overcome the coulombic energy barrier of parallel orientation if they are in a sufficiently polar solvent or if the adsorption energy term is sufficiently large.

4. End-to-End Orientation

a. Polyalanine

Figure 2.20 shows the coulombic energy as a function of separation for two orientations of polyalanine helices (n=10, 15, and 18): head-to-head and head-to-tail. In both cases, the coulombic energy is of the same order of magnitude as for the side-to-side orientations (Fig. 2.10). Two carboxylic acid ends are brought into contact in the head-to-head case. The dipoles oppose

one another, and therefore the coulombic energy is repulsive at all separations. The carboxylic end of one helix and the amine end of the other helix are brought into contact in the head-to-tail case. The dipoles are oriented in the same direction, and the coulombic energy is always attractive.

The dipole-dipole interaction is dependent on molecular weight; this result is contrary to published work which claims that only the last several terminal residues affect the dipole-dipole interaction. [109] The difference is due to the fact that the charges were screened by solvent in the simulation by Aqvist et al. and were in vacuum in the present case.

Figures 2.21 and 2.22 show the van der Waals and coulombic energy contributions to the total energy for a pair of 18-mer polyalanine helices oriented head-to-tail and head-to-head, respectively. In both orientations, the coulombic energy is the dominant contributor to the energy; the van der Waals interaction is weak and short-ranged in comparison. The relative magnitudes of the coulombic and van der Waals energies are dramatically different from the side-to-side orientations (Figs. 2.11 and 2.12), in which the van der Waals energy was the dominant influence.

The head-to-tail orientation is energetically allowed at all separations, and most favored at the van der Waals hard-core limit. The head-to-head orientation is not stable at any separation; approximately 4 kcal/mol are required to bring the helices into close contact (approx. 1Å separation).

b. Poly(Methyl Glutamate)

Figures 2.23-2.25 show the analogous information for poly(methyl glutamate). The end-to-end orientations show anomalous behavior in that the magnitude of the coulombic energy is not much lower than for the case of

polyalanine, see Figs. 2.23 and 2.20, respectively. One would expect the energy to be lower for the PMG helices since the direction of the dipole moment of the backbone opposes the side-chain moments resulting in a smaller overall dipole moment. However, the van der Waals and coulombic energies are more balanced at small separations than for polyalanine. The same orientational stability behavior is observed.

C. Comparison of Analytical Model and Simulation

In this section, the agreement between the analytical model of Section A and the Biosym computer modelling of Section B is analyzed. The analytical model considered the parallel, side-to-side orientation of helices. Helix length, solvent environment (i.e. dielectric constant), dipole moment, degree of tilt, and separation are variables which can be defined. The Biosym modelling was performed for helices in vacuum.

Figure 2.26 compares the analytical model with the Biosym coulombic energy prediction for parallel, 18-mer polyalanine helices. The computer simulation was done in vacuum, so the results should compare with the literature value of the dipole moment for polyalanine, 4.5 D. [82, 83] Compared to the Biosym simulation, the equation for the dipole-dipole energy overestimates the energy. This seems to indicate that the value for the dipole moment for the helix backbone is too high. The simulation data fits well to a value of $\mu = 2.2$ D.

Figure 2.27 compares the simulation results for the coulombic energy of parallel 18-residue PMG helices in vacuum to the analytical model. A value of 2.3 D was used for the vacuum dipole moment of PMG. [82, 83] The equation fits the data very well. The interpretation of this data as compared

with the polyalanine data implies that the side-chain contribution is negligible. A backbone dipole moment of 2.2 D fits the polyalanine simulation data. A dipole moment of 2.3 D fits the PMG data. Therefore, the only contribution to the helix dipole is inherent in the backbone. This is consistent with a random orientation of side-chain carbonyls in the simulated molecules as suggested by infrared spectroscopy and NMR results. [104-108]

The equation for the dipole-dipole energy was expected to be poorly approximated by the line of dipoles model, especially at small separations. This is due to the fact that the dipole moment in the mainchain and the side-chain were averaged and assumed to reside at the helix axis. As the separation between chains decreases, the averaging of the dipole moments becomes a progressively poorer approximation.

Treating the helix as a string of dipoles overestimates the coulombic repulsion energy as compared to the Biosym simulation. The simulation was for two chains in vacuum so the measured coulombic energy is greater than the real case in which the dipoles would be screened by solvent. Even overestimating the coulombic energy, the chains are predicted to densely pack because the van der Waals energy becomes the dominant contribution to the total energy at small separations. Including the dielectric screening and the surface adsorption energy would further support the prediction of dense packing.

D. Conclusion

Modelling of the α-helix dipole has shown that the coulombic interaction plays an important role in the relative stability of parallel and antiparallel orientations. The antiparallel orientation is more energetically

favorable at all separations. In a system involving only coulombic and van der Waals interactions in vacuum, parallel orientations are only energetically allowed for a small range of separations. Antiparallel orientation of helices are predicted for rod-coil diblock copolymer aggregates in solution. At surfaces, end-functionalized helices (including rod-coil diblocks with an adsorbing coil block) are predicted to adsorb into parallel orientations if the adsorption energy is sufficiently high.

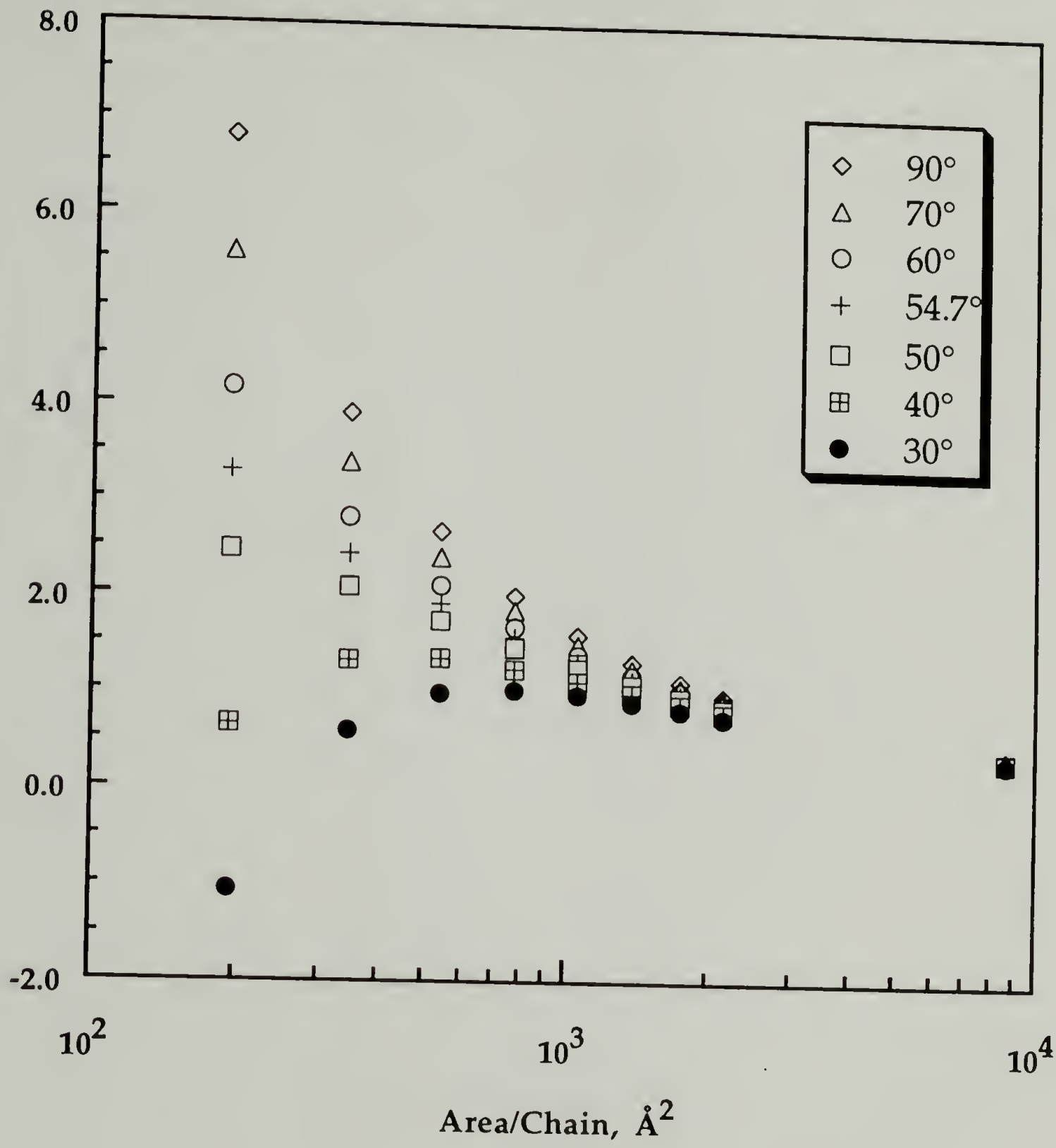

Figure 2.4. Dipole-dipole interaction energy as a function of area per chain, calculated for different values of the tilt angle, for unconstrained helices.

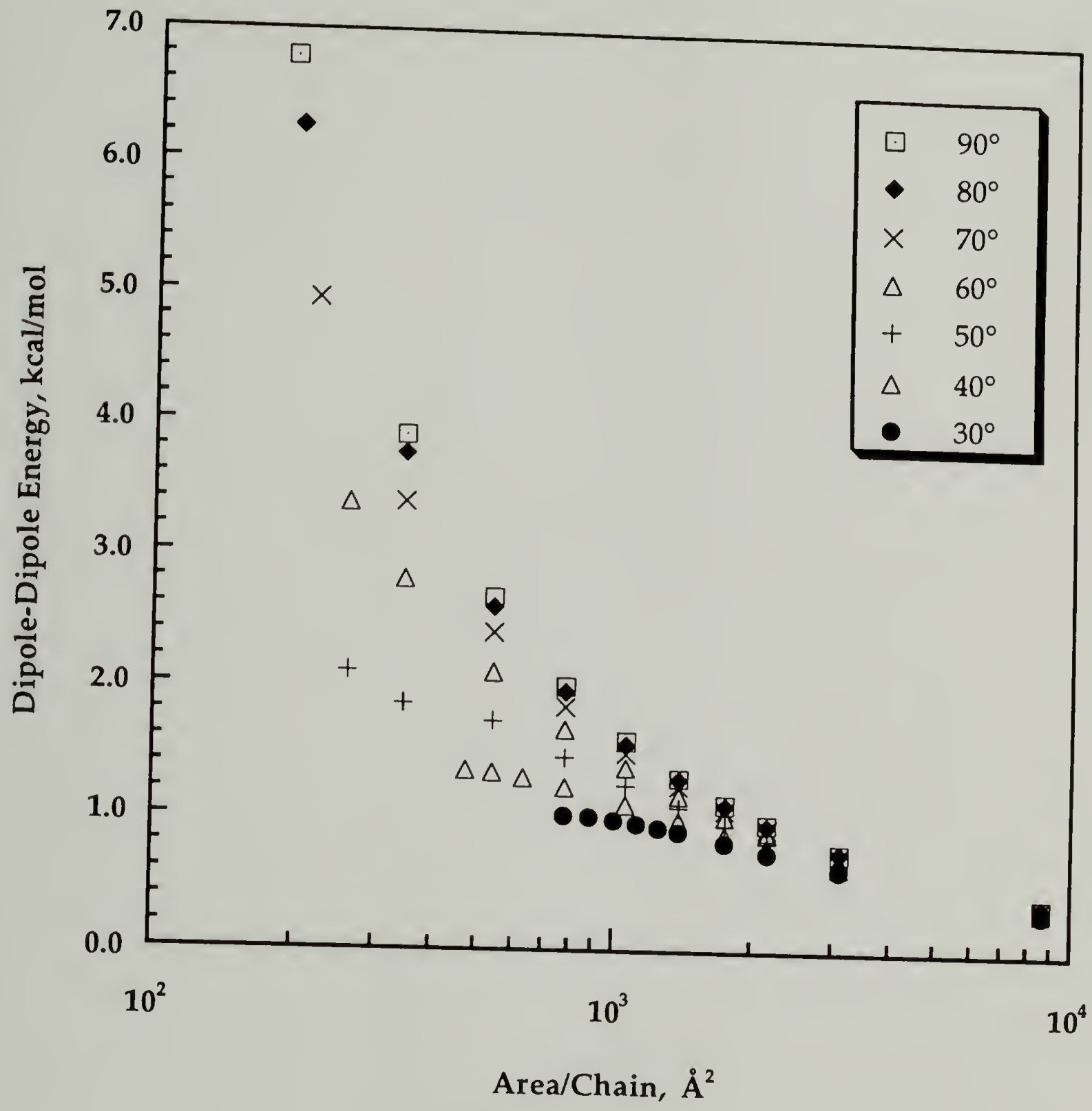

Figure 2.5. Dipole-dipole interaction energy as a function of area per chain, calculated for different values of the tilt angle, for constrained helices. Compared with Figure 2.4, this figure considers the helix excluded volume in the minimum allowable area per chain for each tilt angle.

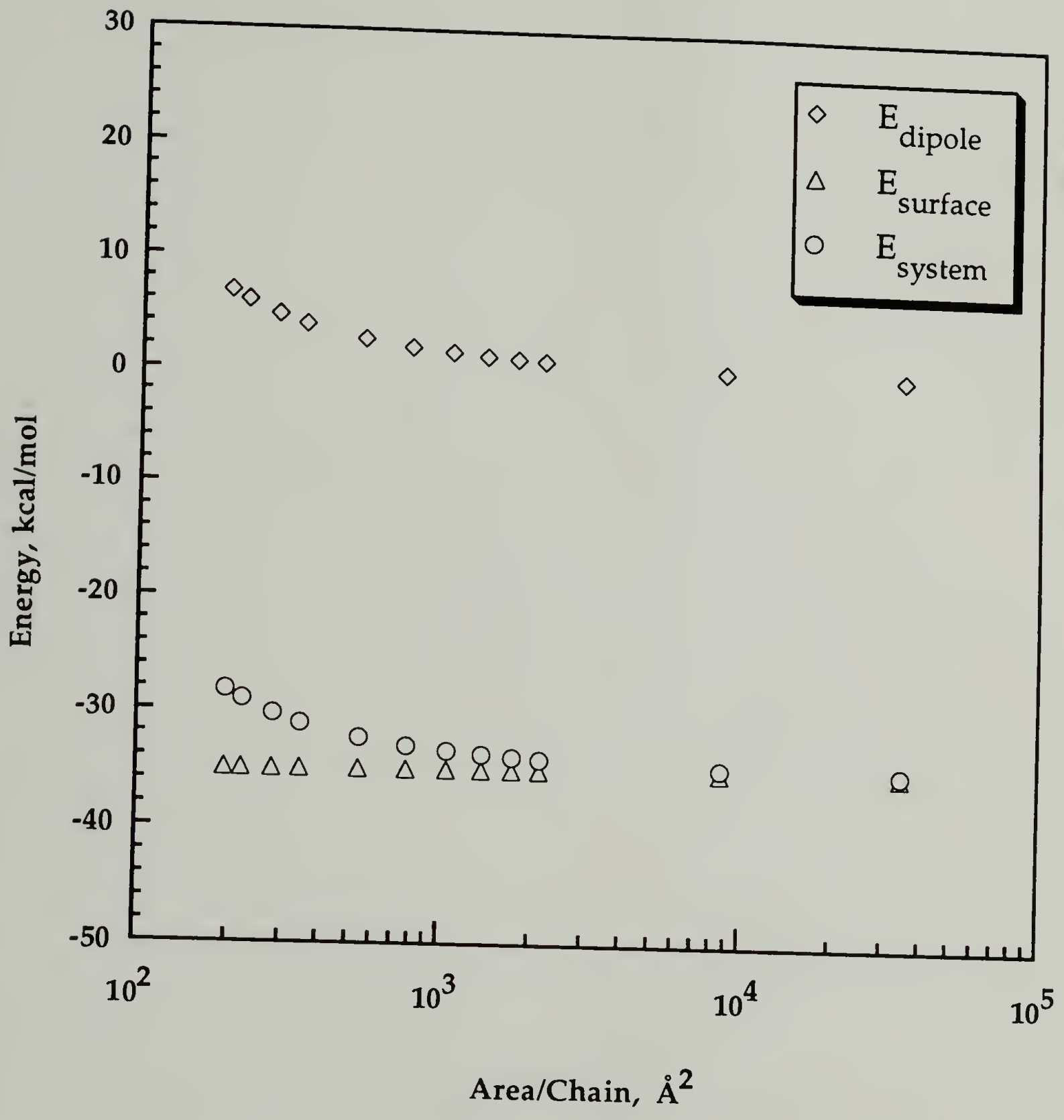

Figure 2.6. Dipole-dipole, surface, and system energy per mole versus area per chain for chains oriented perpendicular to the substrate.

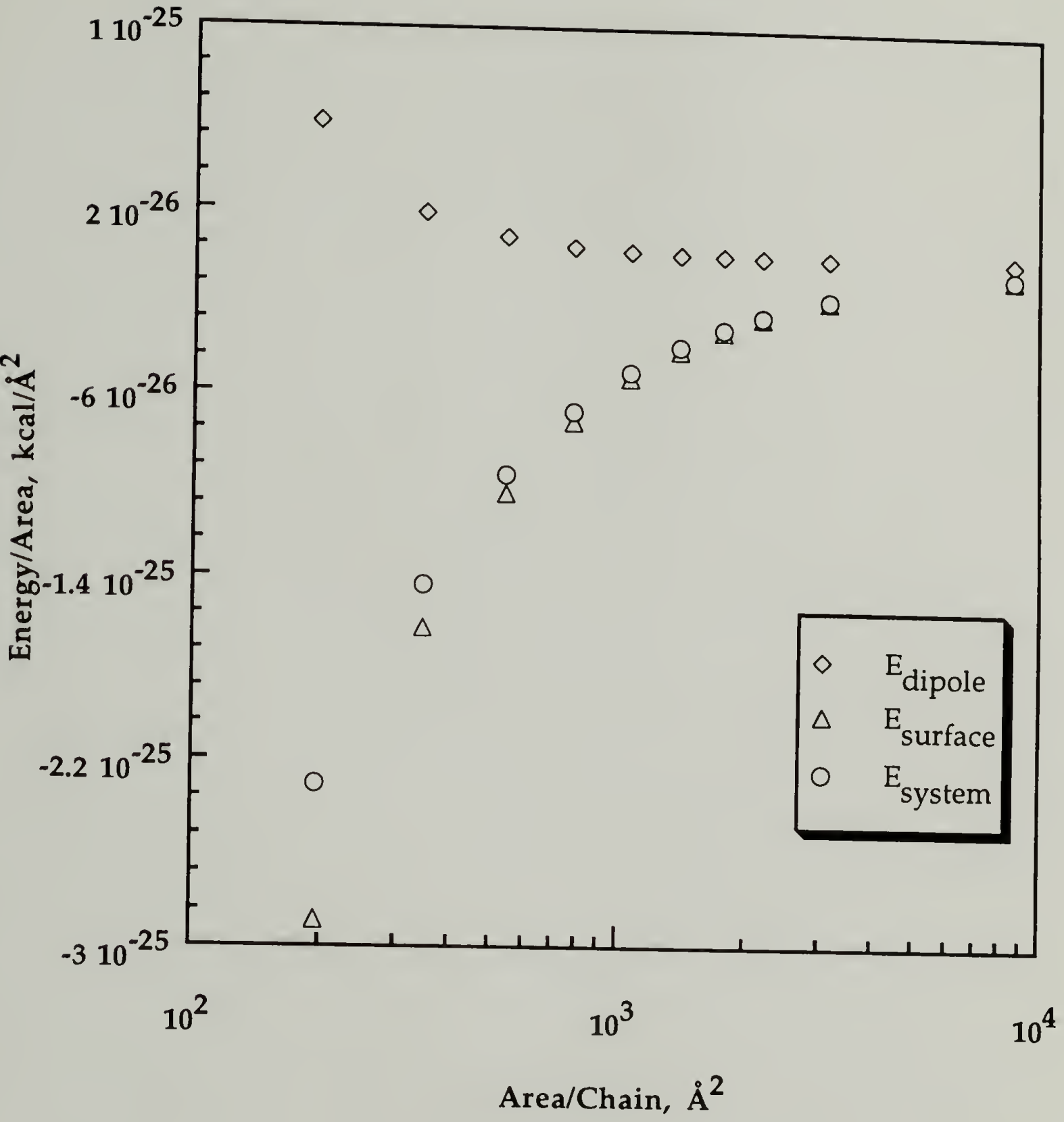

Figure 2.7. Dipole-dipole, surface, and system energy per unit area for chains oriented perpendicular to the substrate.

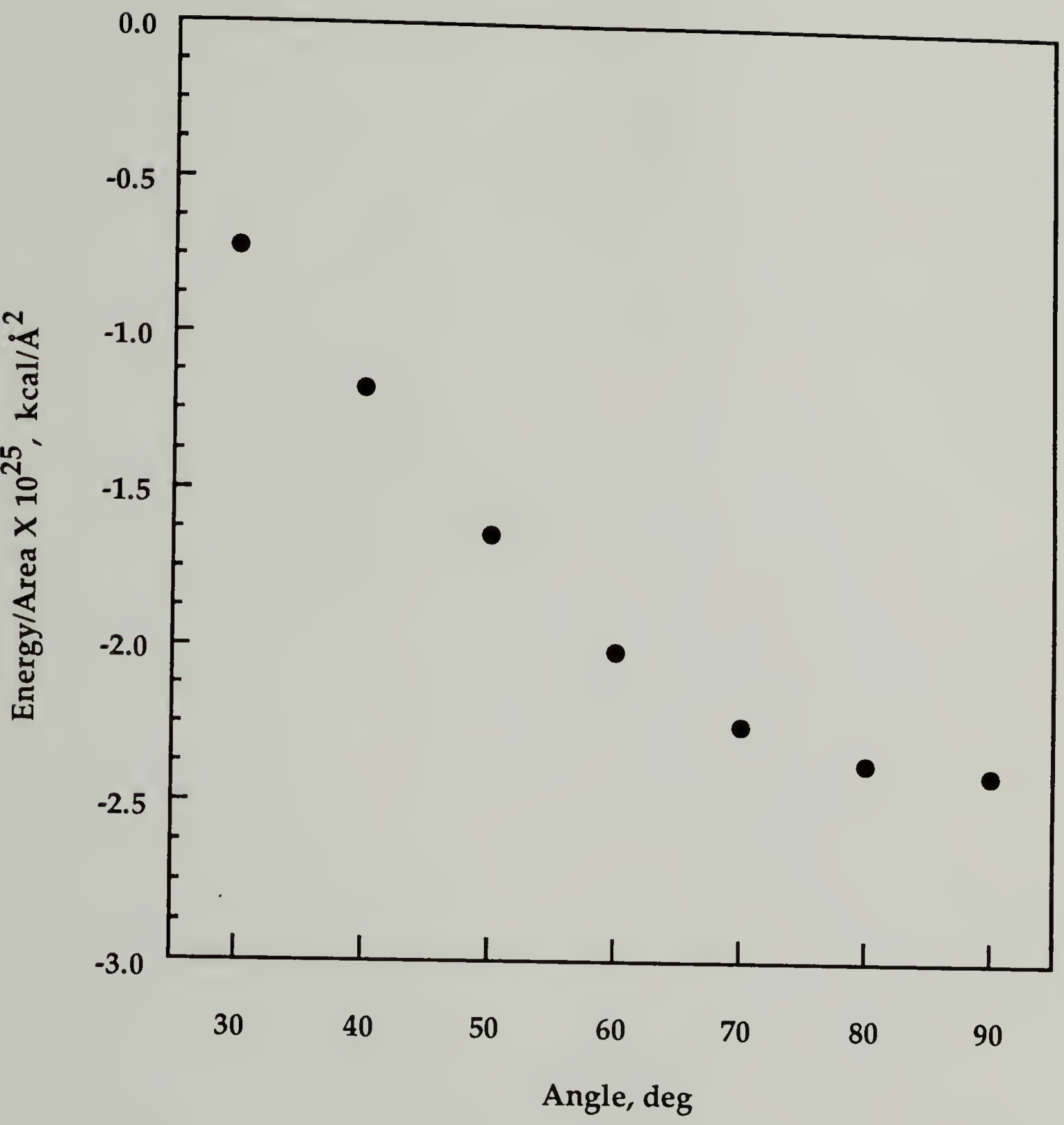

Figure 2.8. System energy per unit area for closest packing (l=15Å) at each tilt angle.

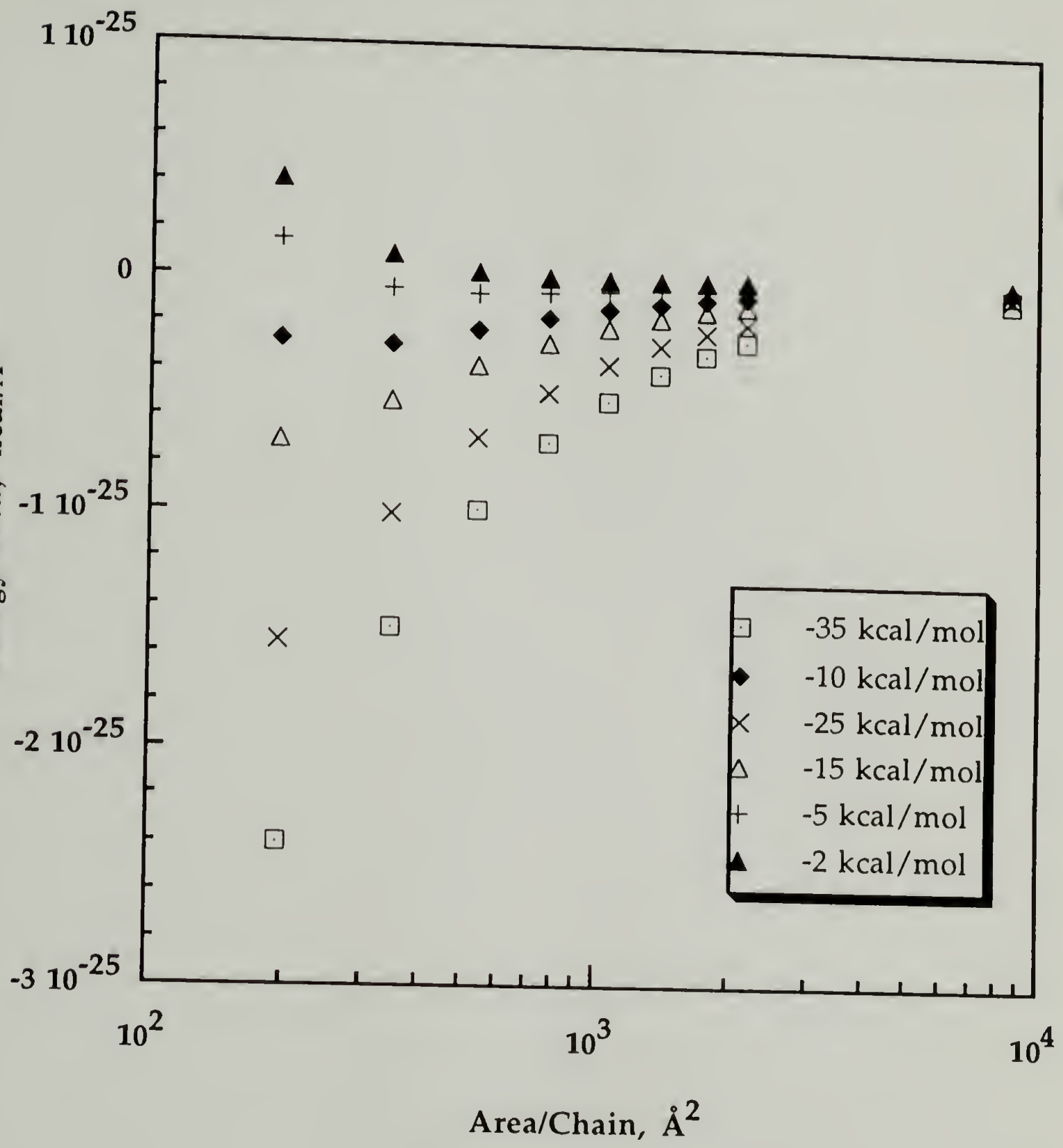

Figure 2.9. System energy as a function of surface interaction energy for a chain tilt of 90°.

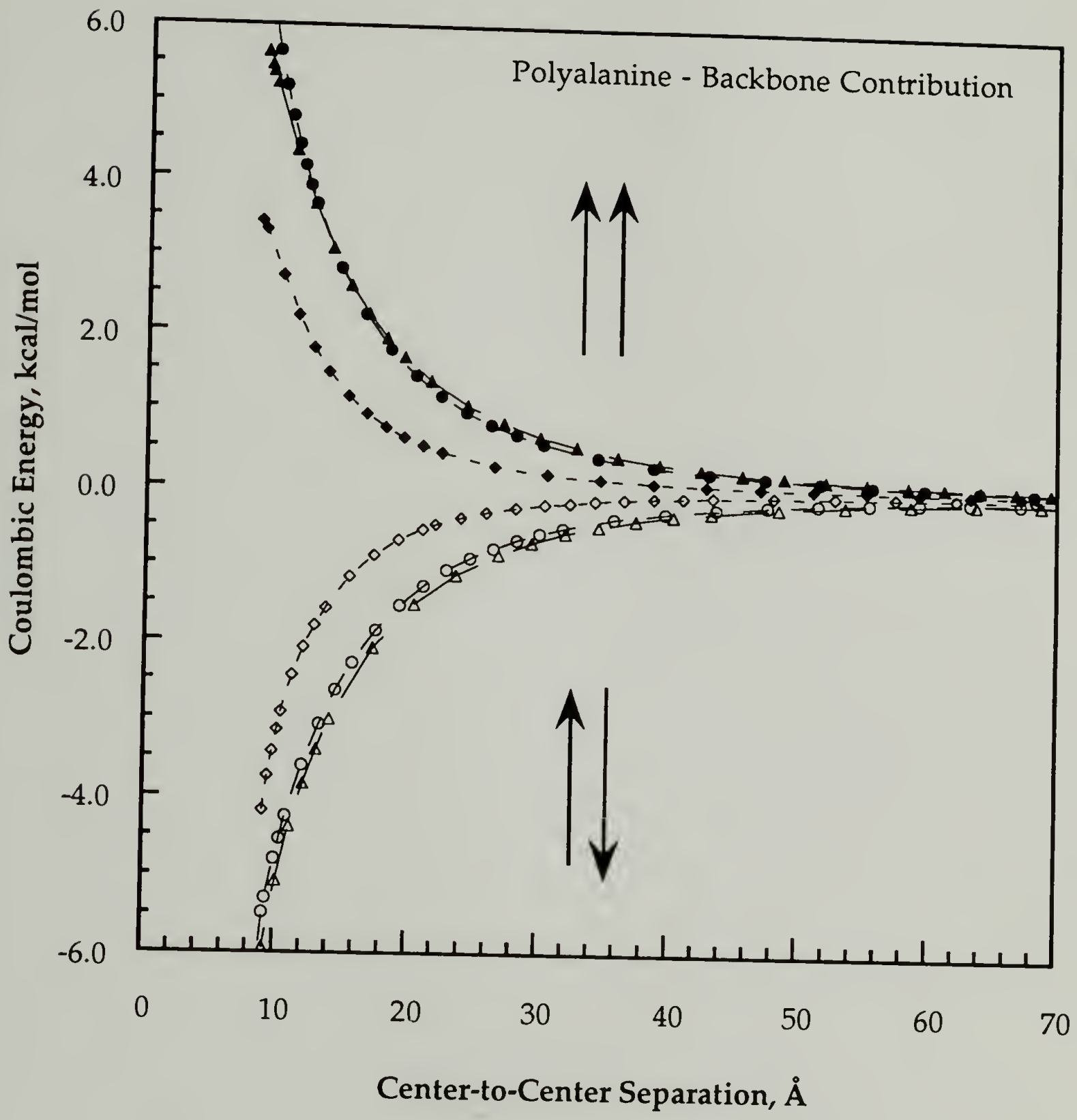

Figure 2.10. Coulombic energy as a function of separation for polyalanine helices oriented side-to-side. The three curves correspond to 10 (diamonds), 15 (circles), and 18 (triangles) repeat units per helix.

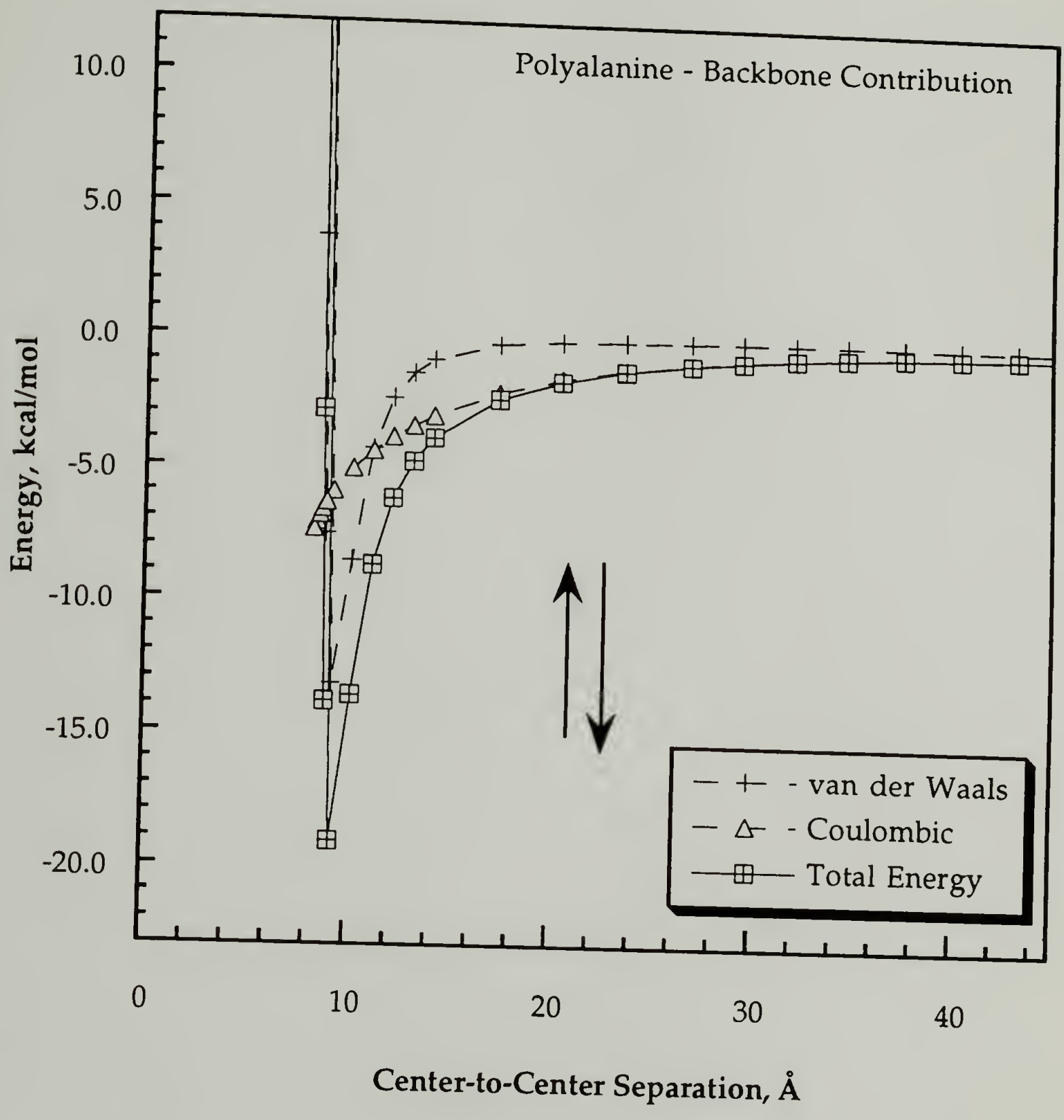

Figure 2.11. Coulombic and van der Waals contributions to the total energy for anti-parallel orientation of polyalanine helices (n=18).

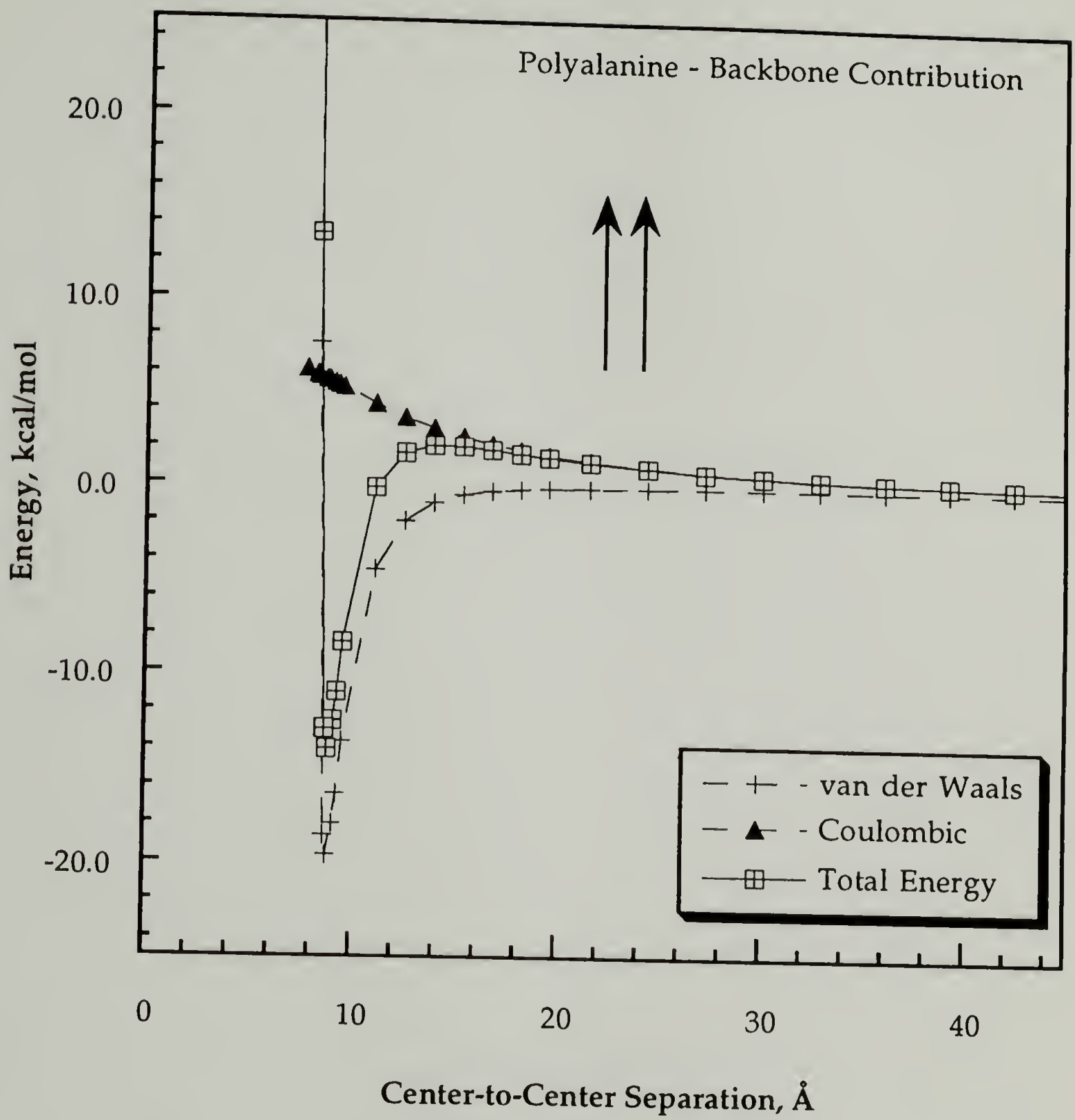

Figure 2.12. Coulombic and van der Waals contributions to the total energy for parallel orientation of polyalanine helices (n=18).

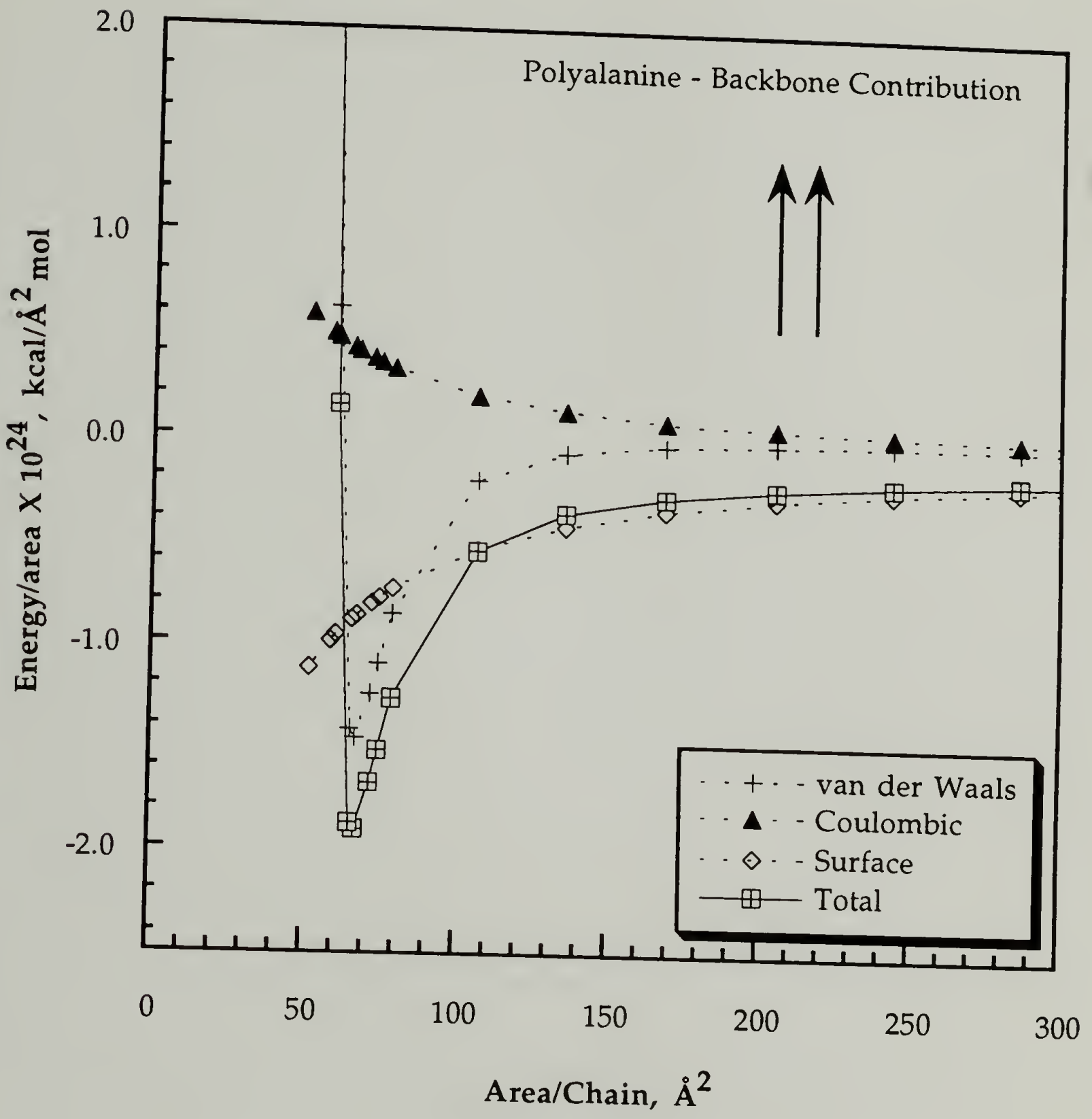

Figure 2.13. Coulombic, van der Waals, and surface energy contributions to the total energy for parallel orientation of polyalanine helices (n=18).

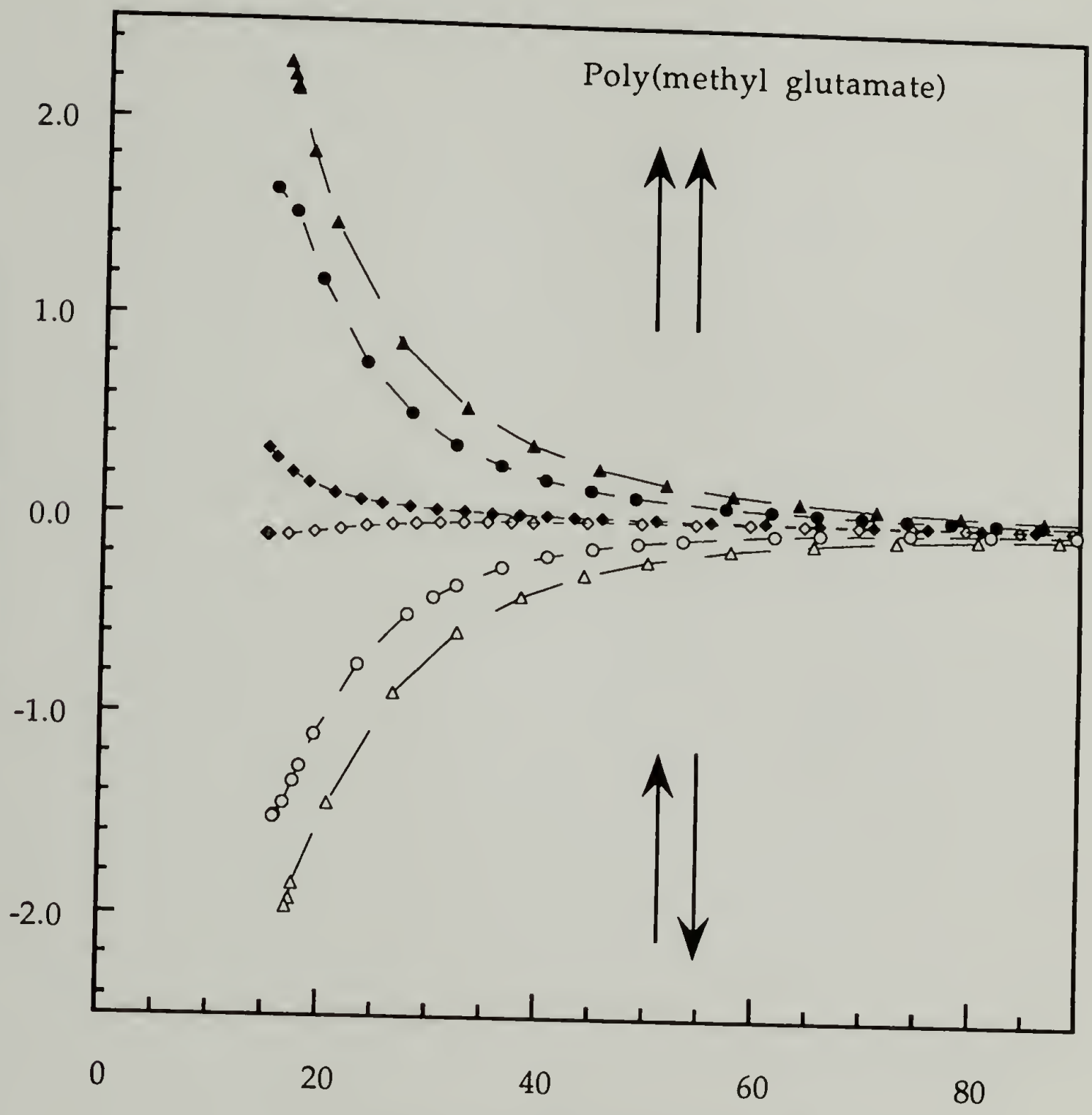

Figure 2.14. Coulombic energy as a function of separation for poly(methyl glutamate) helices oriented end-to-end. The three curves correspond to 10 (diamonds), 15 (circles), and 18 (triangles) repeat units per helix.

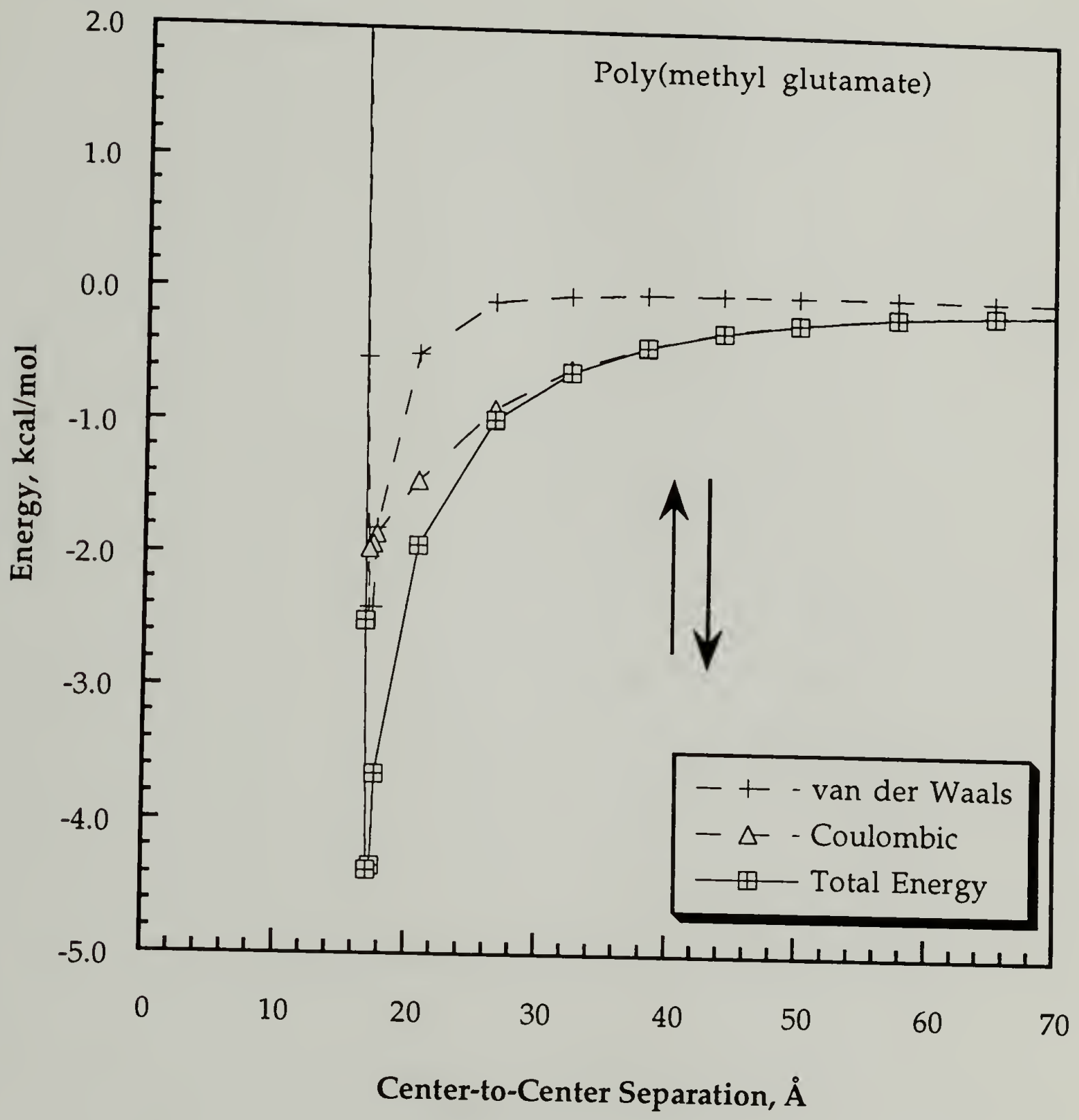

Figure 2.15. Coulombic and van der Waals contributions to the total energy for anti-parallel orientation of poly(methyl glutamate) helices (n=18).

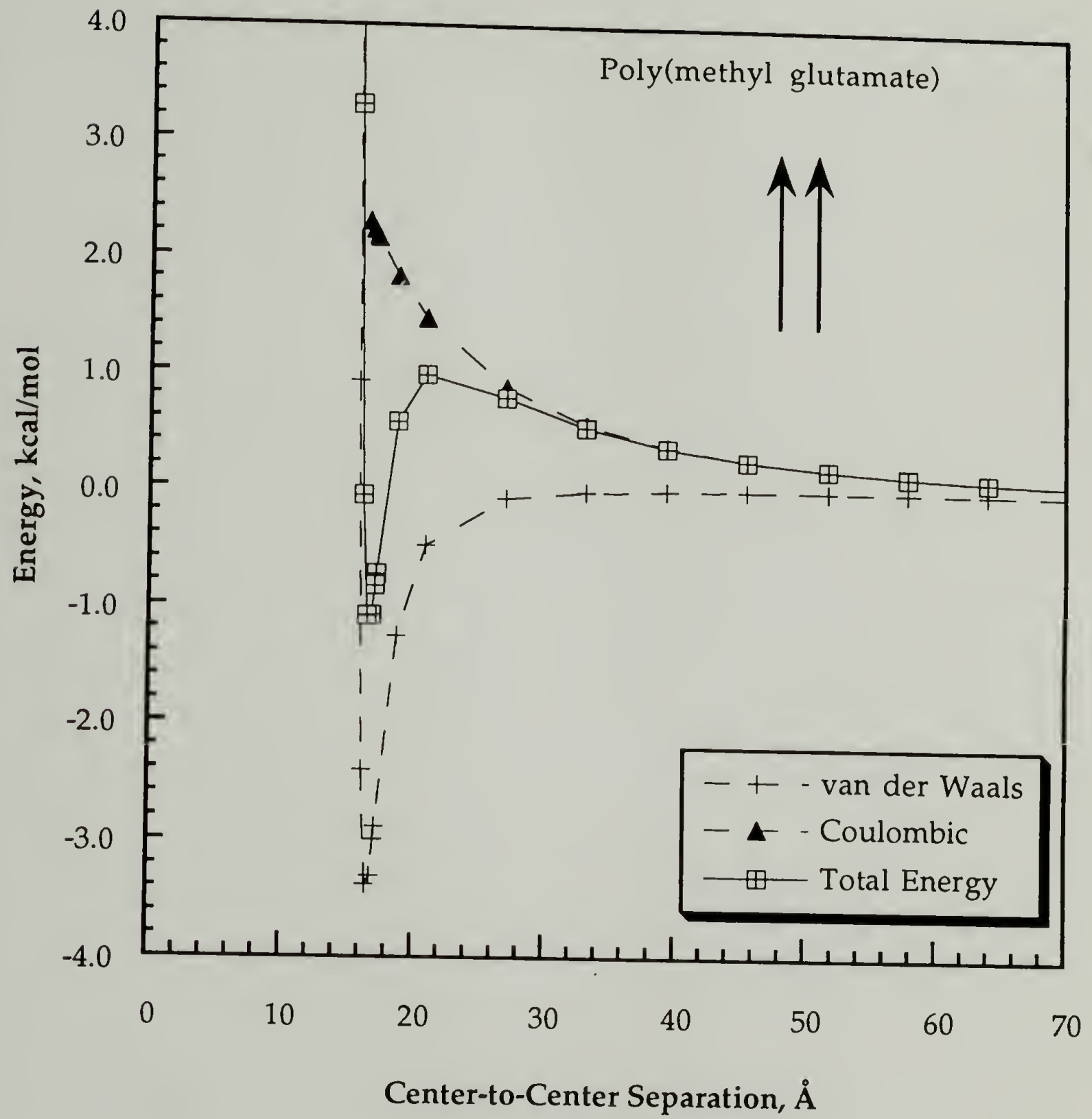

Figure 2.16. Coulombic and van der Waals contributions to the total energy for parallel orientation of poly(methyl glutamate) helices (n=18).

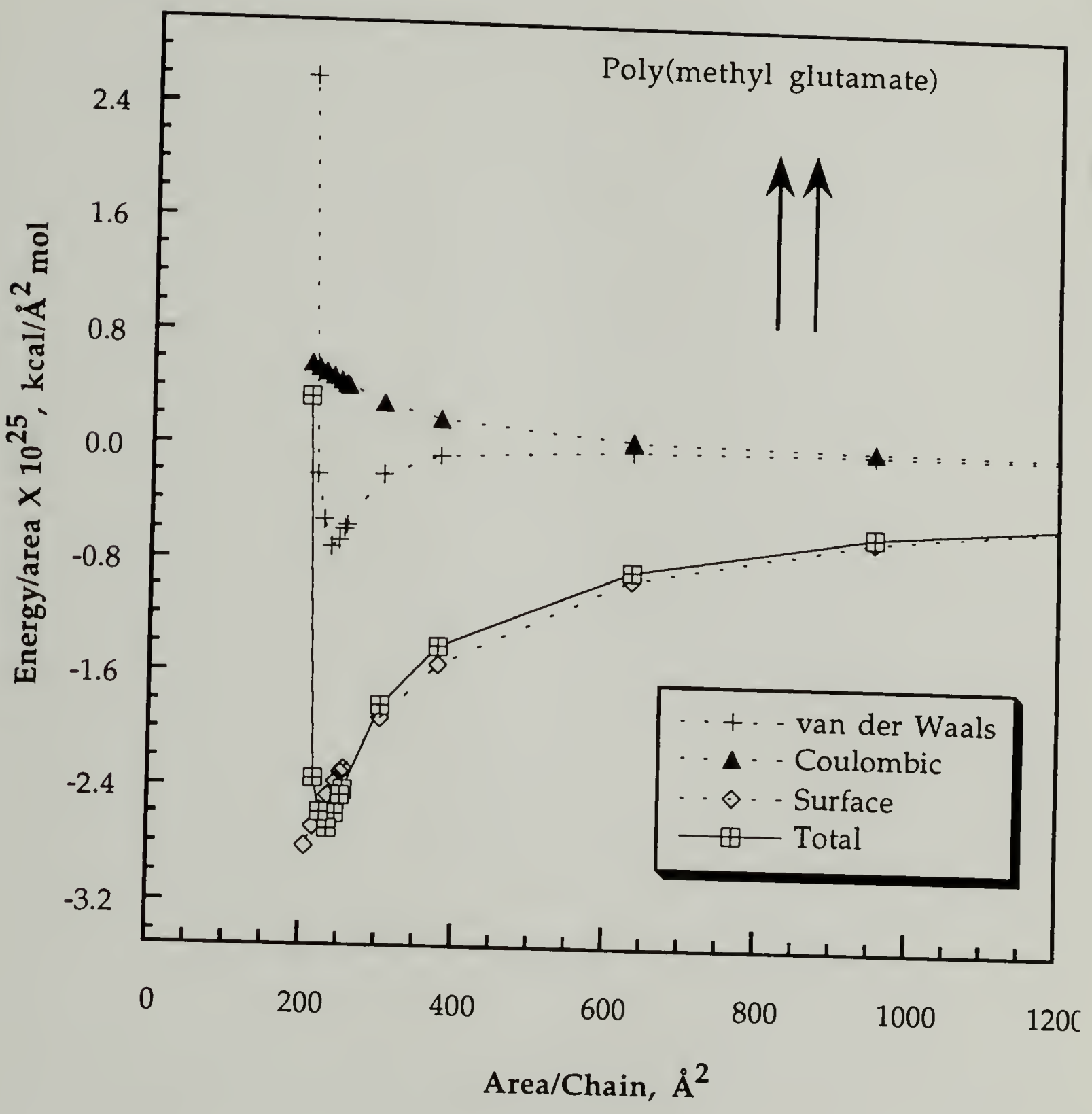

Figure 2.17. Coulombic, van der Waals, and surface energy contributions to the total energy for parallel orientation of poly(methyl glutamate) helices (n=18).

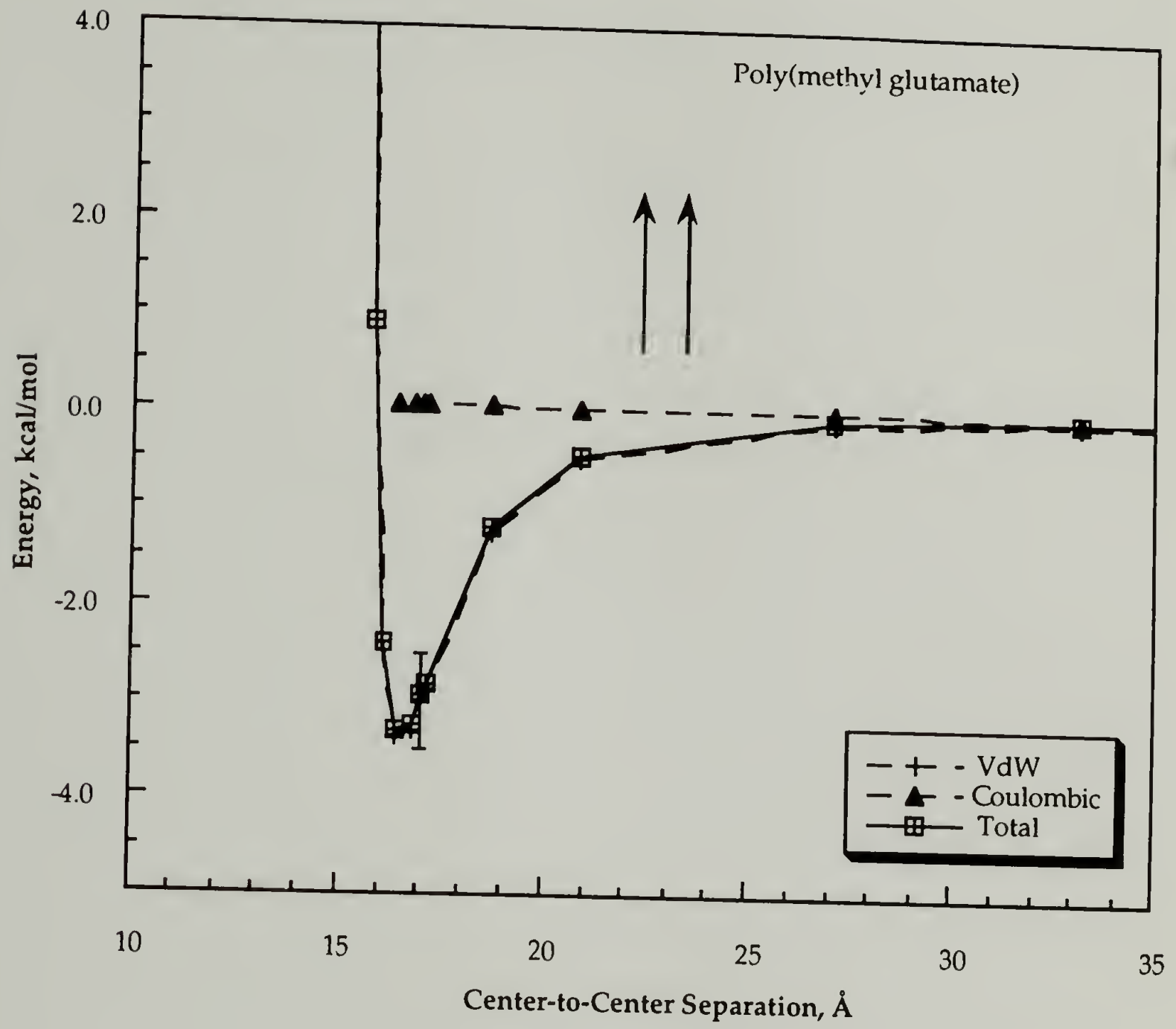

Figure 2.18. Coulombic, van der Waals, and surface energy contributions to the total energy for parallel orientation of poly(methyl glutamate) helices (n=18). The coulombic energy is scaled by the dielectric constant of N,N-dimethylformamide (36.7) to approximate the behavior in this solvent. Induced dipole effects are ignored. Error bars are based on the uncertainty in the energy due to rotation around the helix axis, as shown in Figure 2.19.

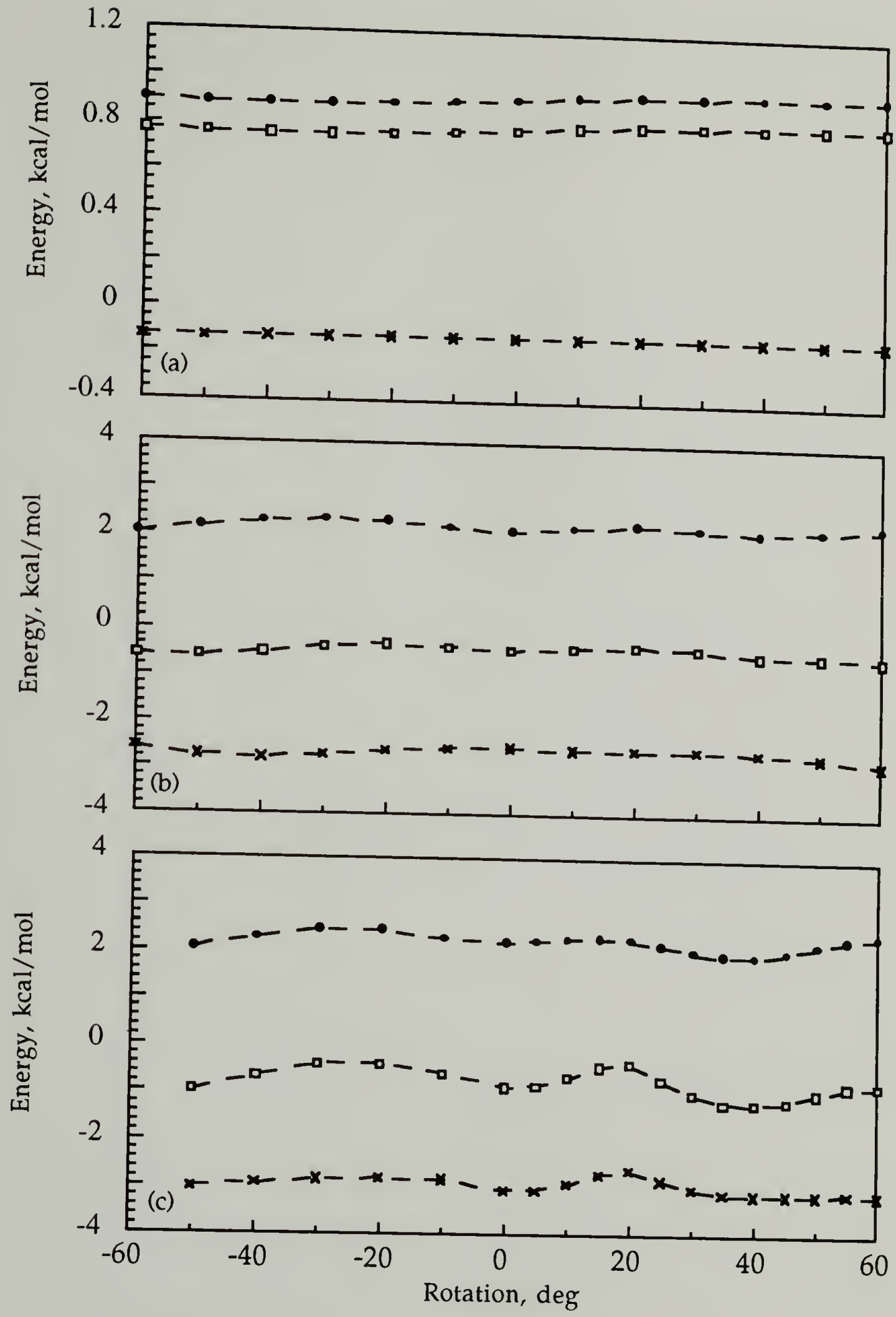

Figure 2.19. Effect of rotation on the coulombic (circles), van der Waals (X's), and total energies (squares). Shown for three center-to-center separations of parallel PMG (18-mer): (a) 25.1± 0.1, (b) 17.1 ± 0.1, (c) 16.7 ± 0.1.

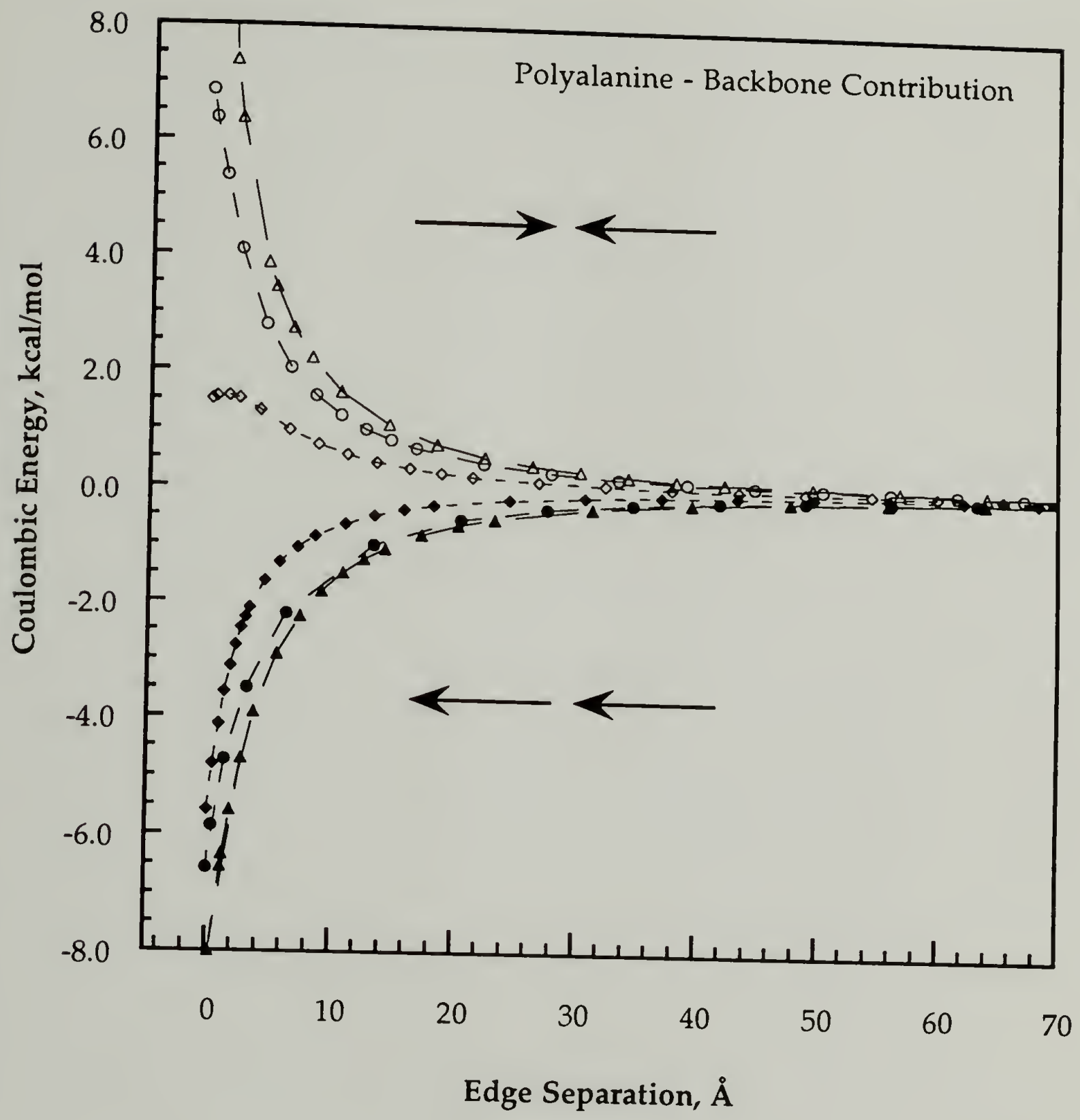

Figure 2.20. Coulombic energy as a function of separation between approaching ends of polyalanine helices. The three curves correspond to 10 (diamonds), 15 (circles), and 18 (triangles) repeat units per helix.

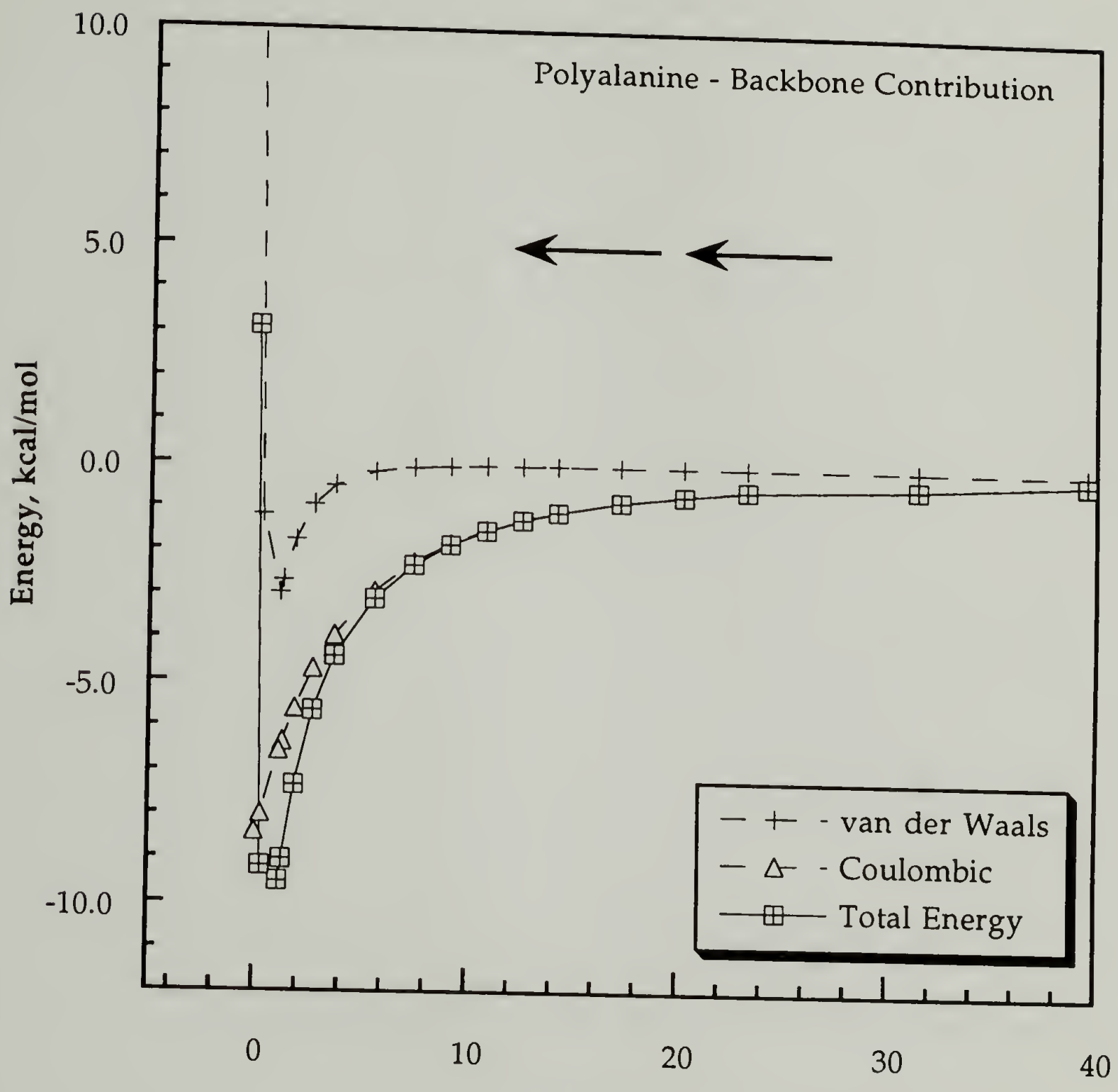

Figure 2.21. Coulombic and van der Waals contributions to the total energy for head-to-tail orientation of polyalanine helices (n=18).

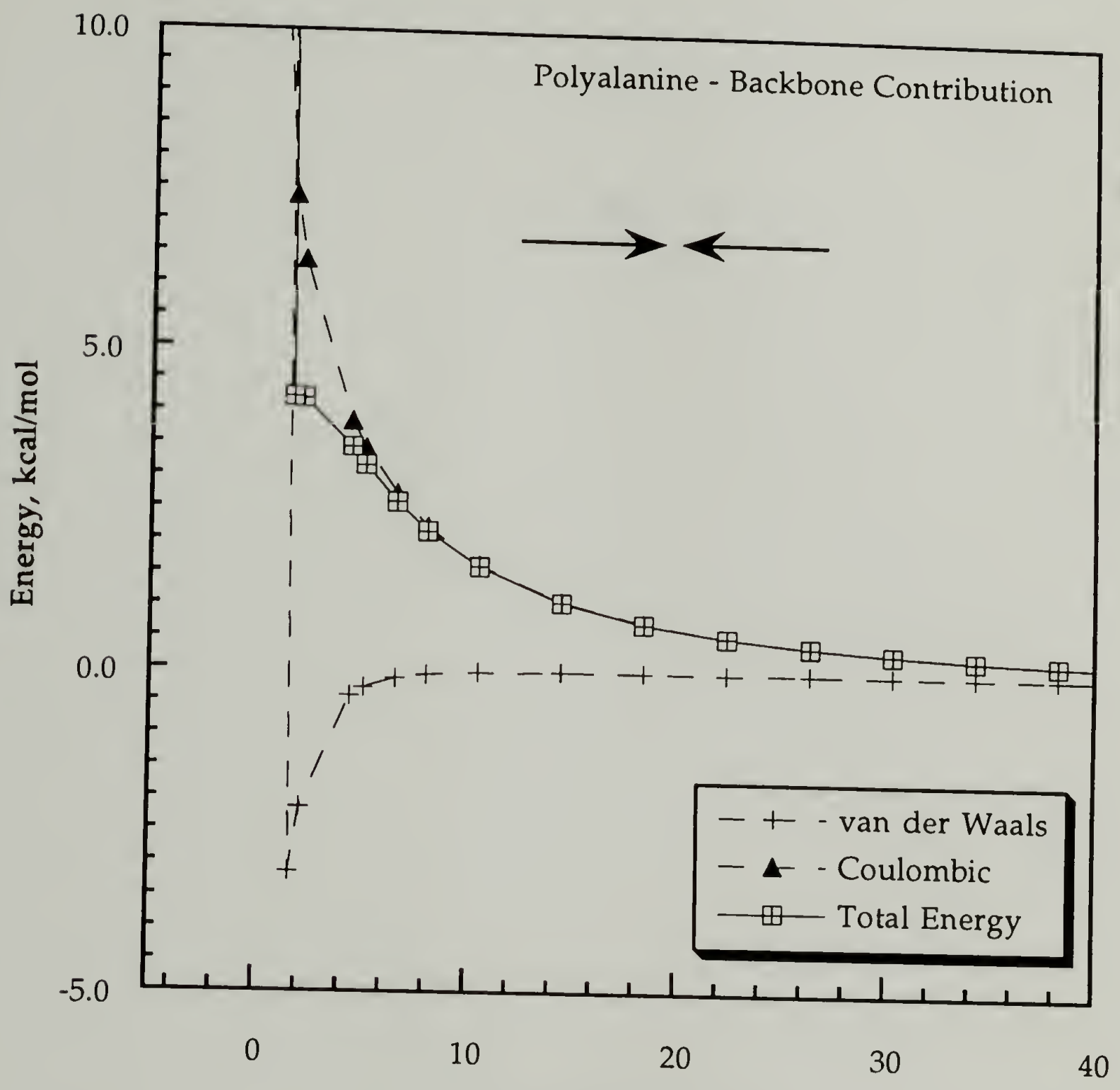

Figure 2.22. Coulombic and van der Waals contributions to the total energy for head-to-head orientation of polyalanine helices (n=18).

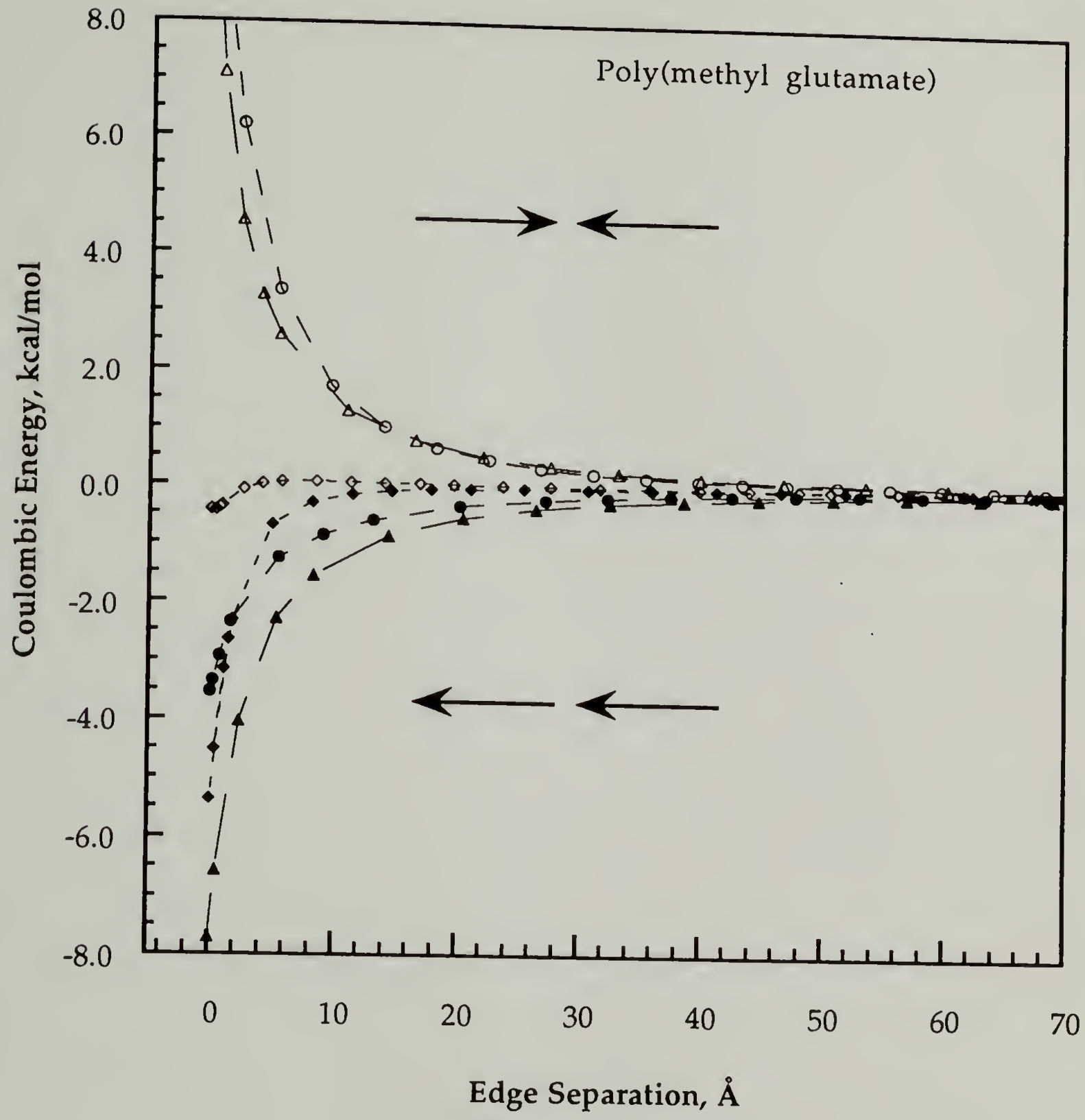

Figure 2.23. Coulombic energy as a function of separation for poly(methyl glutamate) helices oriented end-to-end.

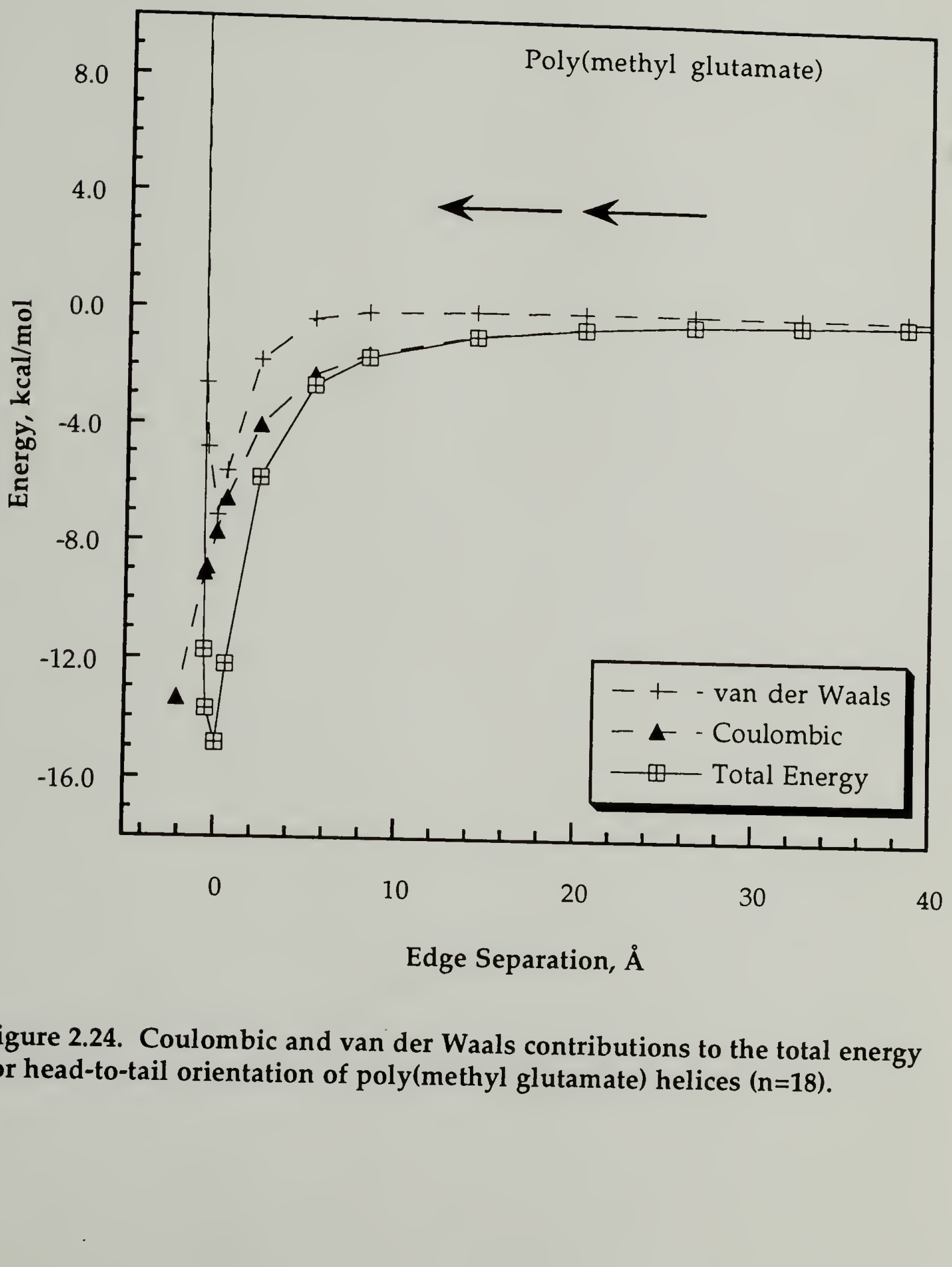

Figure 2.24. Coulombic and van der Waals contributions to the total energy for head-to-tail orientation of poly(methyl glutamate) helices (n=18).

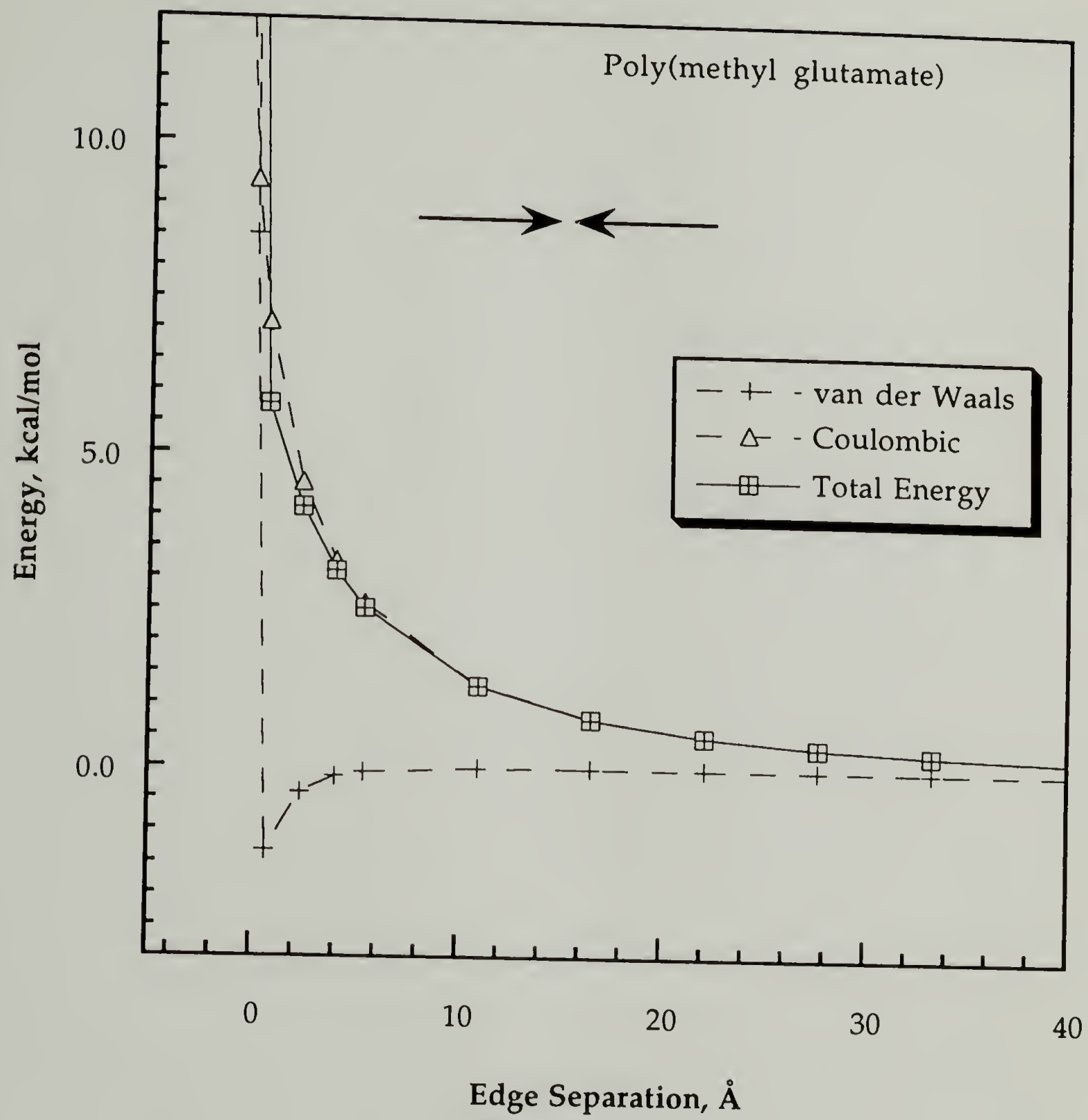

Figure 2.25. Coulombic and van der Waals contributions to the total energy for head-to-head orientation of poly(methyl glutamate) helices (n=18).

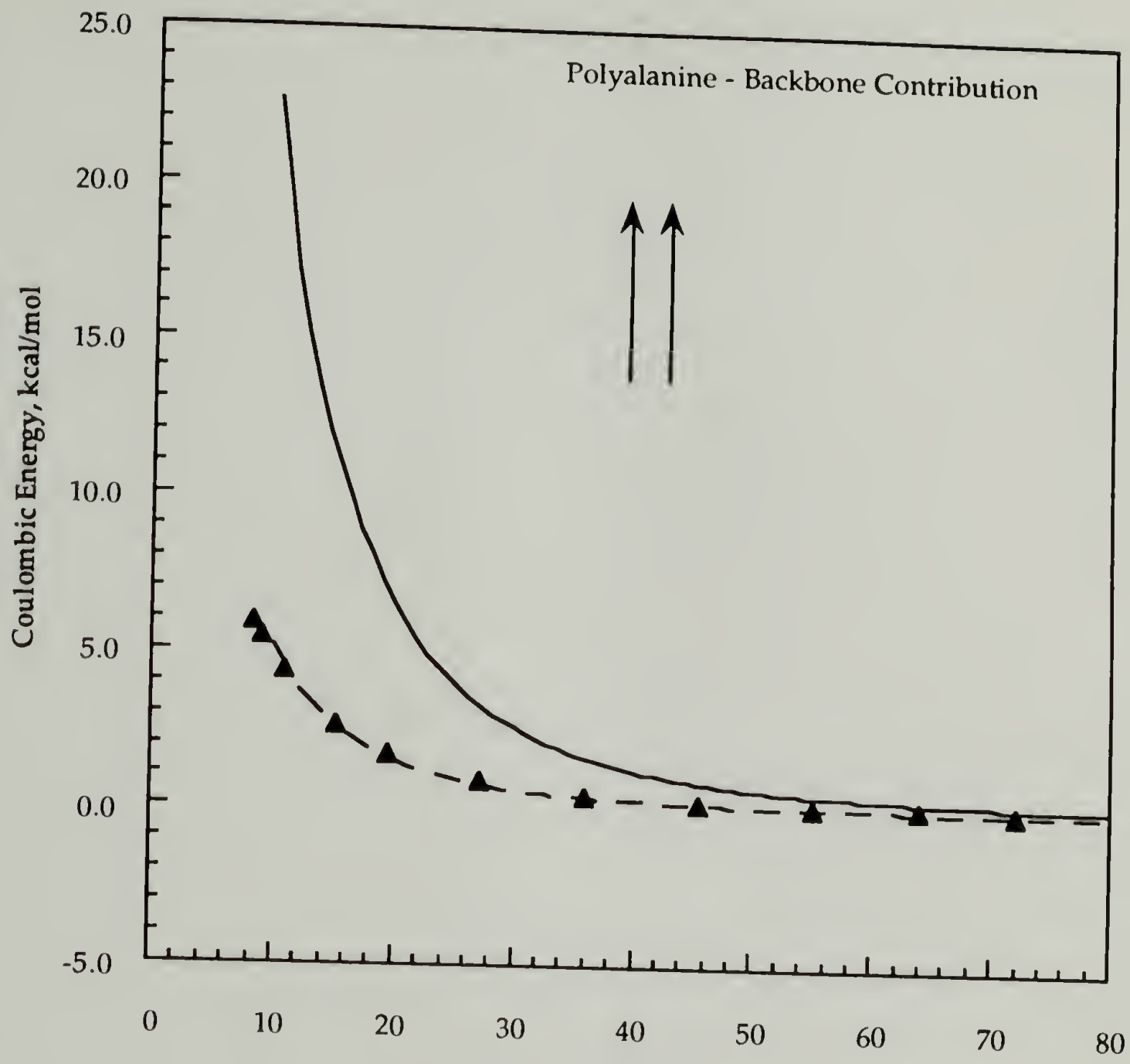

Figure 2.26. Comparison of analytical model (Eqn. 2.7) and Biosym results (triangles) for parallel, 18-mer polyalanine helices. Fits are shown for two values of the dipole moment. Solid curve is based on a literature value [82, 83] of 4.5 D for the dipole moment., and the dashed curve is based on the value of the dipole moment which gives the best fit to the simulation data, 2.2 D.

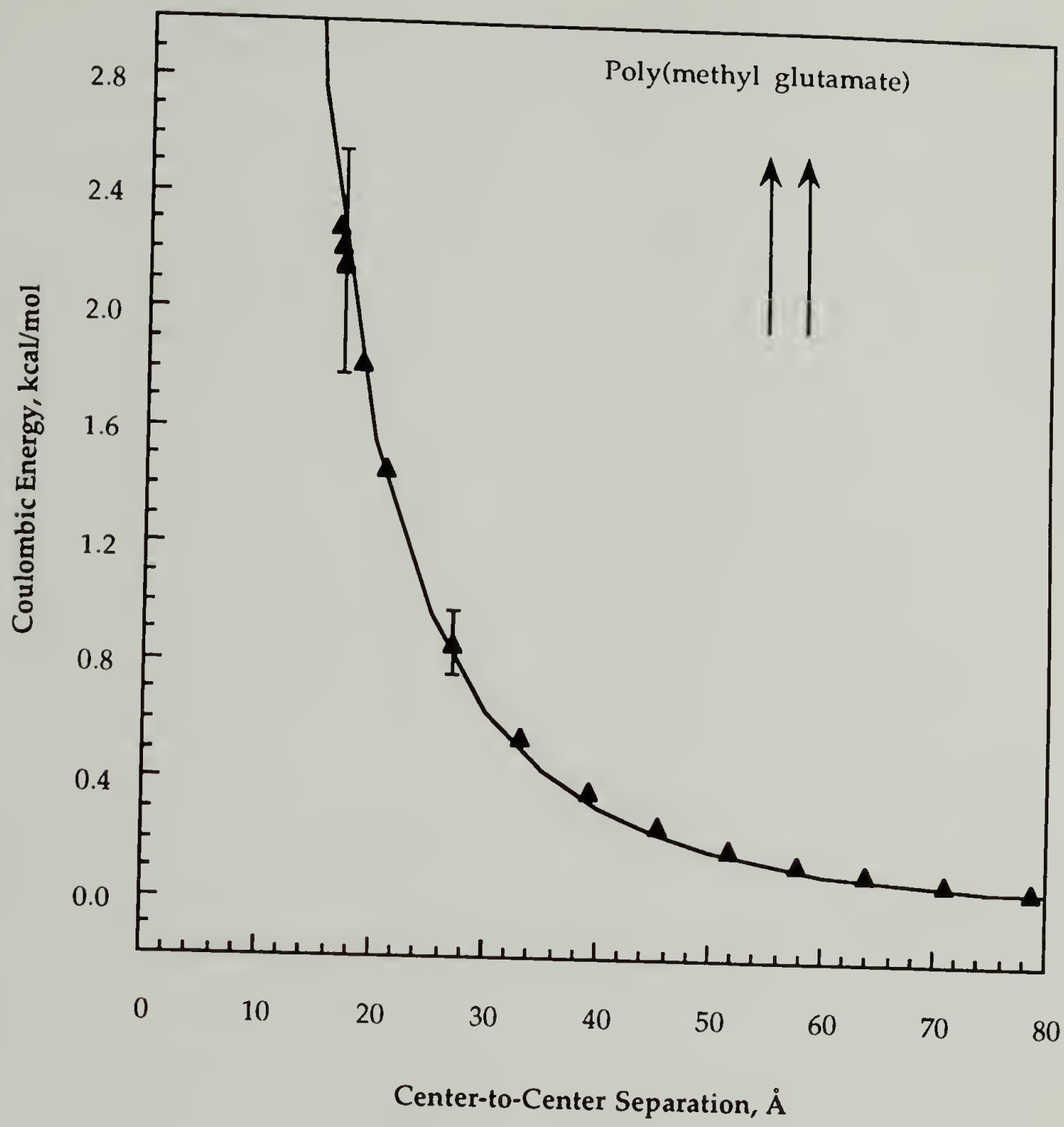

Figure 2.27. Comparison of analytical model (Eqn. 2.7) and Biosym results (triangles) for poly(methyl glutamate) (n=18). Solid curve is the fit to the analytical model based on a literature value [82, 83] of 2.3 D for the dipole moment. Error bars for the simulation data are based on the uncertainty in the energies due to rotation around the helix axis, as shown in Figure 2.19.

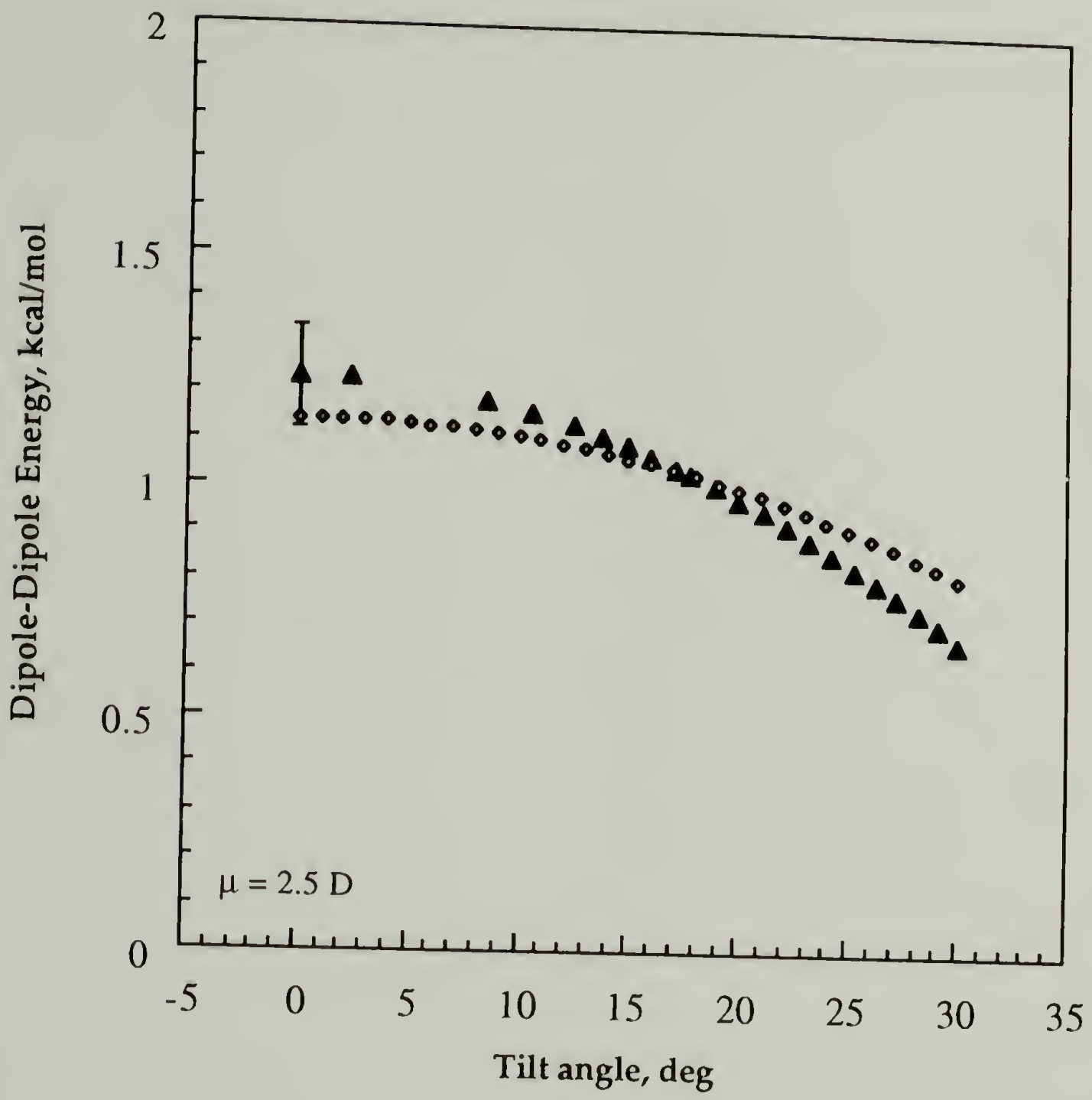

Figure 2.28. Effect of tilt angle on dipole-dipole energy. Comparison of analytical model (diamonds) (Eqn. 2.7) and Biosym results (triangles) for poly(methyl glutamate) (n=18). A dipole moment of 2.5 D was used. Error bar for the simulation data is based on the uncertainty in the energy due to rotation around the helix axis, as shown in Figure 2.19.

CHAPTER III

SYNTHESIS

A. Introduction

This chapter describes the synthesis of the rod-coil diblock copolymers used throughout the dissertation. The diblocks chosen for study are composed of polyisoprene (PI) and poly(γ-benzyl-L-glutamate) (PBLG). PBLG is an α-helix with a semi-rigid secondary structure; the persistence length of PBLG has been reported as 600-1600Å, [110-115] reflecting the difficulty in measuring the persistence length (a) for molecules in which long enough chains (contour length, L >> a) are not available. [116] PBLG was chosen as the "rod" block because of its relevance to biological systems, and the ability of this research group to prepare perfectly monodisperse PBLG via recombinant DNA synthesis techniques. [84] This work serves as a precursor to the work involving these monodisperse analogues.

Polyisoprene was chosen as the flexible coil block for two major reasons. The first reason is that the solubility characteristics of PI allowed for selective solvents to be chosen. Secondly, the glass transition temperature of PI is below the temperature of the experiments (room temperature). This is important for the surface adsorption experiments. A rubbery and mobile anchor block will attain an equilibrium surface arrangement more readily than a glassy one.

The structure of the polymer to be used in this work is shown below:

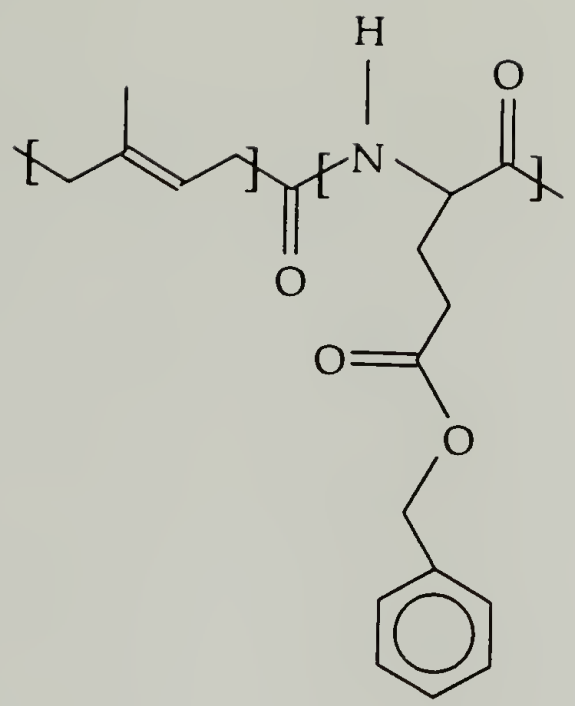

Figure 3.1 Chemical structure of polyisoprene-poly(γ-benzyl-L-glutamate) (PI-PBLG) diblock copolymer.

A series of PI-PBLG diblock copolymers has been prepared in which the molecular weights of each block are varied systematically.

B. Materials

Isoprene (Aldrich Chemical Co.) monomer was purified by successive vacuum distillations from dibutylmagnesium and n-butyllithium (b.p. 2 Torr). Cyclohexane (Aldrich, 99+%) was purified by distillation from polystyryllithium (b.p. 80°C). sec-Butyllithium in cyclohexane (Aldrich) was used as received; active initiator concentration (ca. 1.3 M) was determined by the Gilman double-titration method. [117, 118] Tetramethylethylenediamine (TMEDA) (Aldrich, 99+%) was stirred over calcium hydride and freeze-degassed several times. Dichloromethane (Fisher, hplc) was distilled from molecular sieves (b.p. 40°C). Tetrahydrofuran (THF) (Fisher) and hexane (85%, hplc grade, EM Science) (recrystallization of NCA) were dried over

molecular sieves. Ethyl acetate (Fisher) was distilled from potassium carbonate (b.p. 77°C). n-Butyl amine (Aldrich, 99%) was distilled from calcium hydride (b.p. 78°C). Carbon dioxide (Air Products Anaerobic Grade), poly(γ-benzyl-L-glutamate) (PBLG) MW(viscometry) 25K, 26K, 42K, 118K (Sigma), benzyl-L-glutamate (Sigma), triphosgene (Aldrich, 98%), potassium carbonate (K_2CO_3, Baker), dicyclohexylcarbodiimide (DCCI, Aldrich), and 1-hydroxybenzotriazole hydrate (HOBt, Aldrich) were used as received. Solvents used as received were methanol (EM Science, hplc grade), ethanol, hexane (85%, hplc grade, EM Science) (extraction), N,N-dimethylformamide (DMF, Aldrich, anhydrous, 99+%), deuterated chloroform (99.8 atom% D, Isotec), and trifluoroacetic acid (99+%, Aldrich).

C. Methods

PI-PBLG diblock copolymers were synthesized by a carbodiimide coupling reaction between carboxyl-terminated polyisoprene and amine-terminated PBLG. This section details the synthesis of carboxyl-terminated polyisoprene, the N-carboxy anhydride of benzyl glutamate, poly(γ-benzyl-L-glutamate), and the diblock copolymer. The conclusion of this section describes the purfication strategy used to remove the unreacted homopolymers from the diblock product of the coupling reaction. All NMR spectra were obtained using a Bruker 200 MHz instrument fitted with an autosampler tray. The proton spectra were collected in 64 scans; the carbon spectra were collected during 400 scans. The solvent used in all spectra was deuterated chloroform ($CDCl_3$); in some cases, a few drops of trifluoroacetic acid were added to the solution to improve the sharpness of the spectra.

1. Carboxy-terminated Polyisoprene

Carboxy-terminated polyisoprene (PI-COOH) was anionically synthesized in a purified argon atmosphere. [119] Cyclohexane was stirred with sulfuric acid for several days and then refluxed with n-butyllithium. The addition of styrene monomer caused the cyclohexane to turn orange-red in color. This served as a visual indication of the presence of oligomeric anions and, therefore, the absence of terminating agents (e.g., water) contaminating the solvent. The cyclohexane was refluxed for several hours; the color was maintained.

The 3-liter reactor (which had been heated to 280°C overnight) was evacuated and purged with argon several times. Then, approximately 1200 ml of cyclohexane were distilled directly into the reactor and heated to 40°C. The Gilman double-titration method [117, 118] was used to determine the active lithium component in the *sec*-butyllithium along with the residual (inactive) base. Two 50 ml Erlenmeyer flasks were sealed with rubber septa, flamed under vacuum, and filled with argon. About 2 ml of distilled water were injected into one flask, and about 2 ml of 1,2-dibromoethane (dried with molecular sieves) were injected into the other flask. Exactly 1.00 ml of initiator was injected into each flask using a gas-tight syringe (Hamilton) flushed with argon. The septa were then removed and a drop of phenolphthalein (0.5 wt% in 50:50 ethanol/water) was added to each flask. The solutions were titrated with 0.1N hydrochloric acid. The active initiator concentration was calculated from the difference between the water titration, which gives the moles of total lithium base, and the dibromoethane titration, which gives the moles of inactive lithium base. *sec*-Butyllithium was then added to the reactor, using a gas-tight syringe (Hamilton), followed by the

isoprene. The reaction was allowed to proceed for at least three hours. After this time, a sample of the reaction mixture was cannulated into a small, sealed, argon-filled flask. Degassed methanol was added to terminate the living ends. This resulted in unfunctionalized polyisoprene (PI-H) which was used as a GPC molecular weight reference.

Carbonation involved addition of a large excess of TMEDA (43:1 TMEDA: initiator ratio) to dissociate the living anions; this was accompanied by the reaction mixture changing from colorless to yellow. Then, the reaction flask was pressurized to 0.2 - 0.3 atm with gaseous carbon dioxide, connected via an air-tight line to the reactor. The reaction mixture was not stirred during the addition of carbon dioxide to reduce the fraction of coupling products. [120], [121], [122] The yellow color disappeared within the first minute. After approximately 30 minutes, the carboxylate salt was hydrolyzed with a 1N solution of HCl in methanol followed by precipitation into methanol. The methanol was decanted off (or removed by evaporating for low MW PI), and the polymer was dried under vacuum at room temperature for several days. The reaction conditions are summarized in Table 3.1.

This polymerization produces polymers with relatively narrow molecular weight distributions. The target molecular weight of the polyisoprene block is controlled by reacting initiator and monomer in the appropriate molar ratio: $DP_{polymer} = [monomer]_0 / [initiator]_0$. This simplified expression assumes no termination.

a. Gel Permeation Chromatography

The molecular weight and polydispersity of the polyisoprene were measured with a Waters GPC, equipped with four Phenomenex Phenogel

columns (pore sizes 10^5, 10^4, 10^3, and 500 Å) and a refractive index detector (Model R401), using THF as the eluent and a flowrate of 1 ml/min. The columns were calibrated with five polyisoprene standards (MW 300K, 125K, 25K, 18K, and 5K). The carboxylation reaction can result in two major side-products: a ketone and an alcohol. [120-122] These result from more than one living polymer end reacting with a single molecule of carbon dioxide. The ketone is the dimer product and the alcohol is the trimer. These side products result in a higher molecular weight peak(s) in the GPC trace. However, the addition of a Lewis base such as TMEDA prior to termination results in quantitative yields of the carboxyl product by dissociating the living ends. [120-122] It was determined that the coupling products (the alcohol and the ketone) could be removed by fractionation using THF as the solvent and methanol as the precipitant. The coupling products will not participate in the coupling reaction between PI and PBLG and, therefore, were not removed in subsequent syntheses.

Figures 3.2 through 3.4 show the GPC results for the three polyisoprene samples used in this work and their unfunctionalized analogues. The lowest molecular weight polymer was determined to be 2800 g/mol based on the GPC measurement using the unfunctionalized fraction, PI-H. Consistent with a low degree of polymerization, the polydispersity of this sample (1.34) is relatively high for an anionic polymerization, and the distribution of molecular weight is asymmetric with a low molecular weight tail. Figures 3.2 shows that the carboxy-terminated sample has an additional high molecular weight fraction resulting from the coupling products of termination. The GPC results for the 10,000 and 69,000 g/mol samples show that the polymers have low polydispersities, and the coupling products are minimal. Molecular weights and polydispersities for these polymers are summarized in Table 3.1.

Table 3.1. Carboxy-terminated polyisoprene reactions.

PI-COOH Sample	s-BuLi ml	Isoprene g	Rxn Time hr	Temp/ Pressure ℃ / mm Hg	TMEDA ml	M_n	M_w/M_n
2.8K	5.60	19.3	3.25	40°C / 40	4.5	2060	1.34
10K	3.67	45.8	3.5	40°C / 140	29.9	9790	1.05
69K	0.537	26.8	3.5	40°C / 80	4.4	66,190	1.05

b. Titration

The concentration of carboxy chain ends was determined by titration. Approximately 0.6 g of polymer was dissolved in 30 ml of toluene and stirred for several hours. The solution was titrated to the phenolphthalein end-point with a 8.65 mM potassium hydroxide solution in methanol. The fraction of carboxy-terminated chains was approximately 90% for the 10 and 69K samples, consistent with the GPC results.

c. NMR

Figures 3.5 and 3.6 show the proton and carbon NMR spectra for PI-COOH in $CDCl_3$. ^{13}C NMR (50 MHz, $CDCl_3$): δ 147.2, 135.3, 125.1, 124.3, 111.3, 40.1, 32.3, 30.2, 26.7, 23.5, 18.3, 16.0. ^{1}H NMR (200 MHz, $CDCl_3$): δ 5.12 (s; -CH=), 2.03 (s; $-CH_2$), 1.68 (s; $-CH_3$), 1.60 (s; $-CH_3$). The polyisoprenes were determined to be 72% cis-1,4 addition by integration of methyl peaks in the ^{1}H

NMR spectra; this is the expected stereochemistry for anionic polymerization in a non-polar solvent. The peaks are identified in the figures.

d. Infrared Spectroscopy

Figure 3.7 shows the infrared spectrum of a 23K PI-COOH sample cast from THF onto a sodium chloride plate. The spectrum was collected for 120 scans at a resolution of 2.0 cm^{-1}. The bond motions relating to the measured absorption frequencies are identified in the figure.

2. N-Carboxy Anhydride of Benzyl Glutamate

Poly(γ-benzyl-L-glutamate) was prepared by polymerizing the corresponding monomer, the N-carboxy anhydride (NCA) of benzyl glutamate. This monomer was prepared via the triphosgene method. [123] The mechanism for this reaction is outlined in Figure 3.8. One mole of triphosgene produces 6 moles of HCl, and K_2CO_3 is used in this reaction to scavenge the HCl.

THF was dried on molecular sieves overnight to remove water. A solution of benzyl glutamate and K_2CO_3 (molar ratio 1 : 6) in THF were refluxed (at approx. 65°C) for about 15 minutes. The solution was cooled to 50°C, and a molar equivalent of triphosgene (a three-fold excess of phosgene) was added and allowed to react for two hours. The reaction mixture was filtered to remove the K_2CO_3, then precipitated into hexane and allowed to crystallize at -20°C. The white crystals were washed with additional hexane and reprecipitated from THF into hexane three times. The yield of NCA (m.p. 94-95°C) was approximately 90%.

Figures 3.9 and 3.10 show the ^{1}H and ^{13}C NMR spectra for the NCA which agree well with reported chemical shifts for this compound. [123] ^{1}H NMR ($CHCl_3$): δ 7.37 (s; phenyl, 5H), 6.77 (s; N-H, 1H), 5.15 (s; benzyl, 2H), 4.39 (t; CH, 1H), 2.62-2.55 (m; γ-CH_2, 2H), 2.23-1.85 (m; β-CH_2, 2H). ^{13}C NMR ($CHCl_3$): δ 172.0, 169.1, 134.9, 128.3, 128.0, 66.8, 56.9, 29.6, 26.8. The infrared spectrum of the NCA is shown in Figure 3.11. The characteristic NCA bands are located at 1780 - 1790 cm^{-1} and 1850 - 1865 cm^{-1}. [124]

3. Poly(γ-Benzyl-L-Glutamate)

The synthesis of polypeptides by the NCA method is characterized by a high polydispersity, especially for low molecular weights. This is primarily due to the fact that the rate constants for the polymerization are chain length dependent. The chain length dependence is related to whether the growing chain is in the random coil or the α-helix conformation. [125] The α-helix is only stable for a degree of polymerization greater than approximately 10. [101-126] Once the chain forms the α-helix, the rate constant for propagation increases five-fold. [127]

The polymerization of NCAs can be initiated by bases. There are two mechanisms for initiation: the protic mechanism and the aprotic mechanism. The most common protic initiators are primary and secondary amines. Characteristics of this mechanism include incorporation of the initiator into the growing chain, low molecular weights, high polydispersities, and a bimodal molecular weight distribution. The amine initiates the polymerization by nucleophilic attack at the C-5 position of the NCA, Figure 3.12. The ring is opened, one molecule of carbon dioxide is lost, and a primary amine chain end is generated. Chain propagation proceeds by

subsequent attack of the growing chain end at the C-5 position of the next monomer. The important result of this mechanism is that the carboxy-terminus of the polypeptide chain is blocked by the initiator, and the amine-terminus is free. This is an important consequence since only two functional chain ends are present during the subsequent coupling reaction: a carboxyl group at one end of the polyisoprene and an amine-end on PBLG.

A primary or secondary amine can also attack the C-2 carbonyl or act as a general base and initiate by proton abstraction from the ring nitrogen. The probability of these side-reactions is related to the steric hindrance at the C-5 carbon and the base strength of the initiator, respectively. Attack at the C-2 position leads to chain termination and increases the breadth of the molecular weight distribution of the product.

Termination reactions further increase the polydispersity of the polypeptides. Among the major termination reactions are attack at the C-2 position of the ring which creates a non-propagating carboxyl-terminated chain and end-group cyclization in which the amine chain-end attacks the carbonyl of the side-chain forming a five-membered ring and evolving benzyl alcohol. [125] End-group cyclization can occur during the polymerization or during storage of the polymer. If the cyclization occurs during the polymerization, it will lead to a higher polydispersity due to termination of an active end-group.

The NCA was polymerized in a dry nitrogen atmosphere. The NCA (1.6 g) was dissolved in ethyl acetate (2.5 ml) and dichloromethane (10 ml) and n-butyl amine initiator (2 ml) was added. The solution was refluxed (at approx. 45°C) for 10 minutes and then stirred at room temperature overnight. The polymer was precipitated into methanol to remove any unreacted NCA. The yield of polymer was approximately 88%.

The number average molecular weight is approximately the anhydride to initiator ratio for primary amine initiation. The calculated Mn was approximately 40,000. The weight average molecular weight of PBLG was determined by viscometry measurements in DMF at 25°C. The intrinsic viscosity (0.391 dl/g) was correlated with Mw via Simha's equation with the parameter 'b' equal to 18.2Å: [101, 126]

$$[\eta] = 6.86 * 10^{-4}\left[\frac{\left(M_w b^{-3}\right)^2}{15\left\{\ln\left(0.602 M_w b^{-3}\right) - 1.5\right\}} + \frac{\left(M_w b^{-3}\right)^2}{5\left\{\ln\left(0.602 M_w b^{-3}\right) - 0.5\right\}} + 0.84\right] \quad (3.1)$$

where [η] is in units of ml/g. The measured Mw for this polymer was 59,000 g/mol. The ^1H NMR spectrum of PBLG in $CDCl_3$ is shown in Figure 3.13. ^1H NMR ($CHCl_3$): δ 7.25 (s; phenyl, 5H), 5.05 (s; benzyl, 2H), 4.0 (s; α-CH), 2.45 (s; γ-CH_2), 2.25 (s; β-CH_2).

The remainder of the PBLGs which were used in the preparation of PI-PBLG diblock copolymers were purchased from Sigma. Table 3.2 lists the reported molecular weights from (viscometry and light scattering measurements) for these polymers.

Table 3.2. Molecular weights reported for commercially obtained PBLG.

MW viscometry	MW LALLS	Lot #	Comments
25K	19K	121H5506	
26K	17.3K	52H5521	
42K	30.3K	32H5530	general use
118K	100K	91H5521	

4. Coupling of Polyisoprene and PBLG

The coupling of carboxy-terminated polyisoprene and the amine-terminated PBLG was accomplished by using peptide chemistry techniques. A combination of dicyclohexylcarbodiimide (DCCI) and HOBt was used. DCCI activates the carboxylic acid functionality, and HOBt acts as a trapping agent to suppress side-reactions. [128]. The mechanism for this coupling reaction is shown in Figures 3.14a and b. The coupling strategy, as opposed to sequential synthesis, [27, 28] allowed for the independent synthesis of the blocks and isolated characterization and purification.

DCCI, HOBt, and PI-COOH (molar ratio 1.2 : 1 : 5) were reacted in a dry nitrogen atmosphere in dichloromethane for several hours. A molar equivalent (with respect to HOBt) of PBLG was added and allowed to react for 24 to 48 hours. The solution was filtered to remove the white, crystalline dicyclohexylurea side-product. The polymer was recovered by precipitation into ethanol followed by several reprecipitations from dichloromethane into ethanol. The total yield was between 59 and 96%. Table 3.3 summarizes the conditions of each coupling reaction. Table 3.4 shows the molecular weights of the PI-PBLG diblock copolymers which were synthesized. The system has been designed as a 3X3 matrix. Trends in subsequent characterization of these rod-coil diblock copolymers may be borne out as a function of molecular weight of both the coil and the rod blocks.

Table 3.3. Characteristics of coupling reaction between carboxy-terminated polyisoprene and poly(γ-benzyl-L-glutamate).

PI-b-PBLG	PI-COOH	PBLG	DCCI	HOBt	DCM,	Rxn Time,	Yield
	g	g	g	g	ml	h	%
2.8K-26K	1.4	1.5	0.3	0.09	40	43	43
10K-26K	3.7	1.5	0.8	0.3	45	43	63
69K-26K	2.7	1.0	0.2	0.1	75	39	
2.8K-59K	0.5	0.8	0.07	0.1	50	38	59
10K-59K	2.3	2.0	0.5	0.2	40	18.5	80
69K-59K	4.5	1.5	0.3	0.2	40	18.5	95
2.8K-118K	0.3	2.0	0.07	0.05	50	19	74
10K-118K	1.0	2.0	0.1	0.06	50	19	75
69K-118K	1.7	1.0	0.1	0.03	25	39	

Table 3.4. Molecular weights of PI-PBLG diblocks. The notation lists the molecular weight of the PI block first followed by the molecular weight of the PBLG block, both in thousands.

Mw PI	Mw PBLG	L_{PBLG}, nm
2.8	25	17
2.8	26	18
2.8	59	40
2.8	118	81
10	26	18
10	59	40
10	118	81
69	26	18
69	59	40
69	118	81

5. Purification of PI-PBLG

The product of the coupling reaction was a mixture of homopolymer of the PI and PBLG as well as diblock. Previous reports based on PS-PI diblock copolymer synthesis and purification described the difficulty in removing the uncoupled PS component whereas the uncoupled PI component was readily extracted with hexane (or similar solvents). PS and PBLG have similar solubility characteristics (i.e. phenyl rings and similar solubility in solvents), and it was recognized that the optimum scenario would be the complete coupling of PBLG (and PI).

Figure 3.15 outlines the purification strategy. The first "purification" step used a large molar excess of PI-COOH (5 to 10-fold) during the coupling reaction. This was expected to kinetically and thermodynamically drive the reaction toward completion, leaving primarily uncoupled PI and diblock copolymer. The complete coupling of PBLG chains was anticipated. The ^1H NMR spectrum of the total reaction product of 69K PI-b-59K PBLG reveals the large excess of PI as shown by the relative peak areas of the PBLG phenyl protons (7.25 ppm) and the PI methylene protons (2.03 ppm), Figure 3.16.

a. Removal of Polyisoprene Homopolymer

The sticky, yellowish-white total reaction product was washed with 100 to 200 ml hexane. The insoluble component was white and crumbly and was recovered as the "A-fraction". The component soluble in hexane was isolated by precipitating into methanol. This sticky, yellow-white product was isolated as the "B-fraction." ^1H NMR analysis of the A-fraction reveals a large

decrease in the relative intensity of the PI resonances at 2.0 and 1.6 ppm, Figure 3.17. The polyisoprene homopolymer was extracted into the B-fraction as shown most notably by the absence of the intense PBLG phenyl peak at 7.25 ppm, Figure 3.18.

It is instructive to note that only the homo-PI was soluble in hexane and not the diblock. This is not an intuitively obvious result for two reasons. First, the coil block is approximately the same length as the rod block and could provide the osmotic driving force for dissolution. Secondly, the block copolymer could form micelles with a core of rods and the well-solvated coils as the corona. The fact that these two scenarios do not happen points to the dominant influence of the rod block on the solubility of the diblock copolymer. This work only involves a PBLG rod-block, and therefore it is unclear whether this is relationship will govern rod-coil diblocks in general, although similar behavior was observed for a polyamide rod-coil diblock. [68]

b. Removal of PBLG Homopolymer

The A-fraction is composed of PI-PBLG diblock copolymer and homopolymer PBLG. Many strategies to separate the PBLG homopolymer from the diblock copolymer were tested: extraction with DMF, precipitation with various polyisoprene-selective solvents, fractionation from dichloromethane, "bead purification", selective extraction, and finally selective fractionation.

i. Extraction with DMF One could imagine removing the PBLG homopolymer by selectively dissolving it in a solvent in which the copolymer is insoluble. Published work claimed that the homo-PBLG could

be simply extracted with DMF, [26] but this technique proved unsatisfactory since both the diblock and the PBLG were soluble in DMF.

ii. Precipitation One could imagine the opposite approach to extraction, that is precipitation. In this case, the material is dissolved in a solvent which dissolves the copolymer but *not* the PBLG homopolymer. This solvent would be a polyisoprene (or coil-selective) solvent. Several solvents were tried: hexane, methyl ethyl ketone, ethyl acetate, heptane, amyl acetate, and cyclohexane. In each case, the solvent was good for polyisoprene and a non-solvent for PBLG. The polymer did not go into solution. This result again emphasizes the influence of the PBLG on the diblock solubility behavior.

iii. Fractionation from Dichloromethane The next attempt to separate the homopolymer PBLG from the diblock was made by dissolving the polymer in dichloromethane (DCM) and fractionating with ethanol to the visual cloud point. The precipitate was recovered and determined from ^1H NMR to be composed of only PBLG. ^1H NMR revealed that the polymer which remained in solution contained the diblock copolymer. This is a counter-intuitive result; it was expected that the diblock copolymer (the higher molecular weight component) would precipitate first. PBLG appears to be highly immiscible in ethanol, more so than PI. Even though a separation between the diblock and the PBLG was achieved, this is not a purification strategy which is universally applicable. The solubility behavior of the PBLG and the diblock are intimately dependent on the molecular weight of each species.

iv. Bead Purification A novel approach to the separation was termed "bead purification". The *predicted* adsorption behavior of the diblock copolymer was utilized in this approach. In a selective solvent for the rod, the rod-coil diblock copolymer was expected to adsorb onto solid surfaces via the poorly solvated coil block. The homo-PBLG, having no "sticky foot", was not expected to adsorb, but rather remain in solution. A dilute solution (approx. 0.05 wt%) of the 10K-59K diblock was prepared in benzyl alcohol. A quantity of glass beads (approx. 50 mm dia.) were added to the solution. (The surface area required was calculated assuming the coil blocks adsorb as spheres with a bulk density of 1 g/cc.) The beads were then filtered and the BzOH eluent recovered. No visible precipitate was isolated from the eluent upon addition of methanol. The homopolymer PBLG was expected to be recovered at this point. The beads were then washed with THF. Both the beads and the THF eluent were recovered. The polymer recovered from the THF was analyzed with NMR and shown to be only PBLG. Diffuse reflectance IR measurements of the beads after rinsing with THF showed that there was still polymer attached to the beads. The large surface area requirement necessitated the use of very small beads, but these were difficult to remove from the polymer by filtration and/or centrifugation techniques. The inability to recover homo-PBLG coupled with experimental difficulties and low recovery of polymer made this an unacceptable method of purification.

v. Selective Extraction A selective extraction approach was also attempted. [129, 130] The polymer was dissolved in a mixture of two solvents. This first solvent (DMF) was selective for the rod block; the second solvent (hexane) is selective for the coil block. Each selective solvent was *immiscible* with the other block. The 10K-26K (A-fraction) polymer was dissolved in

DMF. Hexane was then added to make a DMF/hexane solution with 40 vol% hexane and 3 wt% polymer. An emulsion is formed upon stirring this solution, but the solvents partition partially when not stirred. The emulsion was centrifuged at 5000 rpm for 5 minutes. A thin layer of white (polymer) precipitate was isolated *between* the two layers of solvent. The polymer is most likely the pure diblock copolymer, but the layer is fragile and perturbations (such as tilting the tube to decant the top layer or pipetting the top layer) cause the polymer to redissolve (emulsify) in the adjacent solvents. The polymer layer generated by centrifugation was unable to be isolated.

The emulsion was then transferred to a separatory funnel. The result was an optically clear, well-stratified hexane layer at the top of the funnel. A relatively wide emulsion zone, containing approximately half of the volume of the solution, lies below the hexane layer. A very diffuse boundary separates the emulsion layer with the DMF phase below. The DMF phase is relatively clear compared with the emulsion, but not as clear as the hexane phase. The observations are consistent with the dominant influence of the PBLG on the diblock solubility (sharp emulsion/hexane interphase), the prior removal of PI homopolymer (clear hexane phase), and the presence of block copolymers (stable emulsion). The diffuse emulsion/DMF boundary is attributed to the compatibility of PI-PBLG with DMF through the formation of micelles. Gravity was a weak driving force to break up the emulsion. The diffuse DMF/emulsion boundary was not amenable to the separation of homopolymer PBLG (segregated to the DMF phase) from the diblock (emulsion).

vi. <u>Selective Fractionation</u> Finally, a novel technique was developed to remove the PBLG homopolymer and termed "selective fractionation".

The homopolymer PBLG was removed by fractionation from anhydrous DMF, a selective solvent for the rod blocks. This results in a large molecular weight difference between the diblock (aggregates) and the homopolymer. The fractionation was performed by adding methanol to a 1% solution of polymer (A-fraction) in DMF until the polymer first began to precipitate, as indicated by the solution becoming cloudy. The gel-like precipitate was recovered by centrifugation and reprecipitated from DCM into methanol. The yield of insoluble fraction from the A-fraction (A-SF1) was approximately 20%. The soluble polymer was recovered from the filtrate by precipitation with methanol; this formed the A-SF2 fraction.

Figure 3.19 shows the ^{1}H NMR spectrum of the A-SF1 fraction of 69K PI-b-59K PBLG in $CDCl_3$. Comparison with Figure 3.17 (A-fraction) reveals that the relative intensities of the PI resonances (2.03 and 1.6 ppm) are greater, consistent with the *removal* of PBLG homopolymer.

Figure 3.20 shows the ^{1}H NMR spectrum of the A-SF2 fraction of 69K PI-b-59K PBLG. A small amount of TFA added to the solution gives a characteristic PBLG spectrum. In the purification of other samples, weak PI resonances at 2.03 and 1.6 ppm were observed, consistent with PBLG and trace amounts of PI-PBLG diblock. The amount of diblock remaining in the fractionation solution is dependent on the amount of methanol added and the estimation of the cloud point. The purification of the 69K PI-b-59K PBLG sample, as followed by ^{1}H NMR, is summarized in Table 3.5. Table 3.6 summarizes the purification analysis for the series of nine diblocks studied in this work. Quantitative removal of uncoupled homopolymer was verified by the repeat unit ratios of PI and PBLG in the diblock samples. The repeat unit ratios were calculated from the areas obtained by deconvoluting the PBLG and PI peaks at 5.05 and 5.12 ppm, respectively. The selective fractionation

purification of the 69K PI-b-118K PBLG sample was ineffective as the sample contains residual PBLG homopolymer. Figures 3.21 through 3.27 show the ^1H NMR spectra of the diblocks which were studied in this work.

Table 3.5. ^1H NMR analysis of diblock copolymer purification route. Repeat unit ratios (PI/PBLG) for each step are shown for 69K PI-b-59K PBLG sample.

	PI : PBLG (Measured)	PI : PBLG (Calculated)	Yield, %
Total Product	10 ± 1	9.6	96
A-fraction	0.2 ± 0.05		22
B-fraction	1.0 ± 0.1		65
A-SF2	0.06 ± 0.05		9.8
A-SF1	3.0 ± 0.5	3.4	4.6

Table 3.6. Summary of diblock copolymer purity by ^1H NMR analysis of monomer ratio, PI/PBLG.

PI-b-PBLG	Diblock Monomer Ratio (PI/PBLG)	
	Measured	Expected
2.8K-26K	0.46 ± 0.2	0.35
10K-26K	0.91 ± 0.4	1.24
2.8K-59K	0.14 ± 0.03	0.15
10K-59K	0.60 ± 0.05	0.55
69K-59K	3.0 ± 0.5	3.49
2.8K-118K	0.086 ± 0.05	0.076
10K-118K	0.22 ± 0.1	0.27
69K-118K	0.46 ± 0.1	1.75

D. Conclusion

In conclusion, carboxy-terminated polyisoprene and poly(γ-benzyl-L-glutamate) were individually synthesized and later coupled. The resulting block copolymer presented significant purification challenges because the diblock solubility was controlled by the PBLG block. Consequently, the PBLG and the diblock were difficult to separate. A number of techniques were attempted, but eventually a new purfication strategy was developed and termed selective fractionation.

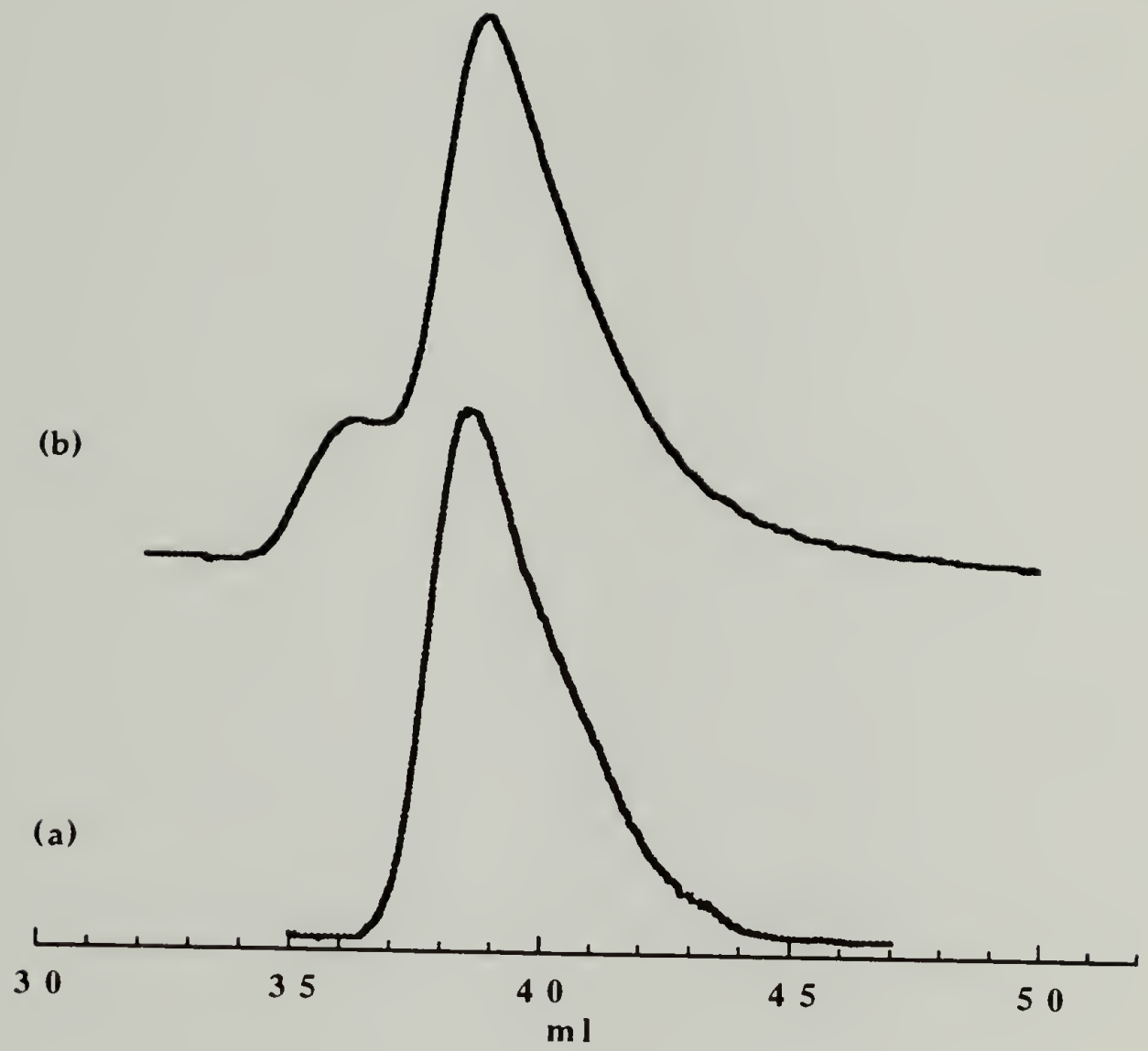

Figure 3.2. GPC spectra of (a) unfunctionalized and (b) carboxy-terminated 2.8K 1,4-cis-polyisoprene.

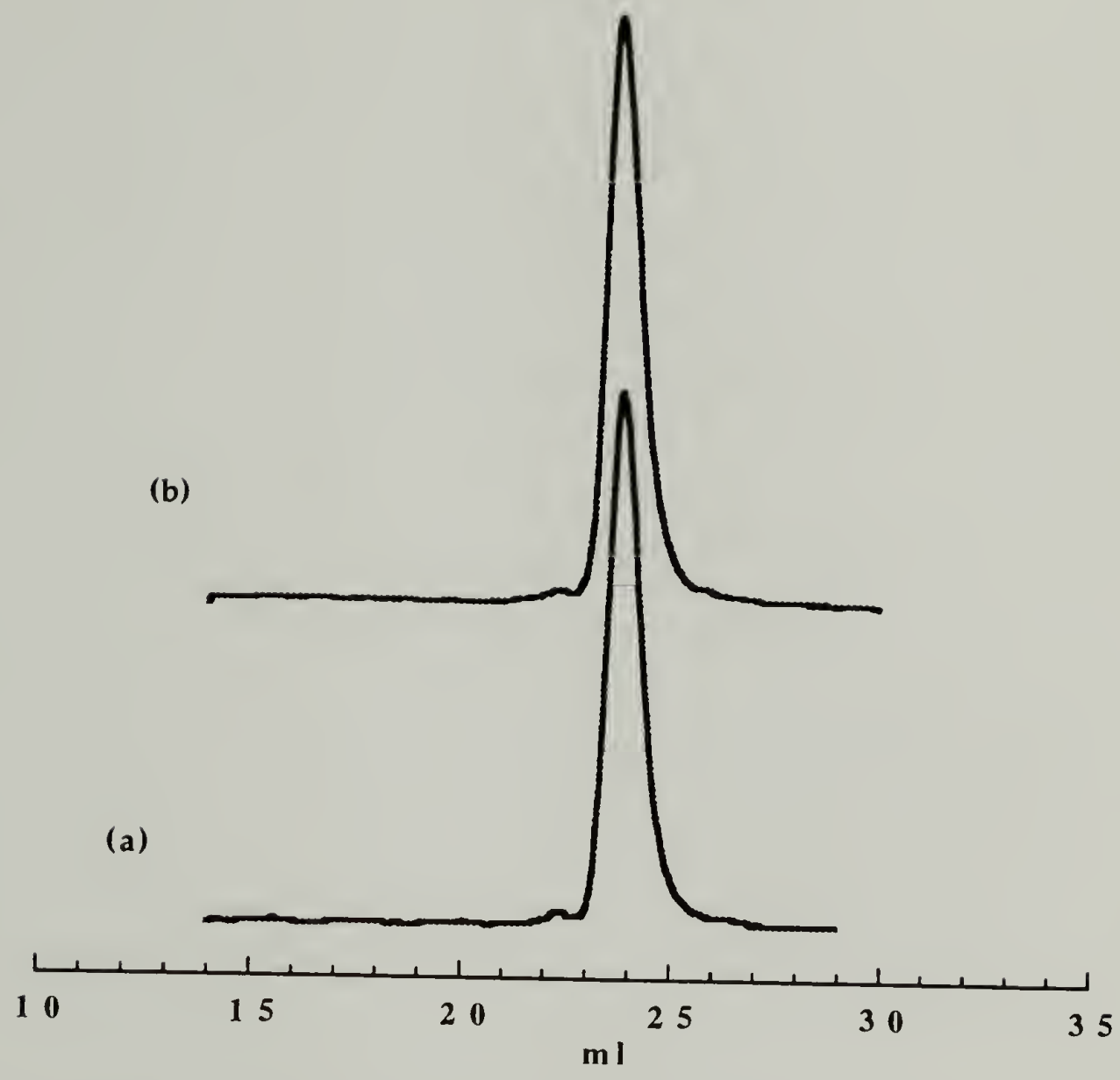

Figure 3.3. GPC spectra of (a) unfunctionalized and (b) carboxy-terminated 10K 1,4-cis-polyisoprene.

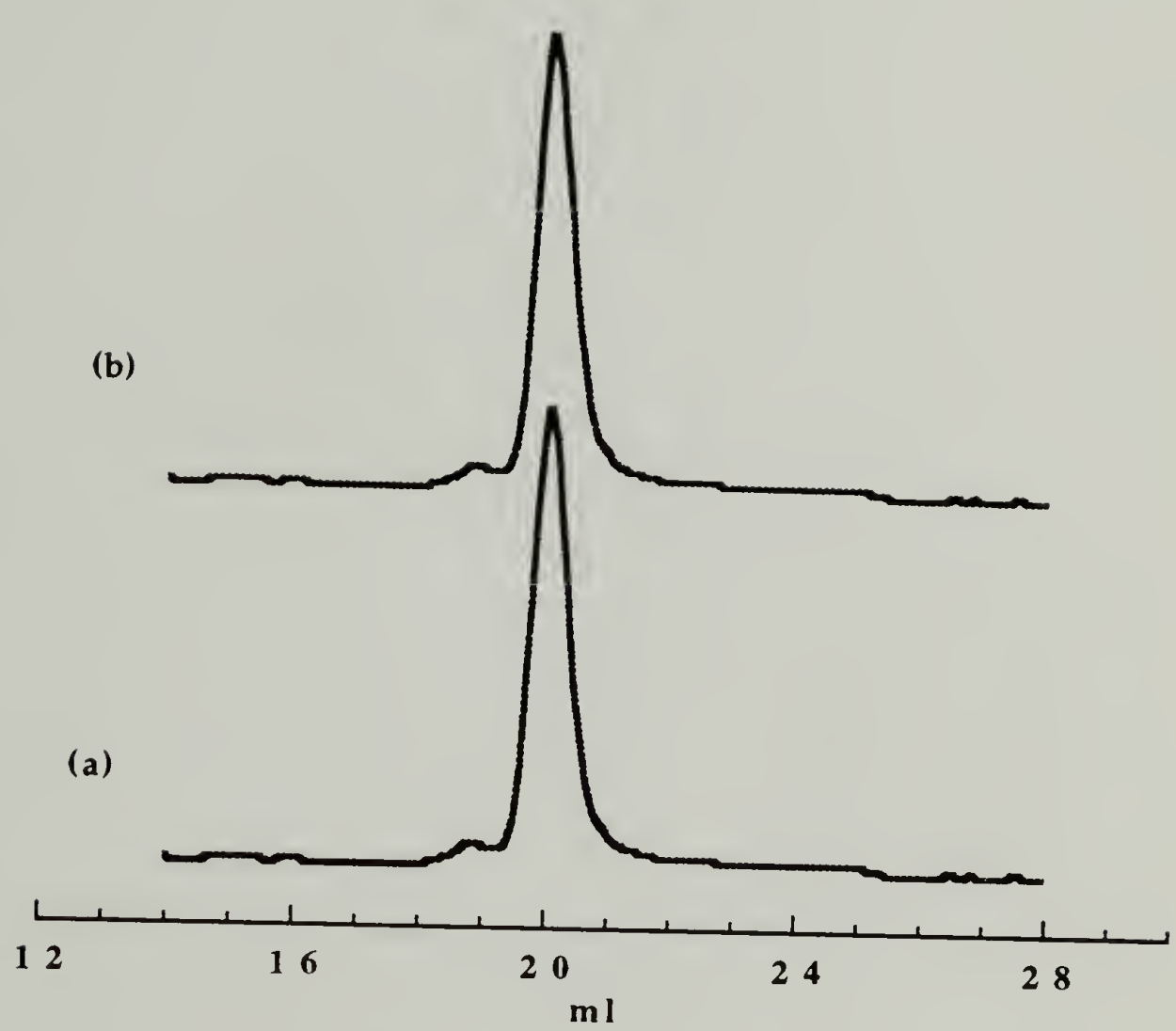

Figure 3.4. GPC spectra of (a) unfunctionalized and (b) carboxy-terminated 69K 1,4-cis-polyisoprene.

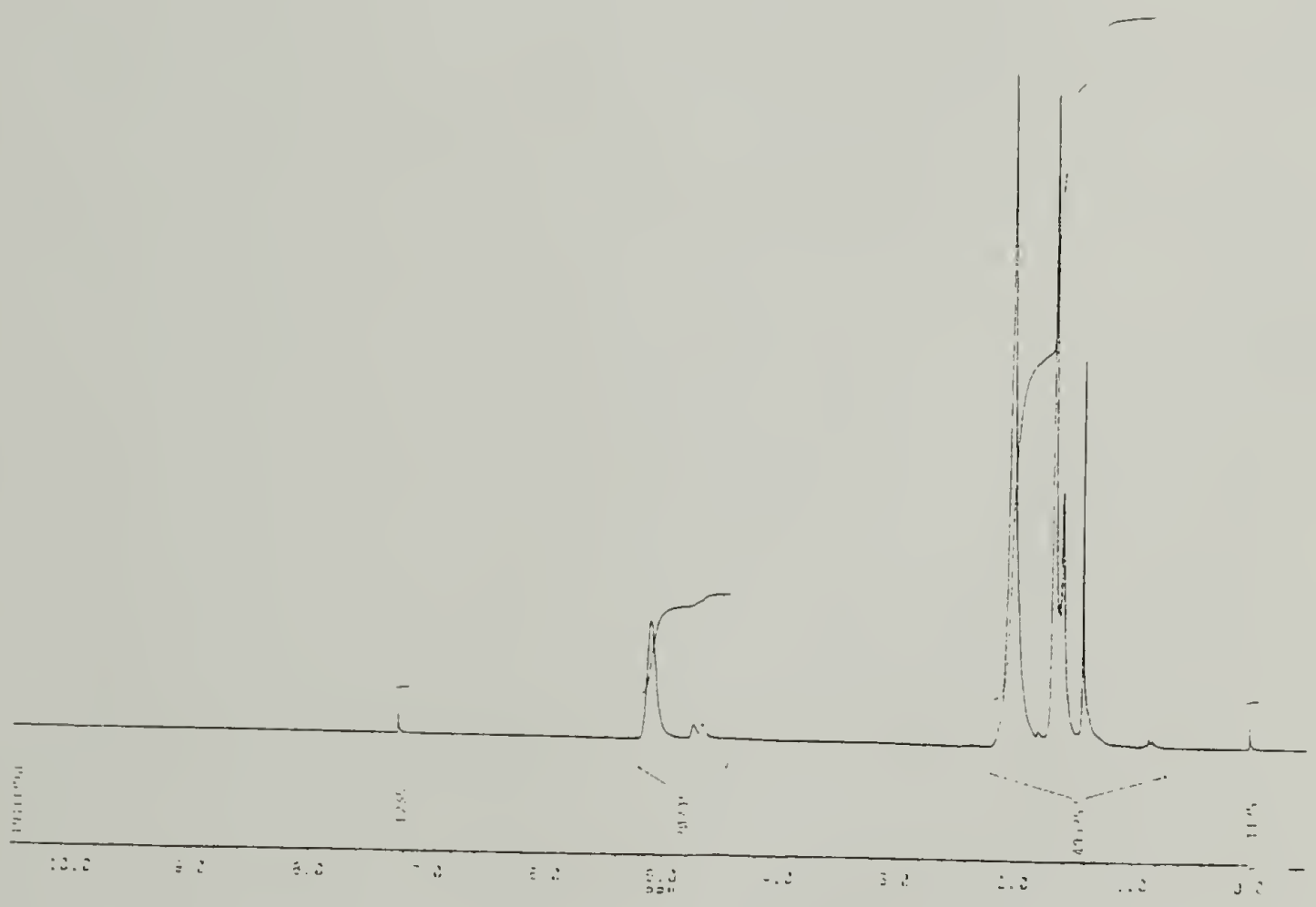

Figure 3.5. ^{1}H NMR spectrum of 10K PI-COOH in $CDCl_3$ (200 MHz).

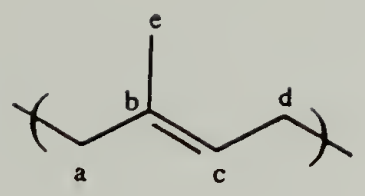

cis-1,4

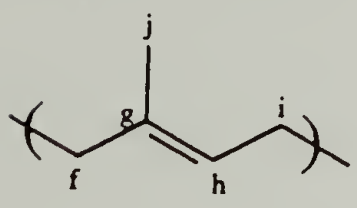

trans-1,4

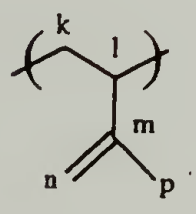

1,2

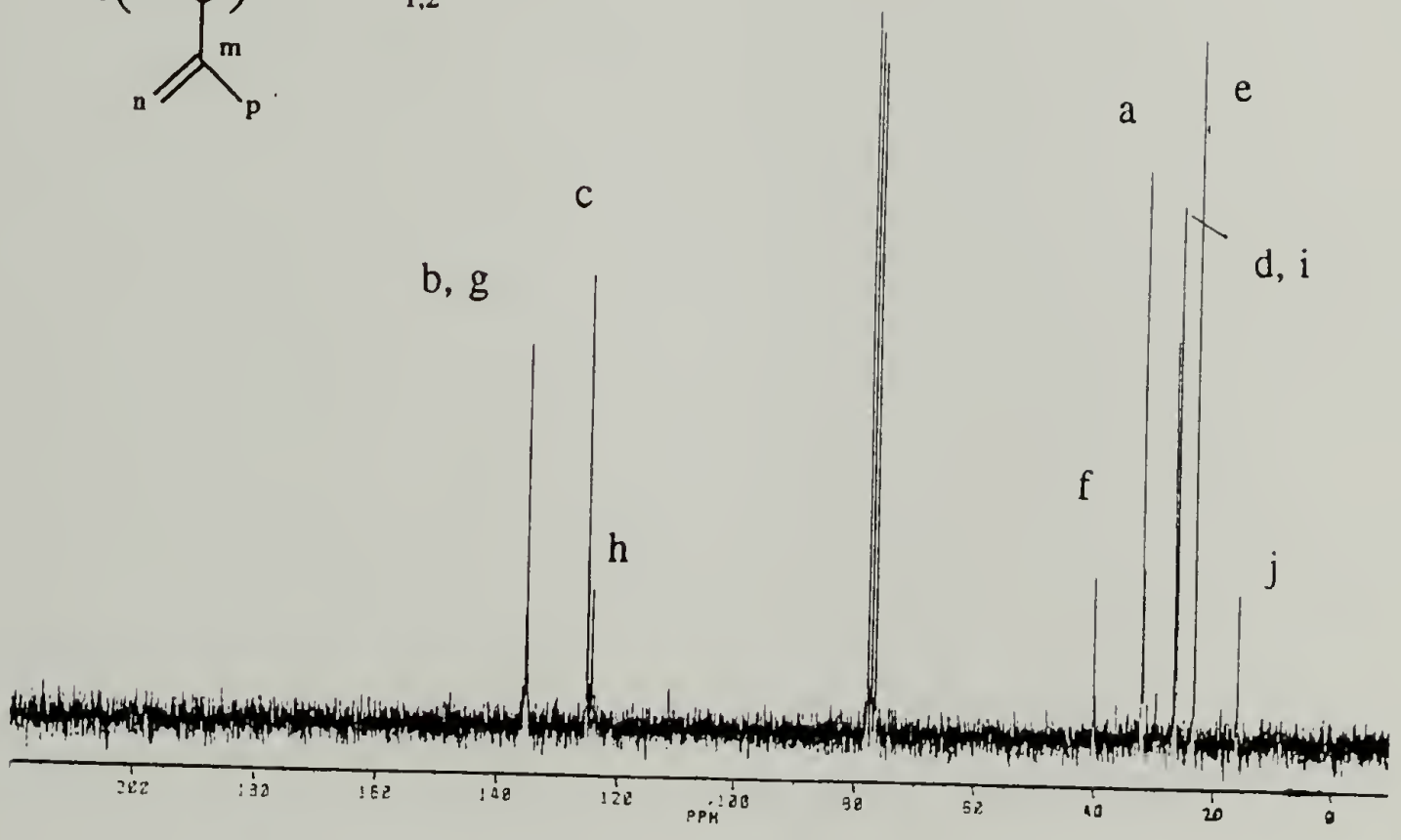

Figure 3.6. ^{13}C NMR spectrum of 10K PI-COOH in $CDCl_3$.

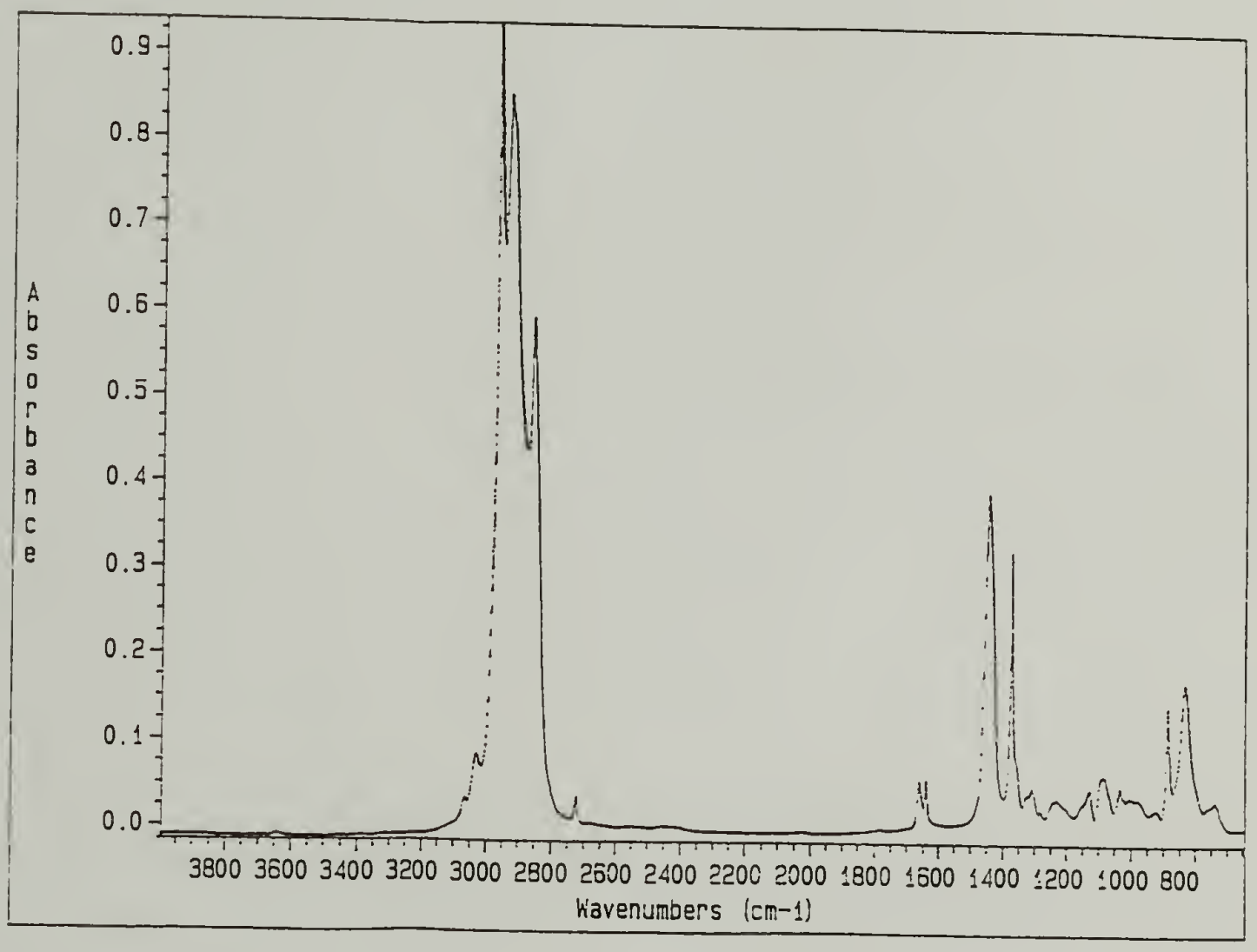

Figure 3.7. IR spectrum of 23K 1,4-PI-COOH cast onto NaCl plate from THF; 120 scans, 2.0 cm^{-1}.

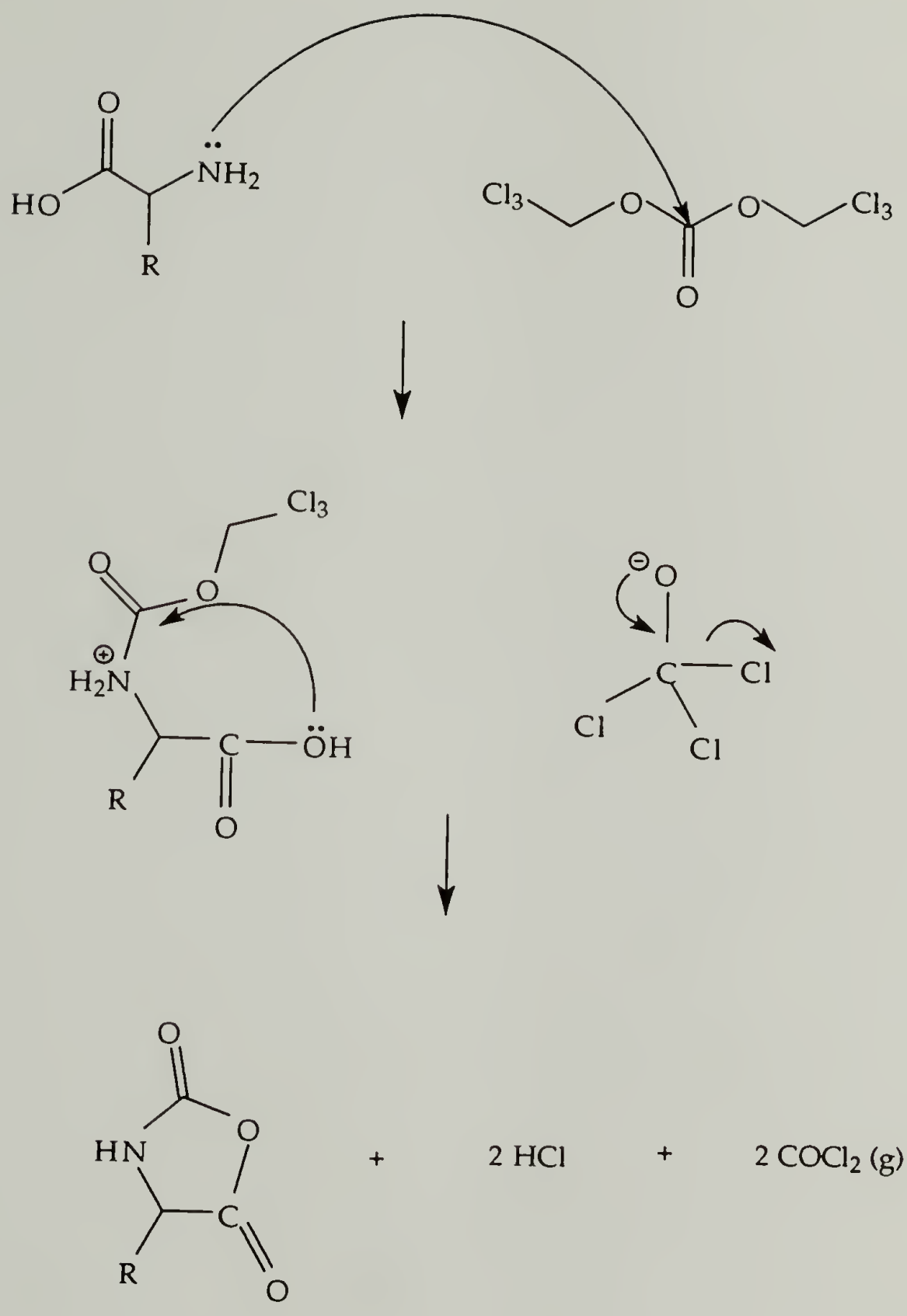

Figure 3.8. Mechanism of N-carboxy anhydride synthesis using triphosgene.

Figure 3.9. ^{1}H NMR spectrum of NCA of benzyl glutamate in $CDCl_3$.

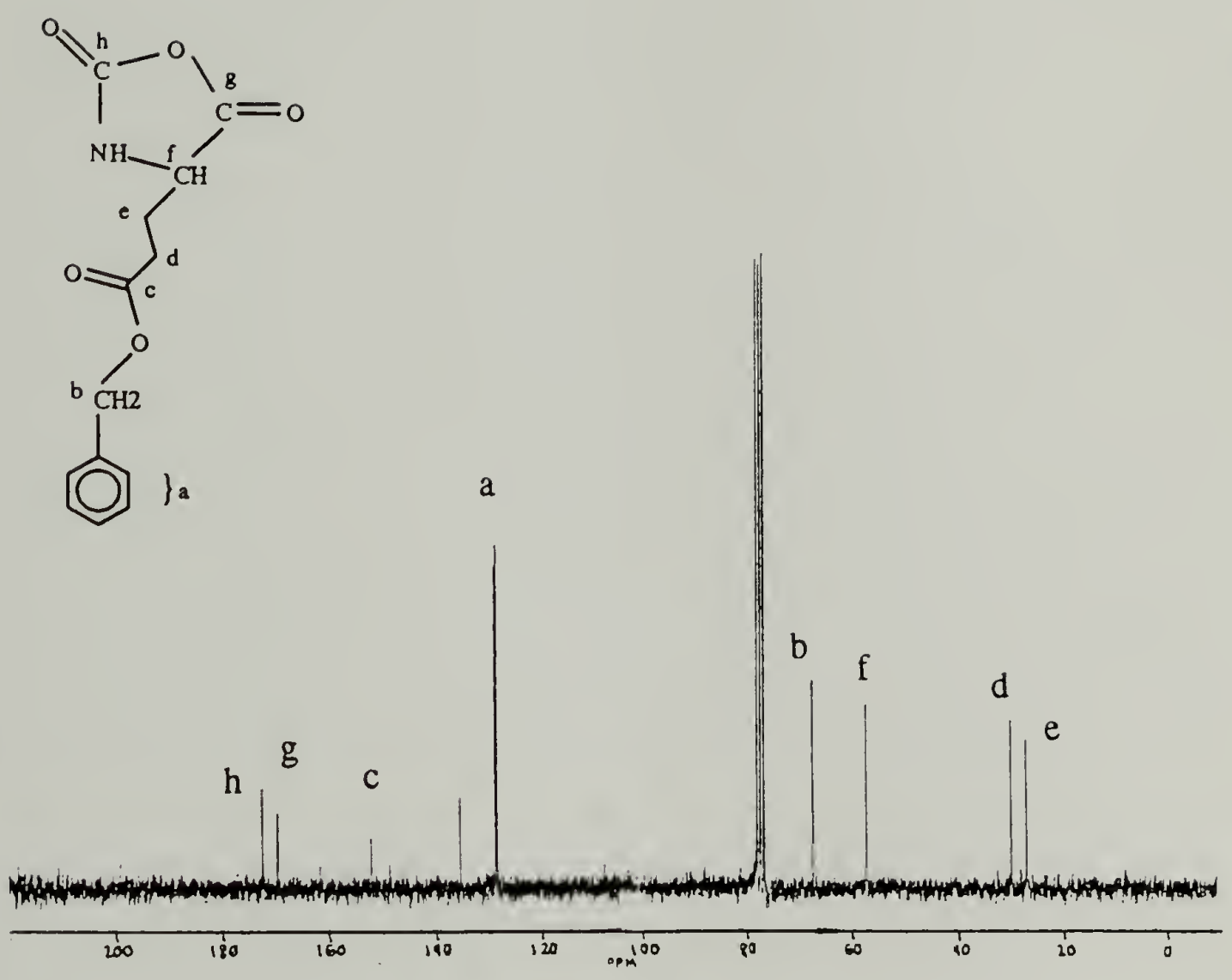

Figure 3.10. ^{13}C NMR spectrum of NCA of benzyl glutamate in $CDCl_3$.

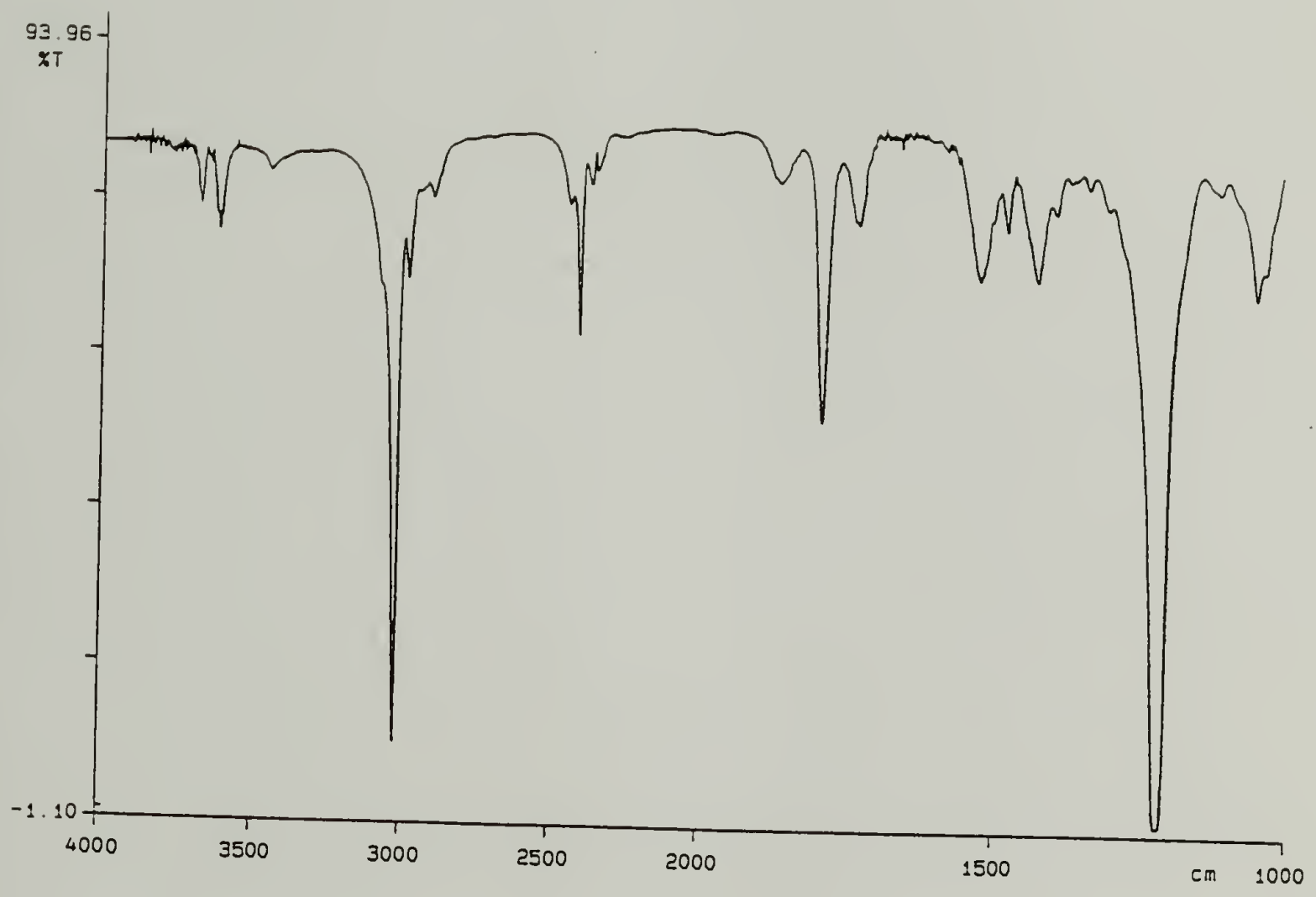

Figure 3.11. IR spectrum of NCA of benzyl glutamate.

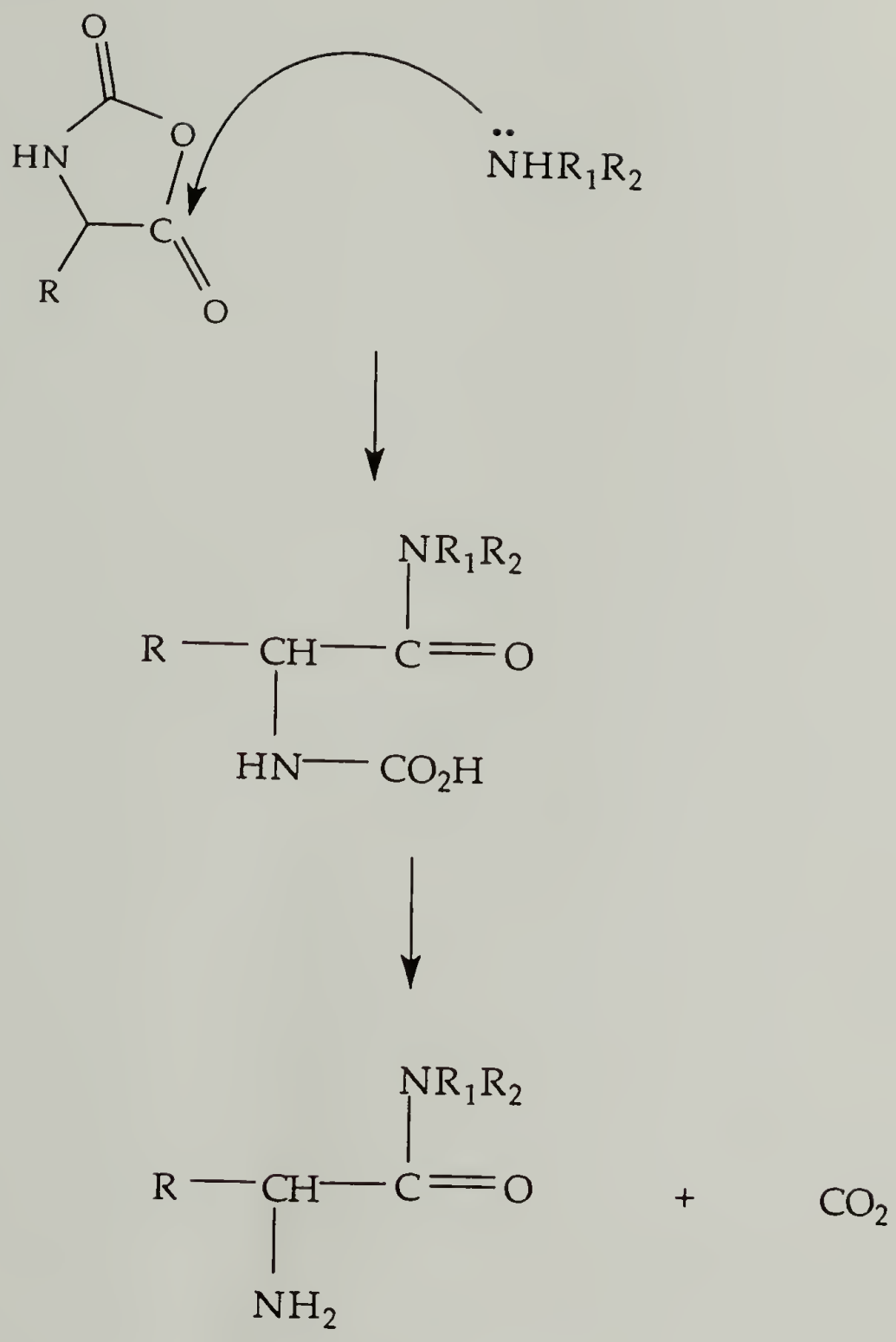

Figure 3.12. Mechanism of NCA polymerization initiated by primary and secondary amines.

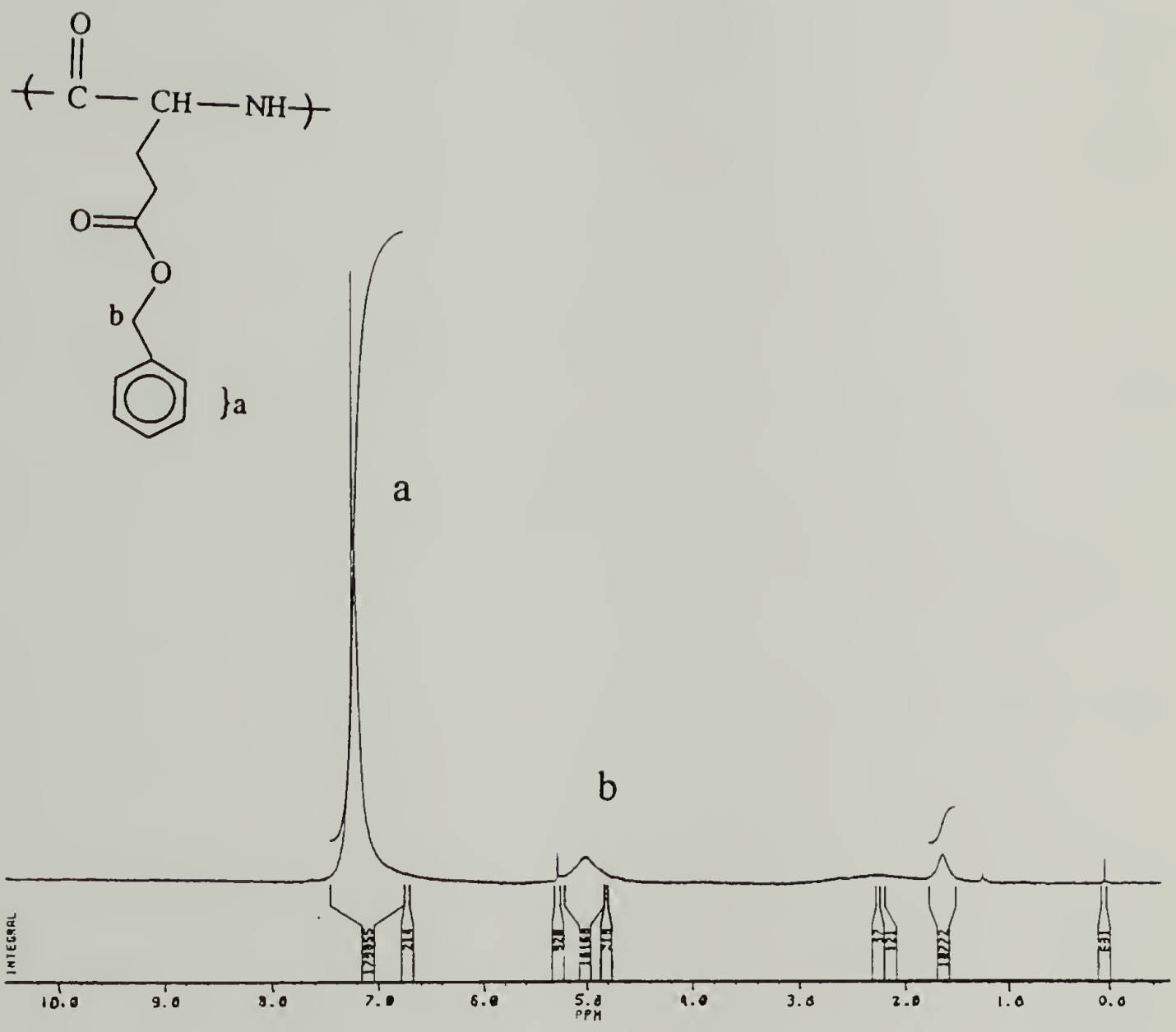

Figure 3.13. ^{1}H NMR of synthesized PBLG (59K by viscometry).

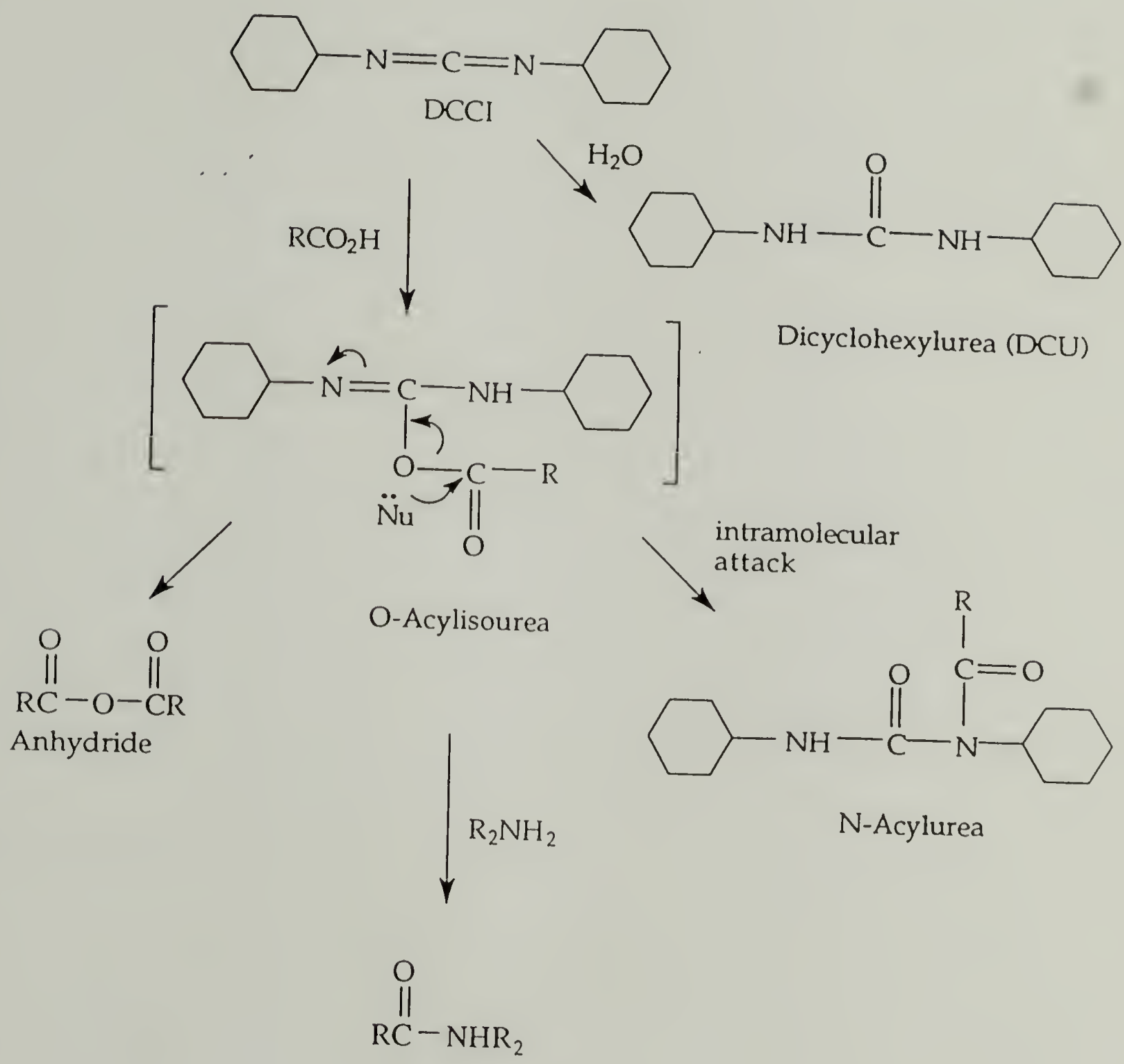

Figure 3.14 Polyisoprene and PBLG coupling reaction.

a. Dicyclohexylcarbodiimide coupling reaction.

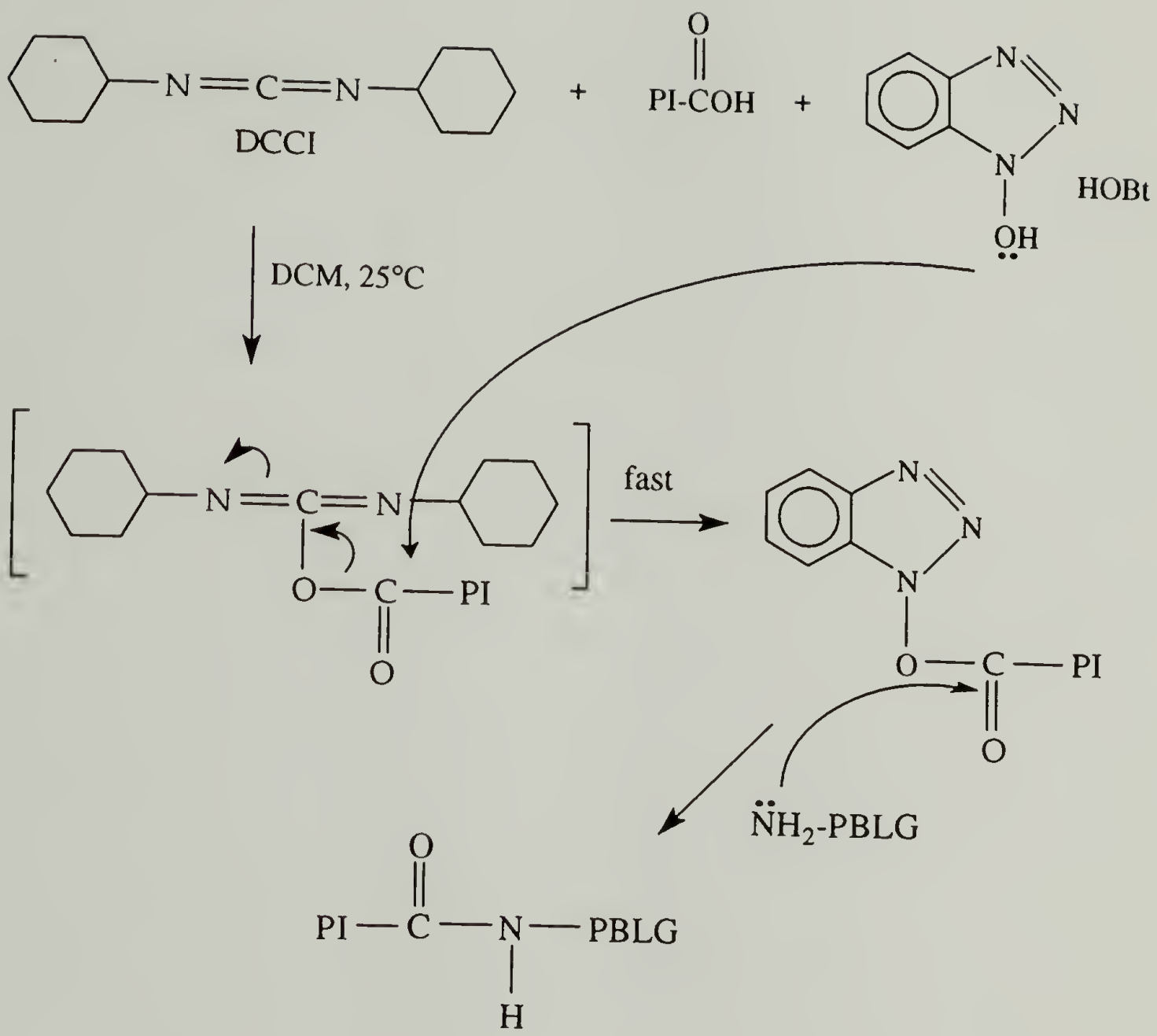

Figure 3.14b. Polyisoprene and PBLG coupling reaction.

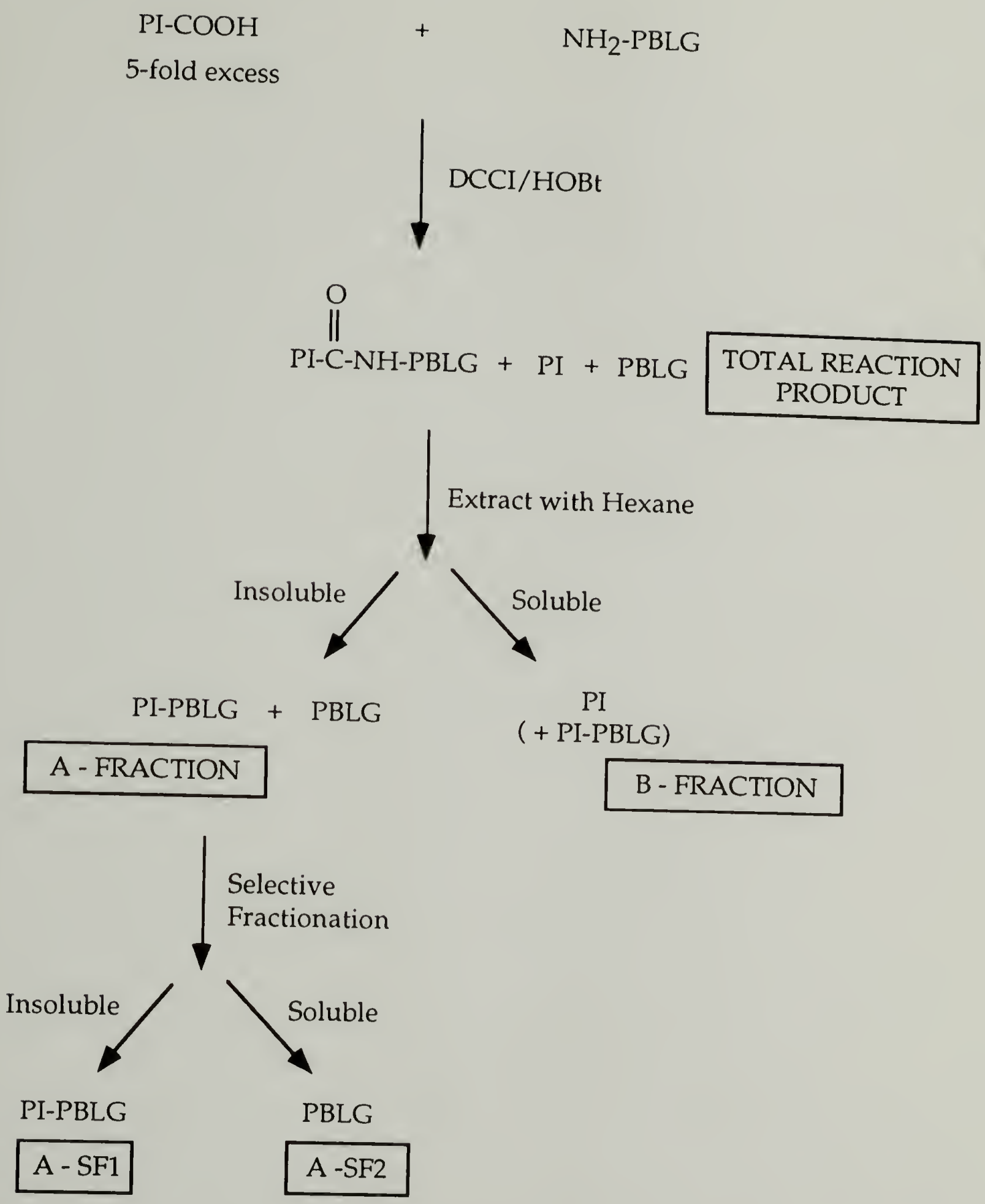

Figure 3.15. Purification strategy for polyisoprene-poly(γ-benzyl-L-glutamate) diblock copolymers.

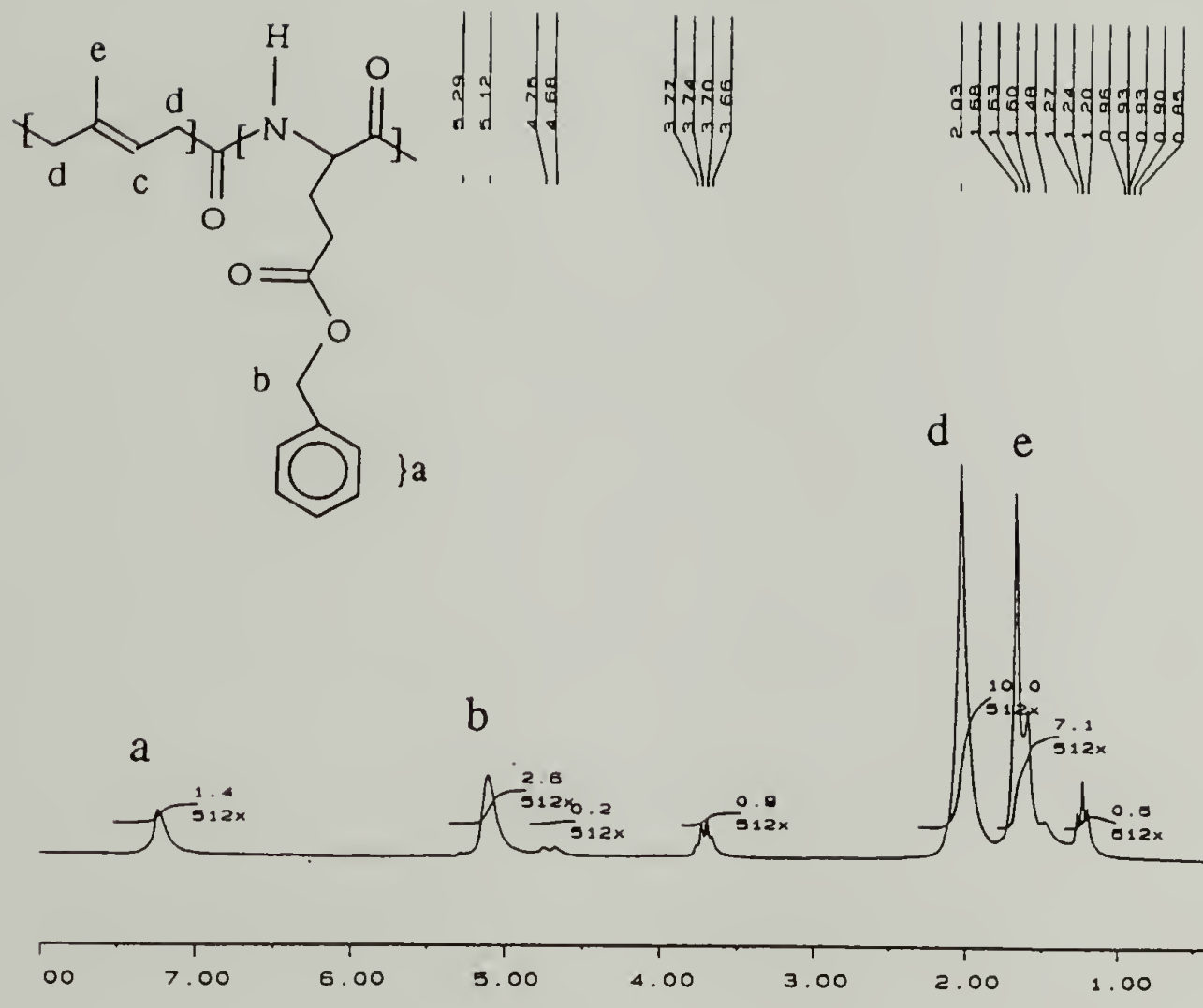

Figure 3.16. ^{1}H **NMR spectrum of the total product fraction of 69K PI-b-59K PBLG in** $CDCl_3$.

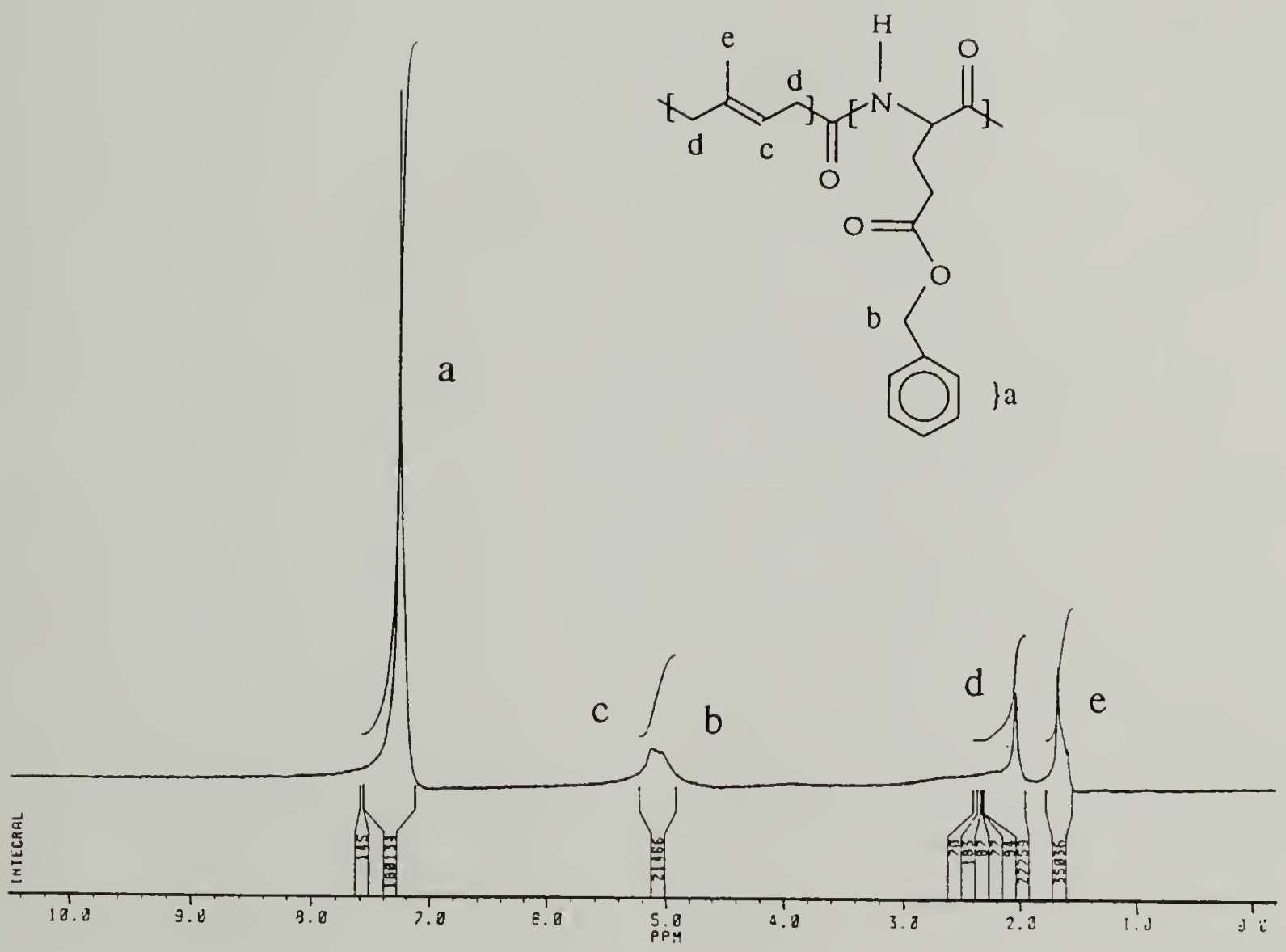

Figure 3.17. ^1H NMR spectrum of A-fraction of 69K PI-b-59K PBLG in $CDCl_3$, fraction insoluble in hexane.

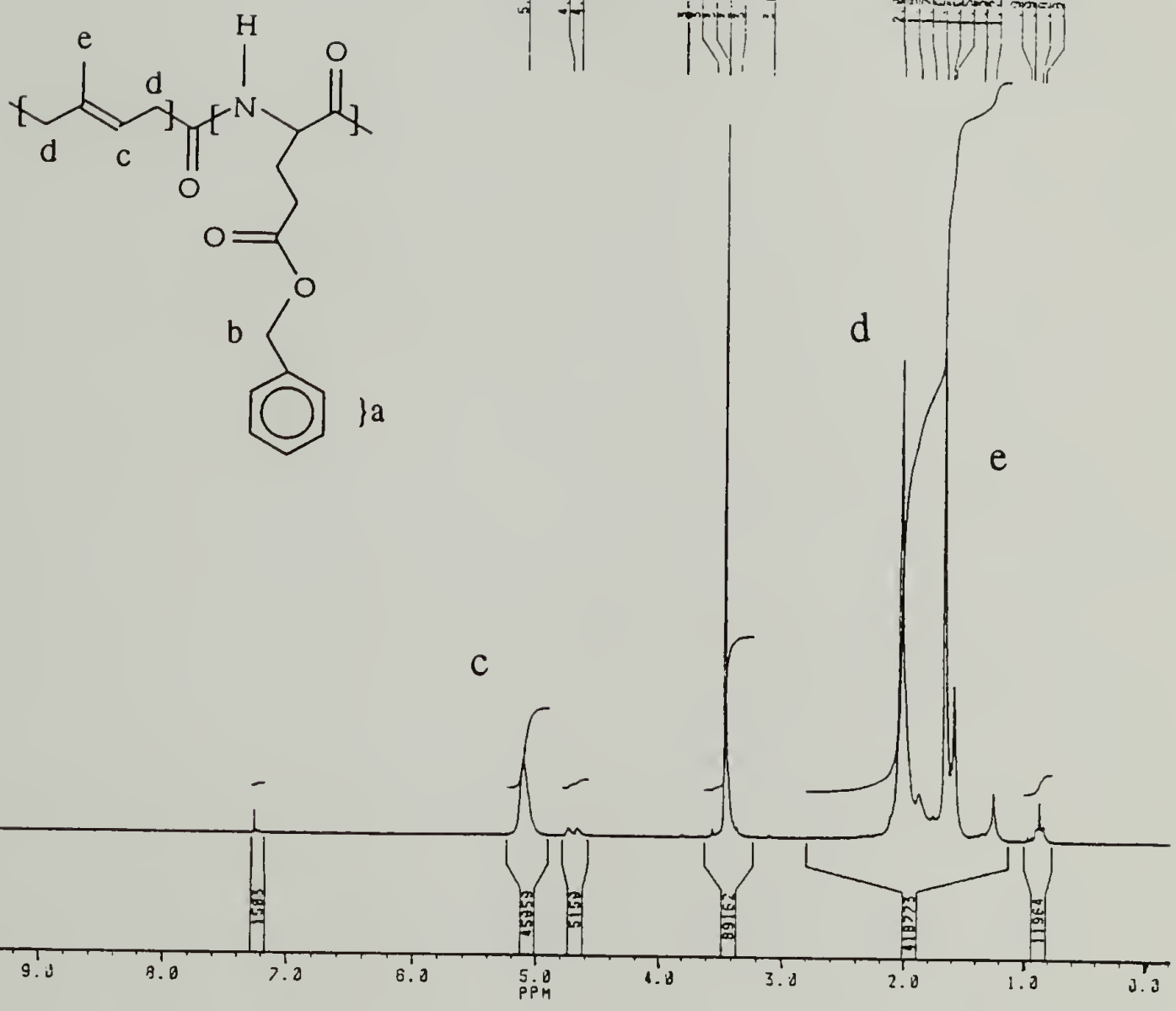

Figure 3.18. ^{1}H NMR spectrum of B-fraction of 69K PI-b-59K PBLG in $CDCl_3$, fraction soluble in hexane.

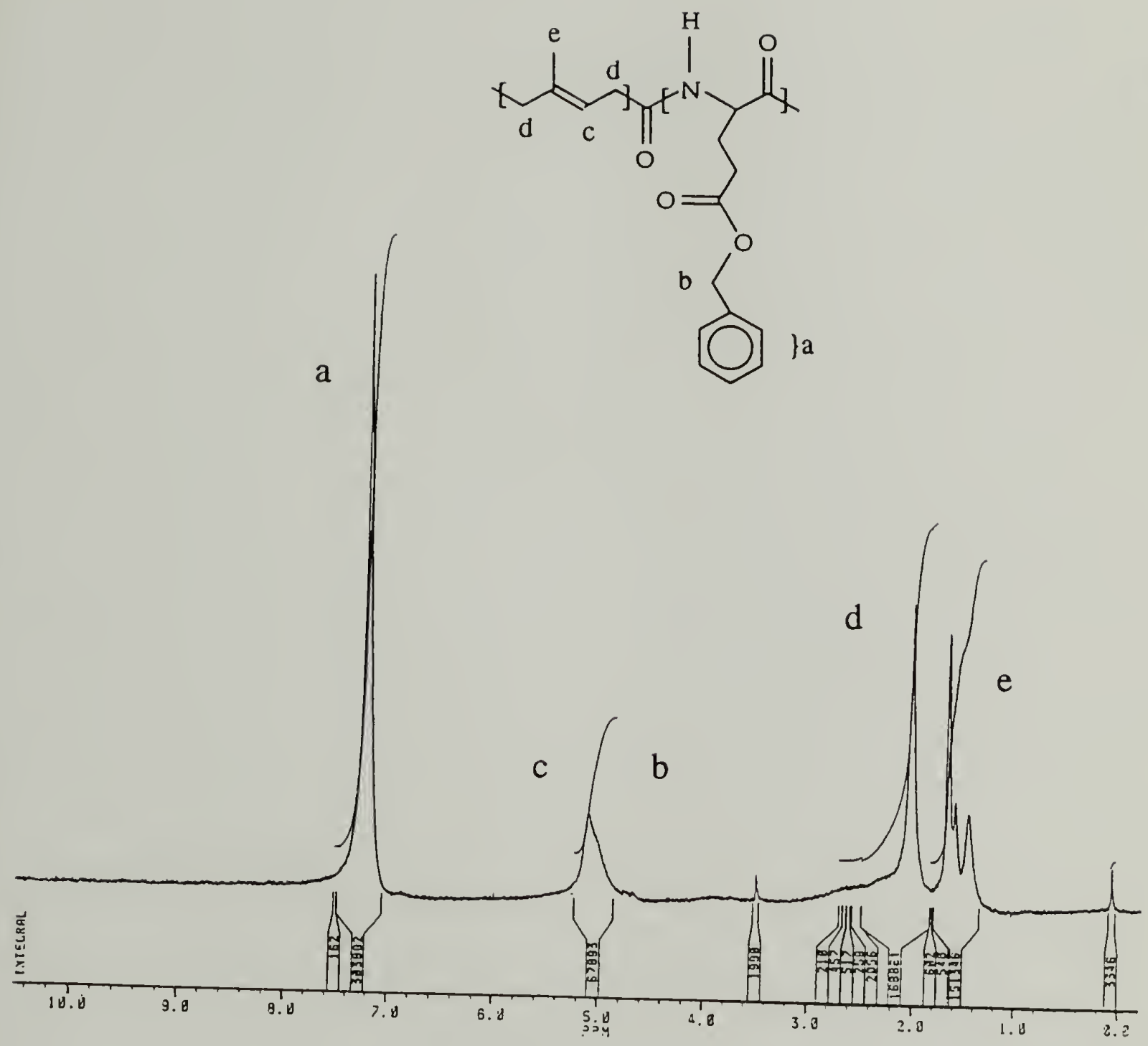

Figure 3.19. ^1H NMR spectrum of A-SF1 fraction of 69K PI-b-59K PBLG in $CDCl_3$.

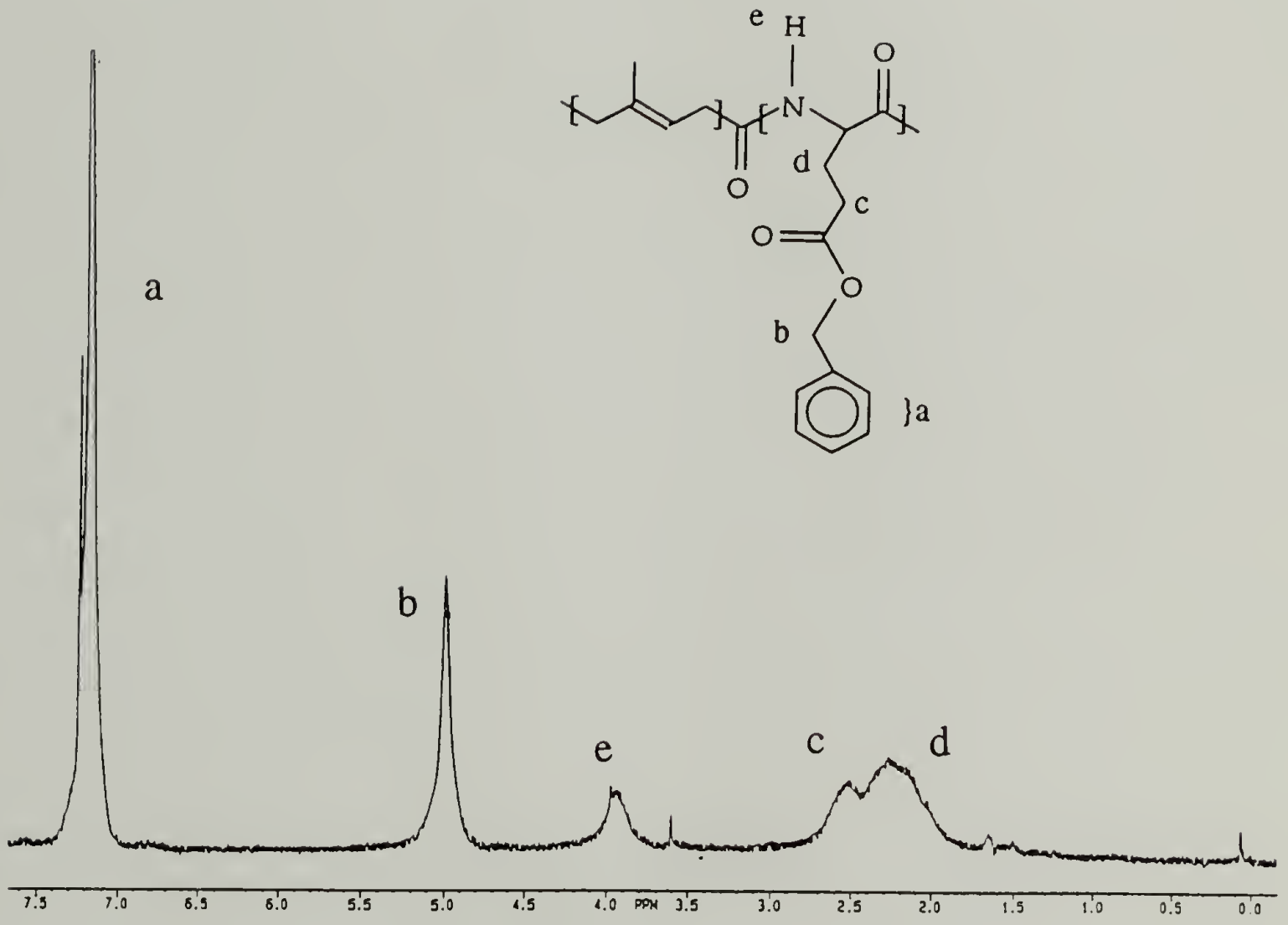

Figure 3.20. ^{1}H NMR spectrum of A-SF2 fraction of 69K PI-b-59K PBLG in $CDCl_3$/TFA.

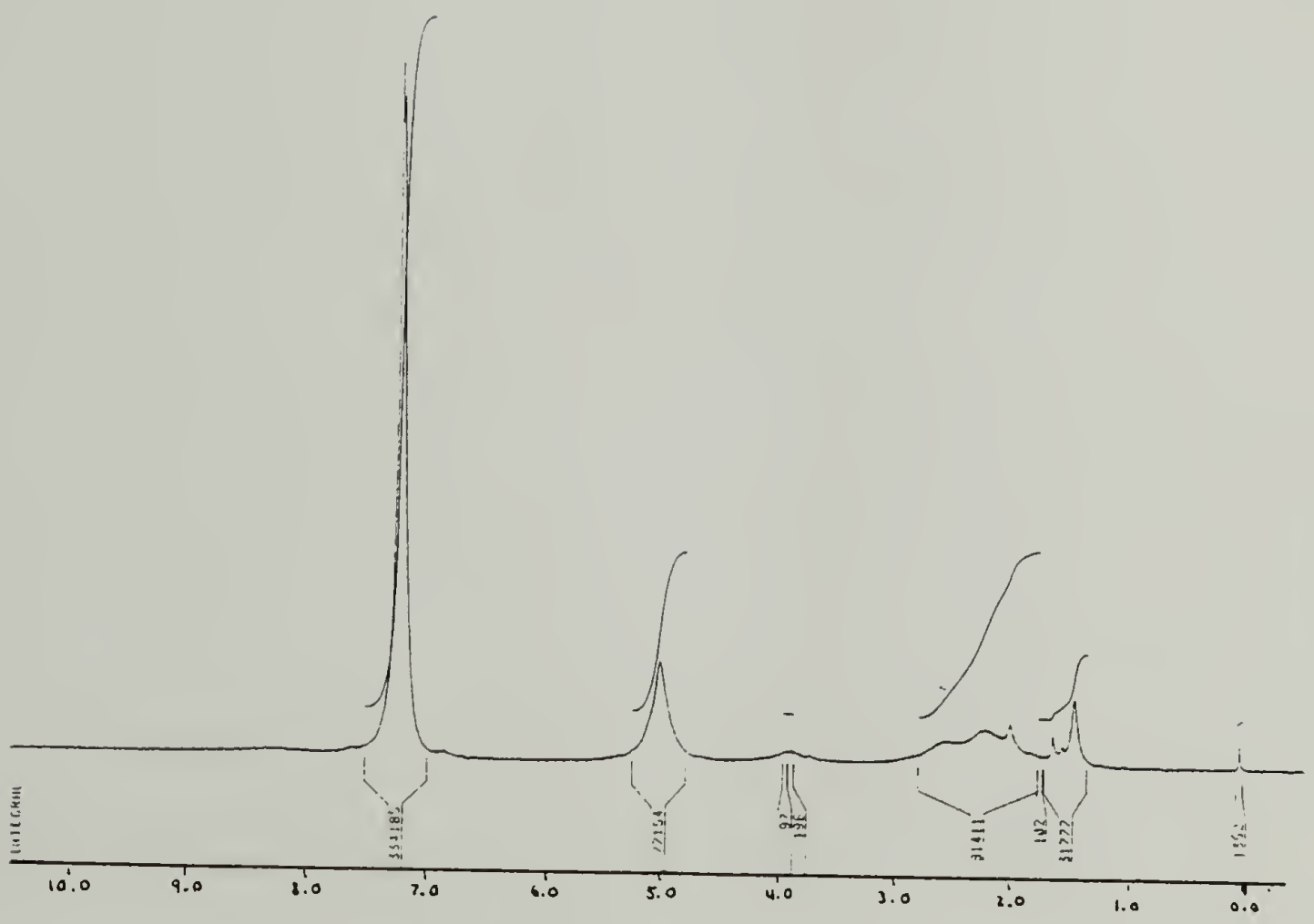

Figure 3.21. ^{1}H NMR spectrum of A-SF1 fraction of 2.8K PI-b-26K PBLG in $CDCl_3$.

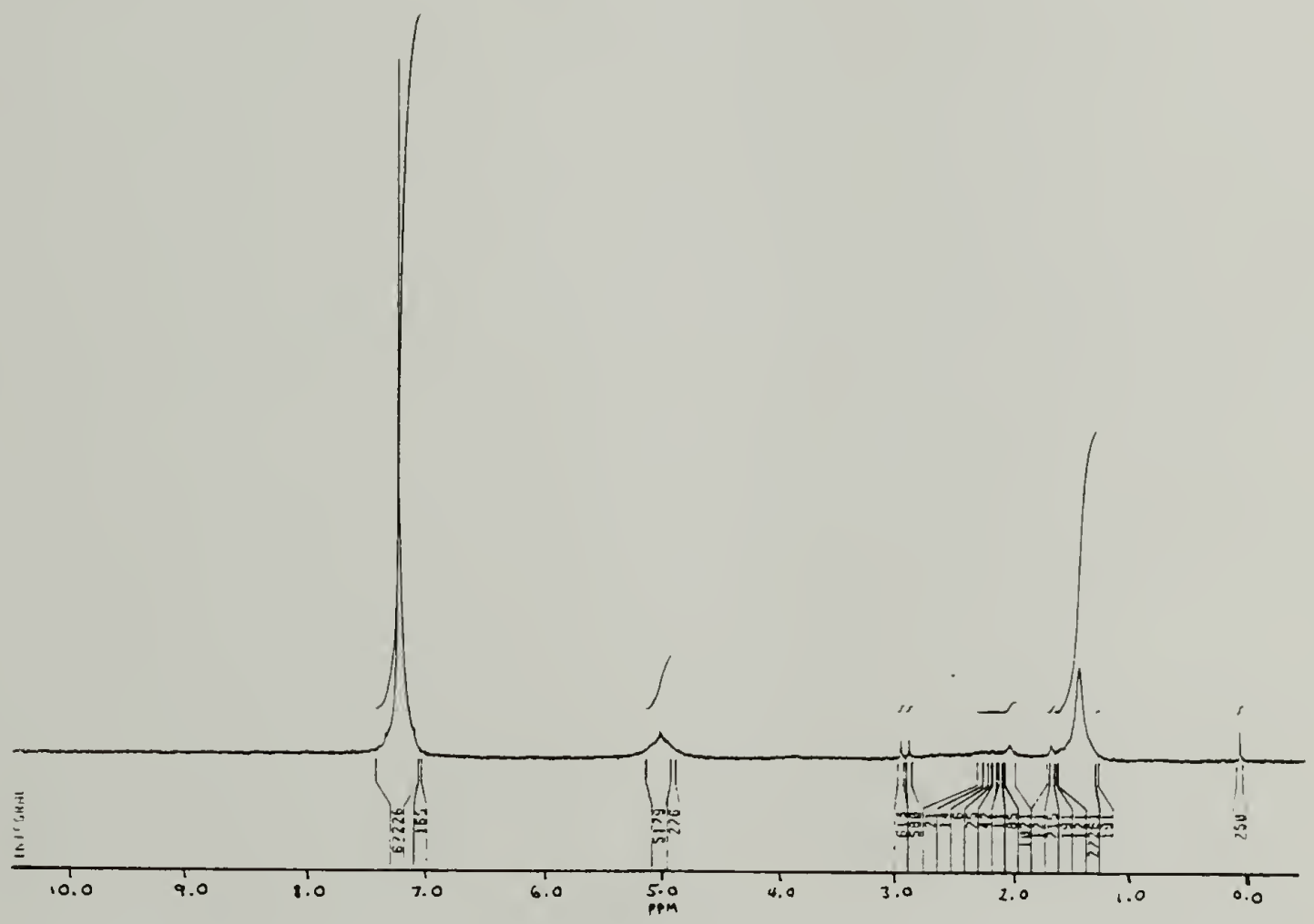

Figure 3.22. ^{1}H NMR spectrum of A-SF1 fraction of 2.8K PI-b-59K PBLG in $CDCl_3$.

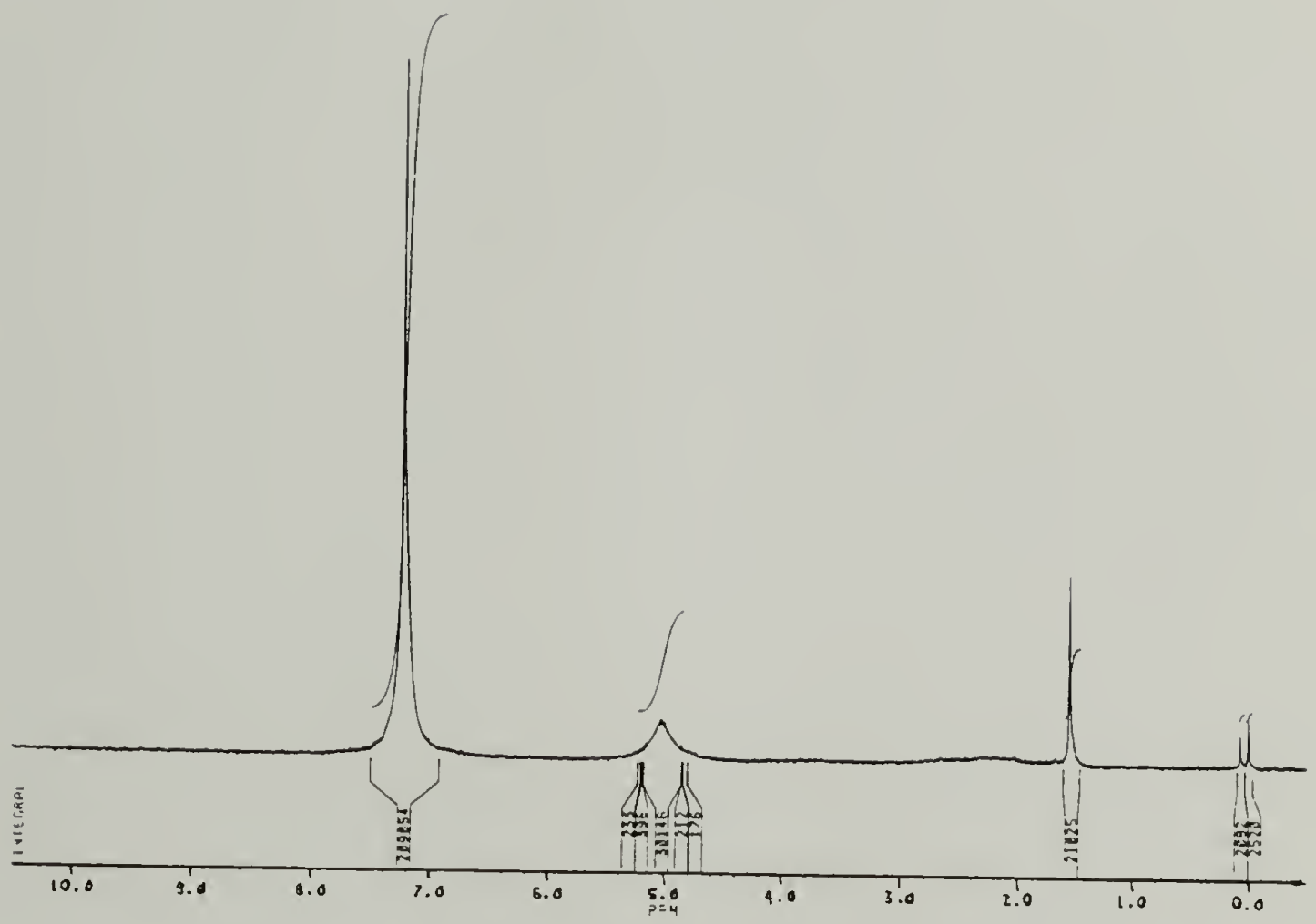

Figure 3.23. ^{1}H NMR spectrum of A-SF1 fraction of 2.8K PI-b-118K PBLG in $CDCl_3$.

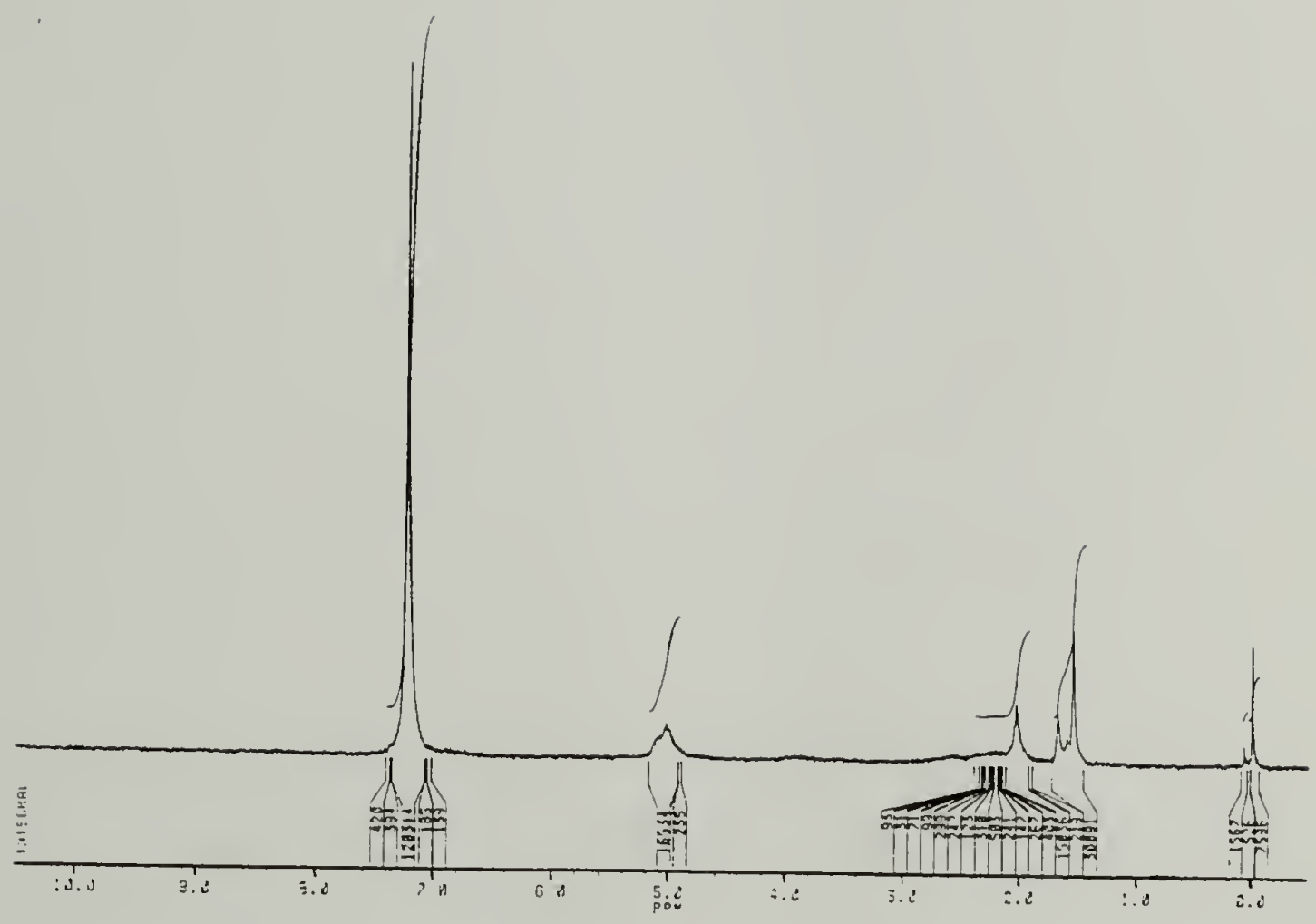

Figure 3.24. ^{1}H NMR spectrum of A-SF1 fraction of 10K PI-b-26K PBLG in $CDCl_3$.

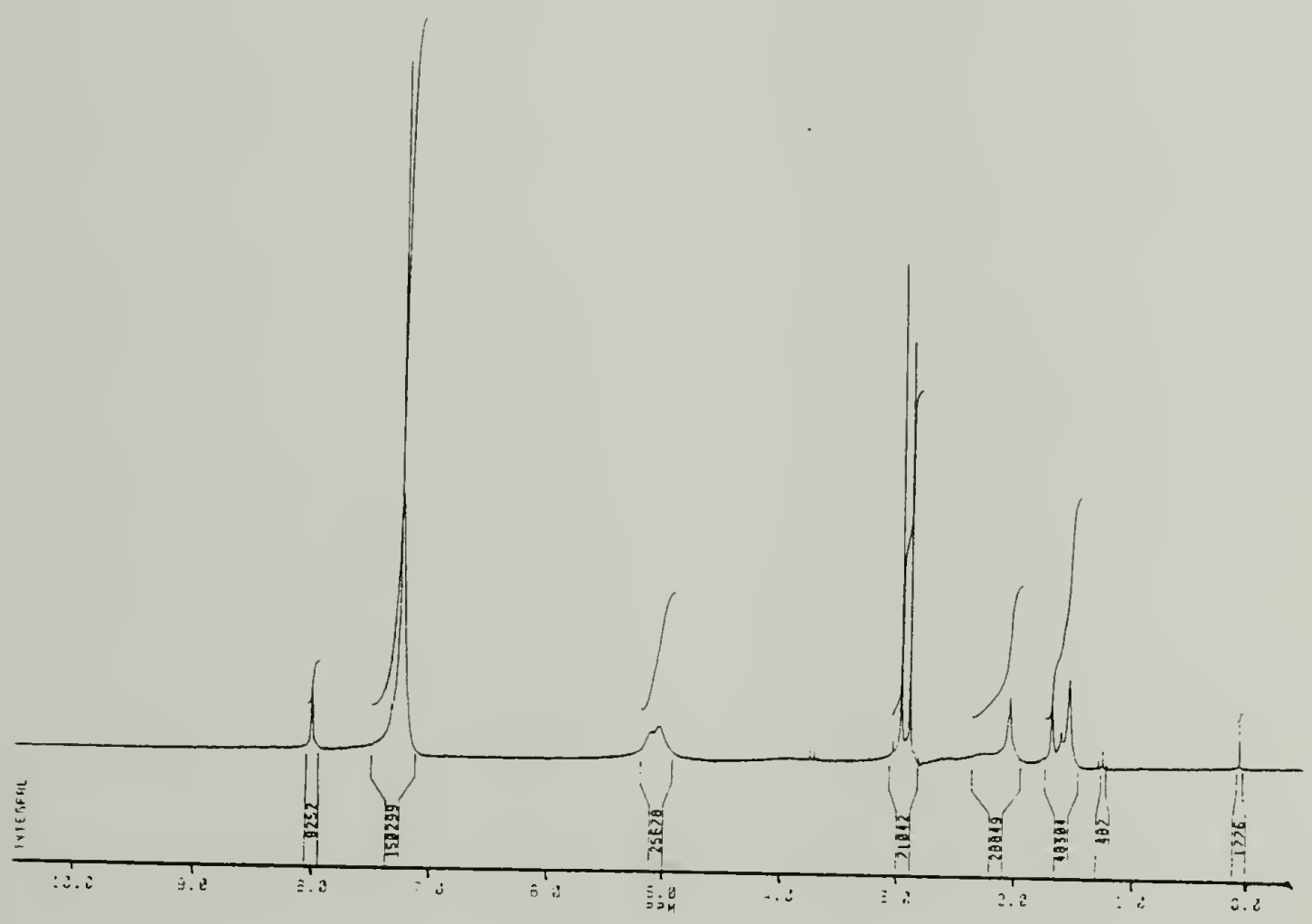

Figure 3.25. ^{1}H NMR spectrum of A-SF1 fraction of 10K PI-b-59K PBLG in $CDCl_3$.

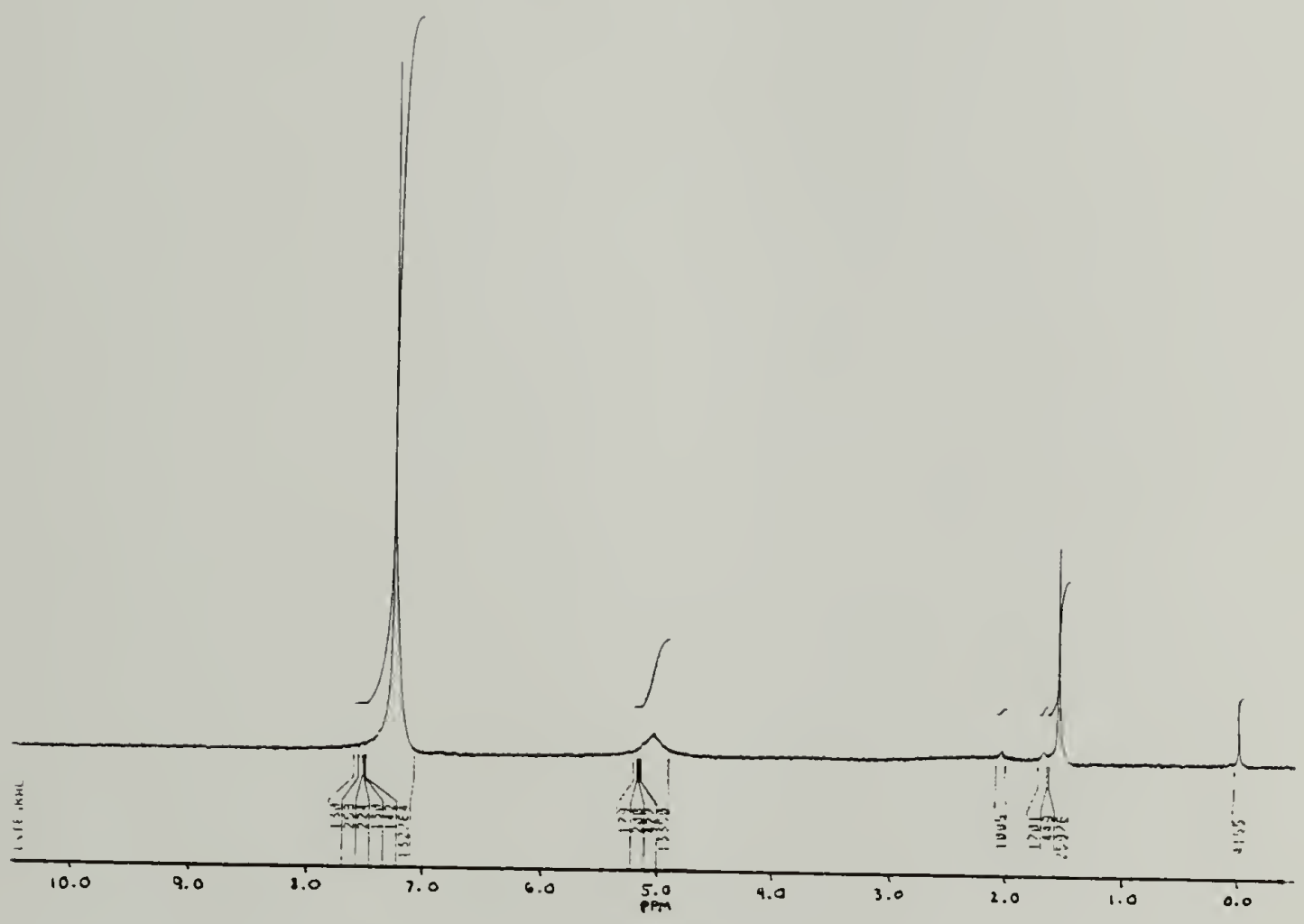

Figure 3.26. ^{1}H NMR spectrum of A-SF1 fraction of 10K PI-b-118K PBLG in $CDCl_3$.

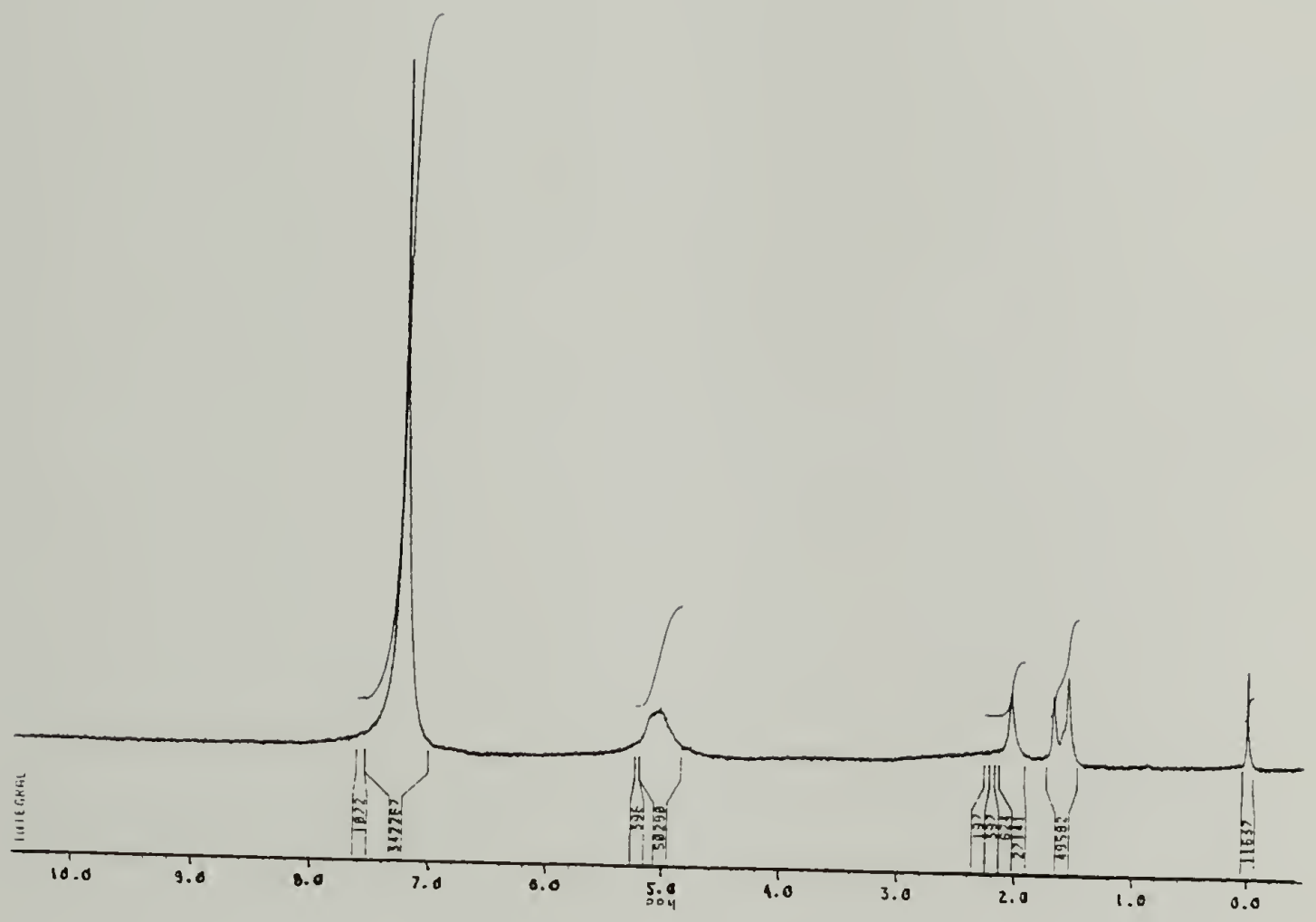

Figure 3.27. ^{1}H NMR spectrum of A-SF1 fraction of 69K PI-b-118K PBLG in $CDCl_3$.

CHAPTER IV
EXPERIMENTAL

This chapter details the theory, sample preparation, measurement, and data analysis for the solution and surface characterization techniques used throughout this dissertation.

A. Light Scattering

This section describes the use of dynamic and total intensity light scattering methods to determine structural information for particles in solution. Dynamic light scattering measures the frequency distribution of the scattered light. Total intensity light scattering measures the spatial distribution of the time-averaged scattered light intensity.

1. Sample Preparation

The concentrations of the sample solutions were determined on a weight basis. The solutions were prepared in pre-weighed sample vials. Typically 10 to 20 mg of polymer were added followed by the *approximate* volume of solvent. Accurate concentrations were then calculated based on the weight of the solvent added. The weight of solvent was then determined. Concentrations of 0.1 wt% were used, unless otherwise specified.

The scattering cuvettes (or cells) were manufactured at the University of Minnesota glass shop. The cells were 6 inches long with a 12 mm diameter and a 10/18 ground glass end. Care was taken to ensure that the cells

remained scratch-free. Organics were removed from the cells by baking in a kiln at 570 °C. Inorganic impurities, especially dust, were removed by rinsing the cells three times with 0.2 μm filtered dichloromethane. The polymer solutions were filtered through 0.45 μm syringe filters directly into the scattering cells; reference solutions containing pure solvent were filtered through 0.2 μm filters. The cells were then sealed with a ground glass stopper and wrapped with teflon tape. The solutions were allowed to equilibrate for at least two days before measurements in order to allow for the escape of trapped air bubbles generated during filtration. Immediately prior to the measurement, samples were allowed to thermally equilibrate at the measurement temperature for fifteen minutes.

2. Apparatus

Light scattering measurements were made using a Spectra-Physics argon ion laser (265 Exciter Model 165) tuned to a wavelength of 488 nm. Typical laser power was 0.1 to 0.2W depending on the scattering of each sample. The scattering measurements were performed using vertically polarized light. A Brookhaven Instruments correlator was used to collect the correlation functions for dynamic light scattering. All light scattering measurements were performed at 25°C unless otherwise specified. The temperature of the sample solution was controlled to within ± 0.1°C with a recirculating water bath.

The scattering cells were placed in a sample chamber containing 0.45 μm filtered toluene. Toluene has nearly the same refractive index as glass, 1.5, and is referred to as a refractive index matched medium. Scattering from the toluene/glass interface was therefore minimized.

Figure 4.1 shows a schematic of the light scattering apparatus. The sample was located at the center of a rotating platform on which was mounted a photon detector. This design allowed the observation angle to be continuously changed while the sample to detector distance remained constant.

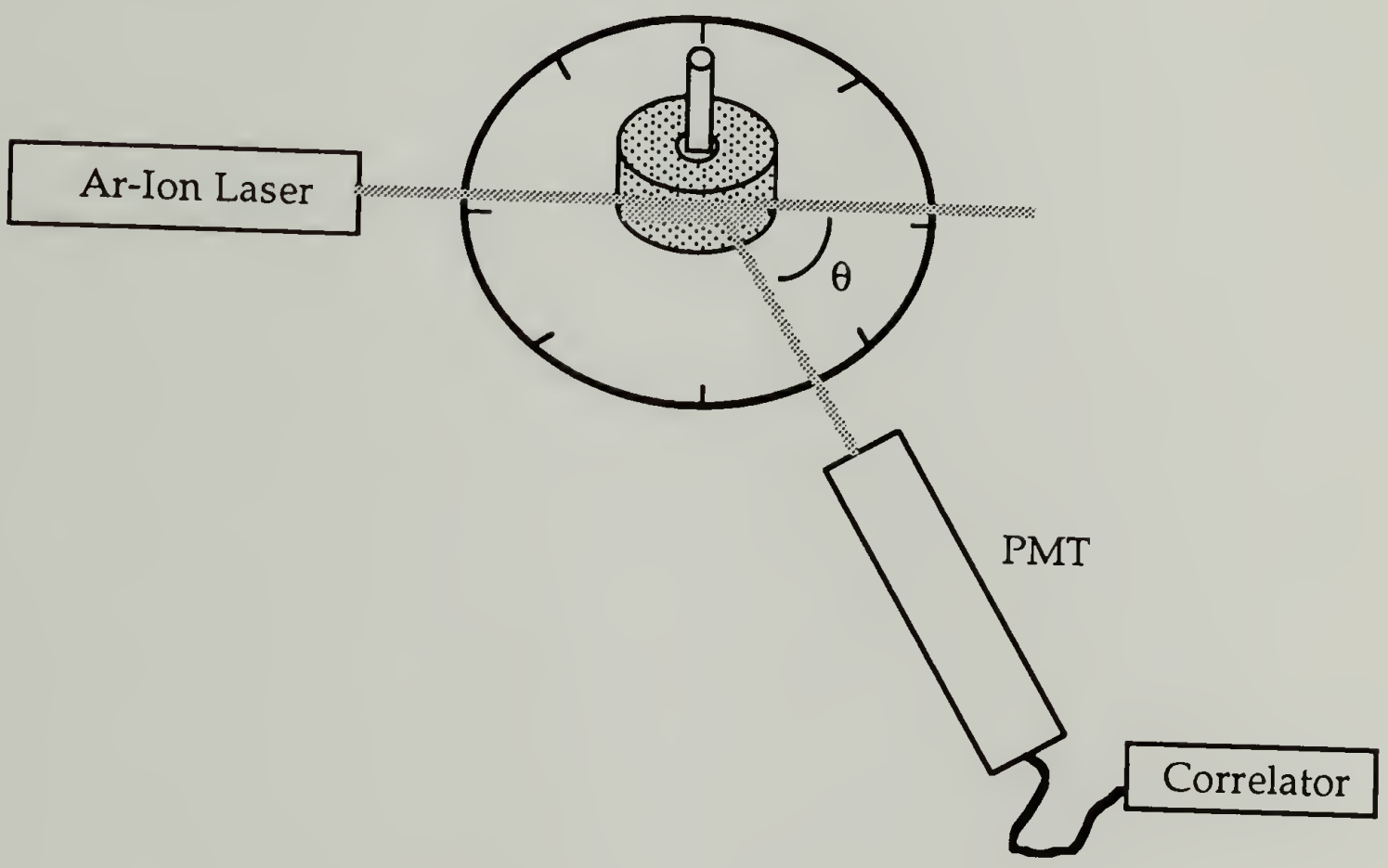

Figure 4.1. Schematic representation of the light scattering apparatus.

3. Dynamic Light Scattering

a. Theory

Dynamic light scattering (DLS) provides information on the rate of Brownian diffusion of molecules in solution. The characteristic size

measured by DLS is the hydrodynamic radius, R_h. The hydrodynamic radius is the radius of an equivalent sphere with the same frictional coefficient as the particle.

The time autocorrelation function of the scattered intensity was collected in the homodyne mode with a Brookhaven Instruments multisample time correlator model BI 2030. A distribution of sample times was used in order to collect the correlation function over a wide range of decay times. The time autocorrelation function is a mathematical representation of the similarity of the scattered intensity at times t and $(t+\tau)$. The autocorrelation function, $C(\tau)$, as a function of the sampling interval (or decay) time, τ, is defined as the average value of the product I(t) and $I(t+\tau)$ over all initial times, t, for the time interval -T to T: [45]

$$C(\tau) = \langle I(t)I(t+\tau)\rangle = \lim_{T\to\infty} \frac{1}{2T}\int_{-T}^{T} I(t)I(t+\tau)dt \qquad (4.1)$$

The characteristic decay time is related to the Brownian motion of the particles; the correlation decays more rapidly for faster moving particles.

Figure 4.2 shows a typical autocorrelation function. At short sampling times ($\tau \to 0$), the correlation function is equal to the average of the squared intensity. At very long sampling times ($\tau \to \infty$), the correlation function is equal to the square of the average intensity.

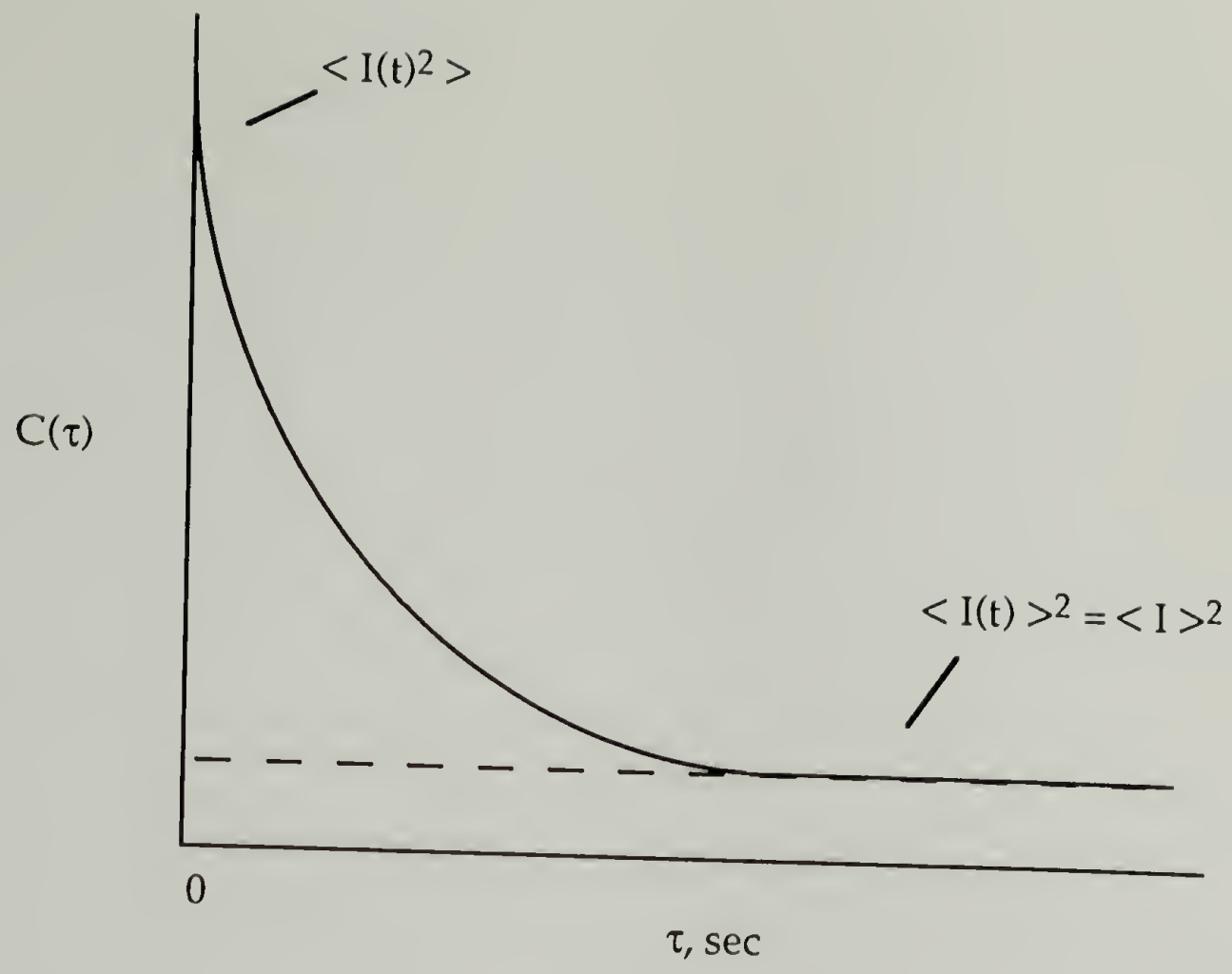

Figure 4.2. A generalized time autocorrelation function. (Adapted from Chu, 1991) [131]

The autocorrelation function, $C(\tau)$, which is measured in the DLS experiment can be expressed in terms of $g_1^2(\tau)$, the square of the normalized scattered electric field autocorrelation function, the baseline of the correlation function, B, and an experimentally determined term which depends on the scattering geometry, b: [132]

$$C(\tau) = B\left(1 + b\left|g_i^2(\tau)\right|^2\right) \tag{4.2}$$

Diffusion coefficients are determined by fitting correlation functions to model predictions for $g_1(\tau)$. The simplest model is that of a single exponential:

$$g_1(\tau) = \exp(-\Gamma t) \tag{4.3}$$

The single exponential fit assumes there is a single diffusion coefficient which characterizes the system. This is, therefore, exact only for modeling the diffusion of monodisperse spherical particles in which there is translational, but not rotational, diffusion. Other models such the double exponential

$$g_1(\tau) = \exp(-\Gamma_1\tau) + \exp(-\Gamma_2\tau) \tag{4.4}$$

or cumulants expansion

$$g_1(\tau) = \exp(-\Gamma\tau + 1/2!\,\mu_2\tau^2 - 1/3!\,\mu_3\tau^3 + \ldots) \tag{4.5}$$

are appropriate for narrow, bimodal distributions and unimodal, polydisperse distributions, respectively. Complex, multicomponent and/or polydisperse systems can be modeled using a weighted sum of exponential decays: [131]

$$g_1(\tau) = \int_0^\infty G(\Gamma)\, e^{-\Gamma\tau}\, d\Gamma \tag{4.6}$$

The distribution function of mobilities, $G(\Gamma)$, defines the set of exponentials required to fit the correlation function and is the inverse Laplace transform of the correlation function. [131] The Laplace inversion was accomplished through the use of a FORTRAN program called CONTIN. [133, 134] This algorithm employs a smoothing technique and is based on the method of regularization. The solution does not require any *a priori* assumptions on the shape or number of diffusive modes.

The diffusion coefficient is related to the rate of diffusion, Γ, and the scattering vector, q: [131, 132]

$$D_T = \Gamma / q^2 \tag{4.7}$$

$$q = \frac{4\pi n}{\lambda} \sin\frac{\theta}{2} \tag{4.8}$$

where n is the refractive index of the solvent, λ is the wavelength of the incident light, and θ is the scattering angle.

The hydrodynamic radius is related to the translational diffusion coefficient at infinite dilution, $D_{T,0}$, through the Stokes-Einstein equation: [45]

$$D_{T,0} = \frac{kT}{6\pi\eta R_h} \tag{4.9}$$

where k is Boltzman's constant (1.381×10^{-23} J/K) and η is the solvent viscosity.

b. Data Analysis

Time autocorrelation functions were collected using four to seven scattering angles between 45° and 135°. The translational diffusion coefficient was determined from the slope of Γ as a function of q^2 (eqn. 4.7). The diffusion coefficient at infinite dilution was approximated by the value in dilute solution (approx. 0.1 wt%). The hydrodynamic radius was determined using equation 4.9 and the solvent data from Table 4.1.

Table 4.1. Solvent information for light scattering solvents at 25°C and 488 nm. [102, 135, 136]

	DMF	DCM	Heptane
Refractive Index	1.4269	1.4279	1.3903
Density, g/ml	0.944	1.3167	0.6795
Viscosity, cp	0.802	0.404	0.386

The refractive index of the mixed solvent systems (dichloromethane and heptane) were calculated using the Gladstone-Dale equation [136]

$$n_{mix} = 1 + \rho\,[(w_1/\rho_1)(n_1 - 1) + (w_2/\rho_2)(n_2 - 1) \qquad (4.10)$$

where ρ is the density of the mixed solvent, w_x is the weight fraction of component x and n_x is the refractive index of component x.

The broadness of the distribution or polydispersity was determined from a cumulants analysis at each scattering angle using the software provided with the correlator. Polydispersity was defined as the second moment of the distribution function normalized by the square of the first moment, μ_2/Γ^2. [131] Monodisperse systems have a polydispersity of 0.0.

4. Total Intensity Light Scattering

a. Theory

Electromagnetic radiation creates oscillatory induced dipoles in a medium. These induced dipoles re-radiate energy in all directions. If there are polarizability differences within the sample, then there will be a net

scattering of light. [137] Polarizability differences may arise due to temperature or concentration fluctuations. In the present case, concentration fluctuations due to the presence of large particles are of primary interest. [131]

In the case of larger particles ($\lambda/20$; Debye scatterers), different volume elements from the same particle will scatter light. [131] The path length from each scatterer to the detector will be different, as shown in Figure 4.3. The result is a decrease in the scattered light which reaches the detector due to destructive interference. The path length difference is zero in the propagation direction and increases as the angle of obervation increases. This asymmetric scattering profile is the result of intramolecular interference and leads to a wealth of information on the size and shape of the scatterer.

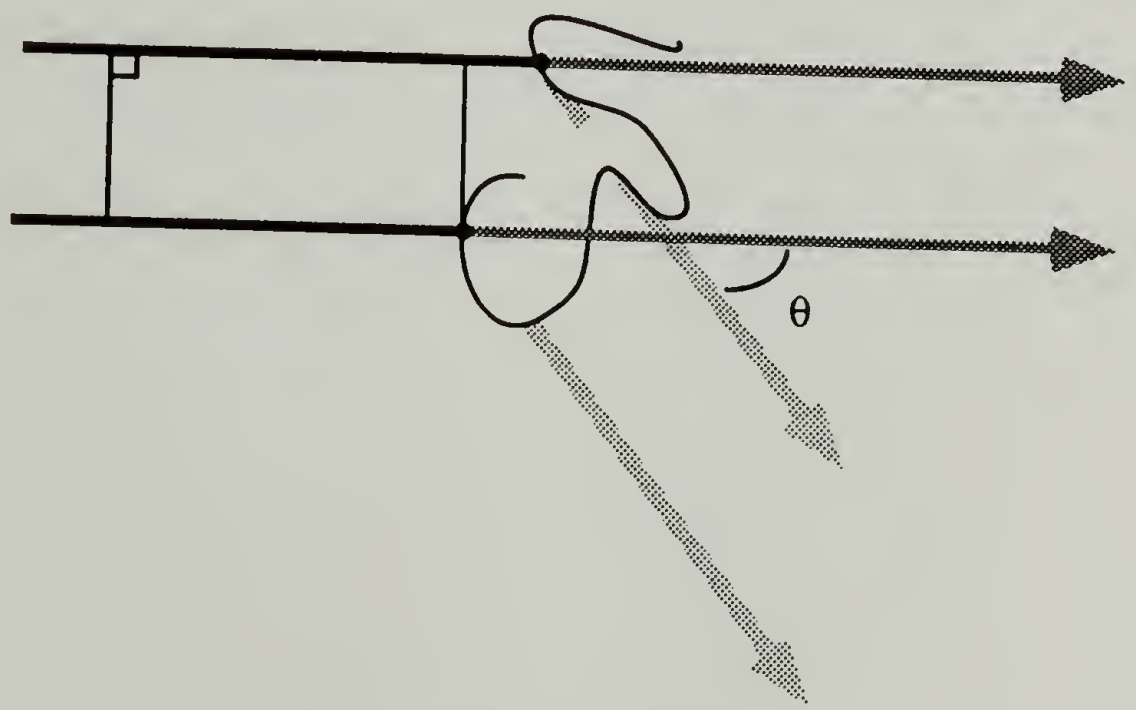

Figure 4.3 Schematic representation of the interference due to intraparticle scattering.

The excess Rayleigh ratio is the scattered intensity from the polymer at each angle normalized by the incident light intensity, I_0: [131]

$$R_{\theta,\,ex} = \left(I(\theta,c) - I(\theta,0)\right)\frac{r^2}{I_0} \tag{4.11}$$

where $I(\theta, c)$ is the scattering from the polymer solution, $I(\theta, 0)$ is the scattered intensity from the solvent, and r is the distance from the sample to the detector.

The particle scattering factor, $P(\theta)$, describes the effect of intraparticle interference on the intensity of scattered light reaching the detector: [131]

$$P(\theta) = R_{\theta,\,ex} / R_0 \propto I(\theta, c) - I(\theta, 0) \tag{4.12}$$

where $R_{\theta,\,ex}$ is the Rayleigh ratio of the scattered light (with interference) and R_0 is the Rayleigh ratio in the absence of interference and equals $8\pi^4a^2/\lambda^4$. The particle scattering factor can be defined in terms of a phase factor $e^{ik\bullet\rho r}$: [131]

$$P(\theta) = \iint_V e^{ik\bullet\rho r}\,dr_1 dr_2 \tag{4.13}$$

For any shape of particle, the particle scattering factor reduces to

$$P(\theta) = 1 - q^2Rg^2/3 + \ldots \tag{4.14}$$

in the limit of $qRg < 1$. [136] However, the form of $P(\theta)$ is dependent on the shape of the particle for larger particles ($qRg > 1$). For spheres,

$$P(\theta) = \left[\left(\frac{3}{q^3R^3}\right)\left(\sin(qR) - (qR)\cos(qR)\right)\right]^2 \tag{4.15}$$

where R is the radius of the sphere. [136]

Equation 4.16 relates the scattering from a dilute solution to the molecular weight, taking intraparticle interference and interparticle interactions into account: [131]

$$\frac{Kc}{R_{\theta,ex}} = \frac{1}{MP(\theta)} + 2A_2c \tag{4.16}$$

$$K = \frac{4\pi^2 n^2}{\lambda^4 N_A}\left(\frac{dn}{dc}\right)^2 \tag{4.17}$$

where M is the molecular weight of the scatterer, A_2 is the second virial coefficient, n is the refractive index of the solvent, N_A is Avagadro's number, and dn/dc is the differential refractive index increment.

b. Measurement

The time-averaged scattered intensity was measured for 15 angles between 45 and 135° for each polymer solution and the corresponding pure solvent. The polymer solution and the solvent samples were measured consecutively to ensure identical experimental conditions for the two measurements. Photons were collected for 10 seconds, and the recorded value at each angle was based on at least 10 measurements.

c. Data Analysis

Total intensity light scattering measurements were used to determine the radius of gyration (Rg) of the diblock copolymer aggregates. The radius of

gyration was from equation 4.14. The scattered intensity from the polymer was calculated by measuring the scattering from the solution and subtracting the scattering from the pure solvent. The scattering at each angle was normalized for scattering volume by dividing by the scattering from a reference solution, typically the pure solvent:

$$I_{ex}(\theta, c) = \frac{I(\theta,c) - I(\theta,0)}{I(\theta,0)} \qquad (4.18)$$

The particle scattering factor is proportional to the excess scattered intensity (Eqn. 4.12) and equation 4.14 can then be written as

$$P(\theta) = I_{ex}(\theta, c) \text{ X constant} = 1 - q^2Rg^2/3 \qquad (4.19)$$

then,

$$I_{ex}(\theta, c) = 1/\text{Constant} - q^2Rg^2/3 \text{ X Constant} \qquad (4.20)$$

Therefore, the limiting slope of a plot of $I_{ex}(\theta)$ against q^2 gives the radius of gyration of the scatterer:

$$Rg = (-3 \text{ X slope/y-intercept})^{1/2} \qquad (4.21)$$

A plot of $P(\theta)$ against q^2 has the added advantage of providing additional structural information in the limit of $qRg > 1$. [138]

An alternative method of determining the radius of gyration is based on the dissymmetry ratio:

$$d(\theta) = \frac{I_{ex}(\theta)}{I_{ex}(180-\theta)} \equiv 1 + \frac{(4\pi n)^2}{3\lambda^2} Rg^2 \cos\theta \qquad (4.22)$$

in the limit of $qRg < 1$. Rg can be determined from the slope of a plot of $d(\theta)$ versus cos θ:

$$Rg = \frac{(3 \times \text{slope})^{1/2}}{4\pi n/\lambda} \qquad (4.23)$$

The determination of molecular weights by equation 4.16 requires the absolute scattered intensity. This was determined by using a benzene reference solution. The Rayleigh ratio of benzene is 29.1 X 10^{-6} cm^{-1} for a scattering angle of 90°, a wavelength of 488 nm, and 25°C. Knowledge of the Rayleigh ratio of benzene allows for the ratio of r^2/I_0 to be determined from the scattered intensity of the benzene solution at 90°:

$$R_{\theta,\text{benzene}}/I_{s,\text{benzene}} = r^2/I_0 \qquad (4.24)$$

The excess Rayleigh ratio of the polymer follows directly, using Eqn. 4.11.

B. Differential Refractometry

1. Theory and Background

Differential refractometry was used to determine the refractive index increment, dn/dc. An interferometric differential refractometer, based on

rotation of light (or wave front shearing), was used. [139] A schematic is shown in Figure 4.4:

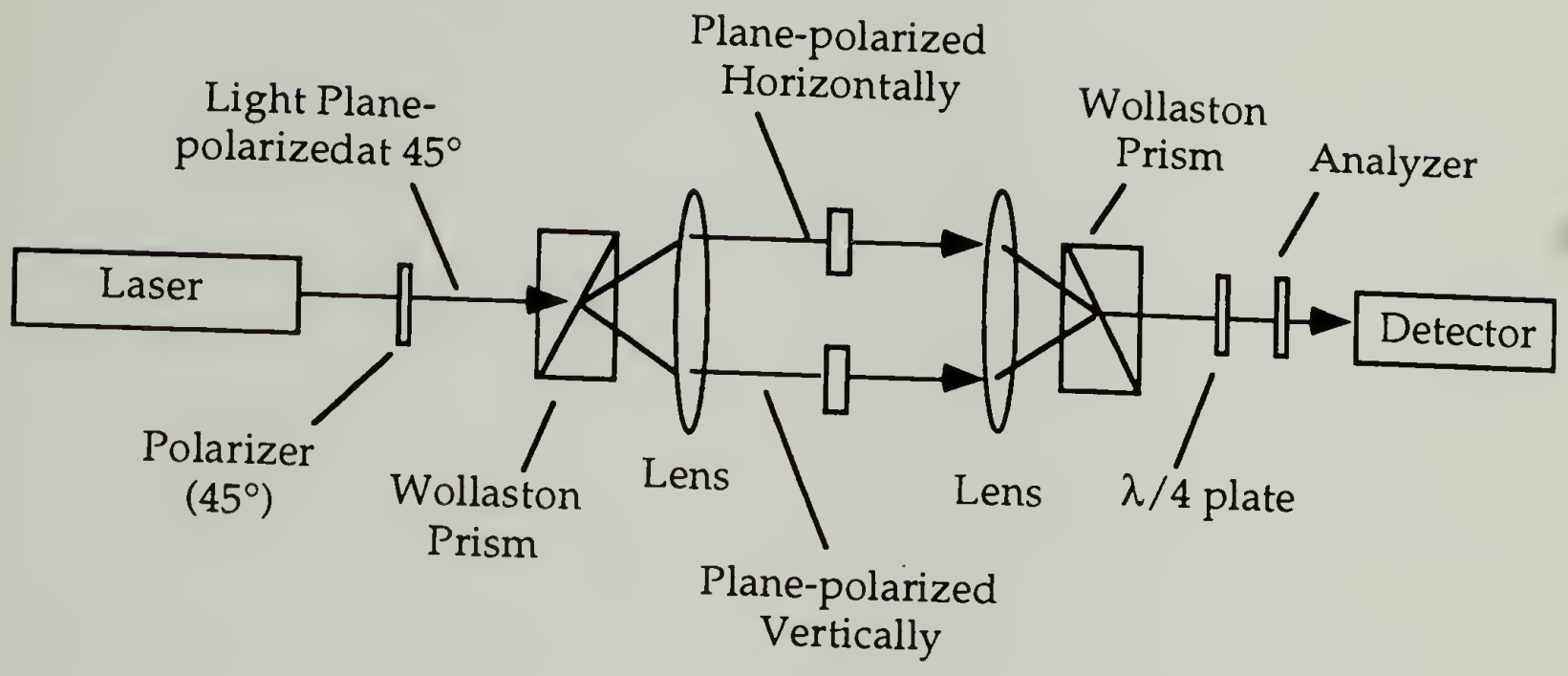

Figure 4.4. Schematic of interferometric differential refractometer.

Light from a He-Ne laser (632.8 nm) is plane polarized at 45°. The beam is then passed through a Wollaston prism which generates two equal intensity, in-phase and orthogonally polarized beams: one horizonatally polarized and the other vertically polarized. The initially coherent beams are then passed through 1 mm sample cells containing a polymer solution and a reference solution, respectively. The refractive index, n, of each solution determines the wavelength of the beam passing through the solution,

$$\lambda = \lambda_0 / n \tag{4.25}$$

where λ_0 is the wavelength of the light in vacuum.

The number of wavelengths propagated in each cell equals l/λ where l is the cell path length (1 mm). The difference in the number of wavelengths, ν, is given in the following relation: [139]

$$\nu = \left(\frac{l}{\lambda_s} - \frac{l}{\lambda_r} \right) \tag{4.26}$$

Each wavelength difference corresponds to 2π radians. The phase difference, φ, between the two beams follows from a combination of equations 4.25 and 4.26: [139]

$$\varphi = 2\pi l \left(\frac{n_s}{\lambda_0} - \frac{n_r}{\lambda_0} \right) \tag{4.27}$$

or

$$\varphi = 2\pi l \Delta n / \lambda_0 \tag{4.28}$$

where Δn is the refractive index difference between the sample and reference solutions.

The beams emerging from the sample cells are then collimated with a Wolaston prism and a quarter-wave plate. The quarter-wave plate creates a 90° phase difference between the orthogonal waves and therefore creates circularly polarized light. In this set-up, the quarter-wave plate is oriented at 45° so that the horizontally polarized beam emerges circularly polarized in a counter-clockwise direction (left), and the vertically polarized beam becomes circularly polarized clockwise (right). The two circularly polarized waves have the same wavelength at this point because both are in the same environment (air). A plane polarized beam emerges from the quarter-wave plate because the two oppositely polarized waves add to form a single plane polarized wave. [140] The beam has been rotated away from the incident

polarization (45°). The measured phase shift, θ, is equal to half of the phase difference, φ: [139]

$$\theta = \varphi/2 = \pi 1\Delta n/\lambda_0 \tag{4.29}$$

Eqn. 4.29 relates the phase shift to the refractive index difference between the two solutions.

2. Measurement

The phases of light emerging from several solution pairs were measured with a polarizer at 10° intervals. The first pair of solutions were both solvent. This served as a reference and accounted for path length differences caused by minor differences in the dimensions of the glass cells or other misalignments. The next pair of solutions examined were the most dilute polymer solution and the pure solvent, in cells one and two respectively. The next lowest concentration was then paired with the lowest concentration, as diagramed in Figure 4.5. This design allowed the measured phase shifts to be kept within the experiment limits.

Cell 1	Cell 2	ΔC
0	0	0
0.004	0	0.004
0.004	0.006	0.002
0.008	0.006	0.002
0.008	0.01	0.002

Figure 4.5. Typical experimental design of differential refractive index measurement based on polymer concentrations 0.01 g/ml, 0.008 g/ml, 0.006 g/ml, and 0.004 g/ml.

3. Sample Preparation

Polymer solutions were prepared by dilutions from a stock solution. The stock solution was prepared in a 10 ml volumetric flasks using approximately 50 to 100 mg of polymer. The dilutions were made in 5 ml volumetric flasks. For each polymer/solvent system of interest, four polymer concentrations and one pure solvent sample were prepared.

4. Data Analysis

For each solution pair, the intensity of light impinging on the detector was measured as a function of polarization angle. The data was fitted to a $\sin(2\theta)$ function to determine the phase of the light. The refractive index difference was then calculated from eqn. 4.29. The data was plotted in two forms. The dn/dc values for each pair were plotted against concentration. Second, the cumulative refractive index difference between the sample and the solvent was plotted as a function of concentration. The slope was equal to dn/dc.

C. Infrared Spectroscopy

1. Transmission

Transmission infrared spectra are useful for measuring the infrared absorption of bulk, unoriented polymer. The sample is prepared by

dissolving the polymer in the chosen solvent and dropping the solution onto a sodium chloride disk. The spectra were collected once the solvent had evaporated.

2. Reflectance

a. Theory and Background

Adsorption onto reflecting surfaces (such as gold) can be studied by using the technique of reflectance infrared spectroscopy. [141] In the grazing (or reflectance) geometry, only radiation polarized parallel to the plane of incidence contributes to the infrared spectrum of the surface layer. The plane of incidence is the plane which contains the incident, reflected, and refracted rays, as shown in Figure 4.6 as the plane of the paper. The s-polarized light is perpendicular to the plane of incidence; the p-polarized light is parallel to the plane of incidence. In the grazing angle geometry, the angle φ is approximately 80-88°.

Consequently, only p-polarized light is used for the incident beam. This means that for the grazing angle experiment, the electric vector will be perpendicular to the surface.

Polarized infrared spectroscopy is a powerful tool for probing the orientation of grafted polypeptide rods. The structure of a polypeptide α-helix is uniquely suited for orientational study. PBLG has been well-studied and the assignments of the bands are known. [104-106, 141] If the helices are lying nearly flat on the surface, the electric vector will be perpendicular to the helix axis. Alternatively, if the chains are adsorbed normal to the surface then the electric vector will be parallel to the helix axis.

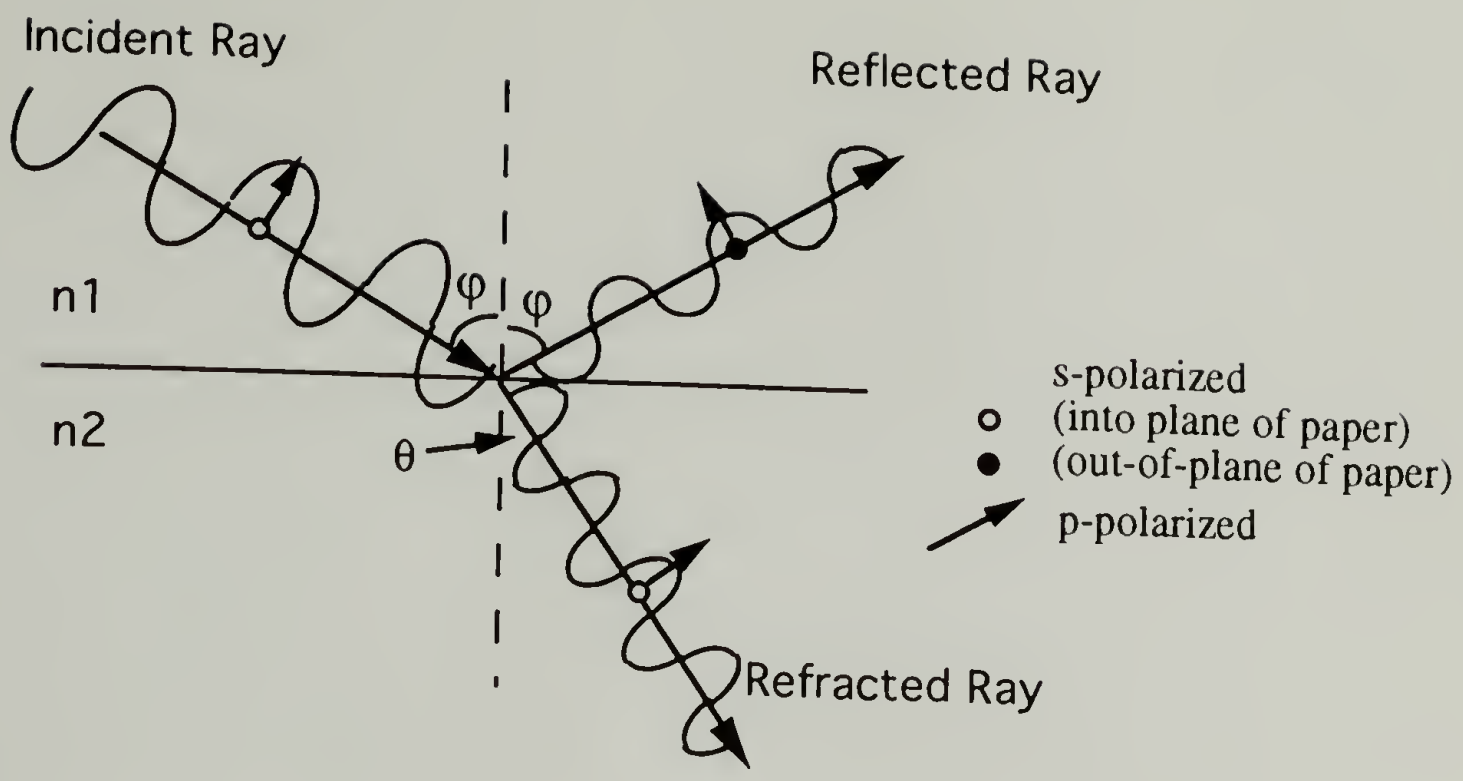

Figure 4.6. The geometry of reflection and refraction of light incident on a denser medium (n2 > n1). [140]

b. Experimental Procedure

i. Substrate Preparation The substrates for the reflectance infrared experiments were gold-coated silicon wafers. The silicon wafers were cleaned in a microelectronics clean room. The four-inch wafers were dipped in a 10% solution of hydrogen fluoride for 10 seconds to remove the native oxide layer, then rinsed for 5 minutes in distilled, deionized water (DI water). Next, a new oxide layer was grown on the surface in a solution of sulfuric acid and hydrogen peroxide at 120°C, then rinsed for 5 minutes with DI water. This oxide was then removed by soaking in 10% HF for 5 minutes, followed by another 5 minute DI water rinse. The wafers were rinsed and spin dried in a wafer-drying oven.

An electron beam evaporator was used to deposit a layer of chromium (150 Å) on the wafers followed by a layer of gold (2000 Å). The film thicknesses were measured using a quartz crystal. The resonant frequency of the crystal is dependent on the density and thickness of the deposited layer. The wafers were then cut with a diamond knife to approximately 1 inch by 2 inches.

ii. Adsorption The wafers were placed in beakers containing approximately 0.1 wt% polymer solutions in anhydrous N,N-dimethylformamide (Aldrich, septa sealed, reported <0.005% water). The polymer was allowed to adsorb over several days. The substrates were removed from the solution (without rinsing) and dried with a nitrogen gun. The grazing angle spectra and ellipsometry measurements were then done. The substrates were then placed in beakers containing the pure solvent (anhydrous DMF) for several days. The substrates were removed and dried with nitrogen and analyzed.

iii. Measurement The grazing angle infrared spectra were measured using a Nicolet infrared spectrometer with a "sea gull" attachment to ensure correct sample alignment. After aligning the sample substrate into the beam, the sample chamber was purged with nitrogen for several minutes to evacuate water. The adsorbed water on the substrate was monitored. The spectra were collected at a resolution of 2.0 cm^{-1}.

The spectra were measured at several grazing angles. The spectrum of a bare gold substrate was recorded as the background. The spectra were recorded for the samples after adsorbing and after rinsing.

D. Ellipsometry

Ellipsometry is an optical technique which can be used to measure structural and dielectric properties of a material. The change in the polarization state, the amplitude and phase, of a beam of linearly polarized light is measured after emerging from a sample. Usually, the sample is a dielectric material on a reflecting surface.

Ellipsometric measurements on the dry adsorbed layers were used to obtain information on the surface density of chains and on the corresponding layer thickness. Layer thickness is an indirect measure of the order in the rod layer. A layer thickness approximately equal to the length of the rods would indicate that the rods are standing-up normal to the surface. Otherwise, the layer thickness can be used to calculate an average tilt angle of the rods.

1. Theory

The refractive index of a material, $\nu(T, \lambda)$, is the ratio of the velocity of light in vacuum to the velocity of light in the material:

$$\nu(T, \lambda) = c / v \tag{4.30}$$

c = speed of light in vacuum

v = velocity of light in medium.

The refractive index is a function of temperature and wavelength. The refractive index is related to the polarizability, the ability of electrons to be

distorted by the light, which is wavelength dependent. The density of the material is the origin of the temperature dependence of the refractive index.

The refractive index, n, is the real component of the complex refractive index, N.

$$N = n - ik \tag{4.31}$$

The imaginary component is the extinction coefficient, k. The extinction coefficient is responsible for changing the amplitude of the light and the refractive index affects the phase.

The ellipsometer measures a parameter ρ, the ratio of the parallel and perpendicular components of the reflected light: [142]

$$\rho = Rp / Rs = \tan \psi \, e^{j\Delta} \tag{4.32}$$

where Rp and Rs, the complex Fresnel reflection coefficients for p- and s-polarizations, are ratios of the reflected and incident amplitudes. The reported parameters are ψ and Δ, which correspond to the amplitude and phase change, respectively, of the incident light after reflection from the sample.

2. Measurement

A spectroscopic ellipsometer was used to measure the ellipsometric parameters for the rinsed and unrinsed substrates. Psi and delta were measured for multiple wavelengths.

The macroscopic parameters of film thickness and refractive index of a bulk sample are completely specified by the ellipsometric parameters delta and psi. A database of the complex refractive index as a function of wavelength for each component in the mixed layer was compiled by ellipsometric measurement on bulk films of the pure components. The film thickness and the polymer volume fraction were adjusted in the model until the predicted values of phi and delta agreed with the experimental values.

CHAPTER V
STRUCTURE IN SOLUTION

A. Introduction

Rod-coil diblock copolymers possess an inherent structural richness as compared with conventional flexible-coil diblocks. This chapter probes the macromolecular structure of rod-coil diblocks in solution and characterizes their unique macromolecular shapes and structures. The solvent quality is shown to change the identity and geometry of the core and coronal regions and consequently the geometry of the resulting micellar building blocks.

The focus of this chapter is the use of light scattering to study the self-assembly of rod-coil diblocks in three solvents: anhydrous N,N-dimethylformamide (DMF), a selective solvent for the rod block; dichloromethane (DCM), a good solvent for both blocks; and a mixed solvent of dichloromethane and heptane, a solvent system selective for the coil.

Dynamic light scattering (DLS) provides information on the rate of diffusion of the rod-coil diblocks in solution and is used in conjunction with the Stokes-Einstein equation to calculate the hydrodynamic radius (R_h) of the aggregates. Total intensity light scattering measurements allow determination of the radius of gyration (R_g). R_g is calculated both from the dissymmetry ratio of the intensity of scattered light, for $qR_g < 1$, and from the slope of the particle scattering function, for larger particles. The relationship between R_g and R_h is used to obtain information on the shape of the micelles.

1. System

a. Rod-Coil Diblock Copolymer

The specific system chosen was a polyisoprene coil block linked to a poly(γ-benzyl-L-glutamate) α-helical rod block. The polypeptide is rigid by virtue of an α-helical secondary structure. The result is a relatively "thick" rod (diam. 18-20 Å) as compared to mainchain rigid rods (rigidity in the primary structure) and flexible coils. The asymmetry in rod and coil diameters may be important in the structures which form for this rod-coil diblock. Another characteristic specific to this rod is the α-helix dipole, which as discussed in Chapter II, results in different potential energy profiles for parallel and antiparallel orientations. In addition, it has been proposed that α-helices may fold in concentrated solutions, [27] although evidence for this effect in dilute solution has not been presented.

A system composed of ten rod-coil diblocks was investigated. Three different rods of varying molecular weight were coupled with three different coil blocks of different molecular weights. The synthesis and characterization of these materials was described in Chapter III. This 3X3 matrix of rod-coil diblocks allows the solution properties to be probed as a function of each block length. Table 5.1 lists spatial characteristics of the diblocks used in this investigation. The repeat unit molecular weight for PBLG is 219 g/mol and the axial rise per repeat unit is 1.5Å. The length, in Angstroms, of the PBLG rod was calculated as the number of repeat units, $MW_{polymer}$ / 219, times 1.5. The unperturbed radius of gyration of the polyisoprene coil, $R_{g,0}$, was calculated from the following relation:

$$R_{g,o} = \frac{aM^{1/2}}{\sqrt{6}} \qquad (5.1)$$

where R_g is in nanometers and a=0.085 for 100% cis-1,4-polyisoprene. [135] The contour length, L, was calculated as the number of PI repeat units times a repeat unit length of 4Å.

Table 5.1. Spatial characteristics of PI-b-PBLG.

PI-PBLG	M_{PBLG}/M_{PI}	L_{Rod}, nm	R_{gCoil}, nm	L_{Coil}, nm*
2.8K-25K	8.9	17.1	1.8	16.5
2.8K-26K	9.3	17.8	1.8	16.5
10K-26K	2.6	17.8	3.5	59
69K-26K	0.4	17.8	9.1	406
2.8K-59K	21.1	40.4	1.8	16.5
10K-59K	5.9	40.4	3.5	59
69K-59K	0.9	40.4	9.1	406
2.8K-118K	42.1	80.8	1.8	16.5
10K-118K	11.8	80.8	3.5	59
69K-118K	1.8	80.8	9.1	406

* Based on a 4Å repeat unit length

Rod block lengths ranging from 26K to 118K and coil lengths ranging from 2.8K to 69K and their inherent structural differences are the origin of the structural variety observed for this polymer system. The diblocks range from mostly polyisoprene (M_{PBLG}/M_{PI} = 0.4 for 69K-26K) to predominantly PBLG (M_{PBLG}/M_{PI} = 42 for 2.8K-118K).

b. Solvents

Accessiblity of selective solvents was considered prior to the selection of polyisoprene as the coil block. Many coils were amenable to the selection of non-selective and coil-selective solvents with PBLG. A limited selection of solvents were known to support the α-helix structure and also inhibit side-to-side and end-to-end aggregation. The requirement for a rod-selective solvent was a helicogenic, non-aggregating solvent for the PBLG and a poor or non-solvent for the coil. Polyisoprene was chosen as the coil block because two rod-selective solvents were known for this system: N,N-dimethylformamide and benzyl alcohol. Polyisoprene also has the advantage of a low glass transition temperature which allows the coil to be rubbery at the experimental temperatures.

i. Non-Selective Solvent Dichloromethane is a good solvent for both PBLG and polyisoprene. Dichloromethane supports the α-helical structure of PBLG. [125] Scattering from the diblock in DCM was strong due to the relatively large difference in refractive index between DCM and the polymers, as shown in Table 5.2.

ii. Rod-Selective Solvent Benzyl alcohol was used in initial experiments, but the solutions in this solvent were highly viscous and difficult to filter. Another experimental difficulty with benzyl alcohol was the low refractive index contrast with the polymer, 1.5371 compared with 1.54 and 1.52, for PBLG and PI, respectively.

Anhydrous N,N-dimethyl formamide was used for the experiments reported in this work. Ample refractive index contrast is available with DMF.

Because DMF is extremely hygroscopic, [143] and PBLG is highly insoluble in water, anhydrous DMF, was used. Anhydrous DMF was purchased from Aldrich in a septa-sealed container and reported to contain less than 0.005% water.

iii. Coil-Selective Solvent As discussed in Chapter III, the solubility of the diblock was dominated by the rod block. Many solvents, such as heptane, hexane, methyl ethyl ketone, cyclohexane, ethyl acetate, amyl acetate, are good solvents for the coil and poor for the rod. However, in each case, the diblock was insoluble. In order to study the diblock in a coil-selective solvent, the polymer was dissolved in a good solvent for both blocks (dichloromethane) and then the solvent quality was made poorer for the rod through the addition of a coil-selective solvent (heptane). Solubility was found to be very sensitive to the fraction of heptane in the mixed solvent. A study of the diblock 69K PI-59K PBLG showed that the polymer was soluble in a DCM/heptane mixed solvent system containing less than 30 wt% heptane. The coil-selective solvent used throughout the majority of this chapter was 88:12 w/w dichloromethane /heptane (80:20 on a volume basis).

Table 5.2. Refractive indices for solvents and polymers used in this work. Values reported for 25°C and 633 nm. [135]

	Refractive Index
Cis-1,4-Polyisoprene	1.5191
PBLG	1.54
DMF	1.4269
Dichloromethane	1.4210
Heptane	1.38512

2. Overview of Structure Determination

Light scattering data furnishes a wealth of information regarding the structure of scatterers. It was found to be a valuable tool in determining the characteristics of micelles formed by rod-coil diblocks.

a. Dynamic Light Scattering

Dynamic light scattering allows the determination of hydrodynamic radii. Not only does this provide a characteristic size of the scatterer but also a means to determine its geometry. Relations have been developed to correlate the size and shape of scatterers to hydrodynamic radii. [144-146] Table 5.3 lists Perrin's [144] relations for spheres and oblate (disks) and prolate (cigar-shaped) ellipsoids. The parameter ρ is the ratio of the semi-axes, b/a. The R_h of spheres is, by definition, the radius. The relations describing the R_h of ellipsoids are empirical. Other relations, such as Broersma's and Kirkwood-Riseman, can also be used. [45, 145, 146]

The distribution of molecular mobilities, $G(\Gamma)$, is another source of structural information. A broad distribution signifies a wide range of translational diffusion rates (or similarly, size) of the scatterers indicative of polydispersity. A broadening or narrowing of the distribution indicates a fundamental change in the system which may be correlated with aggregate structure.

Table 5.3. Empirical Relations for Various Geometries. [144]

Geometry	R_h
Sphere	R
Oblate Ellipsoid ($\rho > 1$)*	$\frac{a\left(\rho^2-1\right)^{1/2}}{\arctan\left[\left(\rho^2-1\right)^{1/2}\right]}$
Prolate Ellipsoid ($\rho < 1$)**	$\frac{a\left(1-\rho^2\right)^{1/2}}{\ln\left[\left(1+\left(1-\rho^2\right)^{1/2}\right)/\rho\right]}$

* major axis = 2b

** major axis = 2a

b. Total Intensity Light Scattering

Total intensity light scattering provides a characteristic size of the scatterer, the radius of gyration. The radius of gyration is related to the geometry of the scatterer. Geometric relations presented in Table 5.4 are specific to isotropic scatterers. For a spatially segregated block copolymer, this requirement translates into identical refractive index increments for each block in the solvent of interest.

Table 5.4. Geometrical dependence of the radius of gyration for isotropic scatterers. [147]

Geometry	R_g
Sphere	$(3/5)^{1/2} R$
Oblate Ellipsoid ($b > a$)*	$(2b^2/5 + a^2/5)^{1/2}$
Prolate Ellipsoid	$(L^2/12 + r^2/2)^{1/2}$

* major axis = 2b

A plot of the particle scattering form factor, $P(\theta)$, as a function of q^2 allows the determination of R_g, from the initial slope, and provides shape information for large scatterers where $qR_g > 1$. $P(\theta)$ relations for spheres, coils, rods, and other geometries are known. [136, 147] Shape dependence characteristics are most easily observed by plotting the *inverse* of $P(\theta)$ versus q^2. The function is nearly linear for coils, but diverges to large values for large spheres and to smaller values for large rods. [136] The effect of scatterer shape on $P(\theta)$ is dependent on the experimental parameters (λ, n, θ) which determine the scattering vector. The scattering vector and its inverse (equal to R_g at $qR_g = 1$) as a function of angle are shown in Table 5.5 for scattering from DMF. In the system of Table 5.5, spheres with radii of gyration greater than approximately 40 nm may begin to show non-linearity in $P(\theta)$.

Table 5.5. Scattering vector for n = 1.4269 (DMF) and λ = 488 nm for the experimental range of scattering angles (35 to 135°).

θ, deg	q, nm^{-1}	q^{-1}, nm
35	0.0110	90.5
45	0.0141	71.1
55	0.0170	58.9
70	0.0211	47.4
80	0.0248	40.3
90	0.0260	38.5
100	0.0281	35.5
110	0.0301	33.2
120	0.0318	31.4
135	0.0339	29.5

The aggregation number of the scatterer can also be used to understand structure by influencing the plausibility of certain structural models. The aggregation number is determined from the aggregate molecular weight divided by the unimer molecular weight.

c. R_g/R_h

Structural information can be extracted from the ratio of the radius of gyration to the hydrodynamic radius through the relations in Tables 5.3 and 5.4. Spheres of all radii are characterized by a single ratio equal to $(3/5)^{1/2}$ or approximately 0.775. Less symmetrical structures require at least two

parameters to specify their geometry, and the value of the ratio varies with size and shape.

d. Models

Spheres are predicted for rod-coil diblocks in rod-selective solvents because the coils would be able to pack into a spherical core and the rods would fan out into the solvent. The symmetry of spheres requires only one parameter to completely characterize the overall size and geometry. The specifics of the core and coronal regions are obviously not considered.

Rigid-rod stars, with 2 to 6 arms, have been prepared synthetically in order to exploit the reinforcing properties of rigid rod molecules. [7] Typically rods only have good mechanical properties parallel to their axis. [148] The rigid-rod star structure allows an opportunity to disrupt the typical highly ordered, unidirectional, liquid-crystalline structures to create a structure in which the rods are able to provide isotropic reinforcement. [7, 149] The self-assembly of rod-coil diblock copolymers is expected to provide a much simpler avenue toward these structures.

Prolate and oblate ellipsoids, Figure 5.1, represent the simplest models of aggregation of rod-coil diblock copolymers in coil-selective solvents. As shown in the next section, these are structures have been theoretically predicted. The rods are predicted to pack axially, consequently, the radius of the micelles is a function of the aggregation number and the rod diameter. The prolate ellipsoid length or, equivalently, the oblate ellipsoid height are equal to twice the corona height plus the rod length or twice the rod length for monolayer or bilayer micelles, respectively. Using the relations presented in Tables 5.3 and 5.4, the hydrodynamic radii, radii of gyration, and the ratio

of R_g and R_h were calculated for several models of prolate and oblate ellipsoids, Tables 5.6 and 5.7, respectively. The rod-coil system included three rods which were each twice the length of the former. This design allowed the number of models to be reduced since the bilayer structure for the shortest rod was nearly equivalent to the monolayer structure for the next longer rod.

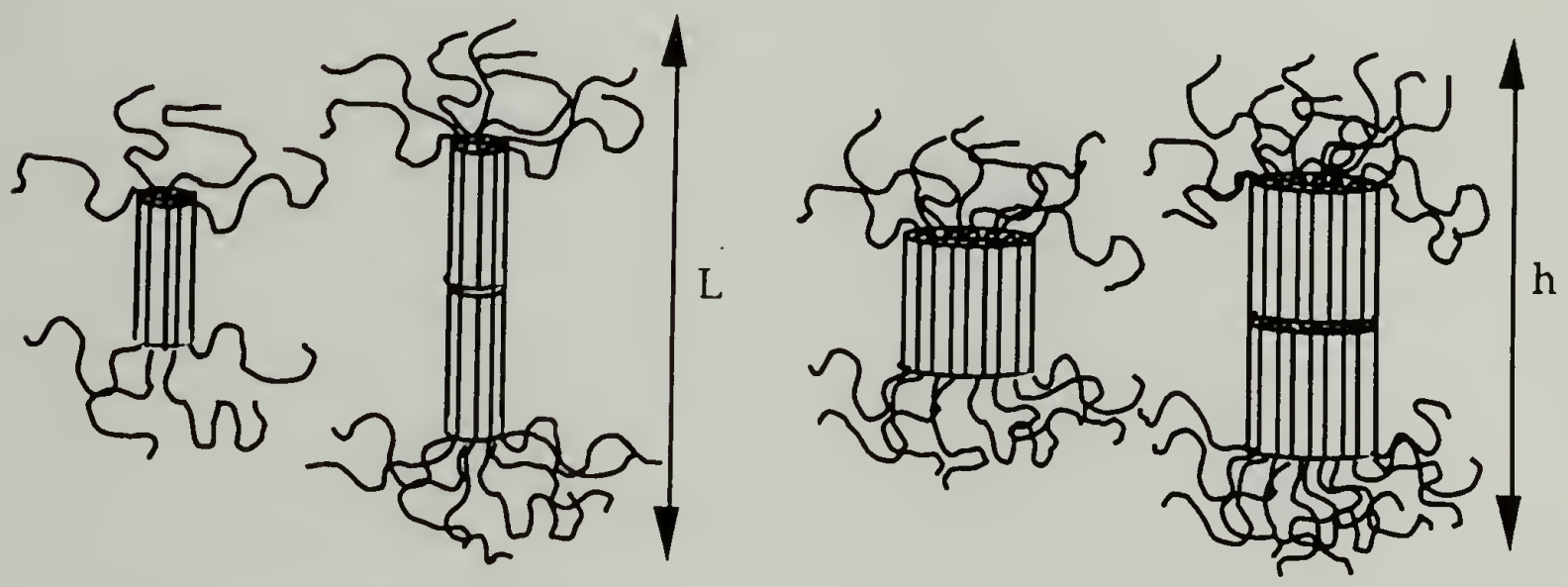

a. Prolate Ellipsoid

b. Oblate Ellipsoid

Figure 5.1. Proposed structures for rod-coil diblock aggregates in coil-selective solvents, (a) prolate ellipsoid (b) oblate ellipsoid.

The Rg and Rh of a PBLG homopolymer is calculated as an example of the information in Table 5.6. Choosing an α-helix which is 20 nm in length, the polymer is modeled as a prolate ellipsoid of length equal to 20 nm and diameter equal to 2 nm. [96] From Table 5.4, the radius of gyration is equal to $(L^2/12 + r^2/2)^{0.5}$, which in this example gives an Rg of 5.8 nm. From Table 5.3, the parameter ρ is equal to the ratio b/a of the semi-axes which in this case is 2r/L or 0.1, and 'a' is equal to L. The value of 3.3 nm is calculated for the hydrodynamic radius as shown in Table 5.6.

Table 5.6. Calculated parameters for monolayer and bilayer prolate ellipsoid models for rods of length (L) 20, 40, and 80 nm with diameter 20Å. For each length, several aggregate radii (r) are considered. All dimensions are reported in units of nanometers.

	L = 20 nm			L = 40 nm			L = 80		
r	R_h	R_g	R_g/R_h	R_h	R_g	R_g/R_h	R_h	R_g	R_g/R_h
1	3.3	5.8	1.7	5.4	11.6	2.1	9.1	23.1	2.5
3	5.1	6.2	1.2	7.7	11.7	1.5	12.2	23.2	1.9
5	6.6	6.8	1.0	9.4	12.1	1.3	14.3	23.4	1.6
10				13.2	13.5	1.0	18.8	24.2	1.3
20							26.3	27.1	1.0
30							33.3	31.4	0.9

Table 5.7. Calculated parameters for monolayer and bilayer oblate ellipsoid models for rods of length (L) 20, 40, and 80 nm with diameter 20Å. For each length, several aggregate radii (r) are considered. All dimensions are reported in units of nanometers.

	L = 20 nm			L = 40 nm			L = 80 nm		
r	R_h	R_g	R_g/R_h	R_h	R_g	R_g/R_h	R_h	R_g	R_g/R_h
15	13.3	10.5	0.79						
20	16.5	13.4	0.81						
30	23.0	19.5	0.85	26.6	21.0	0.79			
40	29.4	25.7	0.87	33.1	26.8	0.81			
50	35.8	31.9	0.89	39.5	32.9	0.83	46.6	36.3	0.78
60	42.2	38.2	0.91	46.0	39.0	0.85	53.2	42.0	0.79
70	48.5	44.5	0.92	52.4	45.2	0.86	59.7	47.7	0.80
80	54.9	50.8	0.93	58.8	51.4	0.87	66.2	53.7	0.81
90	61.3	57.1	0.93	65.2	57.6	0.88	72.6	59.7	0.82
100	67.7	63.4	0.94	71.5	63.9	0.89	79.1	65.7	0.83
110	74.0	69.7	0.94	77.9	70.1	0.90	85.5	71.8	0.84

B. Theory of Micelle Formation

1. Coil-Coil

Coil-coil block copolymers are known to form spherical micelles in selective solvents. [32] The poorly solvated block forms a solvent-excluded spherical core. The well-solvated block is tethered to the core and stretches into the solution as the corona.

A scaling approach has been used to determine the dimensions of the coronal chains in spherical [150] and cylindrical micelles. [151-154] Curved interfaces give the coronal chains a larger volume to occupy as the distance away from the grafting interface (the core) increases. The cone-shaped region occupied by each coronal chain can be modeled as a stack of spheres (blobs) which increase in radius, ξ, with distance from the interface, r: [33]

$$\xi(r) \approx r / f^{1/2} \qquad (5.2)$$

The aggregation number, f, is constant with distance, and therefore the segment concentration, φ, decreases with radial distance

$$\varphi(r) \approx (a / \xi)^{4/3} \qquad (5.3)$$

where a is the monomer segment length. [33] This concentration profile leads to an unexpected relationship between the end-to-end distance of the chain, L, and the degree of polymerization, N:

$$L \approx a f^{1/5} N^{3/5} \tag{5.4}$$

which scales in the same manner as a *free* chain in a good solvent. The aggregation number plays a role in the actual chain dimensions by causing the chains to stretch. Each blob is designated as having an energy kT and therefore the number of blobs equals the coronal free energy

$$F_{corona}/kT \approx f^{1/2} \ln (R / R_{core}) \tag{5.5}$$

where R is the radius of the micelle and R_{core} is the radius of the core, only.

The scaling relations for the corona provide the necessary basis for determining the equilibrium properties of the whole micellar aggregate. The free energy of the micelle has three major components:

$$F / kT = F_{int} + F_{core} + F_{corona} \tag{5.6}$$

where F_{int} is the interfacial free energy between the poorly solvated block (designated "B") and the solvent; F_{core} is the stretching energy required by the B block to fill the core to a constant density; F_{corona} is the stretching energy imposed by close-packing of the A chains in the corona. The interfacial term is equal to

$$F_{int} \approx R_{core}^{2} / f \tag{5.7}$$

The interfacial energy favors large aggregation numbers because micelle growth reduces the core contact with the solvent. The free energy due to

stretching in the core is inversely proportional to the bulk, solvent-excluded dimension R_0: [33]

$$F_{core} / kT \approx (R/R_0)^2 \tag{5.8}$$

where

$$R_0 \approx N_B^{1/2} a \tag{5.9}$$

and N_B is the degree of polymerization of the poorly solvated B block. The chains must stretch more to fill the *center* of the core as the aggregation number (and core radius) grows. The corona free energy term is given in Eqn. 5.5. For the corona, lower aggregation number means lower grafting density. Therefore, low aggregation numbers are favored by the two stretching terms.

Two limiting cases can be identified: $N_A >> N_B$ and $N_B >> N_A$ where "A" chains are in the corona and "B" chains are in the core. The first case ($N_A >> N_B$) is that of "starlike" micelles in which a relatively small core is surrounded by an extended corona. In this case, the core free energy is negligible. Minimization of the free energy with respect to aggregation number predicts

$$f \approx (\gamma a^2/kT)^{6/5} N_B^{4/5} \tag{5.10}$$

where γ is the surface energy density of the core-corona interface.

Consequently,

$$R_{core} \approx f^{1/3} N_B^{1/3} a \propto N_B^{3/5} a \tag{5.11}$$

$$R \approx N_B^{4/25} N_A^{3/5} a \tag{5.12}$$

The aggregation number and core radius of starlike micelles are predicted to depend only on the length of the *core* chains. The radius of the micelles is predicted to depend on both block lengths but more strongly on the size of the extended block A.

In the second case, $N_B >> N_A$ causes "crew-cut" micelles to form. The core stretching energy is dominant in this case because the core radius is large and the corona is short. Minimization of the free energy gives

$$f \approx (\gamma a^2/kT) N_B \tag{5.13}$$

It follows that

$$R \approx R_{core} \approx N_B^{2/3} a \tag{5.14}$$

As in the case of star-like micelles, the aggregation number is predicted to scale only with the size of the core block, however in this case the micelle *radius* depends only on the core block length as well. In each case, the scaling exponent of the core radius with B block length, N_B, indicates that the core is expanded in order to achieve constant density.

While the relatively limited structures formed by flexible-coil diblock copolymers are certainly useful in certain applications, they are poor candidates for building block components. The next section describes how rigidity is predicted to provide a variety of building block structures.

2. Rod-Coil

Theoretical work in the area of the solution structure of rod-coil block copolymers has been restricted to the coil-selective solvent case.

Rod-coil diblock and triblock copolymers are expected to form a solvent-excluded core of rods in a solvent which is poor for the rods yet good for the coils. The manner in which this core will form cannot be gleaned from analogy with flexible coil cores. A cylindrical core of axially-packed rods has been proposed. [77] The coils emanate from the ends of the cylinder.

Considering the free energy contributions to micelle formation (Eqn. 5.6), the core free energy is negligible for cores composed of rods since the rods do not (and cannot) deform. Two limiting cases have been considered: "star-like" micelles which have long (flexible) coronal chains and "crew-cut" micelles endowed with short coronal chains, Figure 5.2.

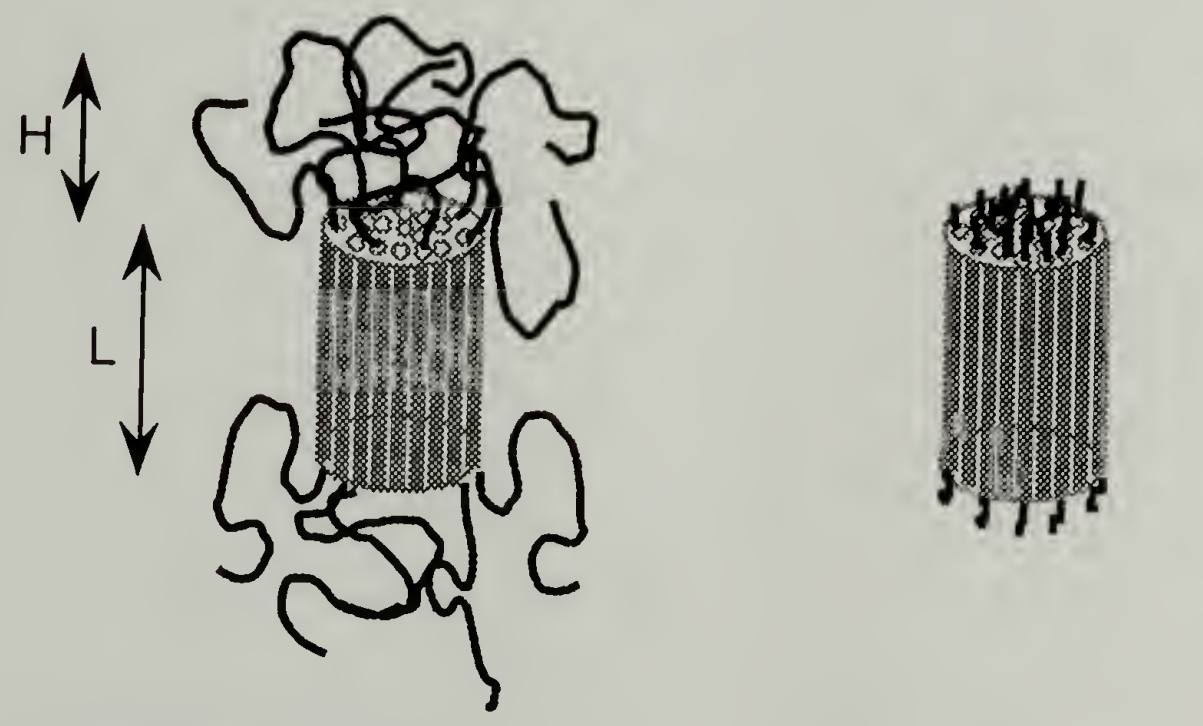

a. Star-like micelle

b. Crew-cut micelle

Figure 5.2. Schematic representation of rod-coil block copolymer aggregation in coil-selective solvents. Crew-cut micelles are not predicted to be stable.

It has been predicted [77] that only star-like micelles will be stable. The relative lengths of the rod (A) and coil (B) blocks affect the stability of the micelle. The coils must be long enough to produce star-like micelles, but be short enough so that the coil regions do not overlap. These conditions are met for

$$N_B^{4/3} >> N_A >> N_B^{1/2} \tag{5.15}$$

Furthermore, the aggregation number has been predicted to scale linearly with the length of the rod block. Geometrically it follows that the core radius will scale with the square root of the rod length:

$$f \alpha N_B \tag{5.16}$$

$$R_{core} \alpha N_B^{1/2} \tag{5.17}$$

The coronal height, H, of the micelle is predicted to scale with both rod lengths:

$$H \alpha N_B^{1/5} N_A^{3/5} a \tag{5.18}$$

de Gennes [78] has considered the structure of coil-rod-coil triblock copolymers in a coil-selective solvent. An aggregate with f molecules was approximated by a rectangle with width, am_1, and length, am_2, where the scaling factor "a" is equal to the rod diameter and the aggregation number, f, is equal to m_1m_2. The height dimension of the aggregate is parallel to the rods. This structure is nominally termed a "needle" and is equivalent to a

"hockey puck" structure. If the width is only one molecule, the structure becomes a "fence". If both the width and length are very large, the structure becomes a "plate". The effects of rod and coil lengths on the resulting structures were considered. [78]

Plates are predicted for long rods in which the degree of polymerization of the rod block, N_R, and the degree of polymerization of the flexible block, N_F, obey the relation

$$N_R > 2\, N_F^{15/11} / (\gamma a^2/kT)^{4/11} \qquad (5.19)$$

The rods are predicted to tilt due to a balance between coil stretching energy and rod interaction with the solvent. The equilibrium tilt angle is a function of the coil molecular weight. [69, 78]

Large needles (or, more specifically, wide fences) are predicted for shorter rods. These micelles are very long, but their widths are comparable with the brush length. Aggregation numbers for the plates and needles are dependent on both the rod and coil lengths.

C. Rod-Selective Solvent - Experimental Results

The requirement for a rod-selective solvent was a helicogenic, non-aggregating solvent for the PBLG and a poor or non-solvent for the coil. Two rod-selective solvents were identified for this system: N,N-dimethylformamide and benzyl alcohol. Benzyl alcohol was used in initial experiments, but the solutions in this solvent were highly viscous, difficult to filter, and possessed a low refractive index contrast with the polymer.

Anhydrous N,N-dimethylformamide was used for the experiments reported in this work. Ample refractive index contrast is available with DMF. Only anhydrous DMF was used because DMF is extremely hygroscopic and PBLG is highly insoluble in water. [143]

Dilute solutions (0.1 wt%) of ten PI-PBLG diblock copolymers and three PBLG homopolymers in anhydrous N,N-dimethylformamide were studied. The first part of this section deals with the analysis of the PBLG homopolymer rods and compares the experimental values of R_g, R_h, A_2, and intrinsic viscosity to literature values. The dilute solution range of concentration is established as a function of rod molecular weight. Next, the initial diblock experiments involving establishing the stability and reproducibility of the structures, as well as the effects of experimental errors are shown. The stability of the structures was established with the equilibrium study in Part 1. The reproducibility and the magnitude of experimental error due to sample preparation and measurement error were addressed in the reproducibility study in Part 2. Three samples were prepared and analyzed by dynamic and total intensity light scattering. The percent standard deviation in these values was used to estimate the error in reported values of the radius of gyration and the hydrodynamic radius. Part 3 of this section is concerned with the effect of molecular weight of the rod and coil blocks on the resulting structures.

1. Dilute Solution Range

The dilute concentration range was established for the polymers used in this system by first establishing the experimental and theoretical values of

the overlap concentration, c*, for the PBLG rods. [96, 99, 155-157]. Theoretically, c* can be calculated from the following equation:

$$c^*(mg/ml) = 10^{24}\, M/L^3\, N_A \qquad (5.20)$$

where L is the rod length in nanometers, M the molecular weight in g/mol, and N_A is Avogadro's number. This relation assigns c* as the concentration in which each rod occupies a cube of volume L^3. In other words, the rods can freely rotate without encountering other rods. This relation is often given simply as $n^*=1/L^3$ where concentration is in terms of a number concentration (n, $n = c\, N_A/M$). The use of this relation allow a simple method of comparision between rods of different molecular weights and concentrations: at $c^*_{theoretical}$, $nL^3 = 1$.

The theoretical limit of the relation shown as Eqn. 5.20 has been shown by numerous experimental investigations to be as much as 50 to 300 times too low. [99, 155-157] Zero and Pecora [156] studied the depolarized light scattering from solutions of PBLG (150K, 170K, and 210K) in dichlorethane and found that the semi-dilute regine, as determined by a discontinuity in the concentration dependence of the rotational diffusion coefficient, began at 5 mg/ml. This correlates to an overlap concentration of about $cL^3=21$. Tracy and Pecora [96] studied the concentration dependence of the translational diffusion coefficient of a 102 K PBLG homopolymer and found similar results. Specifically, two distinct concentration regimes were observed, with a discontinuity at 8.4 mg/ml. At low concentrations (< 8.4 mg/ml) the diffusion coefficient was a weakly decreasing function of concentration, but at higher concentrations the diffusion coefficient increased with concentration. The onset of the semi-dilute behavior was, therefore, observed for a value of

nL^3 between 15.2 and 20, consistent with the findings from the rotational diffusion coefficient behavior.

This conclusion of a delayed onset of entanglement for PBLG rods was further tested by Zimm plot analysis of PBLG homopolymer and diblock used in this work, Figure 5.3. Practically, the overlap concentration can be determined from the relation:

$$c^* = 1/A_2M \tag{5.21}$$

where A_2 is the second virial coefficient and M is the molecular weight. Based on this relation the overlap concentration for the 118K PBLG homopolymer and the 2.8K PI-b-25K PBLG diblock are 34 and 43 mg/ml, respectively. This agrees well with other work on PBLG in DMF as shown in Table 5.8.

Table 5.8. Experimental determination of the overlap concentration for PBLG in N,N-dimethylformamide.

Reference	M, g/mol	$A_2 \times 10^4$, cm^3molg^{-2}	$c^*=1/A_2M$ mg/ml	nL^3	$[\eta]$, ml/mg	$c^*=1/[\eta]$, mg/ml	nL^3
this work	118,560	2.5	34	93			
	59,000				0.0391	26	17
Russo et al. [97]	179,000	3.1	18	112			
	300,000	3.1	11	192			
Tracy and Pecora [96]	102,000	3.9	25	50.3	0.119	8.4	17
Kubota et al. [99]	299,000	3.1	11	190			
	372,000	3.3	8.1	217			

Another practical definition of the overlap concentration is based on the intrinsic viscosity of the polymer solution, $[\eta]$:

$$c^* = 1/[\eta] \tag{5.22}$$

The intrinsic viscosity was measured as 0.0391 ml/mg for the 59K PBLG sample in DMF. This corresponds to an overlap concentration of 25.6 mg/ml (or $nL^3=17$). This result agrees with the intrinsic viscosity measurement of the overlap concentration by Tracy and Pecora [96], as shown in Table 5.8.

Based on the experimental finding that c^* is 20 times greater than the theoretical c^*, the overlap concentration for the rods used in this work are 150, 30, 7.4 mg/ml. The dilute range is theoretically defined as $c << c^*$, but in practice the dilute concentration range is considered to be at $c^*/c < 5$. [158] The experimental concentration of 1 mg/ml is therefore established as dilute.

2. PBLG Rod Characterization

Hydrodynamic radii of PBLG in DMF have been reported in previous papers [96, 97, 99], and, therefore, serve to establish the reliability of the measurements in this work. The hydrodynamic radius of the rod-like PBLG homopolymer is expected to scale linearly with molecular weight, as shown in Table 5.3 (prolate ellipsoids). Figure 5.4 shows the hydrodynamic radii for the 26K and 59K PBLG homopolymers in DMF plotted in conjunction with literature values of R_h for various PBLG molecular weights. The linear relation is evident and shows that the results are consistent with previously published results.

3. Equilibrium Study

Two diblock samples were studied to evaluate the effect of time on the hydrodynamic radii and radii of gyration of aggregates formed in anhydrous DMF. A low molecular weight diblock, 2.8K PI-b-25K PBLG (Table 5.9) and a medium molecular weight diblock, 69K PI-b-59K PBLG (Table 5.10), were chosen in order to ascertain any molecular weight dependence on equilibration. This study not only addressed the time dependence of polymer equilibration, but also consequences of sample preparation, such as the time required for the disappearance of air bubbles generated during filtering of the solution.

Diffusion coefficients for this equilibrium study were determined from a single correlation function at 90°. Values for the hydrodynamic radius (Eqn. 4.9), the polydispersity of the distribution of molecular sizes, and the radius of gyration (Eqn. 4.20) are reported for each system. Radii of gyration were calculated from the slope of $P(\theta)$ as a function of q^2; the error was calculated from the error in the determination of the slope. A single angle was used for determination of R_h and therefore the error in the diffusion coefficient (the slope of Γ versus q^2) was not known. The average and standard deviation for each parameter are shown in the last line of each table.

Aggregates form in less than one day for each of the diblocks studied, and once formed, are stable with time. The equilibrium study established that the time between sample preparation and scattering measurements was not an experimental variable which needed to be controlled. The hydrodynamic radius in the 69K PI-b-59K PBLG system was observed to slowly decrease with time, while the radius of gyration only randomly fluctuated in the same time

interval. The apparent decrease in the hydrodynamic radius is likely due to the fact that the Rh reported for day 10 (95.9 nm) was based on measurement at 4 scattering angles while previous measurements were based only on one angle and would therefore be less accurate.

Table 5.9. Dynamic and total intensity light scattering measurements as a function of time for the system 2.8K PI - b - 25K PBLG in anhydrous N,N-dimethylformamide.

Days	Slow Mode R_h, nm	Fast Mode R_h, nm	R_g, nm
1	51.2 ± 2.5	5.6 ± 0.2	29.6 ± 0.7
2	54.0 *	5.5 *	24.6 ± 1.0
3	52.1 *	5.6 *	23.9 ± 1.5
7	52.5 *	5.9 *	30.7 ± 0.6
Ave	52.5 ± 1.0	5.65 ± 0.15	27.2 ± 3.0

* Only one DLS angle measured

Table 5.10. Summary of dynamic and total intensity light scattering measurements as a function of time for the system 69K PI - b - 59K PBLG in anhydrous N,N-dimethylformamide.

Days	R_h, nm	Polydispersity	R_g, nm
1	113 *	0.1281 ± 9.77%	40.9 ± 0.9
2	112 *	0.1301 ± 9.73%	40.4 ± 0.8
6	109 *	0.1559 ± 8.76%	46.5 ± 1.3
10	95.9 ± 3.5	0.1145 ± 17.14%	45.9 ± 0.9
Ave	108 ± 6.8	0.1322 ± 0.0150	43.4 ± 2.8

* Only one DLS angle measured

4. Reproducibility Study

The effect of sample preparation on the accuracy of the hydrodynamic radius and radius of gyration was established. Three samples of 2.8K PI-25K PBLG in DMF were prepared for each experiment. The concentrations were all approximately 0.09 wt%. Table 5.11 shows the results of this study; the measured values are within 10% for both the slow and fast modes of the hydrodynamic radius and the radius of gyration.

Table 5.11. Reproducibility of dynamic light scattering measurements. The system chosen was 2.8K PI-b-25K PBLG in DMF.

Slow Mode			Fast Mode			
Conc., wt%	D X 10^8, cm^2/sec	R_h, nm	D X 10^7, cm^2/sec	R_h, nm	Conc., wt%	R_g, nm
0.0932	4.19 ± 0.018	65.0 ± 0.3	4.75 ± 0.017	5.7 ± 0.2	0.0977	23.9 ± 1.5
0.0947	4.06 ± 0.061	67.1 ± 1.0	4.04 ± 0.088	6.7 ± 0.2	0.0990	29.7 ± 0.3
0.0919	4.15 ± 0.035	65.6 ± 0.6	4.59 ± 0.067	5.9 ± 0.1	0.0985	30.4 ± 0.3
Ave	4.13 ± 0.05	65.9 ± 0.9	4.46 ± 0.30	6.1 ± 0.4	Ave	28.0 ± 2.9

5. Effect of Block Length on Structure

The PI-b-PBLG system under investigation is composed of three rod blocks and three coil blocks. This section explores the effect of changes in coil block length for short rods (18 nm), medium rods (40 nm), and long rods (81 nm).

a. Short Rods

Block copolymers possessing "short" PBLG rods are the first four polymers listed in Table 5.1. A typical time autocorrelation function and its calculated distribution function are shown in Figure 5.5 for the sample 10K PI-b-26K PBLG in anhydrous N,N-dimethylformamide. The quality of the fit is demonstrated by the small residuals.

Figure 5.6 shows the effect of increasing the coil size on the distribution functions for 26K PBLG homopolymer and three block copolymers with progressively larger coil blocks. Curves are shown for scattering at 90°. Increasing the coil to 2800 g/mol results in a dramatic change in mobility of the scatterer which is attributed to polymolecular aggregation. A similar effect was seen for the 10 K coil and was accompanied by a sharpening of the distribution function. The latter effect is consistent with the formation of thermodynamically stable aggregates with a well-defined equilibrium aggregation number. The increased driving force toward aggregation is consistent with the increased size of the insoluble block.

Further increasing the incompatible block to 69,000 g/mol makes the copolymer approximately 70% PI; the most polyisoprene-rich diblock studied. This block copolymer is not completely soluble at 0.1 wt%. Figure 5.6 shows the distribution function of 69KPI-26K PBLG in DMF at a concentration near its solubility limit. The weak scattering (evidenced by the noise in the correlation function), the enhanced mobility of the scatterer, and the broad distribution function are consistent with unimolecular scattering. The solubility limit of 69K PI-26K PBLG in DMF is likely below the critical micelle concentration.

Figure 5.7 shows a representative Γ versus q^2 plot used to determine the diffusion coefficient (Eqn. 4.7) which leads to the hydrodynamic radius (Eqn. 4.9). Each of the homopolymer and diblock copolymer samples in each solvent system was analyzed with this type of analysis to determine the diffusion coefficient. Figure 5.8 shows the data analysis used to calculate radius of gyration from Eqn. 4.20. The pure solvent scattering is analyzed first to determine the range of angles for which there stray light affecting the measurement. The scattered intensity from a solvent would be independent of angle if the scattering volume was constant with angle. The scattering volume is actually a $\sin\theta$ function of angle, and therefore the $I\sin\theta$ plot, shown in Figure 5.8, allows the determination of the allowable range of scattering angles for each experiment. From Figure 5.8, it can be seen that the lowest and highest angles (35° and 135°) fall outside the 5% deviation window. These angles are not used in the determination of the radius of gyration. Figure 5.9 shows the inverse of the particle scattering form factor which for this system is linear with q^2 as expected for $qR_g<1$.

Table 5.12 lists the radii of gyration, hydrodynamic radii, and the ratio of R_g to R_h for the block copolymers with 26K rods. The radius of gyration and the R_g/R_h ratio for the 26K PBLG homopolymer appears to be anamolously high in relation to the calculated values based on a prolate ellipsoid. The shape of the inverse form factor was linear for each system, consistent with the relatively small size of the scatterers ($qR_g < 1$). [136]

The dramatic difference in R_g/R_h for the 69K PI -26K PBLG sample compared with the other two diblock samples indicate underlying structural differences. Scattering from the 2.8K PI-26K PBLG and 10K PI-26K PBLG systems is most consistent with spherical aggregates in which R_g/R_h would be 0.775. The fact that the ratios in this system are lower than predicted is

discussed in the next section. The larger ratio calculated for the 69K PI-b-26K PBLG is consistent with rod-like structure, as calculated in Table 5.6. Considering the R_g and R_h values for this systems, the most probable model is the end-to-end aggregation of two rods to form a bilayer rod structure. The calculated R_g and R_h for such a structure are 11.6 nm and 5.4 nm, respectively.

Table 5.12. Light scattering results for PI-PBLG block copolymers possessing 26K PBLG rods blocks. Dilute (0.1 wt%) block copolymer solutions in DMF. Errors for R_g and R_h were calculated from error in the slopes. Calculated R_g and R_h are based on a prolate ellipsoid of model of unassociated PBLG homopolymer (L=18 nm, d=2 nm).

Polymer (PI-PBLG)	R_g, nm	R_h, nm	R_g/R_h	R_g, calc nm	R_h, calc nm
26K PBLG	15.0 ± 1.3	1.9*	8.0*	5.2	3.1
2.8K-26K	23.5 ± 1.7	40.5 ± 14.5	0.58 ± 0.21		
10K-26K	24.4 ± 0.8	50.6 ± 2.7	0.48 ± 0.03		
69K-26K	17.9 ± 1.3	5.9*	3.2*		

* Only 1 DLS angle measured

b. Medium Rods

Figure 5.10 shows the calculated distribution functions for polymers possessing a 59K PBLG (40 nm) rod block. The results shown in Table 5.13 are analogous to the short rod case as the size of the aggregates appears to scale with the length of the rods. The medium rods are twice as long as the short rods, and the resulting aggregates are twice as large. For example, the

hydrodynamic radius of the 10K PI-b-26K PBLG sample is 50.6 nm. The hydrodynamic radius of the 10K PI-b-59K PBLG sample is 100.5 nm. In contrast to the short rod case, the copolymer with the 69K coil block is soluble at the experimental concentration and forms large spherical aggregates.

Table 5.13. Light scattering results for PI-PBLG block copolymers possessing 59K PBLG rods blocks. Dilute (0.1 wt%) block copolymer solutions in DMF. Calculated R_g and R_h are based on a prolate ellipsoid of model of unassociated PBLG homopolymer (L=40 nm, d=2 nm).

Polymer (PI-PBLG)	R_g, nm	R_h, nm	R_g/R_h	R_g, calc nm	R_h, calc nm
59K PBLG	--	3.7 ± 0.2	--	11.6	5.4
2.8K-59K	31.6 ± 1.4	78.9 ± 1.4	0.40 ± 0.02		
10K-59K	43.8 ± 1.2	100.5 ± 2.5	0.44 ± 0.02		
69K-59K	43.5 ± 0.9	95.9 ± 3.5	0.45 ± 0.02		

c. Long Rods

Unlike the short and medium-size rods, the aggregate size for the three diblocks possessing the largest rods (118K PBLG or 81 nm) did not continue to scale with rod length. Instead the mobility of the aggregates suggested that micelles do not form for these diblocks, Figure 5.11. In each case, a broad distribution of mobilities and a large R_g/R_h ratio suggested non-spherical structures, consistent with unaggregated diblocks. Table 5.14 lists the characteristics of these diblocks in DMF. These values are in excellent agreement with those calculated for a single (unaggregated) 80 nm rod

(R_h=23.1 nm, R_g=9.1 nm, and R_g/R_h=2.5) indicating that the presence of the long PBLG rods inhibits aggregation of the diblock copolymers.

Table 5.14. Light scattering results for PI-PBLG block copolymers possessing 118K PBLG rods blocks. Dilute (0.1 wt%) block copolymer solutions in DMF. Calculated R_g and R_h are based on a prolate ellipsoid of model of unassociated PBLG homopolymer (L=80 nm, d=2 nm).

Polymer (PI-PBLG)	R_g, nm	R_h, nm	R_g/R_h	R_g, calc nm	R_h, calc nm
2.8K-118K	23.2 ± 0.4	10.2 ± 0.7	2.3 ± 0.2	23.1	9.1
10K-118K	23.7 ± 1.1	11.4 ± 0.2	2.1 ± 0.1		
69K-118K	26.7 ± 0.8	10.9 ± 0.6	2.4 ± 0.2		

6. Analysis of Structure in Rod-Selective Solvent

The preceding results have demonstrated that the PI-PBLG diblock copolymers endowed with short and medium-size rods form large aggregates in rod-selective solvents. Assignment of a specific structure to these aggregates requires information regarding how each of the blocks scatters light in this solvent. This is determined by measuring the differential refractive index of the component blocks in DMF. The average number of molecules which aggregate to form the micelles also provides important clues to geometry and is determined by measuring the micelle molecular weight using a Zimm plot analysis.

a. Refractive Index Increment

A knowledge of the differential refractive index of each block comprising the diblocks of this research in the solvent of interest is crucial to interpreting the total intensity light scattering results. If both components of the diblock copolymer have the same refractive index increment, then the scattering from the diblock reduces to the simplest case, a homogeneous or isorefractive scatterer. In other words, the diblock behaves as a homopolymer. A prerequisite to the determination of the change in solution refractive index as a function of polymer concentration, dn/dc, is polymer solubility. In DMF, a rod-selective solvent for PI-b-PBLG, PBLG is soluble but polyisoprene is not. The differential refractive index of PBLG in DMF could be determined directly, whereas, the dn/dc of PI in DMF was determined from the dn/dc of the diblock, $(dn/dc)_{TOT}$, using the following equation: [159]

$$(dn/dc)_{TOT} = \phi_{PBLG}\,(dn/dc)_{PBLG} + \phi_{PI}\,(dn/dc)_{PI} \qquad (5.23)$$

where ϕ_A is the weight fraction of component A in the diblock copolymer.

Figure 5.12 shows the phase shift due to a refractive index difference. Curve (a) is the polarization of the beam for the case of pure solvent in both cells. Curve (b) shows the polarization of the beam for the case of solvent in one cell and a dilute polymer solution in the other. The phase shift (110° in this example) was used to calculate the refractive index difference, Δn, for the given concentration difference, Δc. Figure 5.13 compares the Δn and Δc values for several pairs of solutions. Figure 5.14 compiles the cumulative refractive indices for each concentration, $\Sigma(n-n_o)$. The refractive index increment is equivalent to the slope. Table 5.15 lists the refractive index

increments measured for two PBLG homopolymers and two PI-b-PBLG diblocks in anhydrous DMF.

Table 5.15. Refractive index increments measured in anhydrous N,N-dimethylformamide at 633 nm and room temperature.

Polymer	dn/dc
42K PBLG	0.1123 ± 0.0027
118K PBLG	0.1160 ± 0.0027
2.8KPI-b-25K PBLG	0.1163 ± 0.0032
69K PI-b-118K PBLG	0.1114 ± 0.0016

This data shows that the refractive index increment for the PBLG homopolymer and the diblock copolymer are equal to within experimental error. Therefore, the refractive index increments for the PI and PBLG homopolymers in DMF are equivalent and the diblock behaves homogeneously. The variance of R_g/R_h from the theoretical value of 0.775 is therefore not a result of inhomogeneous scattering from each block, as has been reported for other systems, [159] but possibly a direct consequence of the spherical structure of the micelles. Of course, the R_g/R_h ratios ranging from 0.4 to 0.6 are lower than expected for isorefractive, hard-sphere micelles. The thissle shape will have a lower R_g than a sphere of the same radius because the mass is be more concentrated in the central core of the object than in the corona; this will result in a R_g/R_h ratio less than 0.775. Tsunashima [160] has calculated the particle scattering function and the radius of gyration for thissle-shaped objects (termed "sea urchins"). The radius of gyration was found to depend on the ratio of the radius of the core to the length of the

tethered rod, r_{core}/L, and the weight-fraction refractive index of the core, y. The limit of vanishingly small core is the rigid-rod star ($R_g = (1/3)^{0.5} L$) and the opposite limit, $r_{core} >> L$, is a simple sphere. For a constant value of y, the R_g/R_h ratio increases with increasing core radius to the value for a spherical scatterer (0.775).

The aggregates formed in the rod-selective solvent were analyzed with the "sea urchin" model. The weight-fraction refractive index of the core reduces to the weight fraction of the polyisoprene block in the copolymer because the two blocks are isorefractive in this solvent. The only variable required for the calculation of R_g is the ratio r_{core}/L. The r_{core}/L values which give the best agreement with the experimental data are shown in Table 5.16. As expected, the core radius increases with increasing coil length. However, the calculated core radius is much larger than the radius calculated for a melt-like PI core. For example, the core radius determined from the "sea-urchin" model was 35 nm for the 69K PI-b-59K PBLG sample. The core radius calculated for a melt consisting of 100 chains would only be 13 nm (and only 5.2 nm if the aggregation number in this diblock is the same as for the 2.8K-25K diblock, as discussed in the next section). This implies that the core blocks may be stretching and/or being swelled by solvent, both of which are well-documented processes for flexible coil-coil diblocks. [32] The hydrodynamic radius for these structures was calculated as the sum of the core radius and the rod length. The calculated R_h values are lower than the measured values by 20 to 35%. This disparity is not believed to be the result of hydrodynamic differences between sea urchins and simple spheres since it has been shown that a surface density as low as 10% can result in translational motion similar to that of a sphere of the outer radius. [161] For homogeneous scatterers such as PI-b-PBLG in DMF, the sea-urchin structure has a lower R_g

than a sphere of equivalent outer radius. Therefore, the expected R_g/R_h ratio is lower than the value for spheres, 0.775, as shown in Table 5.16.

Table 5.16. Analysis of light scattering results for PI-PBLG block copolymers forming micelles in DMF. Values of rcore/L are based on the sea-urchin model of Hirata and Tsunashima. [160]

Polymer (PI-PBLG)	R_g, nm	R_h, nm	R_g/R_h	r_{core}/L, calc.	R_h, nm calc*	R_g/R_h, calc†
2.8K-26K	23.5 ± 1.7	40.5 ± 14.5	0.58 ± 0.21	0.83 ± 0.10	32.9 ± 1.8	0.71
10K-26K	24.4 ± 0.8	50.6 ± 2.7	0.48 ± 0.03	1.0 ± 0.05	35.9 ± 2.5	0.68
2.8K-59K	31.6 ± 1.4	78.9 ± 1.4	0.40 ± 0.02	0.25 ± 0.04	50.2 ± 1.6	0.63
10K-59K	43.8 ± 1.2	100.5 ± 2.5	0.44 ± 0.02	0.63 ± 0.04	65.2 ± 1.4	0.67
69K-59K	43.5 ± 0.9	95.9 ± 3.5	0.45 ± 0.02	0.87 ± 0.03	75.0 ± 1.1	0.58

* $r_{core} + L$

† based on measured R_g and R_h, calc

The tabulated values are based on the measured R_g; the value of R_h is derived from the model ($R_h = r_{core} + L$). While R_g/R_h ratios for sea-urchins are lower than for spheres, the measured ratios are still lower than expected for sea-urchins. This is not understood at this point. One hypothesis is that the micelles interact through the rod dipoles and cause a slowing of the diffusion and accordingly an anamalously high R_h. The structure of the micelle in the rod-selective solvent is such that the α-helical rods, and their associated dipole moments, point radially outward. Two approaching micelles will may possibly have the effect of repelling one another at relative large distances, as discussed in Chapter II. This will have the effect of slowing the diffusion of the micelles, lowering the diffusion coefficient, and

increasing the *calculated* aggregate size (R_h). This effect would only affect the dynamics of the aggregates and therefore only affect R_h and not R_g. This hypothesis, as well as the measured R_g of the thissle shape, is consistent with the experimental results and interpretation since this would cause the R_g/R_h ratio to be lower than expected for a sphere.

b. Aggregation Number

Zimm plots were measured for two diblocks and one PBLG homopolymer. A representative Zimm plot is shown in Figure 5.3. The aggregation number of the scatterer can provide information about the organization of block copolymers incorporated into micelles by influencing the plausibility of certain structural models. The aggregation number was determined from the aggregate molecular weight divided by the unimer molecular weight (calculated from the sum of the block lengths). The aggregation number calculated for the 2.8K PI-b-25K PBLG sample in DMF was approximately 5. This is quite low in comparison to micelles of flexible coil-coil diblocks in which aggregation numbers of 25 to several hundred have been reported. [159] This may be related to several effects. First, the dipoles of the neighboring helices may repel one another and thereby favor a larger spacing or equivalently a smaller aggregation number. However, the dipole-dipole repulsion cannot fully explain the low aggregation number because the dielectric constant of DMF is high (36.7) and should screen the dipole-dipole interactions as shown in Chapter 2, Figure 2.18. Another effect which may influence the aggregation number is the large diameter of the tethered rods. Typically values for the diameter of PBLG helices are between 18 and 20 Å. [125] However, a value of 30 Å in dilute DMF has been proposed

to account for the excluded volume due to the solvation shell. [162] Whichever value is chosen, the conclusion is the same: the rod and coil diameters are mismatched. For a given core diameter, the maximum number of tethered blocks is inversely proportional to the square of the diameter and therefore the aggregation number should decrease with the diameter of the tethering block.

7. Summary of Structure in Rod-Selective Solvent

Ten PI-block-PBLG copolymers and two PBLG homopolymers were studied in a rod-selective solvent. The solvent was known to support the α-helical rod-like structure of PBLG and inhibit aggregation of the PBLG rods. An equilibrium study showed that stable micelles form in less than one day, and a reproducibility study showed that the precision of the measurements of R_g and R_h were within 10%. Figure 5.16 summarizes the measured hydrodynamic radii and the R_g/R_h ratios for PI-b-PBLG copolymers in anhydrous N,N-dimethylformamide as a function of block length.

Two basic structures were characteristic for the polymers studied: relatively small, molecularly dispersed polymers and large, spherical micelles. The two homopolymer PBLG samples and the 69K PI-b-26K PBLG diblock sample gave small structures. This result for the homopolymer PBLG was consistent with the low extent of aggregation expected for this non-aggregating solvent. [125] The diblock sample was not completely soluble at the experimental concentration (0.1 wt%) because of the large fraction of insoluble PI. Filtering reduced the concentration of the solution as evidenced by the filter becoming clogged, and the polymer concentration was probably reduced to a value which was below the critical micelle concentration.

The analysis of structure by light scattering was simplified once this diblock-polymer system was shown to scatter homogeneously. Assignment of a spherical structure to the large aggregates in DMF was based on the low R_g/R_h ratios and the low aggregation number. *A priori*, many structures for rod-coil diblock aggregates in a rod-selective solvent may be proposed. These include simple spheres, large multilayer spheres, clusters of spheres, and long worm-like micelles. The relatively low aggregation number for the micelles limited the spherical structure to the simplest case of a simple sphere with a single core composed of coils and a core of radially-packed rods.

The micelles were analyzed using the "sea-urchin" analysis of Tsunashima. [160] The analysis was based on fitting the measured radius of gyration to a sea-urchin structure and calculating the ratio of the core radius to the rod length. The core radius calculated using this model was significantly larger than that for a melt-like polyisoprene core indicating that the core was stretched and/or swelled by solvent. The calculated hydrodynamic radius was smaller than the measured hydrodynamic radius.

This work is the first to show that rod-coil diblock copolymers can form micelles in a rod-selective solvent. Micelles formed for all of the soluble diblocks studied except those possessing the longest rod blocks. The anamolously large radii of the micelles in comparison to the rod block length is an issue which needs to be addressed in future work on this and other rod-coil systems.

D. Non-Selective Solvent - Experimental Results

Dilute solutions (0.1 wt%) of ten PI-PBLG diblock copolymers in dichloromethane were studied. Non-aggregated or weakly aggregated

structures were observed in this non-selective solvent. Dichloromethane is a good solvent for both polyisoprene and PBLG, but dichloromethane does not inhibit aggregation of PBLG helices to the extent in which N,N-dimethylformamide does. [163] Initial experiments involved establishing the stability of the structures.

1. Equilibrium Study

In dichloromethane, the measured hydrodynamic radius and radius of gyration for the 2.8K PI-b-25K PBLG diblock was stable over one week, Table 5.17. Results for the larger diblock, 69K PI-b-59K PBLG, fluctuated more but the fluctuations appeared to be uncorrelated, Table 5.18. The average values and the standard deviations from the repeated measurements are reported.

Table 5.17. Summary of dynamic and total intensity light scattering measurements as a function of time for the system 2.8K PI - b - 59K PBLG in dichloromethane.

Days	R_h, nm	Polydispersity	R_g, nm
1*	7.8 ± 0.5	0.2792 ± 9.85%	21.2 ± 0.6
2	8.1	0.2613 ± 14.20%	19.0 ± 0.6
4	7.5	0.2729 ± 10.94%	16.7 ± 0.6
7	7.1	0.2694 ± 11.57%	20.4 ± 1.1
Ave	7.6 ± 0.4	0.2707 ± 0.0065	19.3 ± 1.7

*Based on 4 angles

Table 5.18. Summary of dynamic and total intensity light scattering measurements as a function of time for the system 69K PI - b - 59K PBLG in dichloromethane.

Days	R_h, nm	Polydispersity	R_g, nm
1	8.5	0.0726 ± 5.95%	24.4 ± 1.0
2	12.1	0.1658 ± 4.11%	24.7 ± 0.9
4	10.6	0.2669 ± 5.41%	24.8 ± 0.7
11	8.4	0.2324 ± 5.19%	27.2 ± 2.3
Ave	9.9 ± 1.5	0.1844 ± 0.074	25.3 ± 1.1

2. Effect of Block Length on Structure

This section explores the effect of changes in coil block length for PI-b-PBLG diblock copolymers possessing short rods (18 nm), medium rods (40 nm), and long rods (81 nm).

a. Short Rods

Figure 5.17 shows distribution functions at 90° for the polymers possessing short (18 nm) rod blocks. This includes a 26K PBLG homopolymer which may be thought of as possessing a coil block of negligible size. The total intensity light scattering data was analyzed as discussed in the preceding section. Table 5.19 summarizes the dynamic and total intensity light scattering results for these diblocks in dilute dichloromethane solution.

Table 5.19. Light scattering results for PI-PBLG block copolymers possessing 26K PBLG rods blocks. Dilute (0.1 wt%) block copolymer solutions in dichloromethane. Errors for R_g and R_h were calculated from error in the slopes. Calculated R_g and R_h are based on a prolate ellipsoid of model of unassociated PBLG homopolymer (L=18 nm, d=2 nm).

Polymer (PI-PBLG)	R_g, nm	R_h, nm	R_g/R_h	R_g, calc nm	R_h, calc nm
26K PBLG	15.4 ± 1.3	5.48 ± 0.06	2.8 ± 0.2	5.2	3.1
2.8K-26K	16.8 ± 3.2	9.25 ± 0.13	1.8 ± 0.3		
10K-26K	16.7 ± 1.5	9.18 ± 0.16	1.8 ± 0.2		
69K-26K	22.0 ± 1.5	8.65 ± 0.05	2.5 ± 0.2		

It was immediately apparent that the size, symmetry, and polydispersity of these structures were dramatically different than those observed for the same polymers in a rod-selective solvent, Table 5.12. This was expected since each block was soluble in dichloromethane, and therefore there was no energetic driving force to form large aggregates. While micellization was not expected to occur because of the choice of solvent, weak aggregation due to dipole-dipole interaction between α-helix rods was, however, anticipated in this solvent. This weak aggregation was clearly observed for the simple case of the 26K PBLG homopolymer. The polymer was more aggregated in dichloromethane as compared with the previous case of a good, non-aggregating solvent (DMF). In DMF the hydrodynamic radius of the 26K PBLG was measured as 1.9 nm while in dichloromethane the hydrodynamic radius was 5.48 nm. A non-polar solvent, such as dichloromethane, cannot not break-up hydrogen bonding and dipole-dipole interactions between α-helices.

The diblocks were larger than would be expected for completely dispersed molecules. Non-associated diblocks would be expected to have values of R_g and R_h in the vicinity of those for the homopolymer rod to which the coil is attached. One model for the association behavior is shown in Figure 5.18. Compared to a single rod of dimensions L and d, 3 or 4 rods associated end-to-end and side-by-side in this manner may be expected to have a translational diffusion coefficient similar to that for a rod of length 3L and diameter 2d. A 26K PBLG rod is 18 nm long and has a 2 nm diameter. The R_g and R_h for the proposed structure would then be based on a prolate ellipsoid of length 54 nm and diameter 4 nm. From the relations in Tables 5.3 and 5.4, the R_h and R_g for a prolate ellipsoid of this length and diameter would be 8.2 nm and 16 nm, respectively. The R_g and R_h predictions from this model are consistent with the measured values shown in Table 5.15. For example, the R_h and R_g of the 10K PI-b-26K PBLG diblock in DCM are 9.18 nm and 19.3 nm, respectively. This implies that the coil blocks do not impede the aggregation as had been anticipated. It was expected that by blocking the amine-end of each helix the dipole-directed end-to-end aggregation would be blocked. The proposed structure in Figure 5.18 suggests that instead of inhibiting aggregation, the polyisoprene coils may participate in the process.

b. Medium Rods

Figure 5.19 shows the distribution functions at 90° for polymers possessing 59K (40 nm) rods. Large polydispersities in size are consistent with weakly or non-aggregated polydisperse polymers. The light scattering results are summarized in Table 5.20 for dilute (0.1 wt%) block copolymer solutions in dichloromethane. The measured radii and R_g/R_h ratios are again most

consistent with end-aggregated rods, similar to the case for short (18 nm) rods, but in this case the data is more consistent with only bimolecular association. For example, the R_g and R_h of a prolate ellipsoid which is 80 nm long and 2 nm in diameter are 23.1 nm and 9.1 nm, respectively. This agrees with the Rg and Rh of the 10K-59K sample: 23.3 nm and 9.2 nm, respectively. The hydrodynamic radii are approximately the same for each of the diblocks and the PBLG homopolymer, however the radii of gyration increase with increasing coil block size. Table 5.6 shows that an 80 nm long and a 40 nm long prolate ellipsoid would have the same hydrodynamic radii but different radii of gyration if the diameters of the two rods were 2 nm and 10 nm, respectively. The radius of gyration of the shorter and wider prolate ellipsoid is lower than that for the longer and thinner structure, 12.1 nm and 23.1 nm, respectively. The trend in the diblock data of Table 5.20 may therefore be indicating a shift in association from end-to-end to side-by-side as the coil block length increases.

Table 5.20. Light scattering results for PI-PBLG block copolymers possessing 59K PBLG rods blocks. Dilute (0.1 wt%) block copolymer solutions in dichloromethane. Errors for R_g and R_h were calculated from error in the slopes. Calculated R_g and R_h are based on a prolate ellipsoid of model of unassociated PBLG homopolymer (L=40 nm, d=2 nm).

Polymer (PI-PBLG)	R_g, nm	R_h, nm	R_g/R_h	R_g, calc nm	R_h, calc nm
59K PBLG	26.6 ± 0.5	10.5 ± 0.2	2.5 ± 0.1	11.6	5.4
2.8K-59K	32.7 ± 3.9	10.9 ± 0.5	3.0 ± 0.4		
10K-59K	23.3 ± 2.9	9.18 ± 0.16	2.3 ± 0.3		
69K-59K	15.4 ± 1.7	10.0 ± 0.5	1.5 ± 0.2		

c. Long Rods

Figure 5.20 shows the distribution functions at 90° for polymers possessing 118K (80 nm) rods. Once again, the distribution of molecular sizes was determined to be highly polydisperse. Table 5.21 compiles the light scattering data for this system. The 118K homopolymer data strongly suggests a completely unaggregated 80 nm rod of 20Å diameter; the calculated R_g and R_h for this structure are shown in the last two columns of the table. The diblock scatterers have only slightly larger values of R_g and R_h as compared with the homopolymer. An increase in size is understood because of the presence of the coil block although the effect cannot be quantified. The diblock data are most consistent with molecularly dispersed rods. The lower extent of association for polymers possessing longer rods was interpreted as a result of the enhanced flexibility in the rod structure as the persistence length (800 - 1000 Å) is approached. There is precedence for a decrease in aggregation number of PBLG homopolymer with increasing molecular weight. [163]

Table 5.21. Light scattering results for PI-PBLG block copolymers possessing 118K PBLG rods blocks. Dilute (0.1 wt%) block copolymer solutions in dichloromethane. Errors for R_g and R_h were calculated from error in the slopes. Calculated R_g and R_h are based on a prolate ellipsoid of model of unassociated PBLG homopolymer (L=80 nm, d=2 nm).

Polymer (PI-PBLG)	R_g, nm	R_h, nm	R_g/R_h	R_g, calc nm	R_h, calc nm
118K PBLG	22.0 ± 0.8	10.2 ± 0.2	2.2 ± 0.1	23.4	9.2
2.8K-118K	25.1 ± 1.3	12.0 ± 0.4	2.1 ± 0.1		
10K-118K	25.5 ± 1.6	12.4 ± 0.4	2.1 ± 0.1		
69K-118K	26.0 ± 0.8	12.8 ± 0.2	2.0 ± 0.1		

3. Summary of Structure in Non-Selective Solvent

The effects of rod and coil block lengths on the association of PI-b-PBLG in dichloromethane are summarized in Figure 5.21. In this solvent, the 26K and 59K PBLG-containing diblock copolymers were characterized by a relatively small size and large R_g/R_h ratio as compared with the same polymers in a rod-selective solvent (DMF). While the 26K and 59K PBLG diblock scatterers were larger than would be expected for molecularly dispersed rods, the results were consistent with the weak association reported for PBLG helices in a similar solvent, dichloroethane. [163] Indeed, this same conclusion was borne out in these results as the identical samples of 26K and 59K PBLG homopolymers were more aggregated in dichloromethane as compared with N,N-dimethylformamide based on a comparison of hydrodynamic radii. The hydrodynamic radii of these homopolymers in DMF were 1.9 nm (26K) and 3.7 nm (59K). In dichloromethane, the hydrodynamic radii were 5.48 nm (26K) and 10.5 nm (59). Both the homopolymer PBLG [125] and the PI-b-PBLG are proposed to associate end-to-end and side-by-side in this solvent because of the hydrogen bonding interactions and dipole-dipole attractions between helices. The fact that the coil block does not appear to inhibit association, but may actually participate in the process, is a striking result and not expected.

E. Coil-Selective Solvent - Experimental Results

Dilute solutions (0.1 wt%) of ten PI-PBLG diblock copolymers in a mixed solvent system of dichloromethane and heptane were studied. The stability of the structures was established with the equilibrium study in Part 1.

Part 2 of this section is concerned with the effect of molecular weight of the rod and coil blocks on the resulting structures. The effect of the composition of the mixed solvent is addressed in Part 3. The last part of this section compares theoretical predictions for the structure of rod-coil diblock copolymers in a coil-selective solvent to the experimental results for this rod-coil system.

1. Equilibrium Study

A dichloromethane/heptane mixed solvent system composed of approximately 70 wt% dichloromethane (or 55 vol% DCM) was used in this equilibrium study. Tables 5.22 and 5.23 present data for 2.8K PI-b-25K PBLG and 69K PI-b-59K PBLG, respectively, and show the stability of the size and polydispersity of the particles in this solvent system.

Table 5.22. Summary of dynamic and total intensity light scattering measurements as a function of time for the system 2.8K PI - b - 25K PBLG in dichloromethane/heptane (70:30 w/w).

Days	R_h, nm	Polydispersity	R_g, nm
1	9.1*	0.4419 ± 13.15%	27.2 ± 0.6
2	9.9*	0.3999 ± 13.00%	25.4 ± 0.8
4	7.9*	0.3694 ± 14.20%	25.6 ± 1.2
9	8.6*	0.2679 ± 10.98%	26.1 ± 0.7
Ave	8.9 ± 0.7	0.3698 ± 0.0642	26.1 ± 0.7

* Only one DLS angle measured

Table 5.23. Summary of dynamic and total intensity light scattering measurements as a function of time for the system 69K PI - b - 59K PBLG in dichloromethane/heptane (75:25 w/w).

Days	R_h, nm	Polydispersity	R_g, nm
1	16.1*	0.2528 ± 7.98%	42.8 ± 0.9
2	14.6*	0.2590 ± 12.64%	34.0 ± 0.7
6	14.6*	0.2630 ± 13.16%	34.7 ± 0.8
11	17.0*	0.2623 ± 11.96%	36.4 ± 0.9
Ave	15.6 ± 1.2	0.2593 ± 0.0040	37.0 ± 3.5

* Only one DLS angle measured

2. Effect of Block Length on Structure

The block length effect was studied in a mixed solvent of 88 wt% dichloromethane and 12 wt% heptane, equivalent to 80:20 on a volume basis.

a. Short Rods

Figure 5.22 shows distribution functions for the polymers possessing short (18 nm) rods. Two characteristics of these distribution functions are especially significant. The most obvious feature is the presence of two relaxation modes for the 69K PI-b-26K PBLG sample signifying the formation of micelles. The slow relaxation mode is attributed to the translational diffusion of the micelles, and the fast mode is due to molecularly dispersed diblocks. Table 5.24 shows that the micelles have a hydrodynamic radius of 44 nm and the unimers are 9.4 nm, in agreement with the size of the other (non-aggregating) polymers in this series. The second significant feature of

these distribution functions is the sharper distribution function for the 69K PI-b-26K PBLG sample which is also characteristic of the formation of micelles. This narrowing of the distribution function of mobilities can be understood because on average each micelle will incorporate the same fraction of each species in the solution, and therefore the micelles will be more similar to one another in size than the component molecules. In fact, the polydispersity of the "slow" mode would be even lower than the value reported which was calculated from a cumulants analysis of a single broad relaxation mode.

Only the block copolymer possessing the longest (69K) polyisoprene coil block was observed to form micelles in this solvent system. While more associated in this mixed solvent as compared with dichloromethane, the other polymers were not observed to form micelles. The hydrodynamic radii of the other diblock copolymers were approximately 10 to 15% larger in this solvent system than in dichloromethane; the 26K PBLG homopolymer was approximately double in the size in terms of the hydrodynamic radius. The enhanced driving force toward association of PBLG helices was apparently mediated by the presence of the coil blocks.

The large R_g/R_h ratios for the weakly associated diblocks and PBLG homopolymer indicate the presence of rod-like structures which are comparable in size to these 18 nm helices associated end-to-end and side-to-side. Conversely, the 69K PI-b-26K PBLG diblock appears to form large, well-defined equilibrium aggregates. Analysis of the structure of these micelles is complicated by the heterogeneity of the scattering of the diblocks in this solvent system, as discussed in the next section. It must be noted that the total scattered intensity is related to the sum of the scattered intensity from both micelles and unimers. Therefore, the measured radius of gyration was

affected by the presence of the smaller particles; the actual radius of gyration (and the R_g/R_h ratio) of the micelles was somewhat lower than that reported in Table 5.24. However, the radius of gyration measured by light scattering is a z-average, and therefore the effect of the presence of smaller scatterers on the measured Rg of the system will be less than for a linear average.

Table 5.24. Light scattering results for PI-PBLG block copolymers possessing 26K PBLG rod blocks. Dilute (0.1 wt%) block copolymer solutions in dichloromethane/heptane 88:12 w/w. Errors for R_g and R_h were calculated from error in the slopes.

Polymer (PI-PBLG)	R_g, nm	R_h, nm	R_g/R_h
26K PBLG	14.3 ± 4.8	11.1 ± 0.4	1.3 ± 0.4
2.8K-26K	24.4 ± 2.2	11.4 ± 0.8	2.1 ± 0.2
10K-26K	21.4 ± 3.6	10.6 ± 0.3	2.0 ± 0.4
69K-26K	37.1 ± 1.6	44.4 ± 5.0	0.84 ± 0.1
		9.4 ± 1.5	

b. Medium Rods

Figure 5.23 shows the dynamic light scattering results for the polymers possessing 59K PBLG rods blocks. The results show the same trends which were observed in the preceding section for the 26K PBLG copolymer. The diblock with the longest coil block (69K) was again the only polymer in the series which formed large micellar aggregates, Table 5.25. As discussed in the next section, the refractive index increments of the PI and PBLG blocks are not the same in this solvent system and therefore information on geometry

cannot be inferred simply from the measured radius of gyration. Even though the 69K PI-b-59K PBLG sample forms very large aggregates, the radius of gyration is still too small to affect non-linearity in the particle scattering form factor.

Non-linearity in $P^{-1}(\theta)$ for the 59K PBLG homopolymer sample was observed, the shape of which was typical of rod-like scatterers, Figure 5.24. The inverse particle scattering function for 59K PBLG in the mixed solvent becomes non-linear and approaches a plateau for $q^2R_g^2$ larger than approximately 1.9. Deviations from linearity in the particle scattering factor for the weakly associated diblock samples, although rod-like in shape, were not observed since the scatterers were relatively small.

Table 5.25. Light scattering results for PI-PBLG block copolymers possessing 59K PBLG rod blocks. Dilute (0.1 wt%) block copolymer solutions in dichloromethane/heptane 88:12 w/w. Errors for R_g and R_h were calculated from error in the slopes.

Polymer (PI-PBLG)	R_g, nm	R_h, nm	R_g/R_h
59K PBLG	41.1 ± 3.7	10.7 ± 0.3	3.8 ± 0.4
2.8K-59K	34.0 ± 2.1	11.6 ± 0.4	2.9 ± 0.2
10K-59K	24.6 ± 3.9	11.4 ± 0.5	2.2 ± 0.4
69K-59K	34.3 ± 1.0	70.3 ± 4.4	0.49 ± 0.03

c. Long Rods

Figure 5.25 shows that the 118K PBLG-containing polymers do not behave very differently in this coil-selective solvent as compared with their

behavior in the non-selective solvent (dichloromethane). There appears to be a lack of tendency for these polymers to aggregate into micelles or even to associate more strongly than in dichloromethane, as shown in Table 5.26. The polymers are best represented as rods composed of unimers or end-aggregated dimers, Table 5.6. These helices are expected to have a semi-flexible character since their length (81 nm) is near the persistence length for PBLG (80-100 nm). [125]

Table 5.26. Light scattering results for PI-PBLG block copolymers possessing 118K PBLG rod blocks. Dilute (0.1 wt%) block copolymer solutions in dichloromethane/heptane 88:12 w/w. Errors for R_g and R_h were calculated from error in the slopes.

Polymer (PI-PBLG)	R_g, nm	R_h, nm	R_g/R_h
118K PBLG	25.3 ± 2.3	10.5 ± 0.8	2.4 ± 0.3
2.8K-118K	27.9 ± 2.2	13.6 ± 0.3	2.1 ± 0.2
10K-118K	28.3 ± 1.9	12.5 ± 0.6	2.3 ± 0.2
69K-118K	31.4 ± 1.3	13.8 ± 0.7	2.3 ± 0.2

3. Effect of Solvent Composition on Structure

The solvent composition for the dichloromethane and heptane mixed solvent system was found to have a profound impact on the size and structure of the diblock aggregates. Understandably, this effect was found to be most dramatic for the two diblock copolymers which were able to form large micellar aggregates. Increasing the percentage of heptane in the mixed

solvent caused the solvent to become increasingly more selective for the coil by virtue of becoming increasing poorer for the PBLG rod. It was determined from early studies using 69K PI-b-59K PBLG that the copolymer was only soluble in a mixed solvent containing less than 30 wt% heptane. The miscibility window was subsequently determined to support a range of aggregate structures, Table 5.27.

The structures increase in R_h from 10 nm in the non-selective solvent (100% dichloromethane) and reach a maximum in size at approximately 88 wt% dichloromethane, which corresponds to the midpoint of the miscibility window for this diblock. In addition, the ratio of R_g to R_h decreased with increasing size of the aggregates. The latter trend agrees with the transformation from prolate to oblate ellipsoids with increased aggregation number. Small structures were observed in mixed solvents with more than 12 wt% heptane. The reason for this discontinuous decrease in aggregate size is not well understood. The best explanation is that the polymer was not completely solvated in the heptane-rich solutions; the solutions may be inhomogeneous with polymer adsorbed on to the cuvette walls or partially precipitated. If this were the case, the concentration of polymer in the solution would be greatly reduced and possibly below the critical micelle concentration. The dynamics of the soluble polymer component would then be understood as resulting from molecularly dispersed or weakly aggregated diblock copolymer in agreement with the discontinuous change in R_g/R_h at 84 wt%.

Table 5.27. Effect of solvent composition on the aggregation of 69K PI-b-59K PBLG in a mixed solvent of dichloromethane and heptane.

DCM:Heptane w / w	R_g, nm	R_h, nm	R_g/R_h
100	17.8 ± 1.2	10.0 ± 0.5	1.9 ± 0.2
96:4	38.5 ± 1.5	35.3 ± 4.4	1.3 ± 0.2
92:8	39.3 ± 1.8	47.9 ± 4.5	0.85 ± 0.09
88:12	34.3 ± 1.0	70.3 ± 4.4	0.60 ± 0.07
84:16	36.5 ± 1.5	12.9 ± 0.5	3.3 ± 0.2
80:20		11.3 ± 0.2	
75:25		15.6 ± 1.2*	
71:29		14.1 ± 0.4	

* Error based on standard deviation from 4 measurements at a single angle

4. Analysis of Structure

a. Refractive Index Increment

The refractive index increment was measured for polyisoprene and two PI-b-PBLG polymers in 88:12 w/w dichloromethane/heptane solution. Table 5.28 shows the results of these measurements where the refractive index increment of PBLG was calculated according to Eqn. 5.23. A mixed solvent in which the components possess dramatically different solubilities makes an extremely experimentally challenging system especially in terms of measuring the refractive index increment. The measurement, described in Chapter IV, requires the precise positioning of the sample cells. The wavelength precision requires that the cells remain fixed during the

experiment and the solutions in the cells exchanged. This means that the solutions cannot be sealed but rather are in contact with the air during the experiment. This was the situation for the mixed solvent of dichloromethane and heptane. Even though the error in these measurements was increased, the data nevertheless indicated that the refractive index increments of polyisoprene and PBLG in this solvent were significantly different.

Table 5.28. Refractive index increments measured in a mixed solvent of dichloromethane/heptane (88:12 w/w) at 633 nm and room temperature.

Polymer (PI-PBLG)	$(dn/dc)_{total}$	$(dn/dc)_{PBLG,\,calc}$
10K PI	0.119 ± 0.004	--
69K-b-26K	0.122 ± 0.011	0.177 ± 0.013
69K-b-118K	0.183 ± 0.006	0.217 ± 0.006

Refractive index increments only affect the measured (apparent) radii of gyration and not the hydrodynamic radii. The apparent radius of gyration is related to the refractive index increments of the scattering centers and also to the structure of the scatterer. This structural dependence can be used to compare the scattering from the micelles to various models via the following relation: [54, 159]

$$R_{g,cal}^{\,2} = R_{g,A}^{\,2} W_A (dn/dc)_A/(dn/dc) + R_{g,B}^{\,2} W_B (dn/dc)_B/(dn/dc) + \Delta^2 (dn/dc)_A (dn/dc)_B W_A W_B /(dn/dc)^2 \quad (5.24)$$

where $R_{g,A}$ and $R_{g,B}$ are the radii of gyration of the A and B blocks, respectively, and W_A and W_B are their mass fractions. The refractive index increments for A, B, and the AB copolymer are represented by $(dn/dc)_A$, $(dn/dc)_B$, and (dn/dc), respectively. Finally, the distance between the centers of mass of the materials is given by Δ. The simplest model is a concentric core-shell model for which Δ reduces to zero. The core is assumed to be composed of a either a monolayer or a bilayer of axially-packed rods such that the length is either L or 2L, respectively, and the width is also L or 2L so that the core approximates a sphere, as depicted in Figure 5.26. Furthermore, the model assumes that the polyisoprene coils fan out into the solvent and form two hemispherical shells. The results of these two models for the two diblocks which formed micelles in the mixed solvent are shown in Table 5.29. The core radii of gyration were calculated from the following equations: [159]

$$R_{g,\,core} = (3/5)^{1/2}\, R_c \qquad (5.25)$$

$$R_{g,\,shell} = (3/5)^{1/2}\, ((R_h^5 - R_c^5)/(R_h^3 - R_c^3))^{1/2} \qquad (5.26)$$

where R_c is the radius of the core. Qin et al. [159] used this type of analysis to understand the low R_g/R_h ratios (0.37-0.64) in their PS-b-PMAc (dioxane: water 80:20 v:v) system as being due to the presence of the more strongly scattering PS block in the core of the spherical micelle which causes a lowering of $R_{g,\,eff}$.

The monolayer concentric sphere model shows excellent agreement with the measured radius of gyration for the 69K-b-59K sample. The monolayer model allows the dipoles to arrange antiparallel to one another; this is an attractive interaction. The bilayer model requires parallel helices;

this will result in a contribution due to dipole-dipole repulsions. However, *a priori* the relative stability of monolayer and bilayer micelles cannot be assessed because in addition to dipole-dipole interactions, there are differences between the micelles in terms of interfacial energies. The bilayer micelle would have a lower repulsive interaction energy contribution due to better rod/coil segregation, as discussed by Williams and Fredrickson for rod-coil diblock melts. [70] The shell thicknesses calculated for the monolayer model is 50 nm.

Table 5.29. Calculation of apparent radii of gyration for concentric sphere models of micelle formation in a coil-selective solvent.

			Monolayer Core		Bilayer Core	
PI-b-PBLG	Rh, nm	Rg, nm	Rc	Rg, cal	Rc	Rg, cal
69K-26K	44.4 ± 5.0	37 ± 1.6	9	26	18	28
69K-59K	70.3 ± 4.4	34 ± 1.0	20	32	40	41

The 69K-b-26K micelles, however, are not as well-described by a concentric sphere model. The experimentally measured radius of gyration was approximately 25% larger than the calculated radii of gyration. This implies that either the core and/or corona are poorly approximated as spherical or the centers of mass of the polyisoprene and PBLG regions are spatially separated ($\Delta \neq 0$). In the first case, the micelles could be more rod-like ($d < L$) or disk-like ($d > L$), as shown in Figure 5.27. Most likely, there are *three* scattering centers for this system, one PBLG core region and two end-flanking polyisoprene core regions, Figure 5.27. There are many models

which will give the measured hydrodynamic radius for this system (44.4 nm). For example, an oblate ellipsoid of diameter 100 nm and length 80 nm has a calculated R_h of 46.6 nm. There are four basis micelle structures, two monolayer core and two bilayer core structures, which could have such a shape, as shown in Figure 5.27. Exact elucidation of structure is not possible at this point. Future work shoud be aimed at determination of core and coronal dimensions through more direct measurements such as neutron scattering or light scattering from contrast and index matching solvents, respectively, for both the core and corona.

b. Comparisons to Theoretical Predictions

The model described above for the 69K-b-26K diblock is interesting because when compared with the concentric sphere model for the 69K PI-b-59K PBLG diblock, two scaling relations for rod-coil diblocks in a coil-selective solvent are elucidated which agree with theoretical predictions. [77] The core radius scales with the square root of the rod length and the coronal height scales approximately with the fifth root of the rod length. However, the predictions for the relative lengths of rod and coil blocks which will form stable micelles (Eqn. 5.15) do not agree with the experimental findings. All of the diblocks, with the exception of 69K PI-b-26K PBLG, possess block lengths within the range predicted to form stable star-like micelles. Table 5.30 lists an asterisk by the diblocks which are predicted by Eqn. 5.15 to form micelles. As discussed previously, *only* this diblock and 69K PI-b-59K PBLG formed micelles in the solvent system studied. The most important factor in producing stable micelles appears to be the presence of long coils. The coil

overlap limit ($N_A << N_B^{4/3}$) [77] is too restrictive; longer coils are still able to explore the area along the edges of the rod core.

Table 5.30. Comparison of block lengths to theoretical predictions of stability limits for rod-coil micelles in coil-selective solvents.

Polymer (PI-PBLG)	N_A	N_B	$N_B^{4/3}$	$N_B^{1/2}$	
2.8K-25K	41	114	553	11	*
2.8K-26K	41	119	585	11	*
10K-26K	147	119	585	11	*
69K-26K	941	119	585	11	
2.8K-59K	41	269	1736	16	*
10K-59K	147	269	1736	16	*
69K-59K	941	269	1736	16	*
2.8K-118K	41	539	4387	23	*
10K-118K	147	539	4387	23	*
69K-118K	941	539	4387	23	*

5. Summary of Structure in Coil-Selective Solvent

The coil-selective solvent chosen for this PI-b-PBLG system was a mixed solvent of dichloromethane and heptane. The size and structure of aggregates in this coil-selective solvent were dependent on the lengths of the rod and coil blocks as well as the composition of the mixed solvent. Only two of the ten diblocks studied formed micelles in a mixed solvent of 88:12 w/w dichloromethane/heptane: 69K PI-b-26K PBLG and 69K PI-b-59K PBLG. The ability to form micelles was attributed to the large coil blocks which are able to explore the volume far away from the core. As the distance away from the core, r, increases the chains are able to explore cone-shaped regions in which

the volume increases with r^{3}. [70] Close to the core, the chains are confined to cylindrical regions by the presence of adjacent chains and the volume scales only as r^{2}. The entropy loss due to micellization is therefore decreased as the coil block length increases.

It follows from this discussion that the 69K PI-b-118K PBLG diblocks should form micellar aggregates. Aggregation was not observed for the diblocks possessing the long (118K) PBLG rods in any of the three solvent systems studied throughout this chapter. This is attributed to the fact that the length of the rod (81 nm) is near the persistence length of the molecule and therefore the rigidity of the rod will be decreased. A rod with semi-flexible character, such as this, may not pack with the same degree of order as purely rigid rods.

The choice of the coil-selective solvent has a great influence on the size and structure of the micelles which form. The majority of the diblocks did not form micelles and their size simply increased in terms of R_g and R_h as compared with the results in dichloromethane as the solvent selectivity was increased (by adding heptane). On the other hand, the micelle-forming diblocks underwent a dramatic transition upon changing solvent composition. Addition of heptane made the solvent more selective and resulted in progressively larger aggregates in terms of both R_g and R_h. The hydrodynamic radius of the diblock ranged from 10 nm in 100% dichloromethane to a maximum radius of 70.3 nm at 88 wt% dichloromethane to a radius of 14.1 nm at 71 wt% dichloromethane. The inability of the 69K-26K diblock to form micelles in solutions of greater than 12 wt% heptane was correlated with the onset of macroscopic dissolution at 30 wt% heptane.

Figure 5.28 summarizes the hydrodynamic radii and R_g/R_h ratios for the ten diblocks in 88:12 w/w dichloromethane/heptane. The most likely micelle structures for the 69K PI-b-26K PBLG diblock are illustrated schematically in Figure 5.27. The apparent radius of gyration for the 69K-b-59K micelle was consistent with the model of a concentric "sphere" in which the measured refractive index increments of the core and corona were incorporated. The spherical micelle was constructed from a cylindrical core of equal height and diameter flanked by a corona of two hemispherical corona regions. The micelles formed by this diblock were modeled as a sphere with radius 70 nm and either a monolayer core (20 nm) or a bilayer core (40 nm). The monolayer structure allows the antiparallel arrangement of helices which is favored by the dipole-dipole interaction. The bilayer structure, which requires the parallel arrangement of helices, has the advantage of segregating the rods and coils more completely. The energetically more favorable structure is therefore related to the magnitude of the interaction parameter.

The model for the 69K PI-b-26K PBLGmicelle was based on the fact that the concentric sphere model indicated that there was a difference in the locus of centers of mass of the polyisoprene and PBLG regions. Four models which incorporate this effect as well as the measured hydrodynamic radius have been proposed. These are monolayer and bilayer oblate and prolate ellipsoids with dimensions 80 nm by 100 nm, depicted in Figure 5.27.

F. Conclusions

This chapter has demonstrated the dramatic influence of block rigidity on the microstructure formation for block copolymers. While most of the

rod-coil block copolymers studied were able to form large, well-organized spherical micelles in a rod-selective solvent, aggregation in coil-selective solvents was much more sensitive to the characteristics of each block copolymer. Only two PI-b-PBLG samples were able to form micelles in the coil-selective solvent. Micellization was attributed to the long coil blocks which were able to explore the additional volume far from the core region. In addition, the composition of the coil-selective mixed solvent was important in the structure evolution. In the limit of pure dichloromethane, the non-selective solvent was reached. In this solvent, each block favors intimate contact with the solvent and non-aggregated or weakly aggregated diblocks were observed. Mild aggregation of the PBLG helices was anticipated in this solvent but does not mask the main conclusion: this solvent suppresses micelle formation and serves as a control for studying micellization in rod-selective and coil-selective solvents.

In the rod-selective solvent, N,N-dimethylformamide, self-assembly led to unusual, star-like arrangements of rods tethered by extended polyisoprene cores. The mutual alignment of the α-helices resulted in a repulsion between the micelles which heralds the potential usefulness of tethered α-helix rods for colloidal stabilization. Another potential application for these rigid-rod stars, besides as supramolecular building blocks, is for material reinforcement. These structures have rods oriented in all directions which will provide isotropic reinforcement.

In the coil-selective solvent, the formation of a typical spherical core geometry is frustrated by the rigidity of the poorly solvated blocks. Cylindrical cores in which rods pack axially, either as monolayers or bilayers, are proposed. Cylindrical arrangements can mimic spherical cores if the height is equal to the diameter. This type of structure is predicted for the 69K PI-b-59K

PBLG sample. The flexible chains can further mimic a spherical corona by forming two hemispherical caps. The other micelle-forming diblock, 69K PI-b-26K PBLG, forms less symmetrical micelles with disk-like or rod-like cores and more extended coronal caps.

Reproducible, varied, and well-defined structures self-assemble from PI-PBLG rod-coil diblock copolymers in solution. These unique structures which are molecular weight and solvent dependent and presumably also dependent on the chemical identity of the rod-coil diblock are expected to be useful as molecular building blocks. Once formed, appropriate chemistry could be used to "stitch-up" the core blocks and even the corona blocks to produce static structures. Cross-linking would be a trivial route toward "stitching" of polyisoprene regions and other chemistry is currently being investigated in the pursuit of linking PBLG helices. [164] The potential and motivation for studying rod-coil block copolymers in solution are substantial.

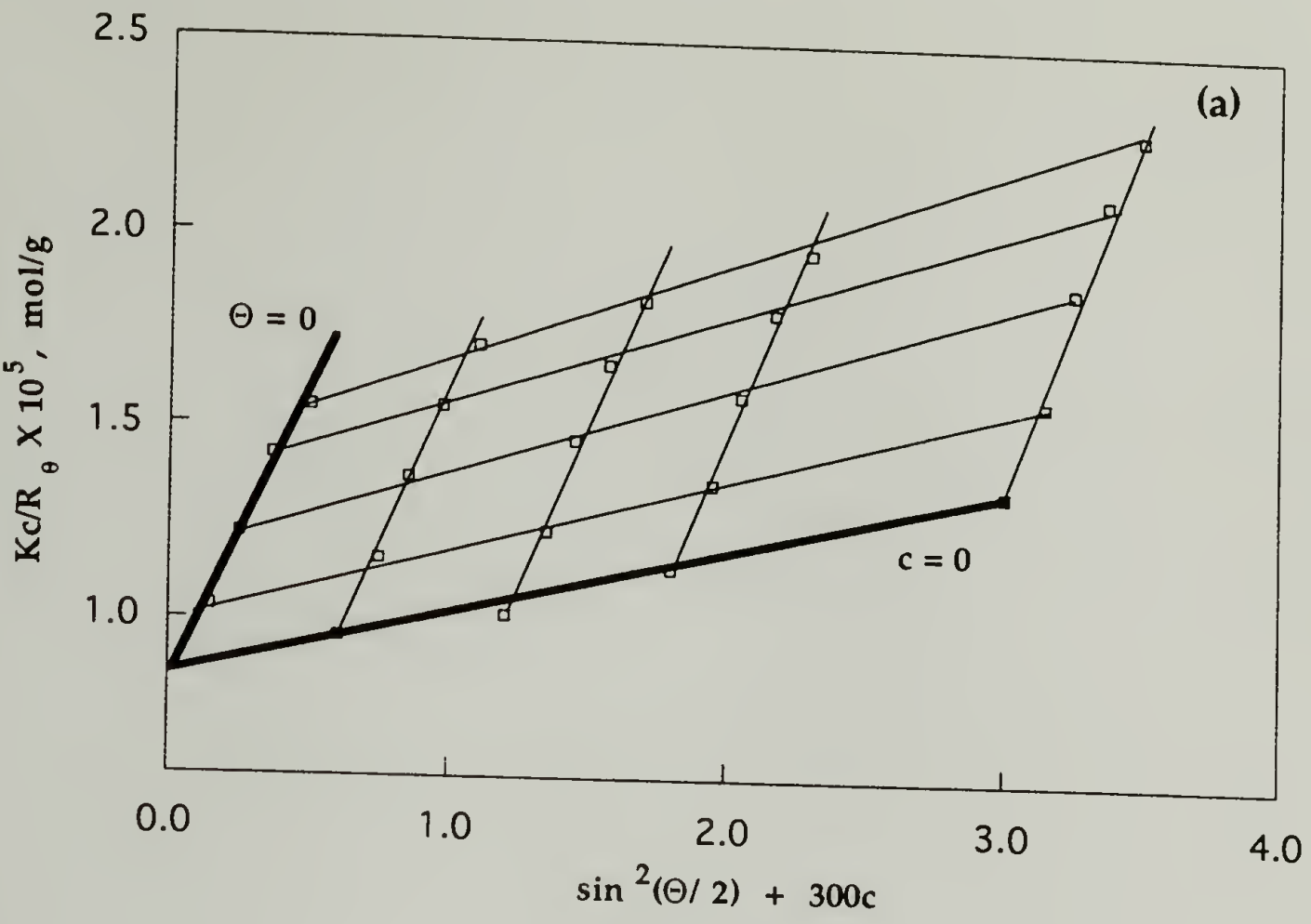

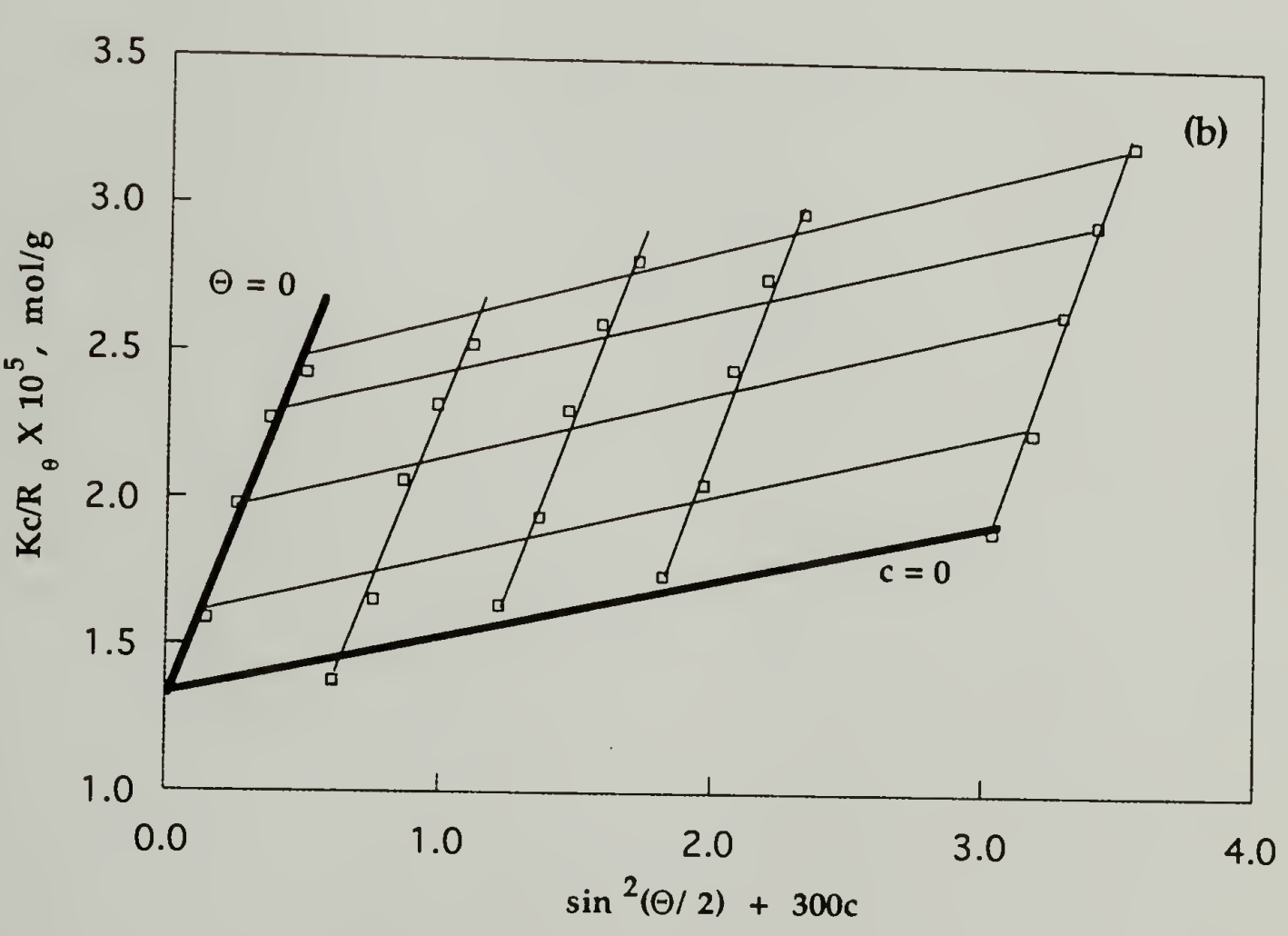

Figure 5.3. Zimm plots for (a) 118K PBLG homopolymer and (b) 2.8K PI-b-25K PBLG diblock in DMF. Concentrations were 10.1, 6.1, 4.0, and 2.0 mg/ml.

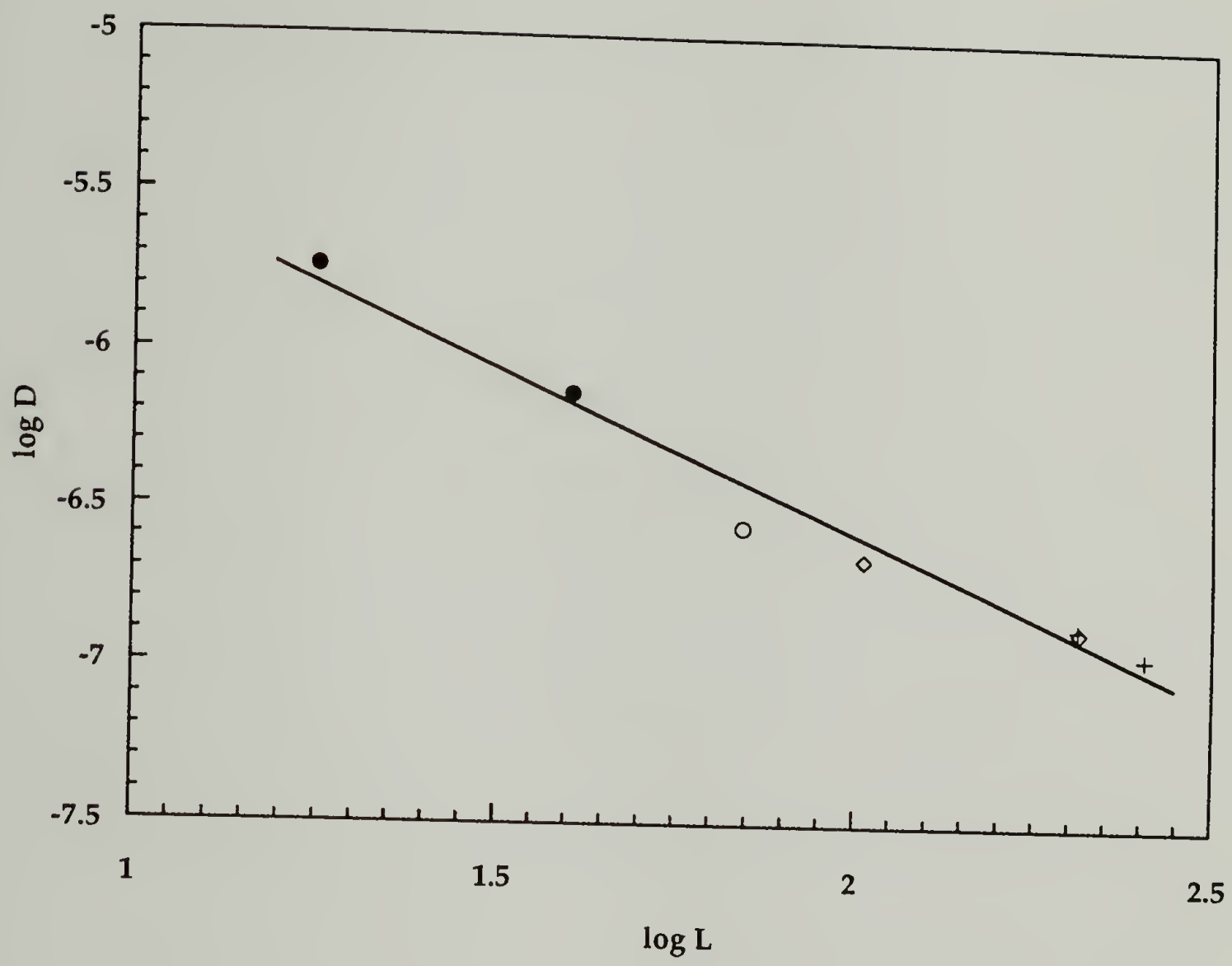

Figure 5.4. Comparision diffusion coefficient of PBLG in DMF with literature values. Symbols: this work (filled circles), Kubota, et al. [99] (+), Russo, et al. [97] (open circles), and Tracy and Pecora [96] (diamonds).

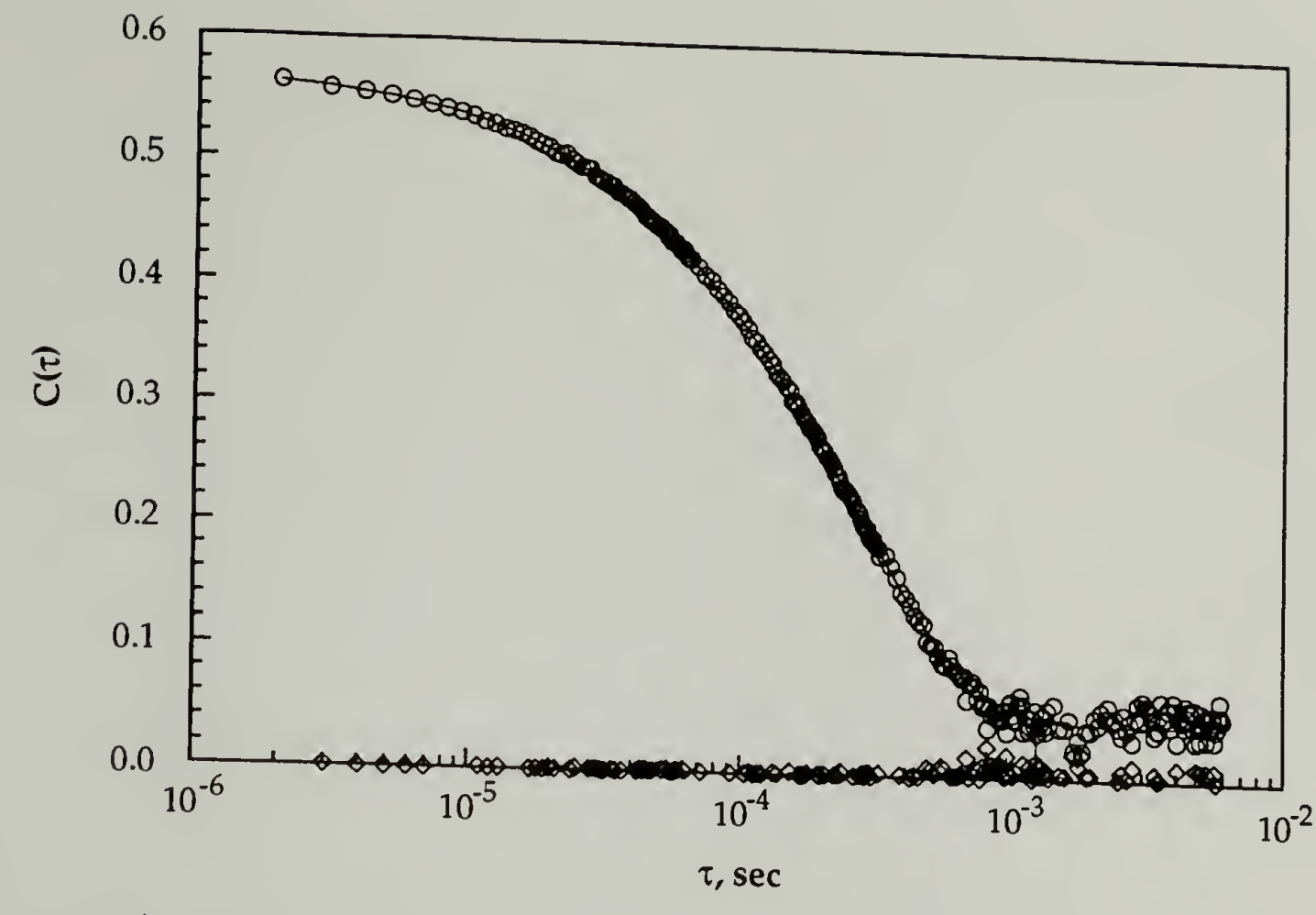

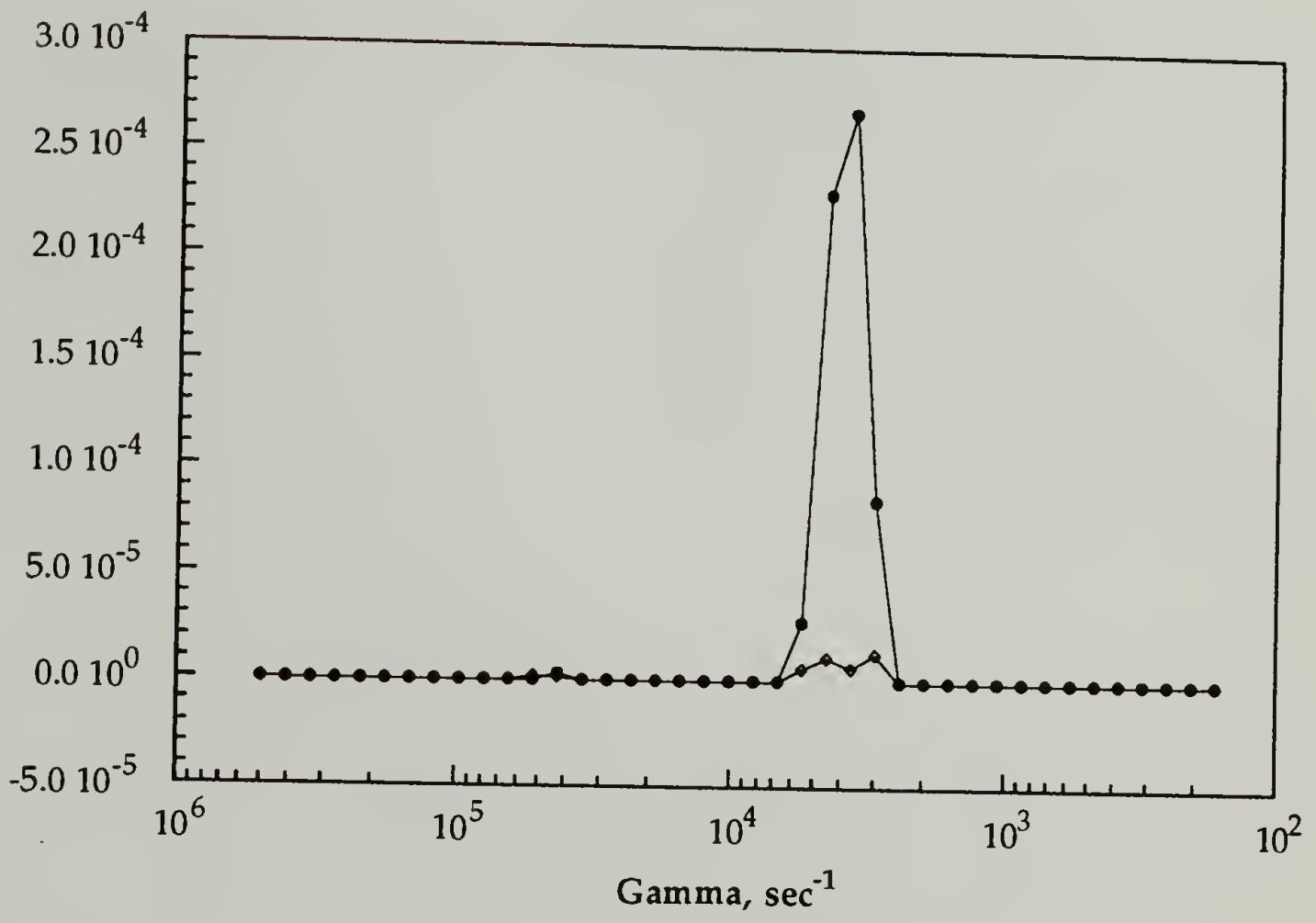

Figure 5.5. Typical dynamic light scattering results. Top plot shows the measured correlation function for the sample 10K PI-b-26K PBLG in DMF (open circles), the calculated fit (solid line), and the residuals to the fit (diamonds). The calculated distribution function resulting from this fit is shown in the lower plot.

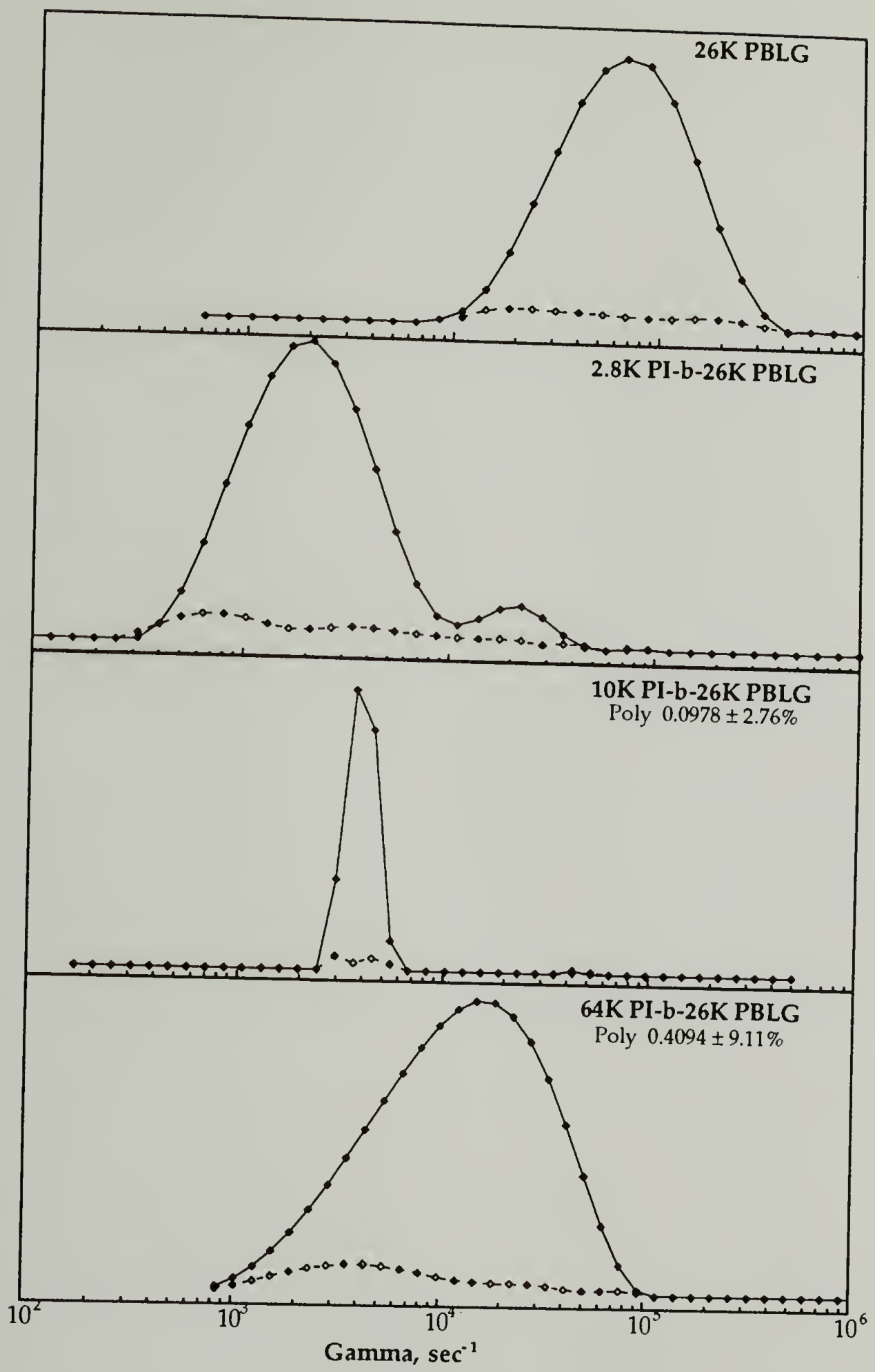

Figure 5.6. Effect of coil block size on distribution functions for block copolymers possessing short (18 nm) rod blocks in anhydrous N,N-dimethylformamide. Distribution functions calculated for scattering at 90°.

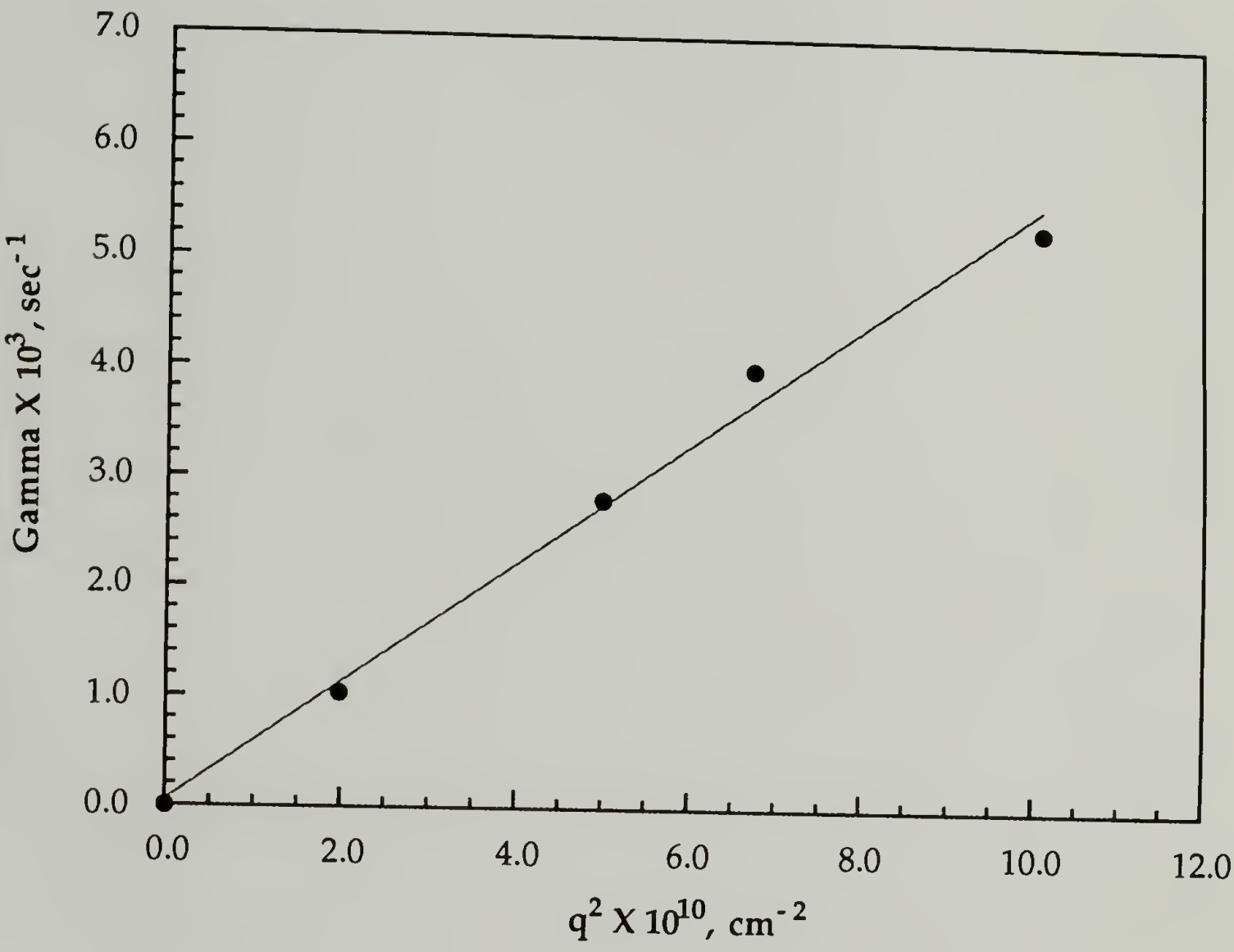

Figure 5.7. Representative plot of the relaxation rate versus the square of the scattering vector where the slope equals the translational diffusion coefficient. Data shown for 10K PI-b-26K PBLG in N,N-dimethylformamide.

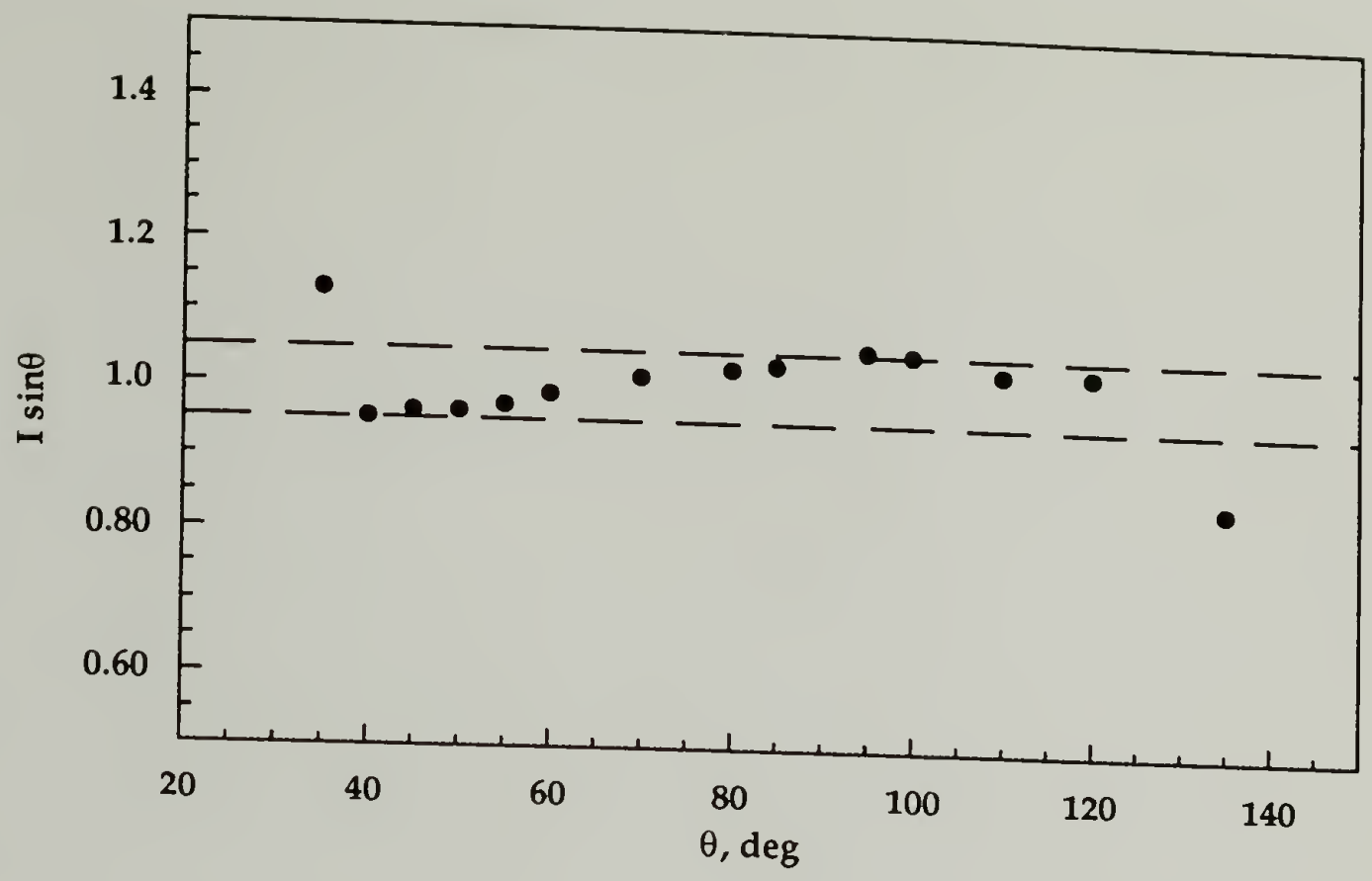

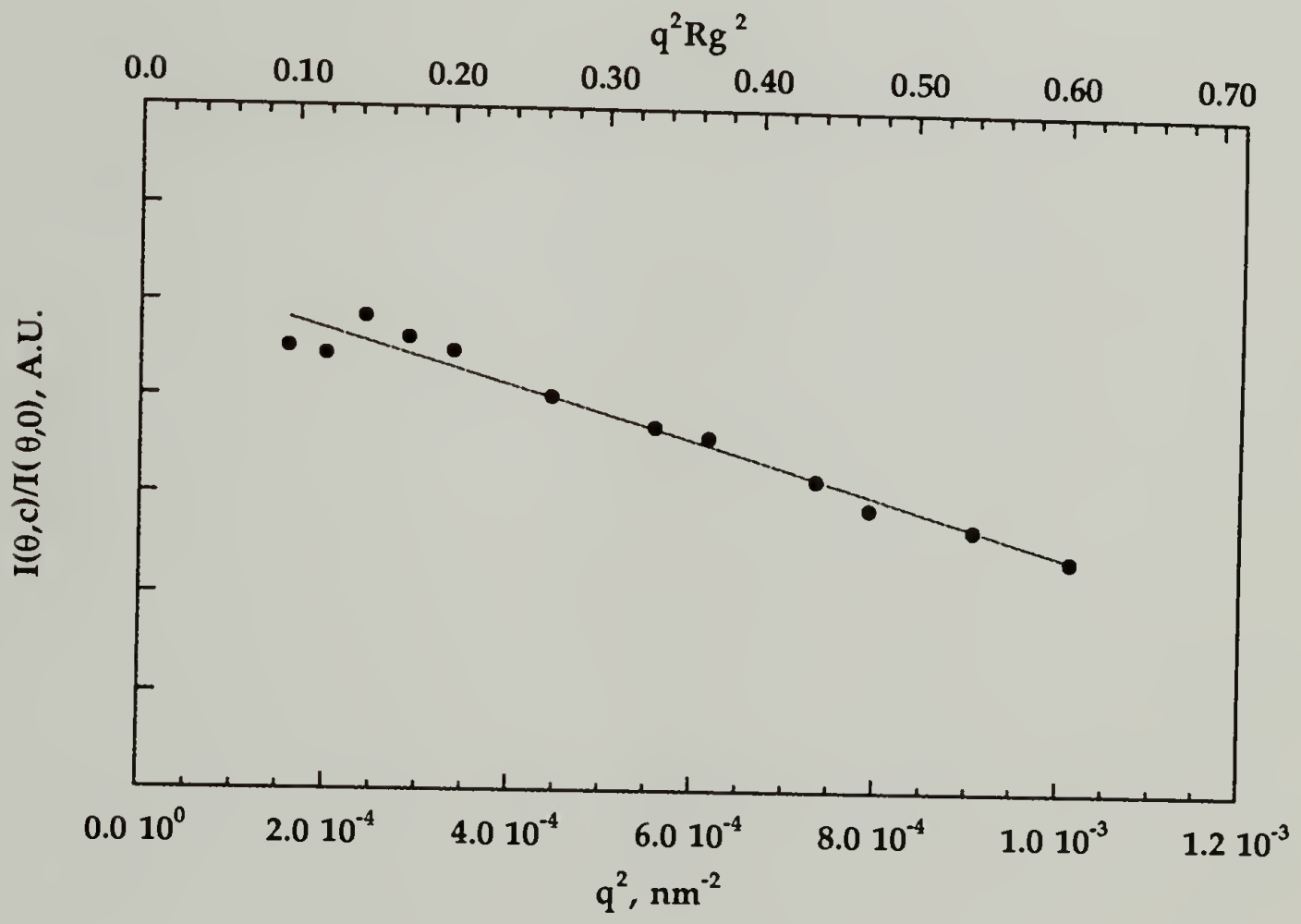

Figure 5.8. Representative plot of the particle scattering factor versus q^2 where the slope is related to the radius of gyration of the scatterers. Data shown for 10K PI-b-26K PBLG in N,N-dimethylformamide. Top plot shows anamolous scattering from the solvent at the lowest and highest angles (45° and 135°).

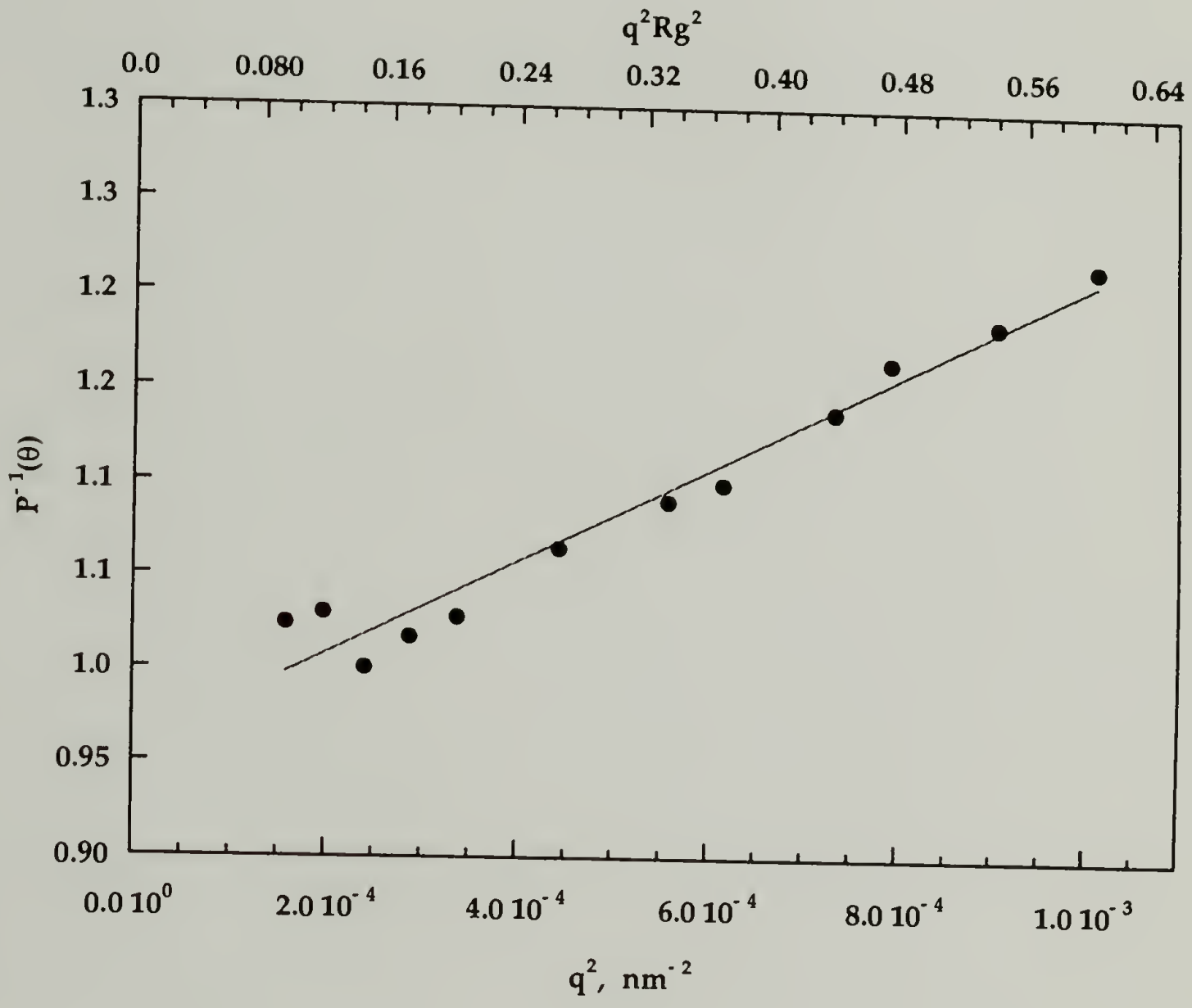

Figure 5.9. Typical plot of the reciprocal particle scattering factor as a function of q^2. Data shown for 10K PI-b-26K PBLG in N,N-dimethylformamide. Linearity in the plot is a result of the relatively small size of the scatterers, $qR_g < 1$.

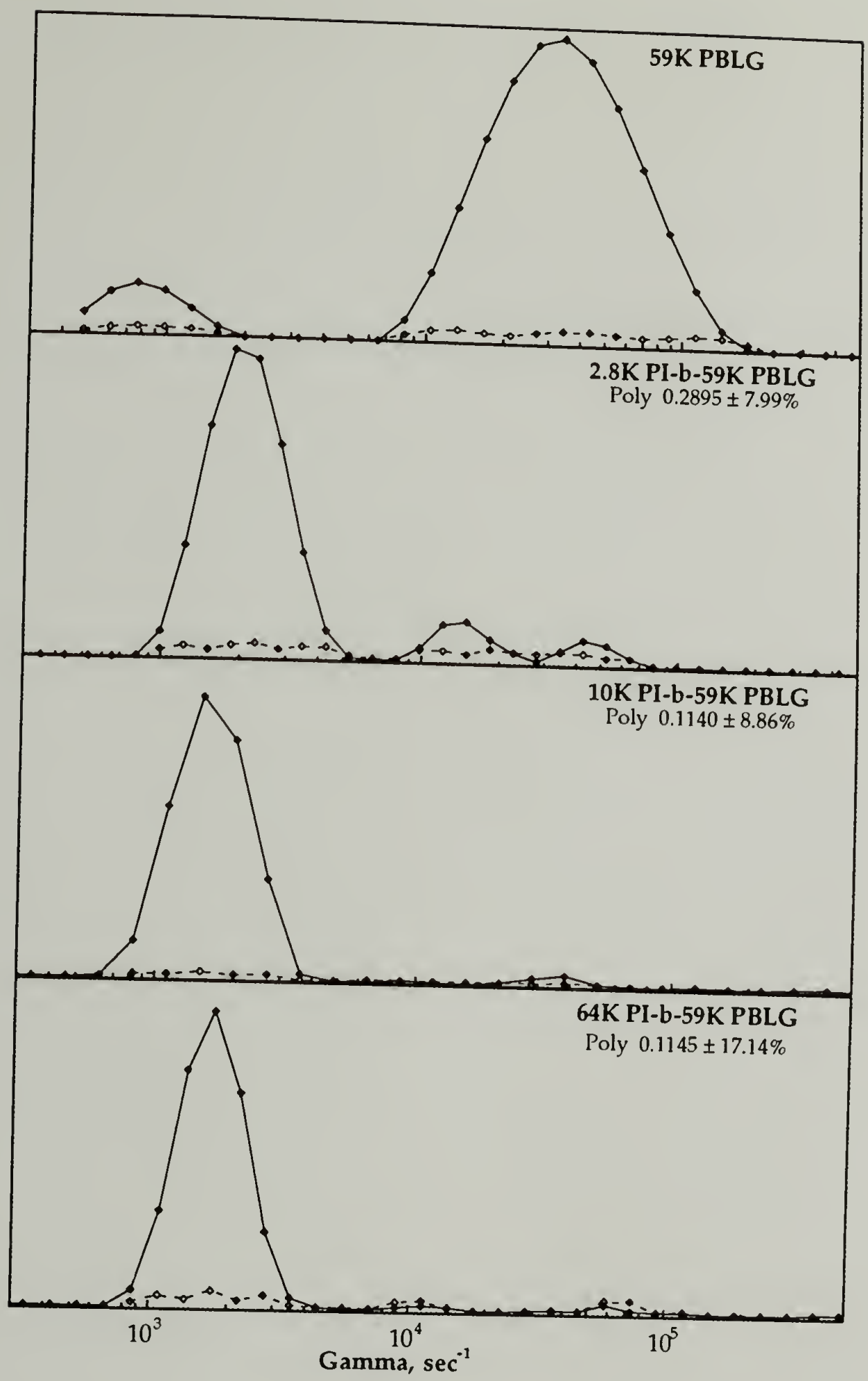

Figure 5.10. Distribution functions at 90° for polymers with medium length rods (59K PBLG, 40 nm) connected to various size polyisoprene coils. Measured for dilute (0.1 wt%) solutions in anhydrous N,N-dimethylformamide.

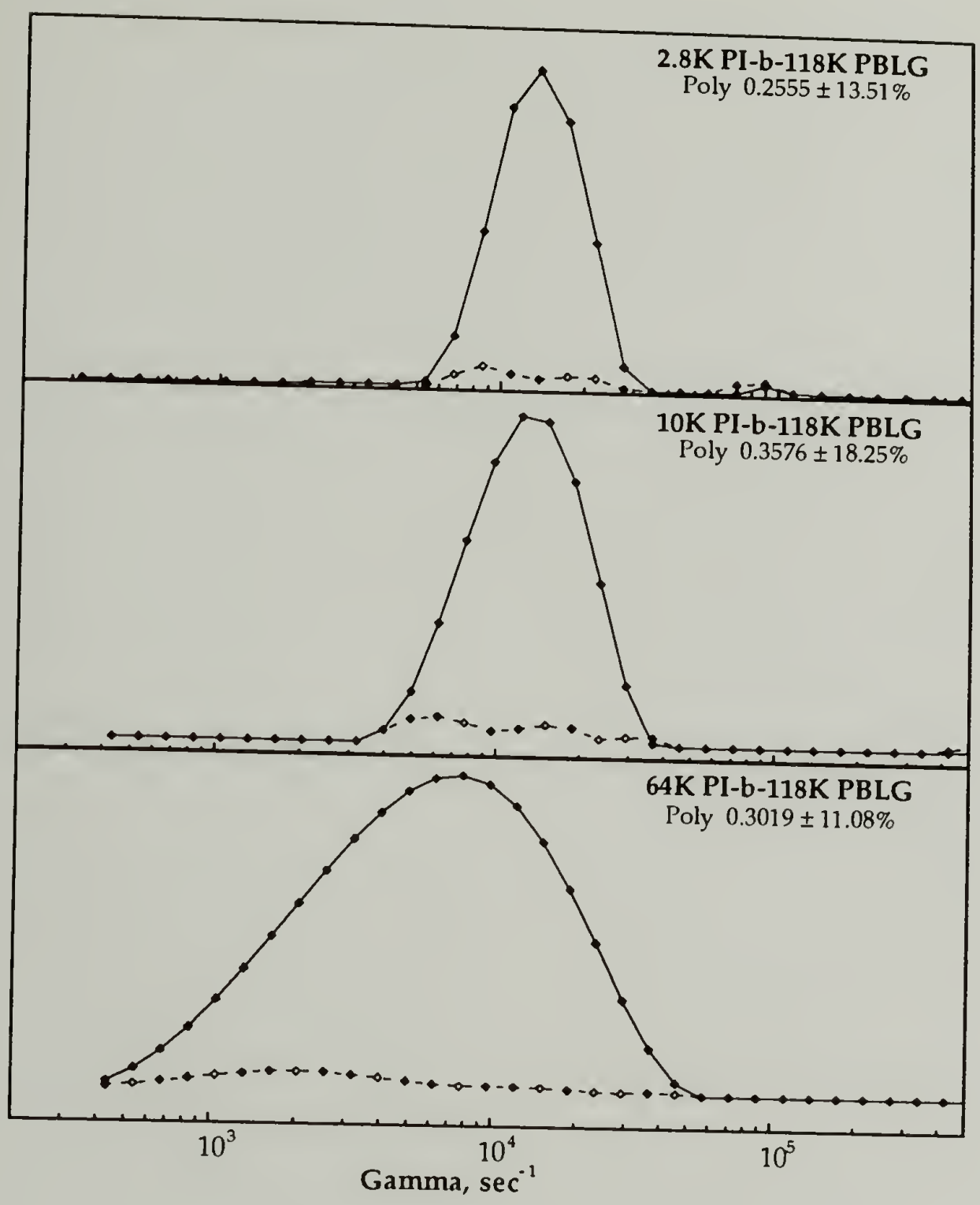

Figure 5.11. Dynamics of polymers with 118K rod blocks in N,N-dimethylformamide. Distribution functions shown for scattering at 90°.

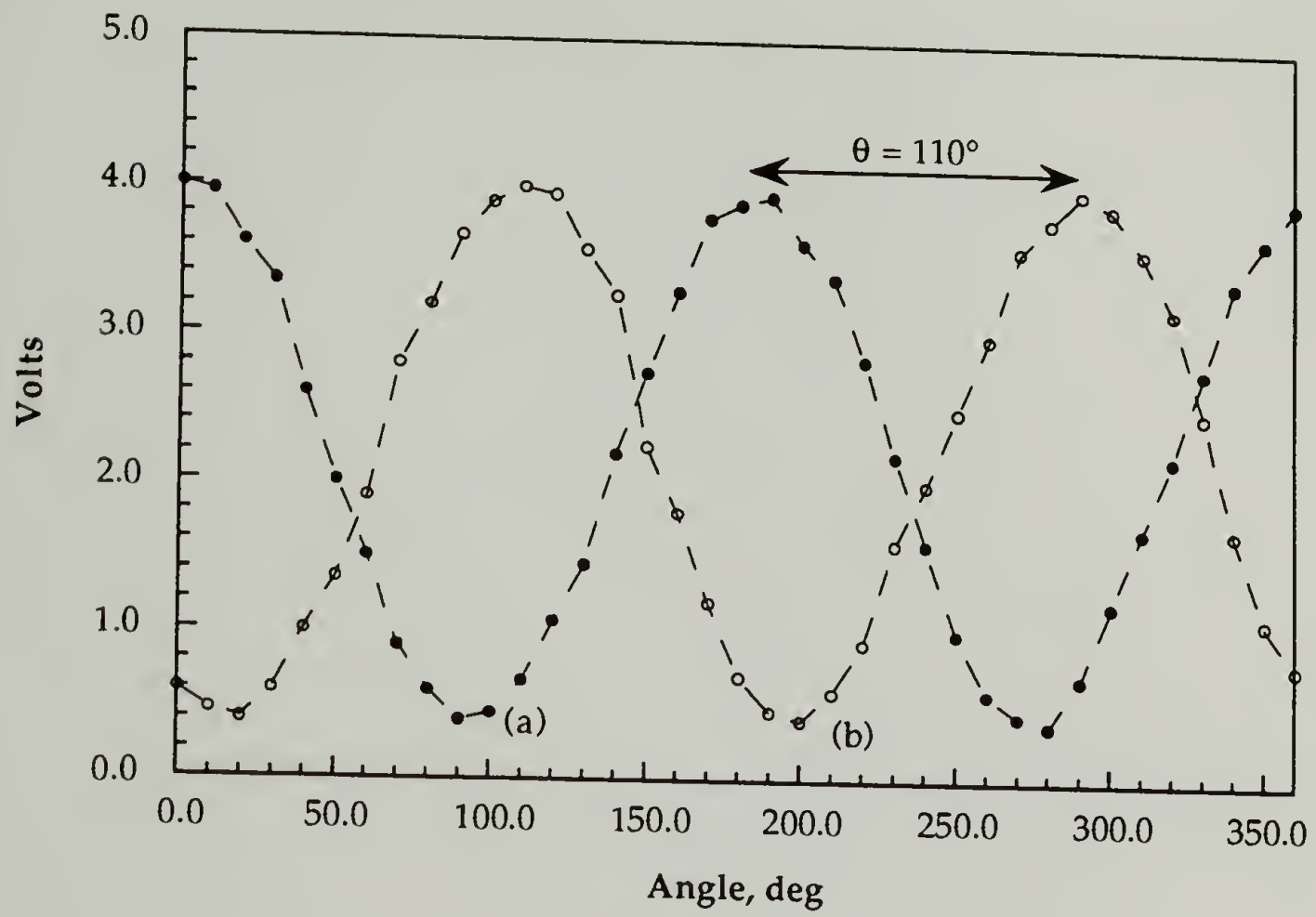

Figure 5.12. Determination of the phase shift, θ, for 69K PI-b-118K PBLG in anhydrous N,N-dimethylformamide. Curve (a), solvent in both cells; Curve (b), 0.002 g/ml in one cell and solvent in the other.

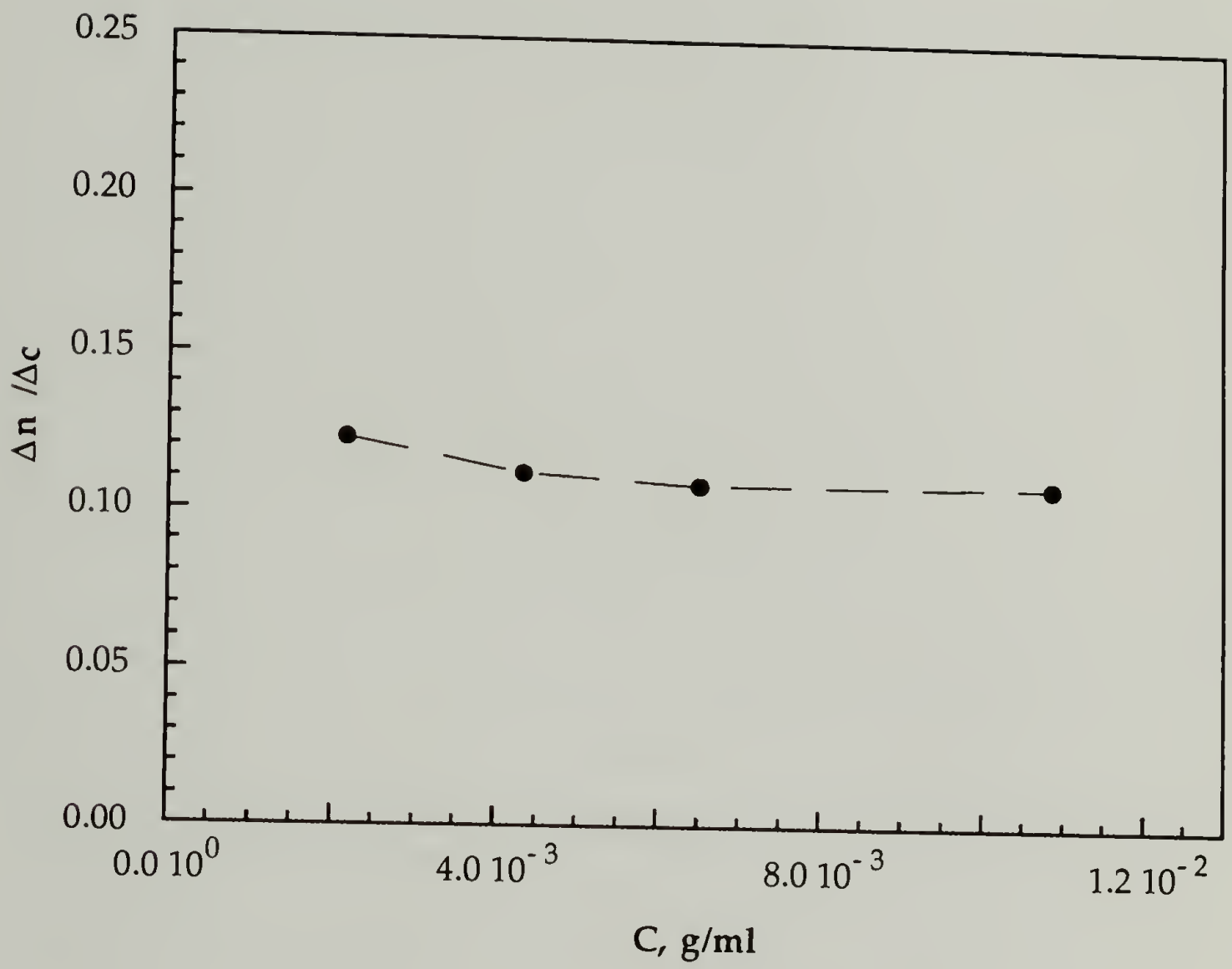

Figure 5.13. Incremental contributions to the refractive index increment for 69K PI-b-118K PBLG in anhydrous N,N-dimethylformamide.

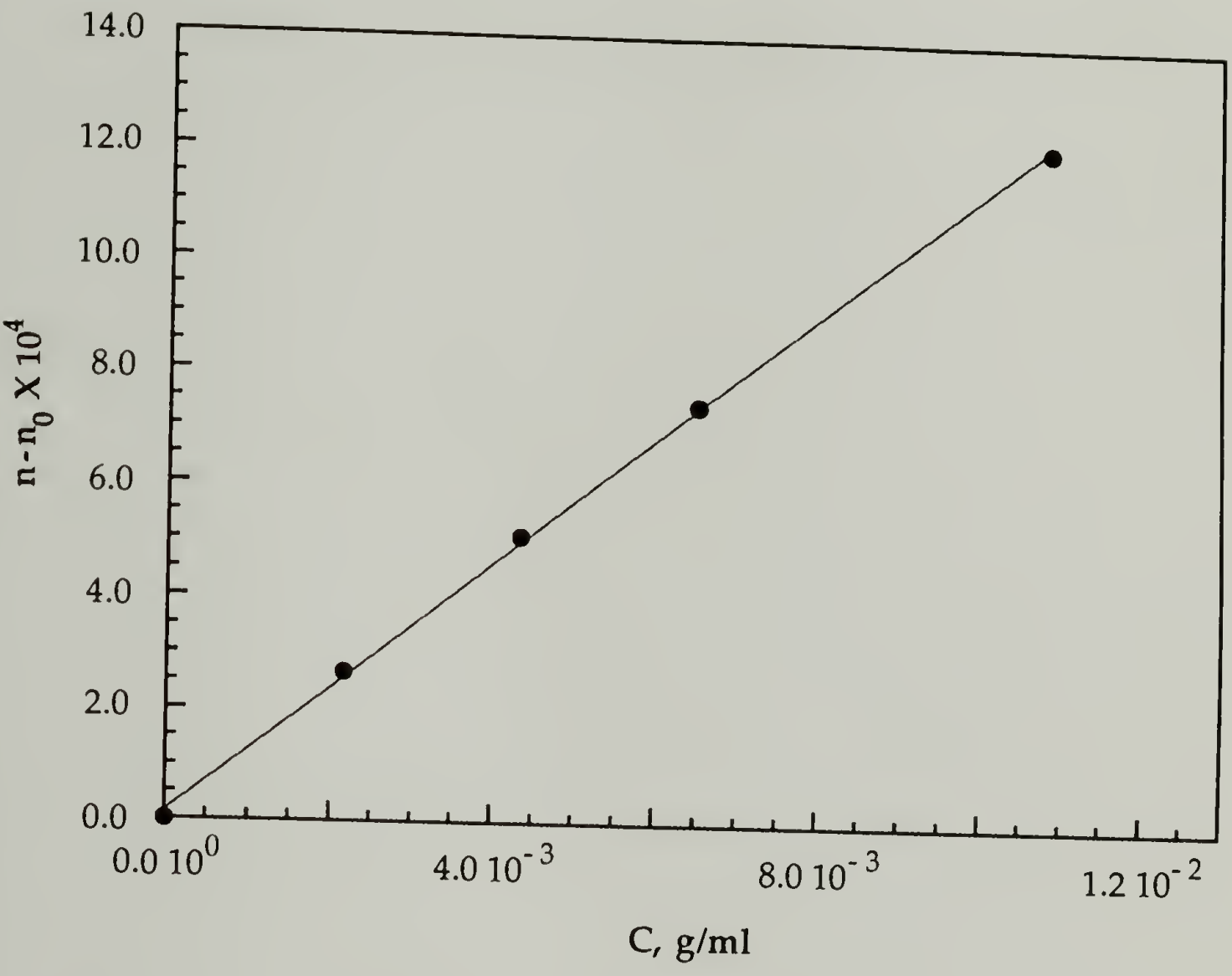

Figure 5.14. Cumulative refractive index as a function of concentration for 69K PI-b-118K PBLG in anhydrous N,N-dimethylformamide. The slope of the curve equals dn/dc.

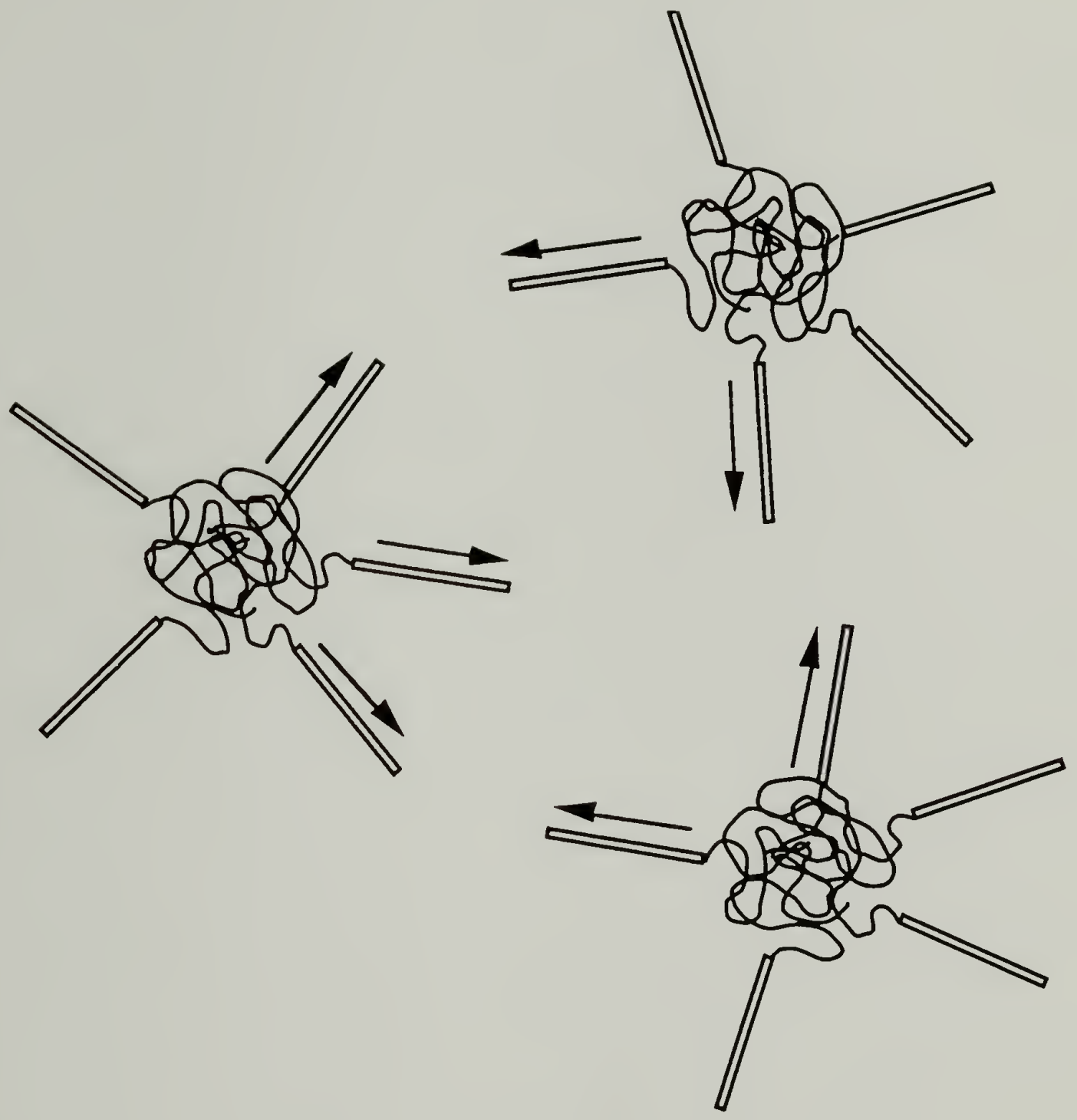

Figure 5.15. Proposed structure of the micelles in N,N-dimethylformamide.

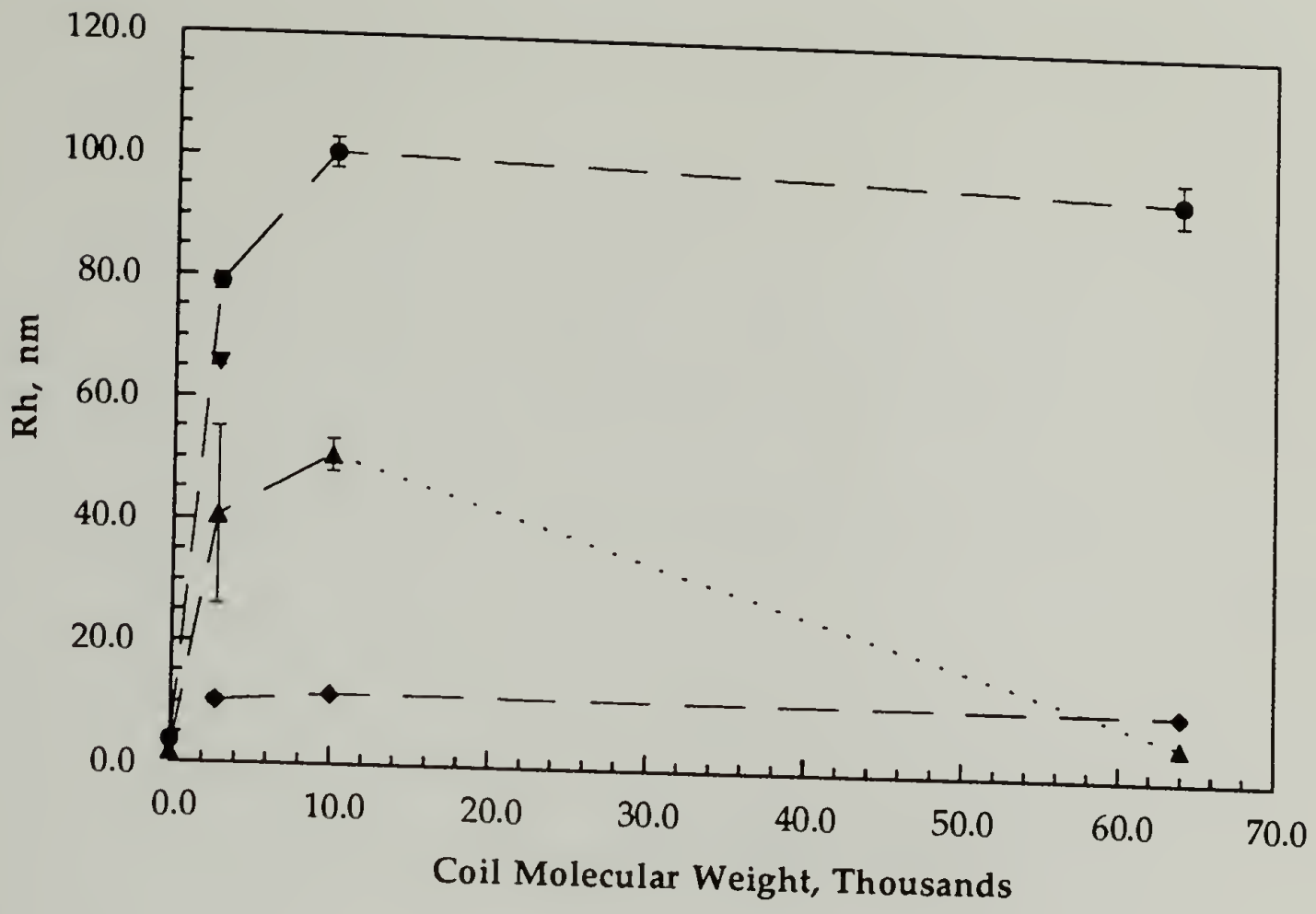

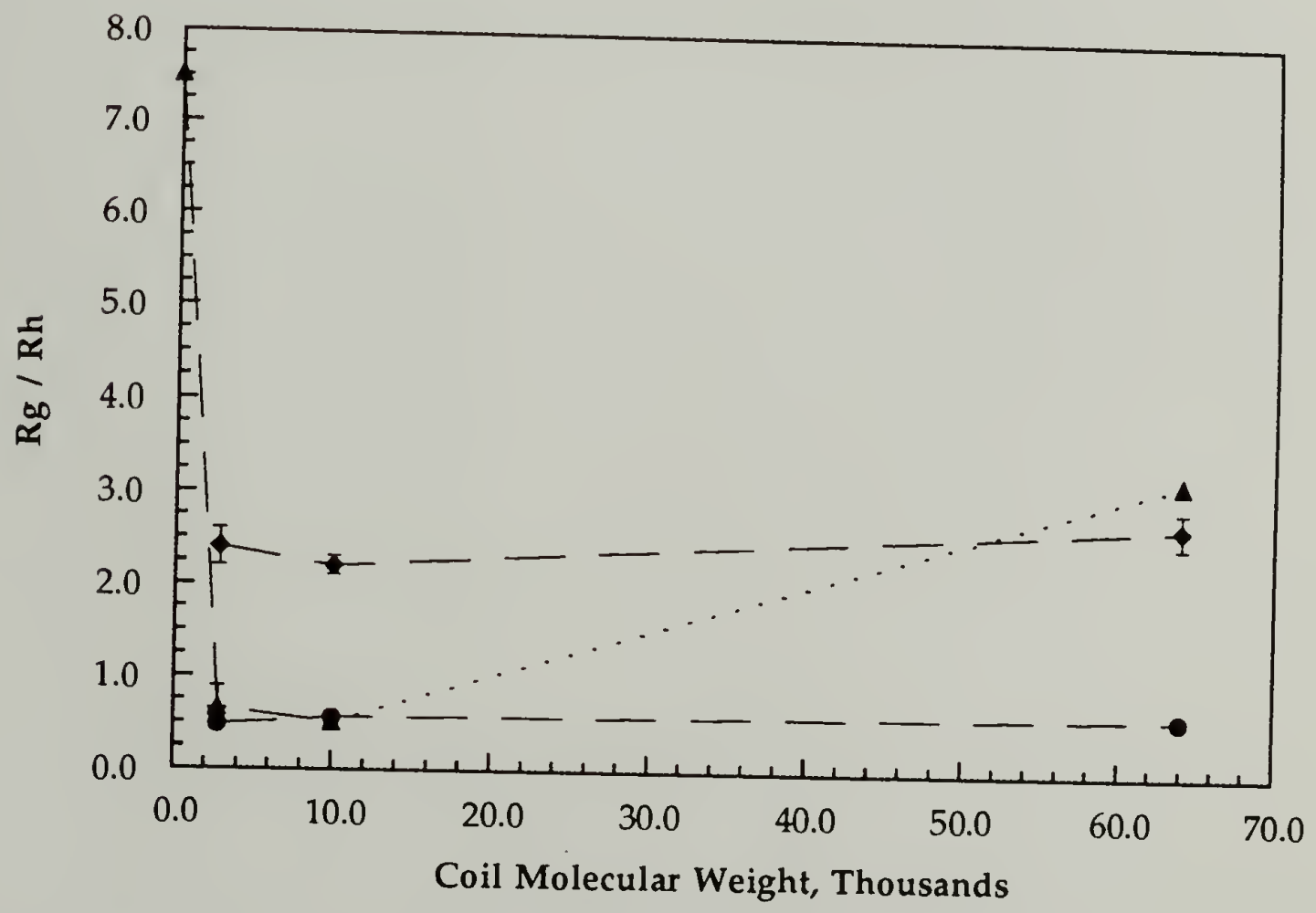

Figure 5.16. Summary of light scattering results for PI-b-PBLG in anhydrous N,N-dimethylformamide. Data shown for block copolymers possessing PBLG rod blocks of molecular weight 26K (triangles), 59K (circles), and 118K (diamonds).

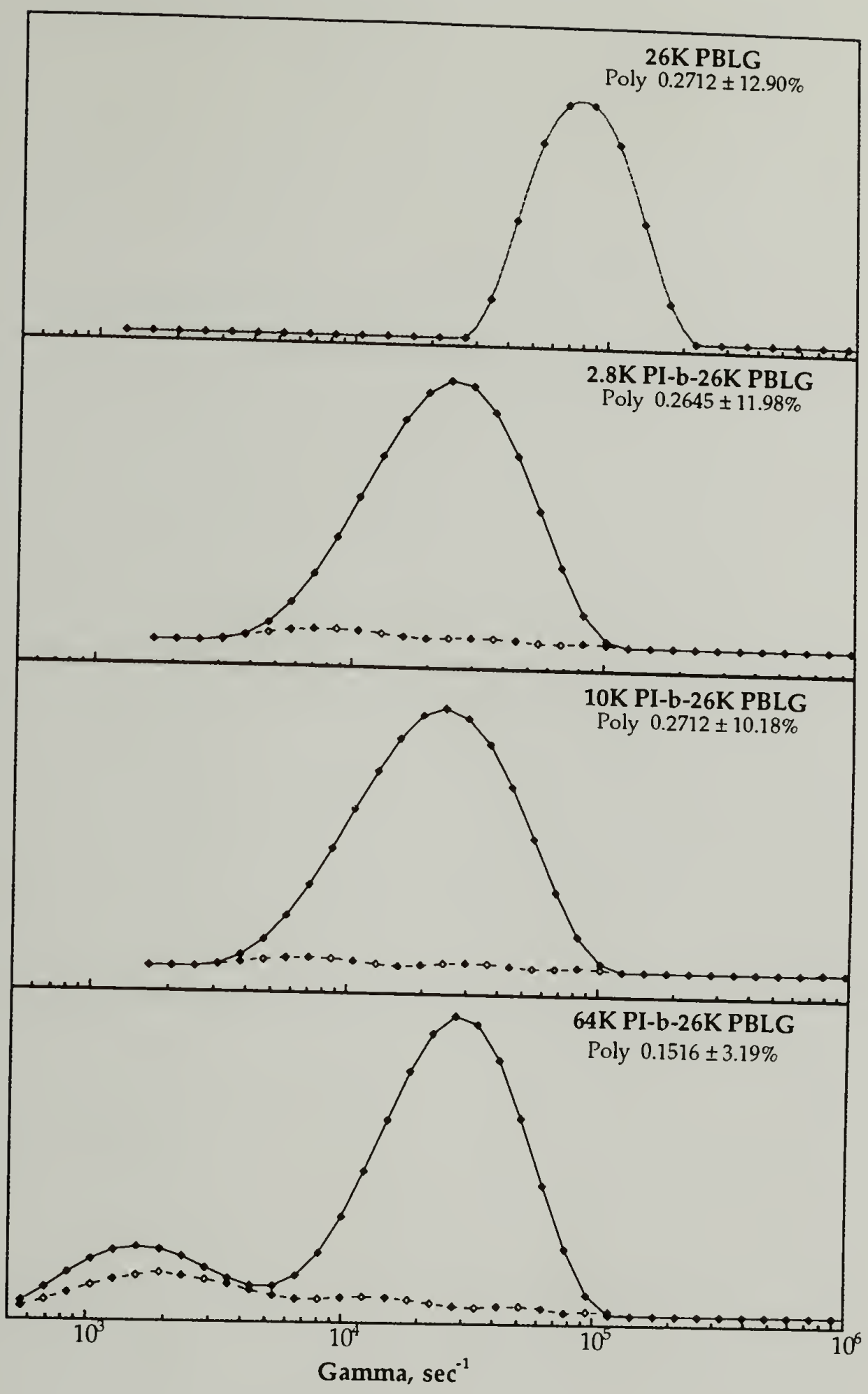

Figure 5.17. Effect of coil block size for diblocks possessing short (18 nm) rod blocks in dichloromethane. Distribution functions shown for scattering at 90° for all except 26K PBLG which was collected at 105°.

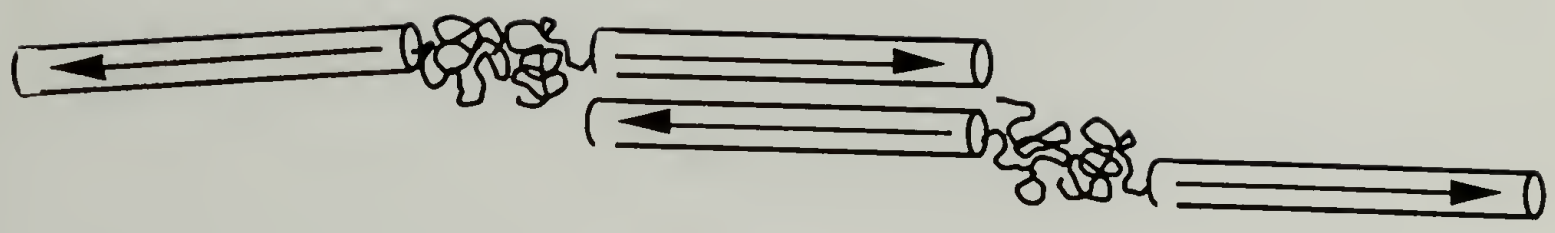

Figure 5.18. Proposed structure for PI-b-PBLG in dichloromethane.

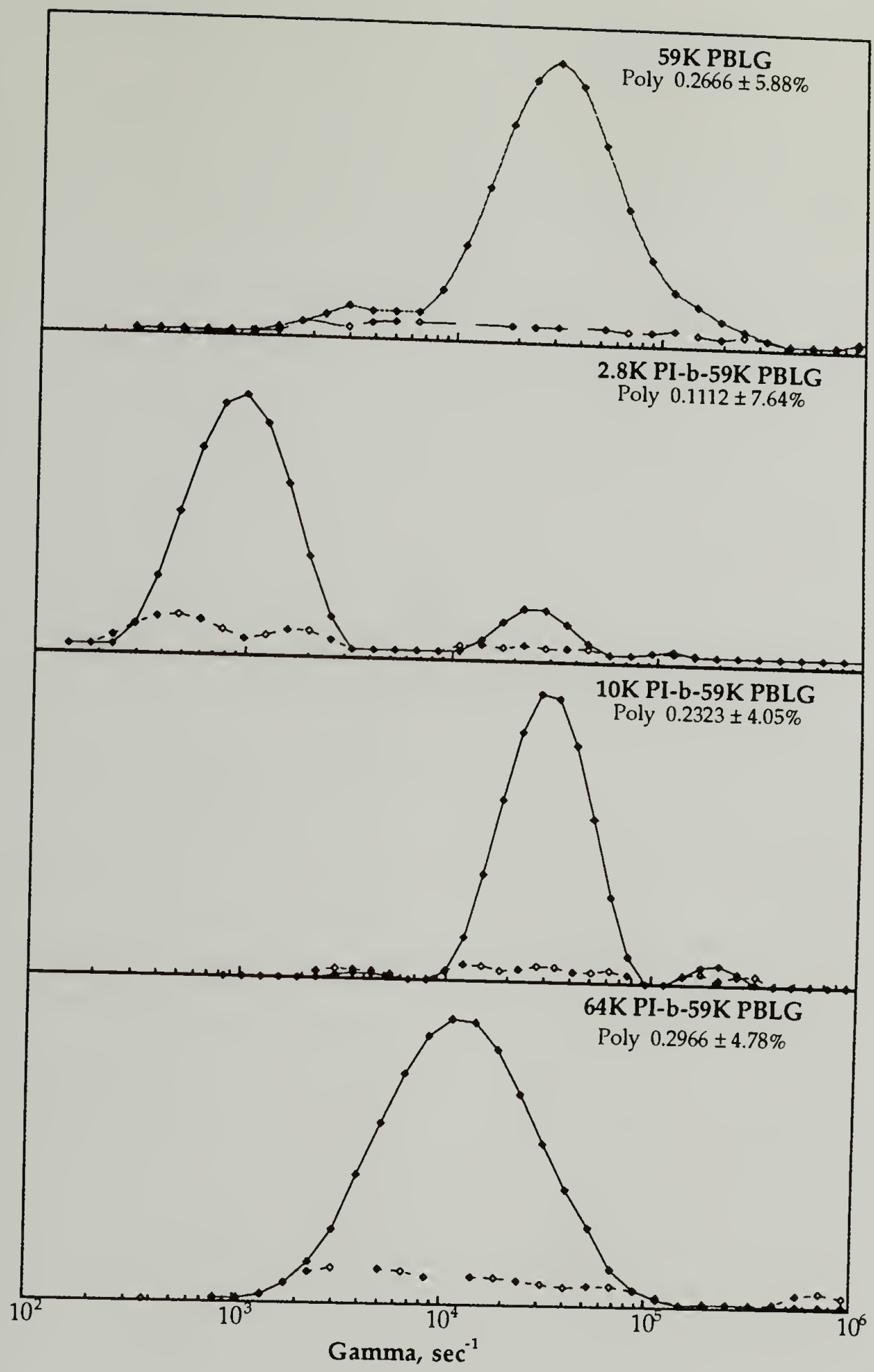

Figure 5.19. Effect of coil block size for diblocks possessing 40 nm rod blocks in dichloromethane. Distribution functions collected at 90° for all except 59K PBLG which was collected at 105°.

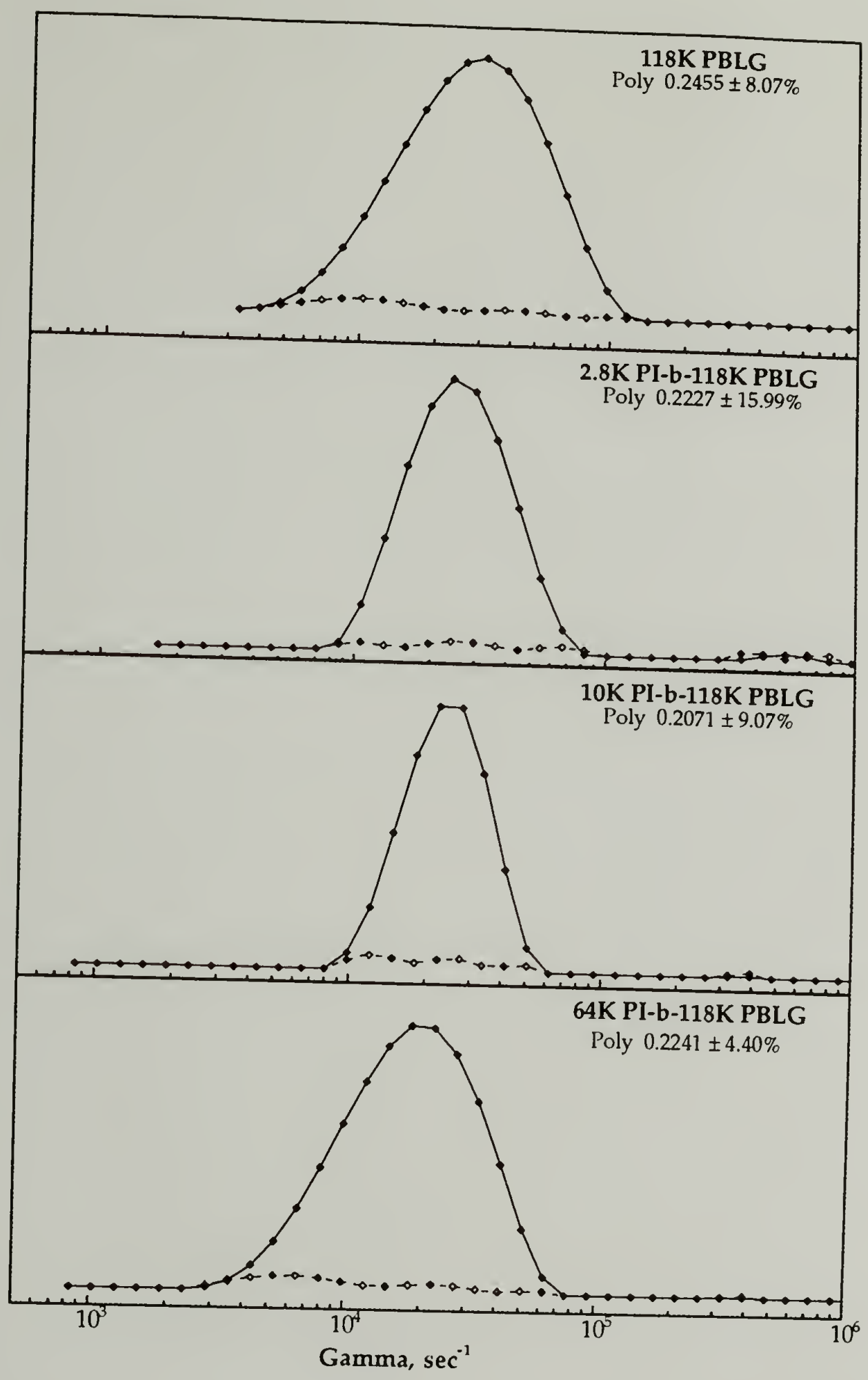

Figure 5.20. Effect of coil molecular weight on distribution functions for long rods (80 nm) in dichloromethane. Distribution function shown for 90° for all samples except 118K PBLG which was collected at 105°.

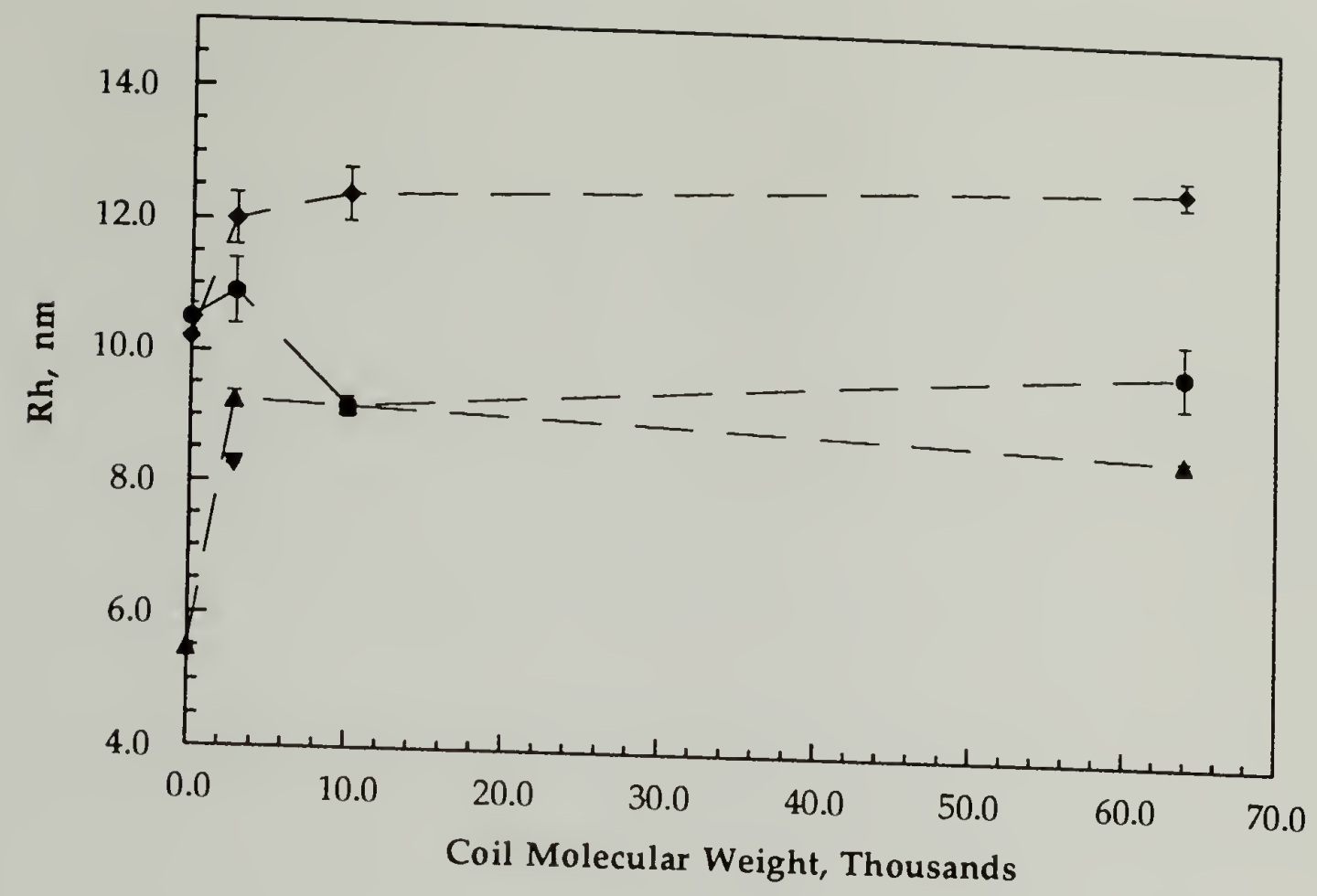

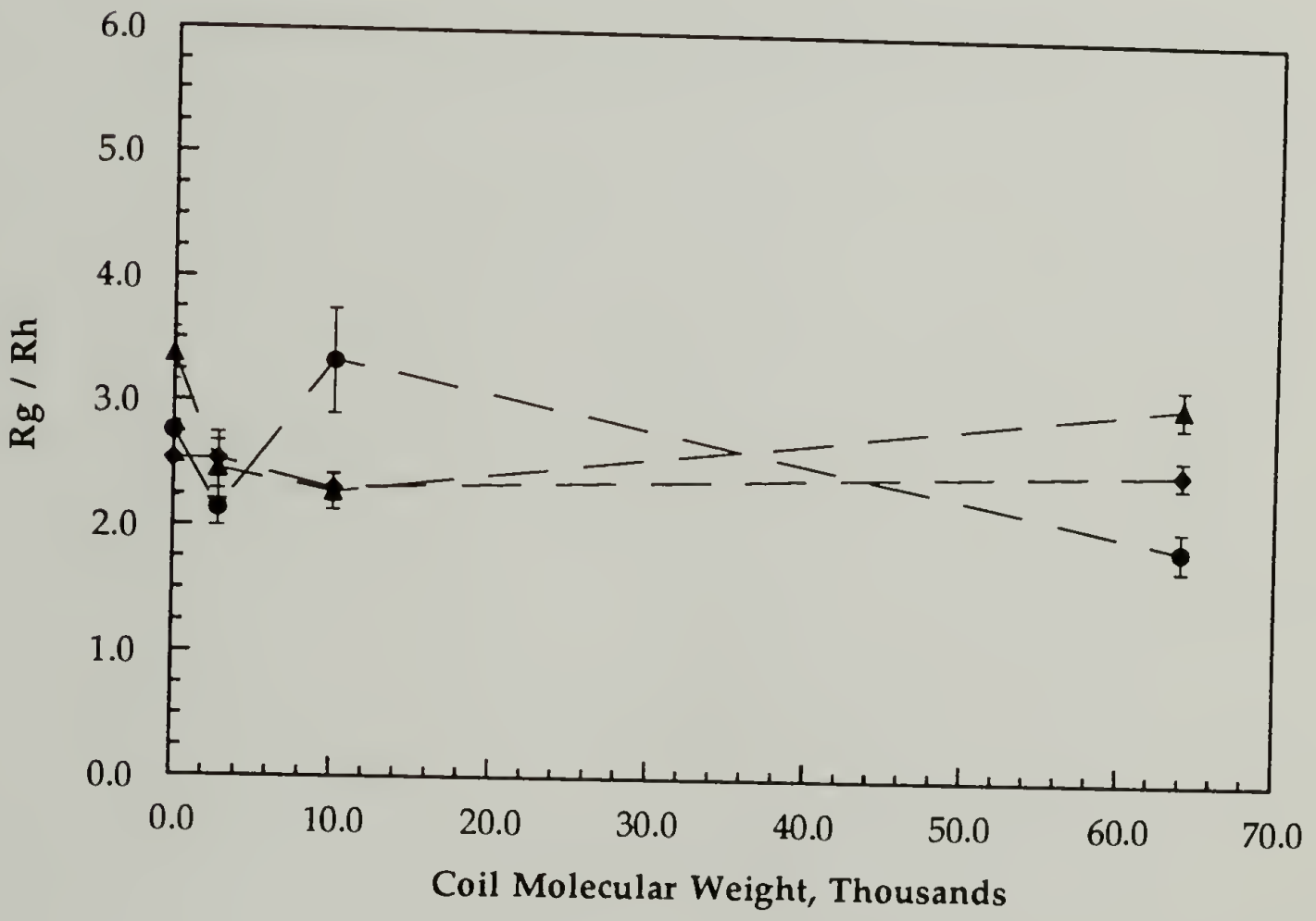

Figure 5.21. Summary of light scattering results for PI-b-PBLG diblock copolymers in dichloromethane. Data shown for block copolymers possessing PBLG rod blocks of molecular weight 26K (triangles), 59K (circles), and 118K (diamonds).

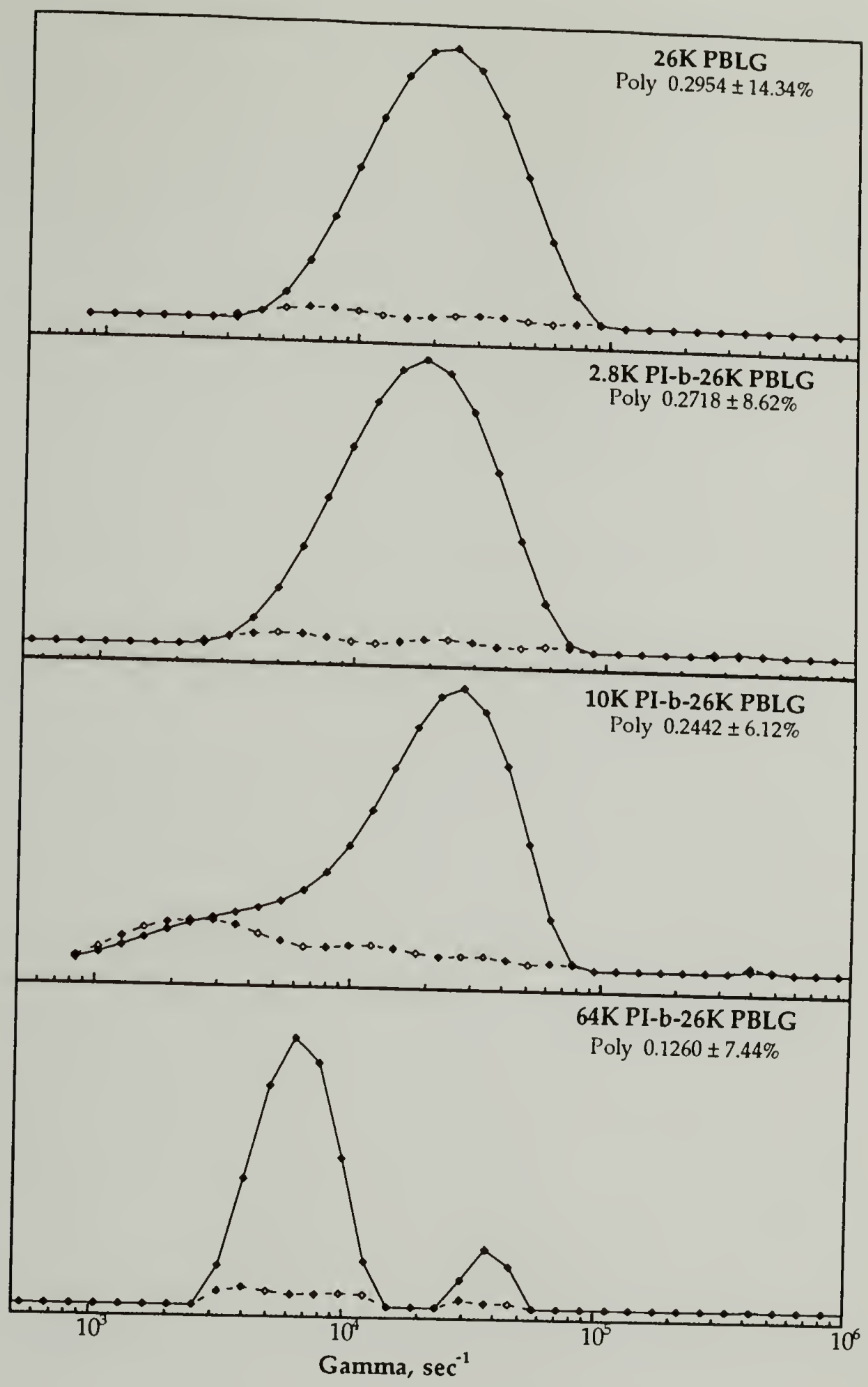

Figure 5.22. Distribution functions at 90° for polymers possessing 26K PBLG blocks in dichloromethane/heptane 88:12 w/w. Open symbols represent the residuals to the fit of the correlation function. Micelle formation is observed only for the diblock with the longest coil block, 69K PI-b-26K PBLG.

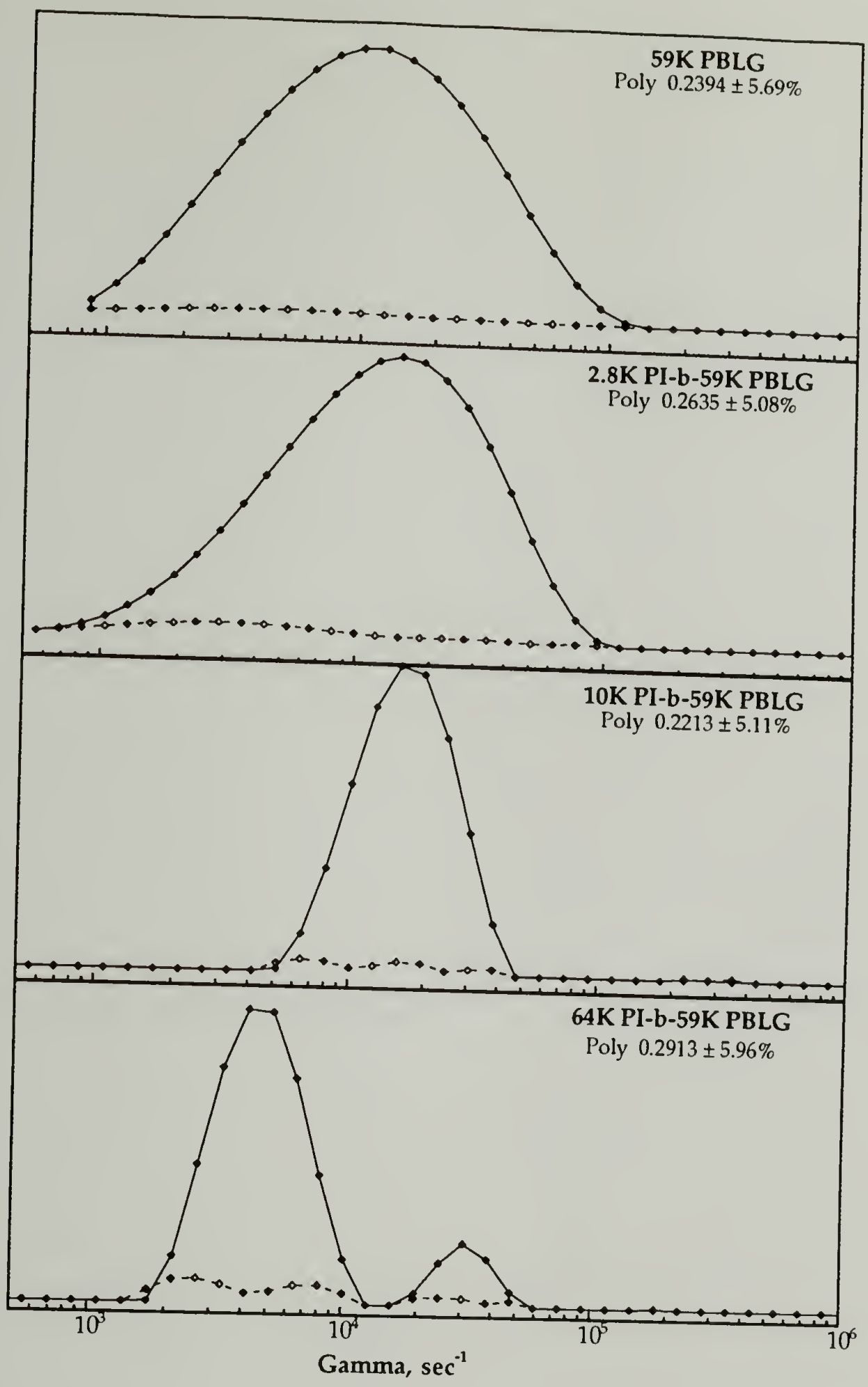

Figure 5.23. Distribution functions for polymers possessing 59K PBLG blocks in dichloromethane/heptane 88:12 w/w. Data from 90° for all samples except 10K-59K which was collected at 75°. Micelle formation is observed only for the diblock with the longest coil block, 69K PI-b-59K PBLG.

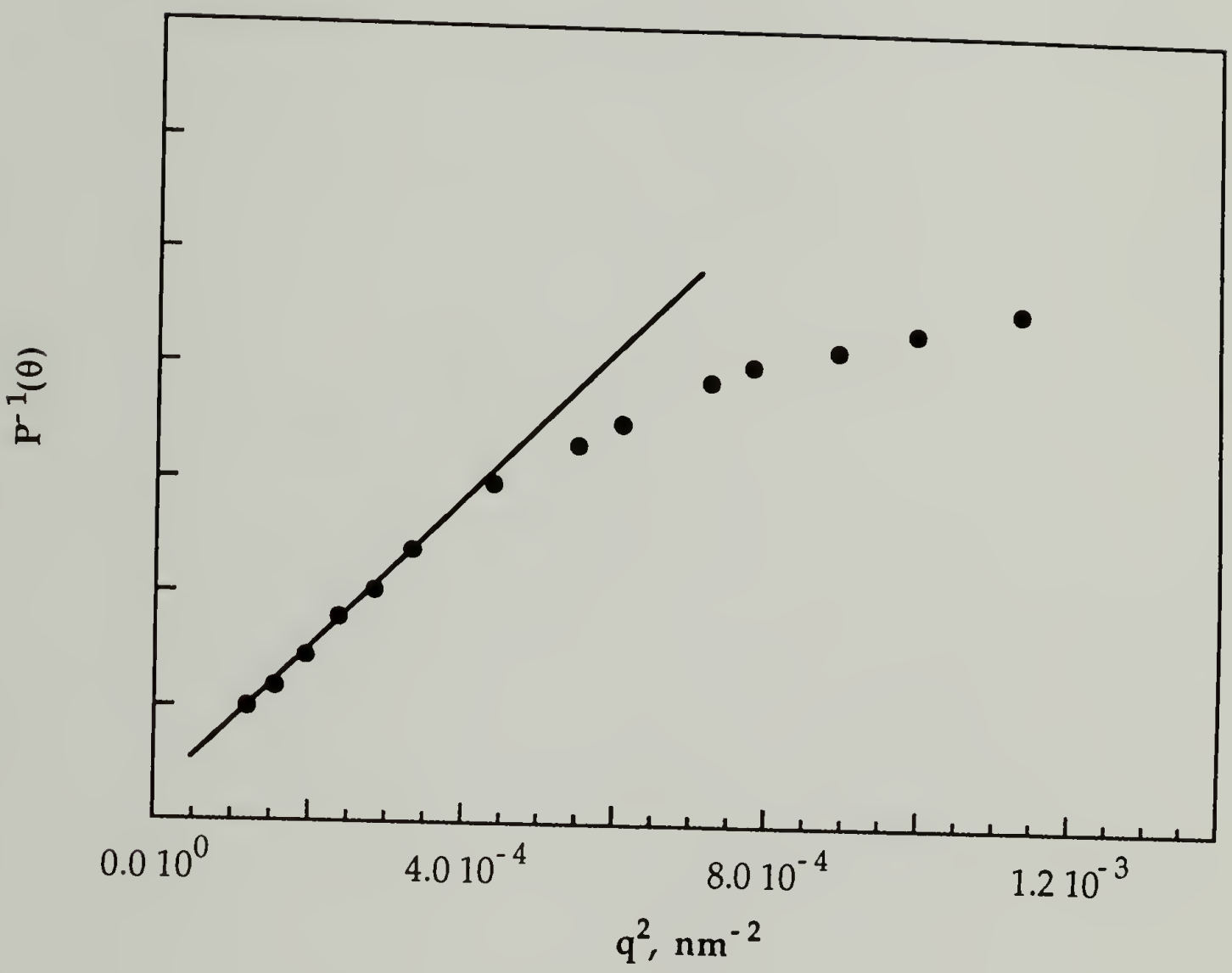

Figure 5.24. Plot showing the non-linearity in the particle scattering factor for 59K PBLG in dichloromethane / heptane 88:12 w/w. Non-linearity occurs at $q^2R_g^2$ approximately 1.9.

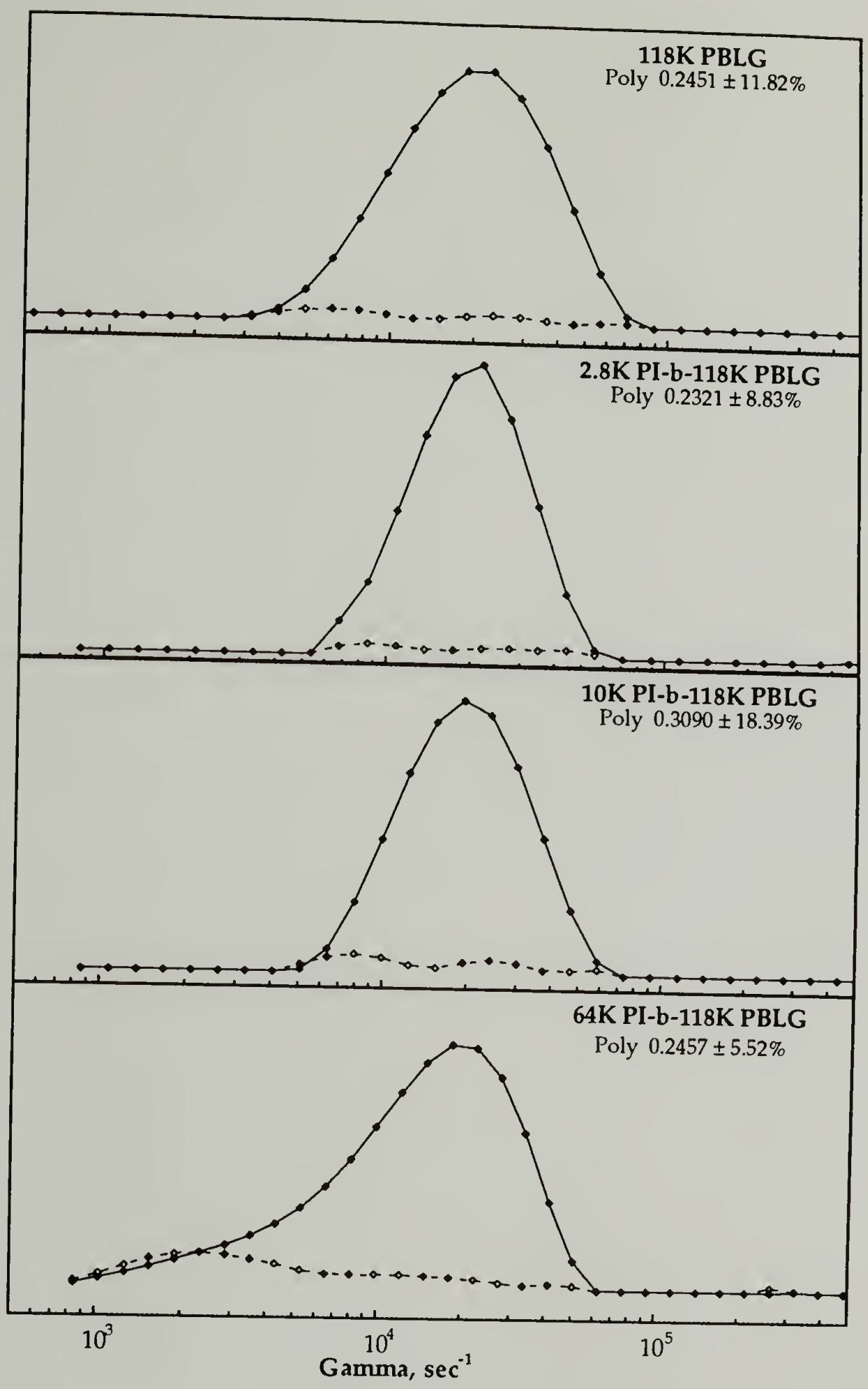

Figure 5.25. Distribution functions for polymers possessing 118K PBLG rod blocks in a mixed solvent of 88 wt% dichloromethane and 12 wt% heptane.

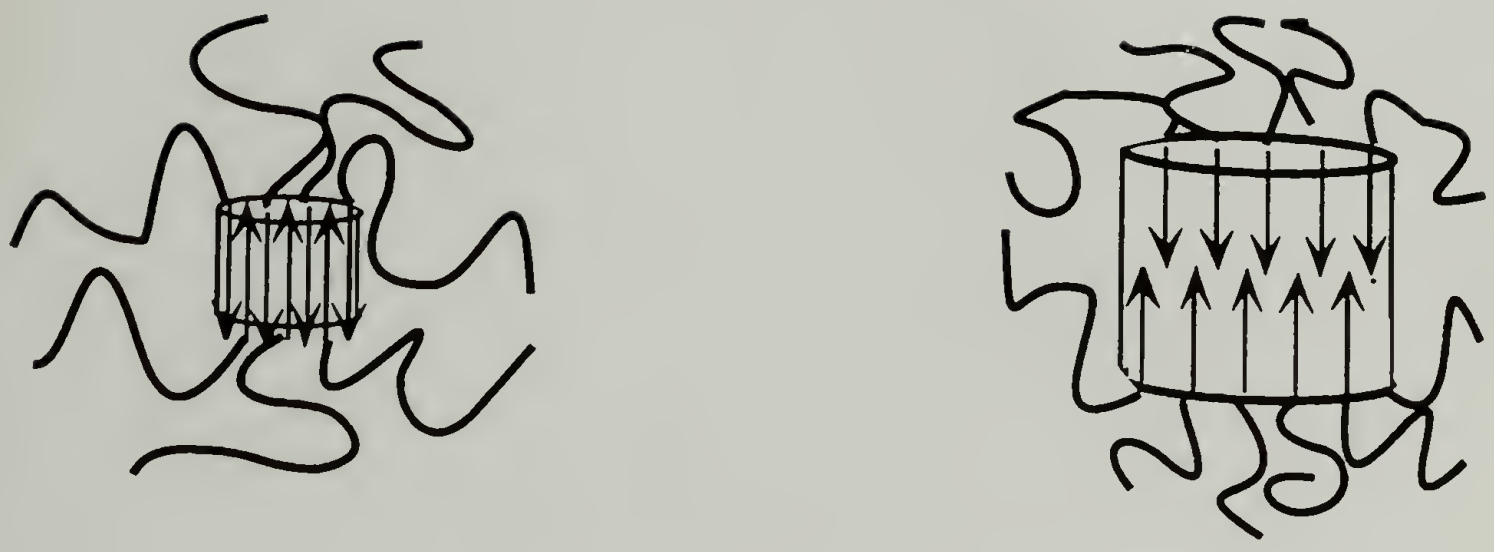

Figure 5.26. Concentric sphere model for PI-b-PBLG micelle formation in a coil-selective solvent. In (a) the core is composed of a monolayer of antiparallel helices. In (b) the core is a bilayer of parallel helices.

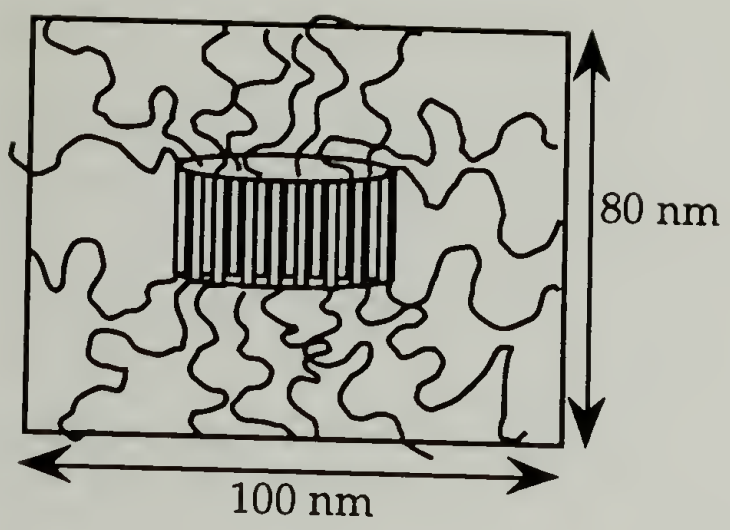

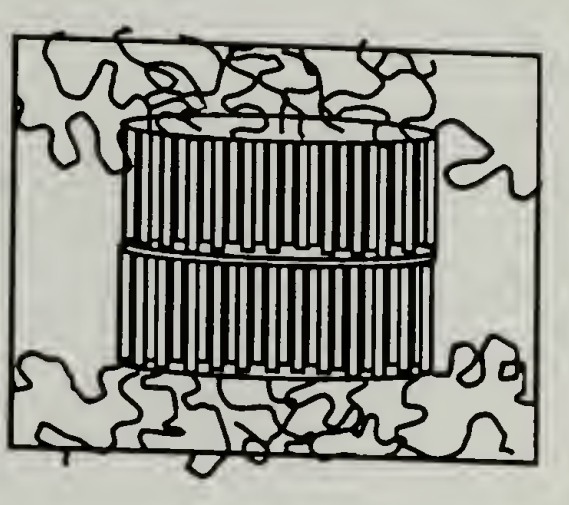

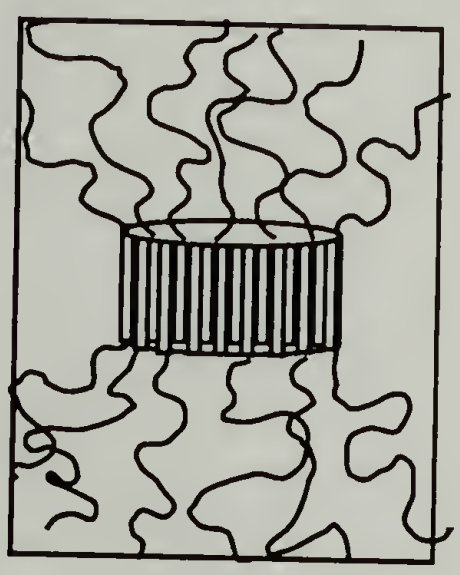

a. Monolayer Cores

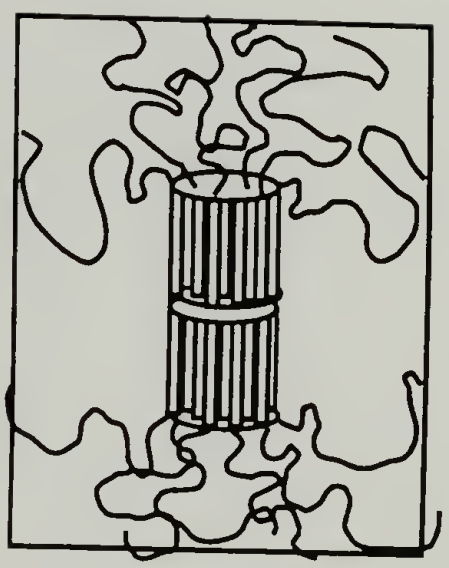

b. Bilayer Cores

Figure 5.27. Possible micelle structures for 69K-b-26K PBLG in a mixed solvent of dichloromethane/heptane (88:12 w/w). All structures have a size of 80 nm by 100 nm but differences in the relative sizes of the rod and coil regions exist. The calculated R_h for an oblate ellipsoid of this size is 46.6 nm. The measured R_h for this sample was 44.4 nm.

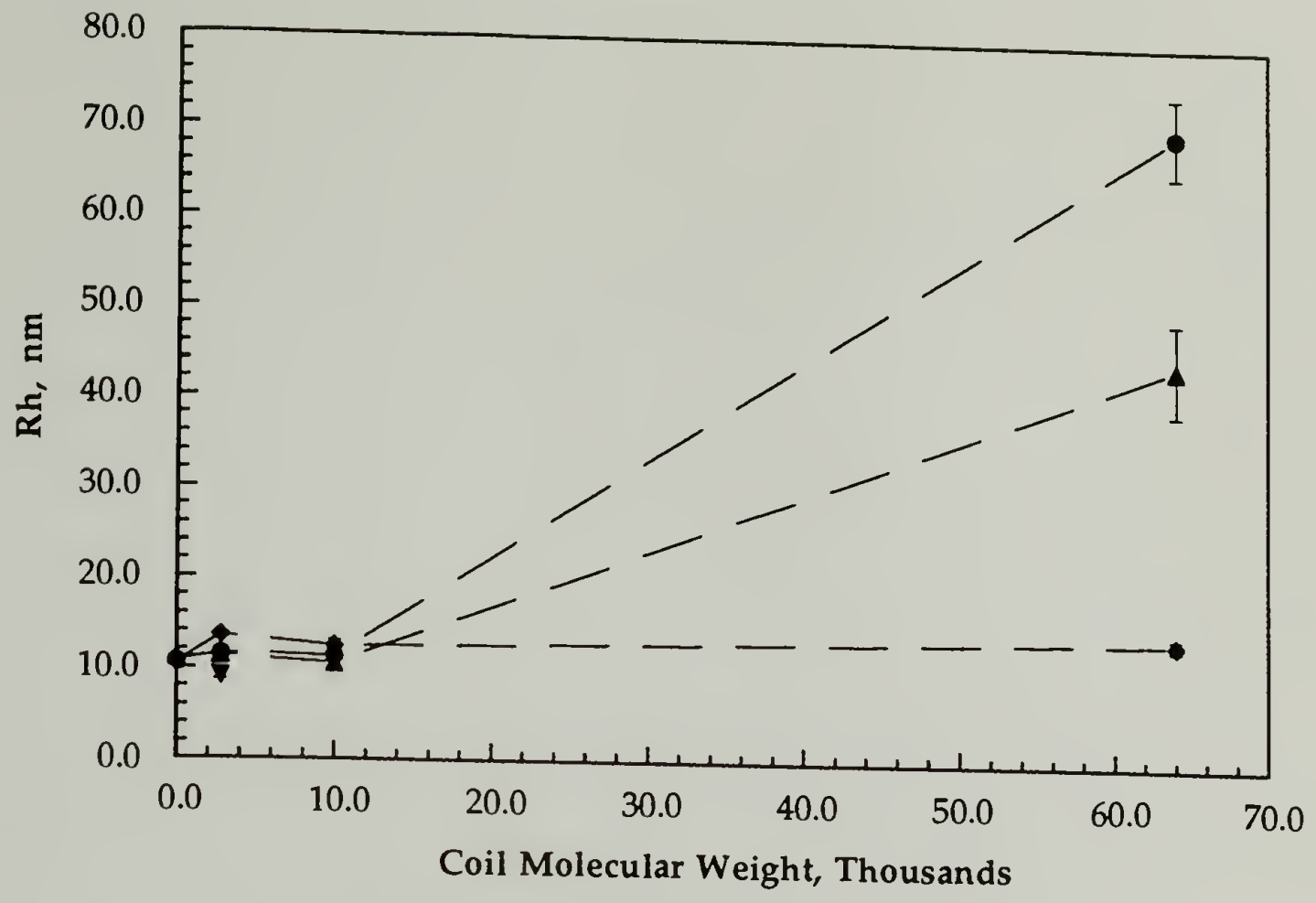

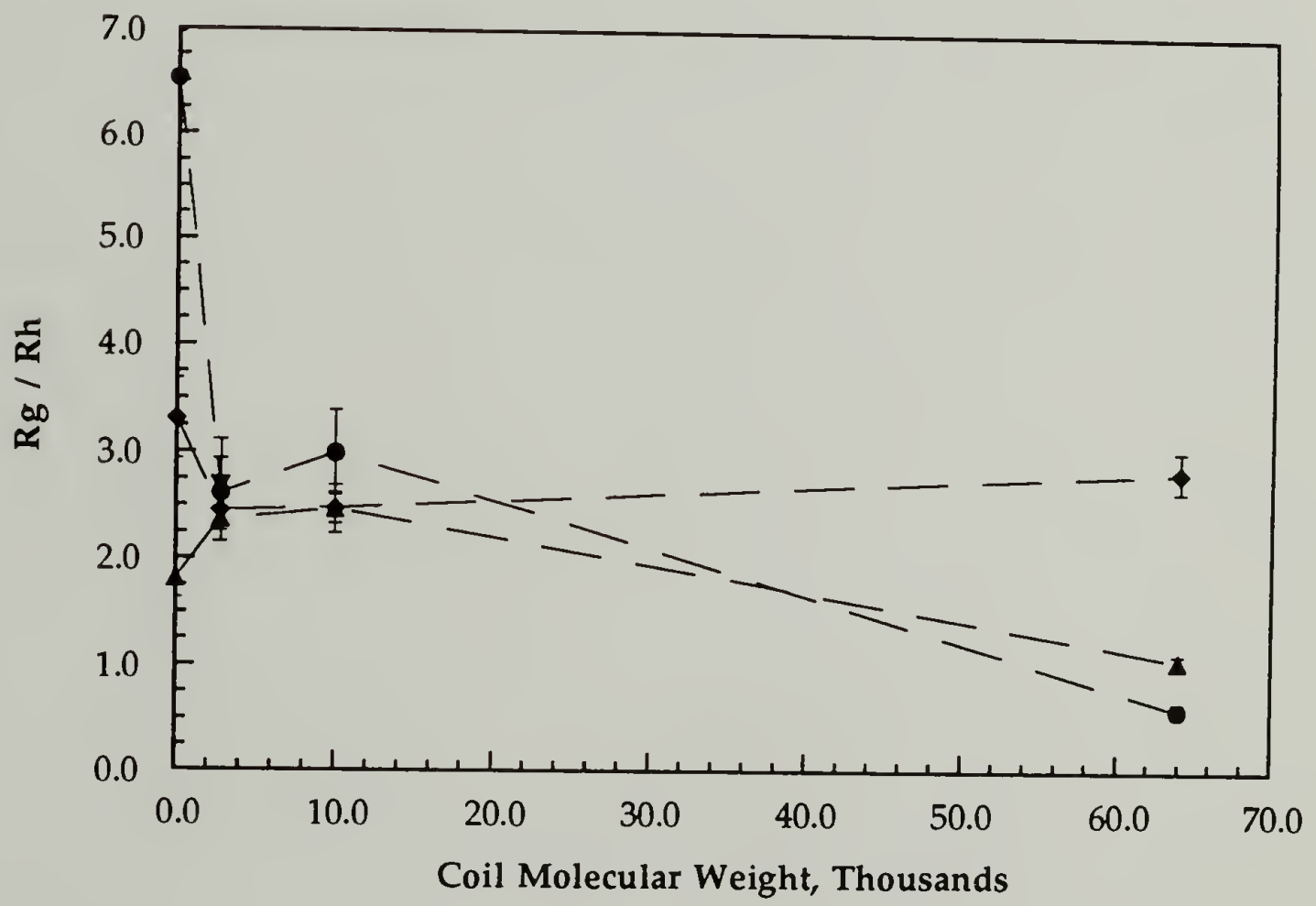

Figure 5.28. Summary of light scattering results for PI-b-PBLG in a mixed solvent of dichloromethane and heptane (88:12 w/w). Data shown for block copolymers possessing PBLG rod blocks of molecular weight 26K (triangles), 59K (circles), and 118K (diamonds).

CHAPTER VI

STRUCTURE AT SOLID SURFACES

A. Introduction

Adsorption of *flexible* block copolymers to interfaces, such as solid surfaces, has been the subject of considerable research because adsorbed layers offer the potential to modify interactions with their surrounding environment. [21, 42, 165, 166] Long flexible coil chains can be tethered to a surface through physical links with poorly solvated "anchor" blocks. The more soluble block forms a tethered "brush" microstructure while the less soluble block anchors by forming a solvent excluded layer at the surface. [167] The main driving force for adsorption is the lowering of the osmotic energy of the anchor block; the density of the adsorbed layer is mediated by the stretching induced in the tethered buoy block. [168] It has been determined that the asymmetry of the anchor and buoy block lengths affects the equilibrium surface density and consequently the overall microstructure. [42] The microstructure of tethered coils is characterized by enhanced orientation perpendicular to the substrate due to stretching of the chains away from the surface. Modelling investigations [169, 170] have shown that the chain ends are not located at a fixed distance from the surface, but, rather, they are concentrated at a short distance from the surface and decrease monotonically in density thereafter. The chains typically tilt away from the normal to maximize van der Waals interactions. [88] Lateral order, parallel to the substrate, is poor due to the random nature of flexible coils.

Tethered rigid-rod polymers potentially offer the advantages of more highly ordered monolayers. Specifically, the location of the chains end would

be known exactly since they would be confined to the plane of the outer surface of the monolayer. Rod-coil diblock copolymers could be expected to form "ideal" monolayers in which the order approaches that of a single crystal. The rod block is unable to deform upon close packing, which eliminates the entropic stretching energy inherent to coil-coil block copolymers. Assuming the rod block is tethered, the absence of entropic stretching is expected to favor rod-block packing at densities greater than what could be achieved in coil-coil copolymers. High surface densities in adsorbed rod-coil diblock copolymers could lead to highly oriented rods which would have a discrete and predetermined thickness. Intermolecular interactions between rods, especially those studied in this work, are expected to affect the energetics of self-assembly. The parallel assembly of α-helices is complicated by the additional energy term due to coulombic repulsion between rods, as discussed in Chapter II. (Conversely, the *anti*parallel assembly of α-helices would be aided by the intermolecular *attraction*.)

Obtaining a surface-ordered rod-coil diblock copolymer could lead to many potential uses. In such a system the location of the ends of the rods would be known precisely and, therefore, functionalization to modify the surfaces with nanometer-scale smectic films could be accomplished. Additionally the tethered rods could be used to create biocompatible surfaces. [27, 28] Sharper force-distance profiles might be expected between surfaces of tethered rods and these could potentially be useful for tailoring the interactions between colloidal particles. Furthurmore, rod polymers can possess dipole moments oriented in a specific direction with respect to the rod axis, as in the case of the α-helix of PBLG. This inherent dipole could be used to generate a new type of colloidal stabilization based on dipole-dipole repulsion effects. The effect of rigidity in adsorbed block copolymers has yet to

be studied, and it is the purpose of this chapter to explore this effect on the formation of surface-adsorbed layers to better understand how these block copolymers can be tailored to modify interfaces.

While the properties of rod-coil diblocks at surface have yet to be studied, there has been a small amount of work in the area of grafted rods at interfaces. The self-assembly of disulfide-modified rods of poly(γ-benzyl-L-glutamate) at gold surfaces has been studied by Samulski, et al. They have shown that the end-functionalization leads to a slightly different adsorption behavior compared to the unfunctionalized PBLG. The unfunctionalized PBLG was found to adsorb parallel to the substrate while the end-functionalized PBLG chains were found to align more with the normal. The functionalized layers were only 1.5 times thicker than the adsorbed unfunctionalized homopolymer indicating weak alignment. Attempts to chemisorb PBLG helices to a solid substrate gave similar results. [71]

The focus of this chapter was to study the effect of changing the anchoring of the PBLG from a single-chemical link to a long physisorbed anchor. A series of polyisoprene-block-poly(γ-benzyl-L-glutamate) diblock copolymers, described in Chapter III, was studied. The block copolymers in the series varied in the molecular weights of both the rod and coil blocks in order to ascertain their dependence on adsorption behavior. The smallest flexible-coil block was chosen such that the size of the solvent-excluded anchor would match with the diameter of the rod and produce a dense monolayer with a packing fraction of unity. The two larger coils were designed to produce accordingly less dense layers, Table 6.1. The calculations were based on a rod diameter of 2 nm and a dense, melt-like solvent-excluded anchor with a density of 1 g/ml. The rod density is defined as the ratio of the rod cross-section to the anchor cross-section.

The diblock copolymers and the corresponding PBLG homopolymers were adsorbed from dilute solutions (approx. 1 mg/ml) of anhydrous N,N-dimethylformamide. Freshly-prepared gold-coated silicon substrates were immersed in solution for several days. After analysis of the adsorbed films, the substrates were rinsed for several days in fresh anhydrous DMF and again analyzed.

Table 6.1. Characteristics of the three polyisoprene-b-poly(γ-benzyl-L-glutamate) diblock copolymer anchor blocks.

Polyisoprene Block	Radius, nm	Surface Area, nm^2	Rod Density, rods/area
2,800	1	3.1	1
10,000	1.6	8.2	0.4
64,000	2.9	26	0.1

B. Theory of Block Copolymers at Interfaces

Tethered polymers, such as selectively-adsorbed block copolymers, are expected to behave differently depending on their rigidity. Increasing the surface density of tethered flexible-coils results in more deformed (stretched) configurations. The same perturbation in rod-coil diblocks should result in a higher order parameter as the rods are forced to align more with the normal to increase packing efficiency.

1. Coil-Coil Block Copolymer

Tethering flexible-coils to an interface leads to unique behavior because the chains are forced to adopt configurations different than in free solution.

In a dilute solution of a good solvent, a coil will adopt a configuration in which the radius of gyration is related to the degree of polymerization, N, as shown: [171]

$$Rg = a\,N^{3/5} \tag{6.1}$$

where a is the mesh size in the lattice model. [171]

Consider the situation in which many coils are grafted to an interface by one of their ends. The surface density, σ, is related to the average distance, d, between the grafted chain ends; $\sigma \propto (1/d)^2$. In the first case, the average distance between grafting points is greater than the radius of gyration of the coil. The coils will be relatively unperturbed by the interface and will assume approximately free solution dimensions, Fig. 6.1a. The layer thickness, L, is proportional to $N^{3/5}$. [56]

In the second case, the grafting density is increased so that the spacing between anchored chains is much less than the radius of gyration of the coils and the chains crowd one another, Fig. 6.1b. Chain overlap is an energetically costly situation since it creates unfavorable polymer-polymer contacts at the expense of favorable polymer-solvent interaction. Therefore, the chains stretch away from the interface to improve this osmotic balance. The degree of chain stretching is limited by the associated increase in the stretching energy. The equilibrium surface density is that which minimizes the system free energy. The result is that the chains stretch to the point at which the layer thickness is proportional to the degree of polymerization, Fig. 6.1c: [56, 168]

$$L \approx N\,a\,(a/d)^{2/3} \tag{6.2}$$

This expression is valid for the case d << Rg. This scaling relation has been experimentally observed through surface forces measurements. [166, 172-174]

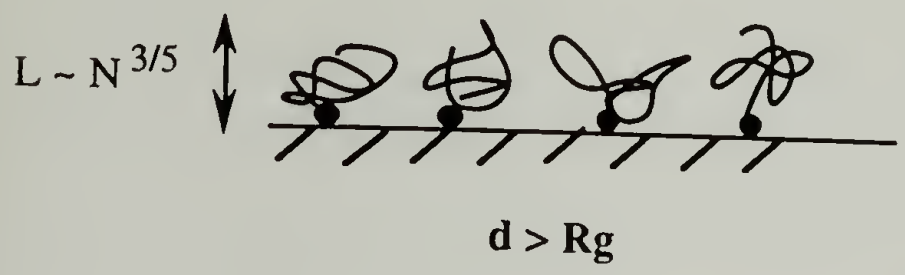

Figure 6.1. Tethered random-coil chains stretch to relieve the crowding at the surface. The size of the anchoring block determines the surface density. (a) low surface density, (b) unstable arrangement at high surface density, (c) chains stretched to relieve crowding at high surface density.

Studies of the selective adsorption of coil-coil diblocks have shown this to be a valuable route to surface modification. [33] As compared to homopolymer adsorption, the adsorption of coil-coil diblocks to surfaces introduces several new variables and the ability to further tailor the resulting

properties. The layer thickness of densely grafted chains scales linearly with chain length of the buoy block and the surface density has been experimentally shown to scale with a parameter, β,

$$\beta = Rg,_{buoy} \; / \; Rg,_{anchor} = N_B{}^{6/5} \; / \; N_A{}^{2/3} \qquad (6.3)$$

where β is the ratio of the sizes (i.e. radii of gyration) of the buoy and anchor blocks in a selective solvent. [42]

2. Rod-Coil Block Copolymer

In rod-coil diblocks the degree of control is further increased compared to coil-coil diblocks. Again solvent interactions with each block are very important, but in this case the rigidity of the rod block allows for the further tailoring of the interface. However, not only is the rigidity of rods important to ordering, but the intermolecular interactions between rods is also important. The dipole moments of the rods are a further key feature which will facilitate (or suppress) ordering at surfaces.

A first-order orientational ordering transition is predicted to occur in monolayers of grafted rods when the interaction energy between rods (A) and the surface adsorption energy (ε) are sufficiently large. [75] This transition is not predicted for non-interacting rigid rods (A=0, ε=0); the order in this system is expected to increase continuously as the surface density increases. [74, 75] The adsorption energy alone is not sufficient to produce the transition, but serves to lower the interaction energy necessary. The interaction energy is sufficient to effect the transition even when ε=0.

At low surface densities the rods lie flat on the surface. As the surface density increases, the rods gradually orient more normal to the surface. If the interaction and adsorption energies are sufficient, the theory anticipates that the rods will jump from a "lying down" configuration to a "standing-up" configuration at a critical surface density, as shown in Figure 1.1. [75]

C. Determination of Orientation of PBLG rods

The orientation of a series of PI-PBLG diblock copolymers and PBLG homopolymers was studied using the combined techniques of reflectance infrared spectroscopy and ellipsometry to measure the orientation of characteristic PBLG bands and the film thickness, respectively.

1. Infrared Spectra of PBLG

Polarized infrared spectroscopy was used to probe the orientation of grafted polypeptide rods. The structure of a polypeptide α-helix is uniquely suited for orientational study because PBLG has been well-studied and the assignments of the bands are known. [71-73, 104-106, 141, 175-177]

Tsuboi [106] has measured the infrared spectra of oriented films of PBLG for two cases: the electric vector parallel to the helix axis (denoted as ll) and the electric vector perpendicular to the helix axis (denoted as ⊥). Table 6.2 lists the wave numbers, dichroic ratios, and transition moment directions for some of the important absorption bands. The angle θ is the angle between the transition moment and the helix axis.

Table 6.2. Wave numbers, transition moment directions, and assignments of some of the absorption bands of PBLG. [106]

Wavenumber		Dichroic Ratio	θ, deg	Assignment
ll	⊥	R(ll/⊥)		
3292	3294	7.3[a]	27	NH stretching (Amide A)
		4.2[b]	29	
1734	1733	1.1	53	C=O stretching (ester)
1652	1655	2.9	39	Amide I
1518	1549	0.18[a]	74	Amide II
		0.25[b]	76	
1498	1498	1.7	46	C-C stretching (phenyl A1)
1453	1453	0.67	61	C-C stretching (phenyl B1)
1328	1314	2.3	40	Amide III
1168	1168	1.0	54	C-O stretching (ester)
697	697	0.65	62	Phenyl B2
---	613	0.1	> 80	Amide VI
563	---	∞	0	Skeletal deformation in a long helix

[a,b] thinner or thicker films used to determine dichroic ratios, respectively

The information in Table 6.2 was used to determine the orientation of PBLG rods in this study. Some of the transition moments absorb at the same wavenumber for parallel and perpendicular orientations but differ in the magnitude of the absorbance. As shown in Table 6.2, the N-H stretching (Amide A) absorbs 7.3 times more energy when the helix axis is parallel to the electric vector compared to the perpendicular orientation. Similarly, the Amide I (C=O backbone stretching) absorbs 2.9 times more when the helix axis is parallel to the electric vector compared to perpendicular. The dichroism is explained by the transition moments oriented nearly parallel to the helix axis.

Some of the transition moments absorb at different frequencies for the parallel and perpendicular orientations. These absorption bands were especially helpful in determining orientation. The Amide II (C-N stretching, N-H bending) absorbs at 1518 (ll) and at 1549 (⊥). Their perpendicular band is at least four times stronger than the parallel. Tsuboi shows that the absorption is very sensitive to orientation. Similarly, the Amide III absorbs at 1328 (ll) and 1314 (⊥); the parallel band is 2.3 times stronger than the perpendicular and selectivity for orientation is high. [106]

The dichroic ratio of the side-chain C=O stretching (1734 cm^{-1}) is close to unity. This makes this band very useful as a measure of the relative amount of polymer on the surface since the intensity of the peak is only related to the number of side-chain carbonyls and not related to the orientation.

The grazing angle IR spectra of a highly oriented (θ=0) monolayer of grafted helices will have characteristic features. The Amide II at 1549 cm^{-1} will essentially disappear and be replaced by a weak absorption at 1518 cm^{-1}. The Amide III at 1328 cm^{-1} will absorb moderately strongly and there will be no peak at 1314 cm^{-1}. The loss of the Amide II 1549 cm^{-1} band may be the best evidence for nearly normal orientation because it is such a strong absorption band.

2. Experimental Results

Transmission infrared spectra of bulk, solution-cast films of PBLG, PI, and a PI-PBLG diblock copolymer, Figure 6.2, show that the polyisoprene does not absorb in the region used to assess the orientation of PBLG rods, (1800 - 1500 cm^{-1}). The relative intensity of the Amide I band was observed to

depend on the thickness of the bulk (unoriented) film, an effect which has been observed by Tsuboi. [106] Thicker films absorbed more strongly in the Amide I region; this difference is attributed to the increased probability of PBLG rods oriented perpendicular to the surface. Thinner films would have a greater proportion of rods parallel to the surface, and a corresponding weaker Amide I. (Figure 6.2a shows a thin film of PBLG cast from a dilute (3 mg/ml) solution.) The important conclusion was that the Amide I was consistently stronger than the Amide II for all film thicknesses.

Figure 6.3 compares this bulk, unoriented spectrum (transmission) with the reflectance spectra for adsorbed polymers. The polymers were adsorbed from dilute solution of anhydrous N,N-dimethylformamide and measured at an incidence angle of 80°. Four PBLG homopolymers were analyzed and the orientation was observed to be independent of molecular weight. A representative spectrum of adsorbed PBLG homopolymer is shown in Figure 6.3b. Compared with the bulk spectrum (Fig. 6.3a) the Amide I is weaker and the Amide II is stronger consistent with a preferential orientation of the helices parallel to the gold substrate. The effect of the presence of polyisoprene coils on the orientation of the PBLG rods was extremely weak and independent of rod block molecular weight. Figure 6.3c shows a representative reflectance spectrum for 2.8K PI-b-26K PBLG diblock film. The Amide I was slightly stronger in relation to the Amide II indicating a very slight perturbation from the parallel orientation. Rinsing the homopolymer and the block copolymer films in pure solvent for several days resulted in the nearly complete removal of the polymer from the surface, Figure 6.3d.

The ellipsometry results confirmed the conclusion that the presence of the polyisoprene anchor slightly enhanced the normal orientation of PBLG rods. Measured thickness for several molecular weights of PBLG

homopolymer were between 1.4 and 2.6 nm. This range of thicknesses corresponds to monolayer films or partial bilayer films of PBLG oriented parallel to the substrate, in agreement with IR results. The diblock films were not substantially thicker than the diameter of PBLG rods (1.5-2 nm), Table 6.3. Complete normal ordering would produce films which were 18 nm, 40 nm, and 81 nm for the 26K, 59K, and 118K PBLG rods, respectively. The thickest films were those with the shortest PBLG rod. Rinsed films were too thin and uneven to accurately measure.

The relative peak areas of the Amide I and the Amide II and the film thicknesses for the unrinsed homopolymer PBLG and diblock films are summarized in Table 6.3. The ratios of peak areas of the Amide I and Amide II bands are in all cases less than that for the bulk PBLG films, indicating that the bulk film has a greater proportion of helices directed away from the surface.

D. Analysis of Results

The rod-coil diblock copolymers did not assemble into highly ordered surface films in which the rods were oriented normal to the surface. In fact, the rods were highly localized to the plane of the substrate. While the enhanced order parallel to the substrate may be interesting, it is the exact opposite of the result which had been anticipated.

Many reasons may be proposed for the inability of this approach and others' efforts to produce well-ordered monolayers of rigid-rods: the high polydispersity of PBLG produced by traditional synthetic routes, the large diameter of PBLG, PBLG's semi-flexible structure, specifics of the side-chain, and the presence of the dipole moment. Chapter II analyzed the dipole

moment effect on self-assembly of monolayers of parallel α-helices. The analysis showed that the large dipole moment of the adsorption solvent (DMF, ε=36.7) caused the magnitude of the dipole-dipole interaction energies to be negligibly small at all separations, Figure 2.18. Therefore, α-helices were predicted to be able to overcome the coulombic energy barrier of parallel orientation if they were in a sufficiently polar solvent or if the adsorption energy term was sufficiently large. The short-ranged van der Waals attractions would be expected to stabilize the densely-packed monolayers.

Table 6.3. Summary of reflectance infrared spectroscopy and ellipsometry results for adsorbed, unrinsed films. Errors are based on standard deviations from two experiments.

Polymer	Amide I/Amide II	Thickness, nm
26K PBLG	0.71 ± 0.10	2.6 ± 0.3
42K PBLG	0.61	1.4
118K PBLG	0.49	2.6
2.8K PI-25K PBLG	0.85 ± 0.02	3.3 ± 0.2
2.8K PI-26K PBLG	0.68 ± 0.10	3.7 ± 0.7
10K PI-26K PBLG	0.81	5.5
64K PI-26K PBLG	0.75	1.4
2.8K PI-59K PBLG	0.94 ± 0.02	2.2 ± 0.3
10K PI-59K PBLG	0.86 ± 0.06	2.1
64K PI-59K PBLG	0.85	2.5
2.8K PI-118K PBLG	0.72 ± 0.03	2.1 ± 0.4
10K PI-118K PBLG	0.68 ± 0.09	2.2 ± 0.4
64K PI-118K PBLG	0.78	3.0
Bulk PBLG	**1.37**	

While the dipole-dipole interaction between α-helices may not inhibit the self-assembly of PBLG helices in this work, experiments can be designed to use this interaction to *promote* monolayer formation. An antiparallel monolayer of α-helices would be expected to self-assemble in a solvent of low dielectric constant because the dipole-dipole interaction in this case is attractive at all separations. An especially promising system would be one composed of a mixed solution of N-functionalized and C-functionalized helices which could adsorb to an interface so that each helix is surrounded by the opposite dipole. In this case, the α-helix dipole would attract the helices toward one another; theory predicts a large order parameter at modest surface densities. [75] Non-interacting rods would also be interesting to study, but high degrees of order are not expected until high surface densities.

E. Conclusions

The adsorption of a series of PI-PBLG rod-coil diblock copolymers from a rod-selective solvent onto gold was studied. Reflectance infrared spectroscopy and ellipsometry results showed that both the PBLG homopolymers and the diblock copolymers formed adsorbed layers in which the PBLG helices were oriented parallel to the substrate. This result is in agreement with two other investigations of tethered PBLG α-helices. [71-73] The modelling analysis of Chapter II showed that the inability of this system to form highly ordered self-assembled monolayers is probably not a result of the repulsive α-helix dipole-dipole interaction in a highly polar solvent such as DMF. While this system did not form the desired structure, other systems having modified or different rods, non-interacting rods or mixed dipole rods could potentially result in dense monolayers.

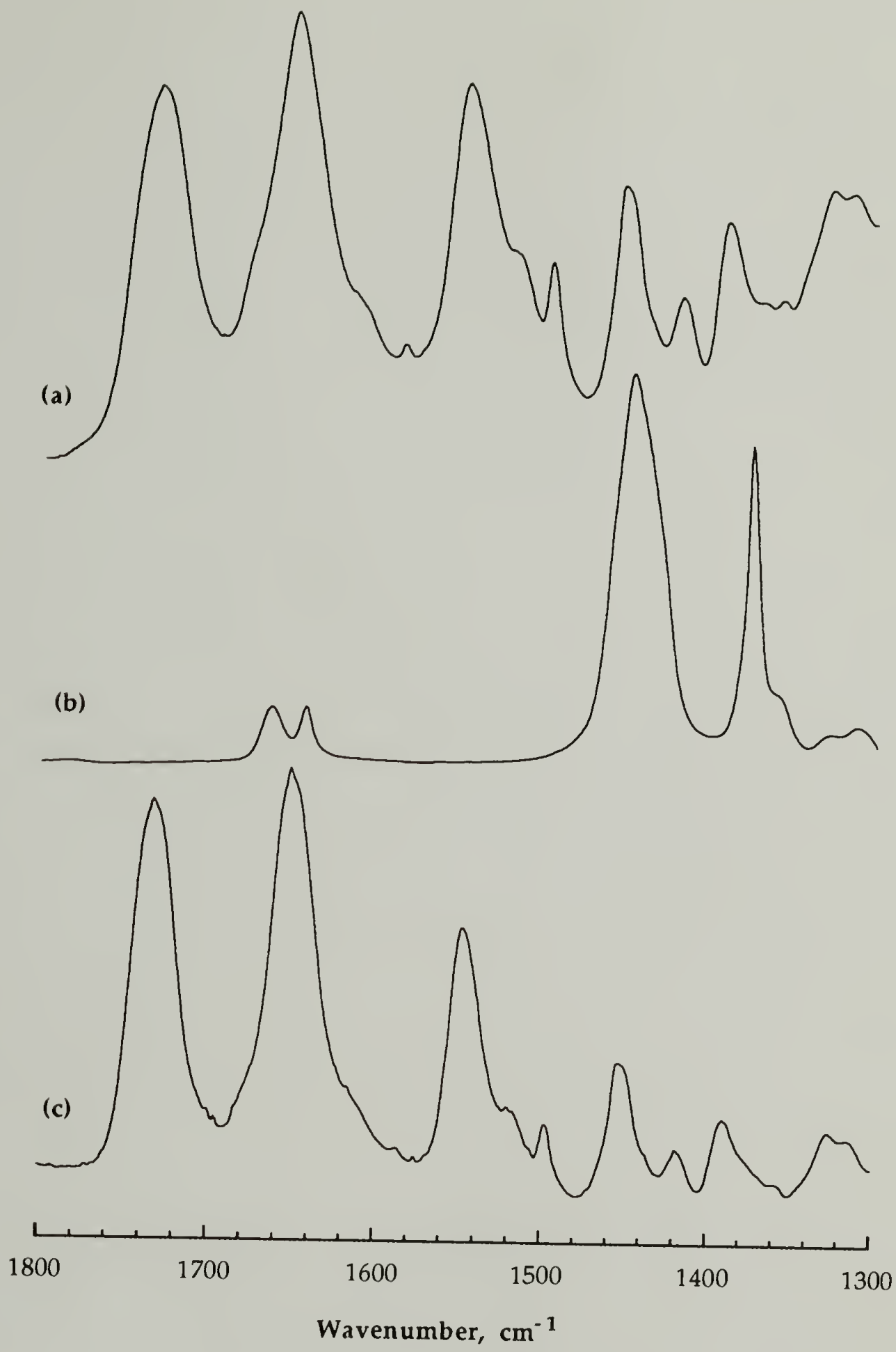

Figure 6.2. Transmission infrared spectra for solution-cast films on NaCl plates. (a) PBLG, (b) cis 1,4-polyisoprene, (c) 64K PI-block-26K PBLG.

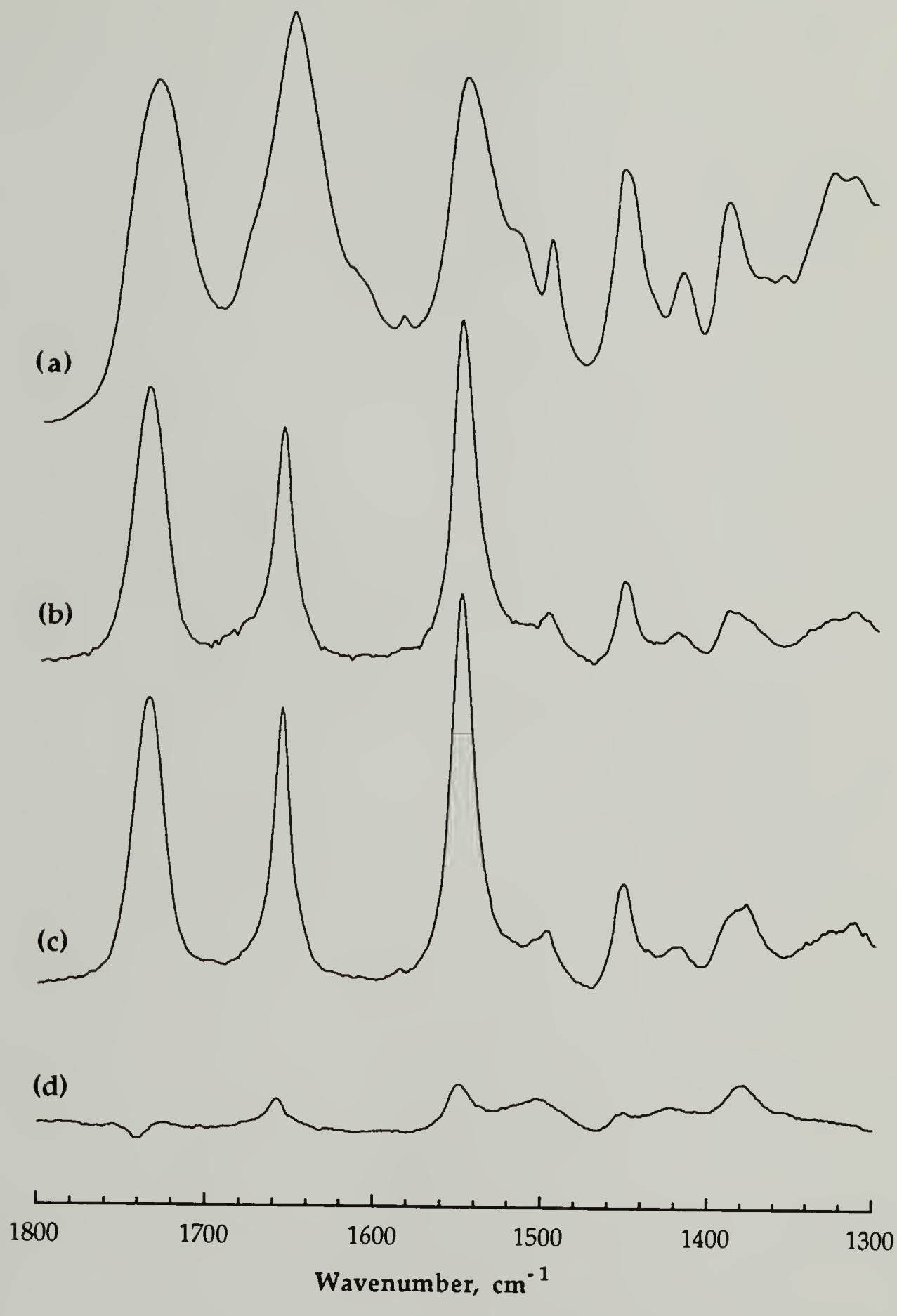

Figure 6.3. Comparison of infrared spectra for PBLG and PI-b-PBLG. (a) Transmission spectrum of solution cast PBLG, (b) Reflectance spectrum of 26K PBLG adsorbed onto gold, (c) Reflectance spectrum of 2.8K PI-b-26K PBLG adsorbed onto gold, (d) Sample from (c) rinsed with DMF.

CHAPTER VII
CONCLUSIONS AND FUTURE WORK

A. Introduction

This chapter summarizes the major conclusions of this dissertation and discusses ideas for future work. An emphasis is given to solution and surface microstructures where novel structures have been proposed. Experimental techniques which probe different features of the microstructures are proposed as well as specific modifications of the rod-coil system. Design modifications are based on the knowledge gained throughout this project and are intended to favor specific microstructures and to facilitate interpretation.

B. Dissertation Conclusions

The primary objective of this research project has been to initiate experimental investigations into a novel field of polymer science: rod-coil block copolymers. The system chosen for study is a series of poly(isoprene-block-(γ-benzyl-L-glutamate)) diblock copolymers with varying molecular weights of each block. This work has served to develop a basic understanding of the influence of block rigidity on structure evolution in selective solvents and at interfaces.

The drive to incorporate rigidity into block copolymers is motivated by the desire to access new microstructures in solution which may be useful as molecular building blocks. Conformational constraints in the rigid block confer an additional measure of order on the system, an important element

for building block components. These building blocks may then serve as components in a complex supramolecular structure, such as a synthetic enzyme. The structure of rod-coil diblock and triblock copolymers in selective solvents may also lead to modified storage and display devices. For example, micellar aggregates may be useful as fast-working ferroelectric and paraelectric media for electrooptic devices. [69, 77]

This work also investigates the organization of a model rod-coil diblock at an impenetrable surface. Tethered rod structures are potentially useful for imparting surface biocompatibility [28] and as model systems for biological membranes and surfactant monolayers. [80] Molecularly thin, surface layers with a precise thickness and an exact placement of functionalities are possible. In addition, adsorbed rods are expected to result in a fundamentally different type of colloidal stabilization. Rods may tilt or interpenetrate to alleviate the compressive stresses. Both tilting and interpenetration are basically prohibited effects in adsorbed coils because the chains will simply retreat from their stretched state and become more coiled as the surfaces are compressed. [33]

Finally, rod-coil diblock copolymers offer the potential for new ways to exploit the liquid crystallinity of rod-like polymers. For example, liquid crystals are important reinforcing components, [65, 81] but their usefulness suffers from the incompatibility of the rods in the (coil) matrix and from the unidirectionality of the reinforcement. The rigid-rod star structures which form in a rod-selective solvent have the potential to remove both of these limitations by providing reinforcement in all directions.

Chapter I was an introductory chapter reviewing relevant literature and theory and defining the goals of the project. Nearly all of the work in the field of block copolymers has focused on flexible-coil block copolymers. With

the exception of the work done in this dissertation, no experimental work has been published in the field of rod-coil block copolymers in dilute solution or at interfaces. Limited work [23, 26-28] has been published concerning the microstructures formed by rod-coil diblock copolymers in the bulk and in highly concentrated solutions.

The rod block is a key component of these structures. This block was studied in detail to determine the influence of the intermolecular dipole-dipole interaction on the relative stability of various helix orientations. Of primary interest, was the magnitude of the coulombic energy for a parallel orientation of α-helices. An analytical model was developed to calculate the coulombic energy of parallel helices as a function of separation, chain length, tilt angle, and dipole moment. This model agreed well with results from a molecular dynamics simulation of the same system. A comparison of the van der Waals and coulombic contributions to the energy of this arrangement indicated that such a monolayer would only be energetically stable over a small range of separations near the van der Waals hard-core limit. At surfaces, end-functionalized helices (including rod-coil diblocks with an adsorbing coil block) are predicted to adsorb into parallel orientations if the adsorption energy is sufficiently high. The second geometry studied was the end-to-end orientation of α-helices. The antiparallel orientation is more energetically favorable at all separations and is predicted for rod-coil diblock copolymer aggregates in solution.

The molecular dynamics modeling was also used to evaluate end-to-end geometries: head-to-head and head-to-tail. Most importantly, repulsion for the head-to-head orientation was shown to be relatively long-ranged, approximately 4 nm. This repulsion appeared to manifest itself in the micelles formed in a rod-selective solvent. The isolation of the polyisoprene

coils to the solvent-poor core region had the effect of orienting the helices radially outward. This led to a head-to-head interaction which affected the rate of diffusion. This enhanced repulsive interaction is expected to provide a unique and useful type of colloidal stabilization. The interaction between approaching colloids would be much more long-ranged relative to stabilization accomplished with conventional flexible-coil chains.

Chapter III described in detail the strategy used to prepare the PI-block-PBLG rod-coil diblock copolymers used throughout this work. The blocks were prepared and purified individually. PBLG has an inherent terminal amine functionality which enabled its coupling to carboxy-terminated polyisoprene via a peptide coupling reaction. It is important to note that this synthetic strategy produced diblocks in which the polyisoprene tail was always on the same end of the PBLG such that the PBLG dipoles point *toward* the flexible coil tails. Structures in which the PI coils are localized to a single plane, such as self-assembled monolayers, will have the helices oriented parallel to one another. Purification pathways were analyzed and the method of selective fractionation was introduced as an effective purification strategy for the removal of PBLG homopolymer.

Chapter IV described the experimental techniques, sample preparation, and data analyses which were used in this work. Dynamic and total intensity light scattering, differential refractometry, reflectance infrared spectroscopy, and ellipsometry were discussed.

Chapter V describes in detail the solution microstructures that were observed in these rod-coil diblock copolymers. This chapter investigated the structures formed by PI-PBLG rod-coil diblock copolymers in three solvent systems: non-selective, rod-selective, and coil-selective. The non-selective solvent chosen was dichloromethane. This solvent is non-polar and does not

break-up aggregation between PBLG α-helices; weak aggregation was observed for the rod-coil diblocks. Aggregation was confined to interactions between the rod blocks as evidenced by similar scattering from PBLG homopolymers and PI-PBLG diblocks. The data from this system served as a control for the two selective solvents.

In the rod-selective solvent, N,N-dimethylformamide, self-assembly led to unusual, star-like arrangements of rods tethered by extended polyisoprene cores. Anomalously low ratios of the radius of gyration to the hydrodynamic radius were attributed to the repulsive interaction between micelles, as discussed above. Large, narrow polydispersity, spherical micelles were formed for the all of the diblocks except those possessing the longest rod blocks. Certainly, theoretical developments in this field would be helpful in understanding the underlying reasons for this molecular weight effect.

Aggregation in the coil-selective solvent was much more sensitive to the length of the polyisoprene coil block. Only two diblocks formed micellar aggregates: 64K PI-b-26K PBLG and 64K PI-b-59K PBLG. Long coil blocks appear to be a prerequisite to micelle formation, as predicted theoretically. [77] These micelles are proposed to be disk-like and are believed to be composed of a central core of axially-packed PBLG helices. A single coil-selective solvent was not identified for this system and consequently a mixed solvent of dichloromethane and heptane was used. The addition of heptane to the system makes the solvent progressively more selective for the coil. Solvent composition had profound effects on the aggregation behavior of the diblocks. A detailed investigation of micelle structure in the miscibility window was undertaken for the 64K PI-b-59K PBLG diblock. Addition of heptane resulted in progressively larger and more disk-like aggregates. At a critical

composition, the diblocks retreated to the small size scale rod-like structures observed for the non-micellizing diblocks.

Chapter VI studied the adsorption of a series of PI-PBLG rod-coil diblock copolymers from a rod-selective solvent onto gold. Reflectance infrared spectroscopy and ellipsometry results showed that both the PBLG homopolymers and the diblock copolymers formed adsorbed layers in which the PBLG helices were oriented parallel to the substrate. The inability of this system to form highly ordered self-assembled monolayers was attributed to the repulsive α-helix dipole-dipole interaction and was related to the effects described in Chapter II.

C. Future Work

Although the technology to prepare rod-coil block copolymers has been available for decades, experimental and theoretical work in this area has been minimal, especially in comparison to the plethora of work which has been devoted to conventional flexible-coil block copolymers. Further advances toward understanding these powerful building block components are essential.

Future work should address three main areas of investigation. First, a more comprehensive understanding of the internal structure of the micelles formed in selective solvents needs to be established. This includes determining the effect of rod and coil block lengths on the dimensions of the core and coronal regions and the structure of these regions. Specifically, the liquid crystalline core which has been proposed for the micelles formed in the coil-selective solvent should be proven experimentally. Future experiments should include light scattering with isorefractive solvents or neutron

scattering with the appropriate choice of deuterated or protonated solvents in which the entire micelle or only the core or the corona would be visible. The latter approach is more practical since the limited availability of rod-selective solvents for PI-PBLG makes finding isorefractive, rod-selective solvents potentially impossible. Solvent limitations will also be a concern for further investigations of micelle structure in coil-selective solvents. Identification of a single coil-selective solvent, as opposed to a mixed solvent, would make data interpretation more straightforward and reduce the number of experimental variables. Direct TEM imaging of freeze-fractured micelles would be very beneficial in characterizing rod-coil diblock micelles. Osmium tetroxide staining of the isoprene residues would distinguish the PI regions and provide a better understanding of the shape and organization of the micelles.

Second, the factors affecting micellization need to be better understood. Concentration and temperature effects on micellization should be examined to determine the critical micelle concentration and temperature for both rod-selective and coil-selective solvents. Future work should also include theoretical predictions regarding the self-assembly of rod-coil block copolymers in rod-selective solvents.

The third major area of future work should involve modified rod-coil diblock copolymers. Certainly the choice of the rod will affect the structures formed. Other rods including main-chain rigid rods and rods with various persistence lengths, axial ratios, diameters, and intermolecular interactions should be investigated using the solution and surface methods of this dissertation. Rod-coil diblock copolymers incorporating monodisperse PBLG rods (prepared by recombinant DNA methodology [84]) may self-assemble more readily into smectic arrangements than the conventional highly polydisperse

analog. Another interesting potential system is a mixed rod-coil system of N- and C-functionalized helices. These mixed diblocks are expected to preferentially assemble into bilayer micelles in a coil-selective solvent. The bilayer arrangement allows for the anti-parallel alignment of helices. It is clear that there are numerous design variables which will affect self-assembled solution microstructures and allow tailoring of rod-coil diblock copolymer building blocks.

Vast potential exists for studying rod-coil block copolymers at interfaces since the desired highly ordered normal arrangement of rods has yet to be prepared. Modifying the nature of the rods may be the key to the formation of the desired microstructure. Films of various types of rod-coil block copolymers should be studied with the techniques used in this thesis in order to ascertain whether the barrier to achieve the desired normal ordering is limited by the choice of the rod or by fundamental thermodynamic considerations such as entropy. A mixture of N-functionalized and C-functionalized PBLG rods is a desirable candidate for adsorption studies since the attractive intermolecular interaction between these (anti-parallel) rods would favor dense monolayer formation at relatively low surface densities, as predicted by theory. [75] Other rods in which intermolecular interactions are negligible should be investigated; theory predicts a continuous ordering with increasing surface density. The ordering transition [75] may possibly be observed if the adsorption is followed in situ using the attenuated total reflection infrared geometry. Other techniques such as neutron reflectance, X-ray scattering, X-ray photoelectron spectroscopy, and AFM or STM would be useful in determining structure of ordered monolayers. Tethered rods which are highly ordered normal to the surface should be studied with the surface forces apparatus in order to understand the interactions between the brushes.

Tethered rods are expected to be useful for colloidal stabilization. Both the surface monolayers and the solution structures formed in rod-selective solvents can utilize the rigid, highly-ordered nature of the rods to specifically locate functional groups on the outer surface of the structures. These functional groups (present at the end of the rod) may be inherently useful or may serve as reactive sites for further chemical modification. Once assembled, surface and solution microstructures can be "cross-linked" either through the residual PI unsaturation or through the PBLG helices or both [164] to "capture" the microstructures especially for use as building block components.

The initial investigations into the solution and surface structure of rod-coil diblock copolymers promise that these molecules will excite and challenge researchers for years to come.

APPENDIX

DERIVATION OF THE DIPOLE-DIPOLE INTERACTION ENERGY

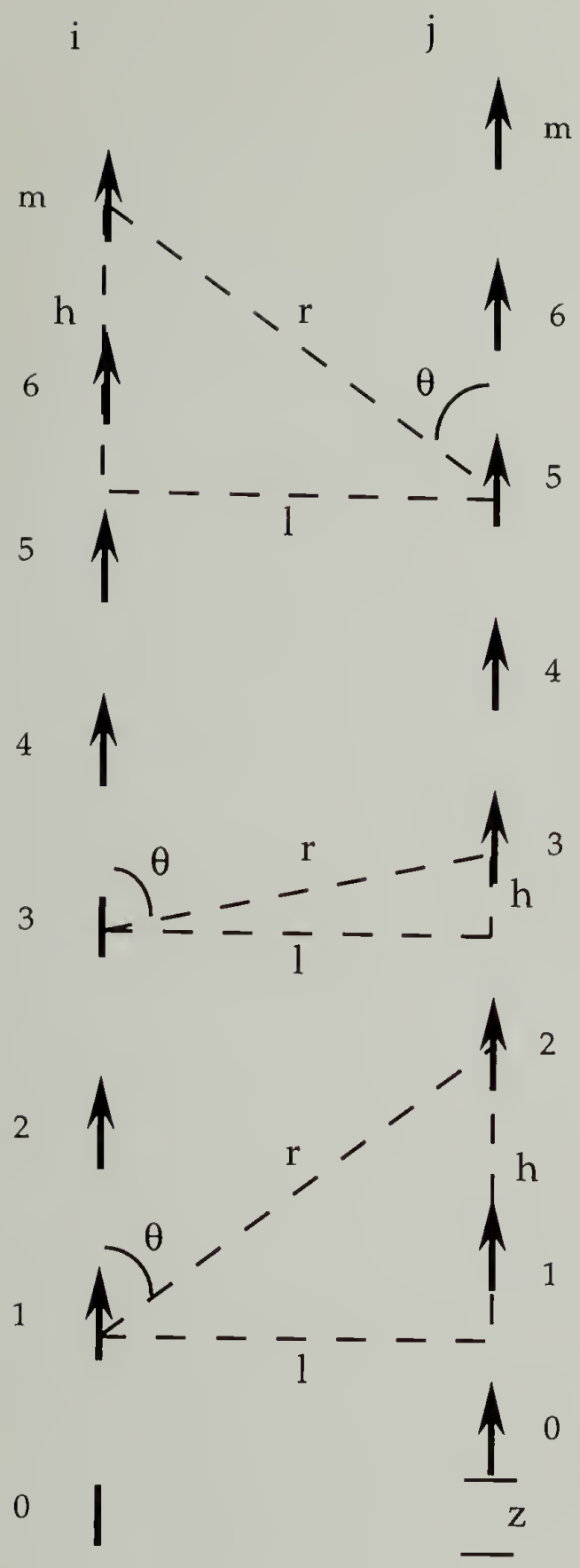

$$h = (i-j)a - z$$

$$i > j \qquad r_{ij}^2 = [(i-j)a - z]^2 + l^2$$

$$\cos\theta = \frac{(i-j)a - z}{[((i-j)a - z)^2 + l^2]^{1/2}}$$

$$h = z$$

$$i = j \qquad r_{ij}^2 = z^2 + l^2$$

$$\cos\theta = \frac{z}{(z^2 + l^2)^{1/2}}$$

$$h = (j-i)a + z$$

$$i < j \qquad r_{ij}^2 = [(j-i)a + z]^2 + l^2$$

$$\cos\theta = \frac{(j-i)a + z}{[((j-i)a + z)^2 + l^2]^{1/2}}$$

Figure A.1. Calculation regimes for evaluating the energy between lines of dipoles. The necessary relationships for each regime are given.

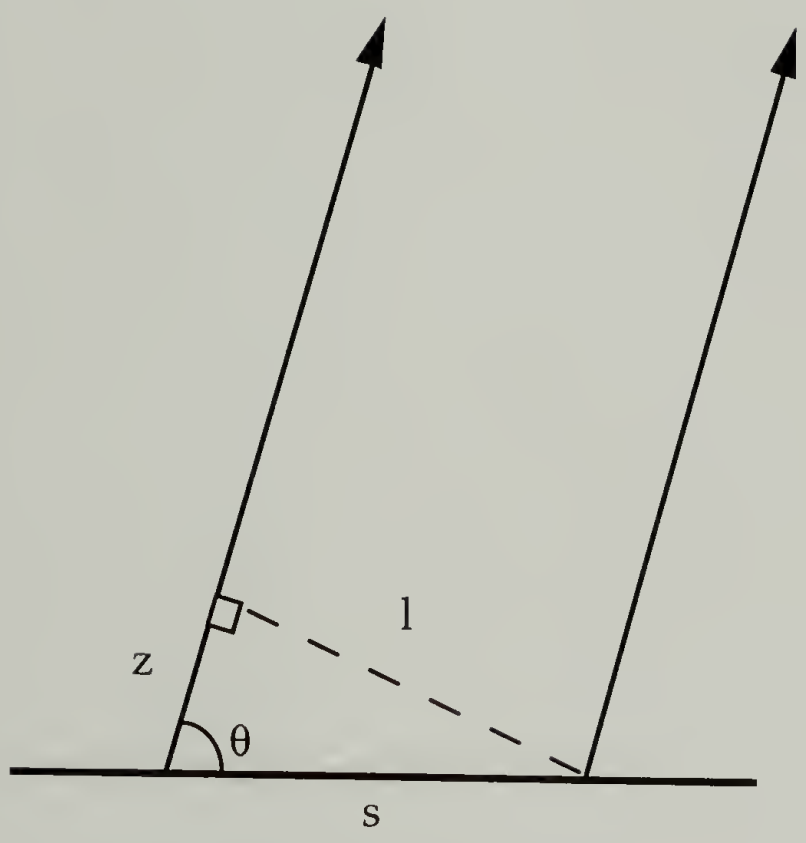

$$\sin\theta = \frac{l}{s}$$

$$\cos\theta = \frac{z}{s}$$

Figure A.2. Schematic of the substitution of z for θ.

$$\frac{4\pi\varepsilon}{\mu^2} E = \sum_{i=0}^{m} \sum_{j=0}^{m} \frac{1}{r_{ij}^3} (1 - 3\cos^2\theta)$$

$$= \sum_{i=0}^{m} \frac{1}{r_{ii}^3} (1 - 3\cos^2\theta) + \sum_{i=0}^{m} \sum_{j\neq i}^{m} \frac{1}{r_{ij}^3} (1 - 3\cos^2\theta)$$

Condition 1: $i = j$

$$h = z$$

$$r_{ii}^2 = z^2 + l^2$$

$$\cos\theta = \frac{z}{(z^2 + l^2)^{1/2}}$$

Condition 2: $i > j$

$$h = (i - j)a - z$$

$$r_{ij}^2 = ((i - j)a - z)^2 + l^2$$

$$\cos\theta = \frac{(i - j)a - z}{[((i - j)a - z)^2 + l^2]^{1/2}}$$

Condition 3: $j > i$

$$h = z + (j - i)a$$

$$r_{ij}^2 = (z + (j - i)a)^2 + l^2$$

$$\cos\theta = \frac{z + (j - i)a}{[(z + (j - i)a)^2 + l^2]^{1/2}}$$

$$= \frac{(m+1)}{(z^2+l^2)^{3/2}} - \frac{3z^2(m+1)}{(z^2+l^2)^{5/2}} + \sum_{j=0}^{m}\sum_{i>j}^{m}\frac{1}{r_{ij}^3}(1-3\cos^2\theta)$$

$$+ \sum_{i=0}^{m}\sum_{j>i}^{m}\frac{1}{r_{ij}^3}(1-3\cos^2\theta)$$

$$= \frac{(L+a)(l^2-2z^2)}{a(z^2+l^2)^{5/2}} + \sum_{j=0}^{m}\sum_{i>j}^{m}\frac{1}{r_{ij}^3}(1-3\cos^2\theta)$$

A

$$+ \sum_{i=0}^{m}\sum_{j>i}^{m}\frac{1}{r_{ij}^3}(1-3\cos^2\theta)$$

B

Solving for "A":

$$\sum_{j=0}^{m}\sum_{i>j}^{m}\frac{1}{r_{ij}^3}(1-3\cos^2\theta)$$

$$= \sum_{j=0}^{m}\sum_{i>j}^{m}\frac{1}{r_{ij}^3} - \sum_{j=0}^{m}\sum_{i>j}^{m}3\frac{\cos^2\theta}{r_{ij}^3}$$

$$= \sum_{j=0}^{m}\sum_{i>j}^{m}\frac{1}{[((i-j)a-z)^2+l^2]^{3/2}} - 3\sum_{j=0}^{m}\sum_{i>j}^{m}\frac{((i-j)a-z)^2}{[((i-j)a-z)^2+l^2]^{5/2}}$$

let $s = ia$; $s' = ja$; $\Delta i = ds/a$; $\Delta j = ds'/a$; $ma = L$

$$= \int_0^L \frac{ds'}{a}\int_{s'}^{L}\frac{ds}{a}\frac{1}{[((s-s')-z)^2+l^2]^{3/2}} - 3\int_0^L\frac{ds'}{a}\int_{s'}^{L}\frac{ds}{a}\frac{(s-s'-z)^2}{[(s-s'-z)^2+l^2]^{5/2}}$$

let $x = s - s'$

$$dx = ds \qquad \int_{s'}^{L} ds = \int_{0}^{L-s'} dx$$

$$= \frac{1}{a^2} \int_0^L ds' \int_0^{L-s'} dx \, \frac{1}{[(x-z)^2 + l^2]^{3/2}} - \frac{3}{a^2} \int_0^L ds' \int_0^{L-s'} dx \, \frac{(x-z)^2}{[(x-z)^2 + l^2]^{5/2}}$$

let $p = x - z$

$$dx = dp \qquad \int_0^{L-s'} dx = \int_{-z}^{L-s'-z} dp$$

$$= \frac{1}{a^2} \int_0^L ds' \int_{-z}^{L-s'-z} dp \, \frac{1}{(p^2 + l^2)^{3/2}} - \frac{3}{a^2} \int_0^L ds' \int_{-z}^{L-s'-z} dp \, \frac{p^2}{(p^2 + l^2)^{5/2}}$$

$$= \frac{1}{a^2} \int_0^L ds' \left[\frac{p}{l^2 (p^2 + l^2)^{1/2}} \right]_{-z}^{L-s'-z} - \frac{3}{a^2} \int_0^L ds' \int_{-z}^{L-s'-z} dp \, \frac{p^2}{(p^2 + l^2)^{5/2}}$$

1 **2**

Solving for "A1":

$$\frac{1}{a^2}\int_0^L ds' \left[\frac{p}{l^2\,(p^2+l^2)^{1/2}}\right]_{-z}^{L-s'-z}$$

$$= \frac{1}{a^2}\int_0^L ds' \left[\frac{L-s'-z}{l^2\,((L-s'-z)^2+l^2)^{1/2}} + \frac{z}{l^2\,(z^2+l^2)^{1/2}}\right]$$

$$= \frac{zL}{a^2 l^2\,(z^2+l^2)^{1/2}} + \frac{1}{a^2}\int_0^L ds' \frac{L-s'-z}{l^2\,((L-s'-z)^2+l^2)^{1/2}}$$

let $t = L - s' - z$

$$dt = -ds' \qquad \int_0^L ds' = -\int_{L-z}^{-z} dt = \int_{-z}^{L-z} dt$$

$$= \frac{zL}{a^2 l^2\,(z^2+l^2)^{1/2}} + \frac{1}{a^2}\int_{-z}^{L-z} dt \frac{t}{l^2\,(t^2+l^2)^{1/2}}$$

$$= \frac{zL}{a^2 l^2\,(z^2+l^2)^{1/2}} + \frac{1}{a^2}\left[\frac{1}{l^2}\,(t^2+l^2)^{1/2}\right]_{-z}^{L-z}$$

$$= \frac{zL}{a^2 l^2\,(z^2+l^2)^{1/2}} + \frac{1}{a^2 l^2}\left[\left((L-z)^2+l^2\right)^{1/2} - (z^2+l^2)^{1/2}\right]$$

Solving for "A2":

$$-\frac{3}{a^2}\int_0^L ds' \int_{-z}^{L-s'-z} dp \, \frac{p^2}{(p^2+l^2)^{5/2}}$$

let $u = p$ $\quad dv = p(p^2+l^2)^{-5/2}\,dp$

$du = dp$ $\quad v = -\frac{1}{3}(p^2+l^2)^{-3/2}$

$$= -\frac{3}{a^2}\int_0^L ds' \left[-\frac{1}{3} p (p^2+l^2)^{-3/2} - \int_{-z}^{L-s'-z} (-\frac{1}{3})(p^2+l^2)^{-3/2}\,dp \right]$$

$$= \frac{1}{a^2}\int_0^L ds' \left[p(p^2+l^2)^{-3/2} \right]_{-z}^{L-s'-z} - \frac{1}{a^2}\int_0^L ds' \int_{-z}^{L-s'-z} dp \, (p^2+l^2)^{-3/2}$$

$$= \frac{1}{a^2}\int_0^L ds' \left[p(p^2+l^2)^{-3/2} - \frac{p}{l^2(p^2+l^2)^{1/2}} \right]_{-z}^{L-s'-z}$$

$$= \frac{1}{a^2}\int_0^L ds' \left[(L-s'-z)((L-s'-z)^2+l^2)^{-3/2} - \frac{L-s'-z}{l^2((L-s'-z)^2+l^2)^{1/2}} \right.$$

$$\left. + \frac{z}{(z^2+l^2)^{3/2}} - \frac{z}{l^2(z^2+l^2)^{1/2}} \right]$$

$$\left. + \frac{z}{(z^2+l^2)^{3/2}} - \frac{z}{l^2(z^2+l^2)^{1/2}} \right]$$

let $t = L - s' - z$

$dt = -ds'$ $\quad \int_0^L ds' = -\int_{L-z}^{-z} dt = \int_{-z}^{L-z} dt$

$$= \frac{1}{a^2}\int_{-z}^{L-z} dt \left[\frac{t}{(t^2+l^2)^{3/2}} - \frac{t}{l^2(t^2+l^2)^{1/2}}\right]$$

$$+ \frac{zL}{a^2}\left(\frac{1}{(z^2+l^2)^{3/2}} - \frac{1}{l^2(z^2+l^2)^{1/2}}\right)$$

$$= \frac{1}{a^2}\left[\frac{-1}{(t^2+l^2)^{1/2}} - \frac{1}{l^2}(t^2+l^2)^{1/2}\right]_{-z}^{L-z}$$

$$+ \frac{zL}{a^2}\left(\frac{1}{(z^2+l^2)^{3/2}} - \frac{1}{l^2(z^2+l^2)^{1/2}}\right)$$

$$= -\frac{1}{a^2}\left[\frac{1}{\left((L-z)^2+l^2\right)^{1/2}} - \frac{1}{(z^2+l^2)^{1/2}} + \frac{1}{l^2}\left((L-z)^2+l^2\right)^{1/2}\right]$$

$$+ \frac{(z^2+l^2)^{1/2}}{a^2 l^2} + \frac{zL}{a^2}\left(\frac{1}{(z^2+l^2)^{3/2}} - \frac{1}{l^2}\frac{1}{(z^2+l^2)^{1/2}}\right)$$

Solving for "B":

$$\sum_{i=0}^{m}\sum_{j>i}^{m}\frac{1}{r_{ij}^3}\left(1 - 3\cos^2\theta\right)$$

$$= \sum_{i=0}^{m}\sum_{j>i}^{m}\frac{1}{r_{ij}^3} - 3\sum_{i=0}^{m}\sum_{j>i}^{m}\frac{\cos^2\theta}{r_{ij}^3}$$

$$= \sum_{i=0}^{m}\sum_{j>i}^{m}\frac{1}{\left[\left(z+(j-i)\,a\right)^2 + l^2\right]^{3/2}} - 3\sum_{i=0}^{m}\sum_{j>i}^{m}\frac{\left(z+(j-i)\,a\right)^2}{\left[\left(z+(j-i)\,a\right)^2 + l^2\right]^{5/2}}$$

let $s = ia$; $s' = ja$; $\Delta i = ds/a$; $\Delta j = ds'/a$

$$= \int_0^L \frac{ds'}{a}\int_s^L \frac{ds'}{a}\frac{1}{\left[\left(z+s'-s\right)^2 + l^2\right]^{3/2}} - 3\int_0^L \frac{ds}{a}\int_s^L \frac{ds'}{a}\frac{\left(z+s'-s\right)^2}{\left[\left(z+s'-s\right)^2 + l^2\right]^{5/2}}$$

let $x = s' - s$

$$dx = ds' \qquad \int_s^L ds' = \int_0^{L-s} dx$$

$$= \frac{1}{a^2}\int_0^L ds\int_0^{L-s} dx\,\frac{1}{\left[\left(z+x\right)^2 + l^2\right]^{3/2}} - \frac{3}{a^2}\int_0^L ds\int_0^{L-s} dx\,\frac{\left(z+x\right)^2}{\left[\left(z+x\right)^2 + l^2\right]^{5/2}}$$

let $p = z + x$

$$dp = dx \qquad \int_0^{L-s} dx = \int_z^{L-s+z} dp$$

$$= \frac{1}{a^2}\int_0^L ds\int_z^{L-s+z} dp\,\frac{1}{\left(p^2+l^2\right)^{3/2}} - \frac{3}{a^2}\int_0^L ds\int_z^{L-s+z} dp\,\frac{p^2}{\left(p^2+l^2\right)^{5/2}}$$

1 **2**

Solving for "B1":

$$\frac{1}{a^2}\int_0^L ds \int_z^{L-s-z} dp \frac{1}{(p^2 + l^2)^{3/2}}$$

$$= \frac{1}{a^2}\int_0^L ds \left[\frac{p}{l^2 (p^2 + l^2)^{1/2}}\right]_z^{L-s-z}$$

$$= \frac{1}{a^2}\int_0^L ds \left[\frac{(L - s + z)}{l^2\left((L - s + z)^2 + l^2\right)^{1/2}} - \frac{z}{l^2 (z^2 + l^2)^{1/2}}\right]$$

$$= \frac{1}{a^2}\int_0^L ds \left[\frac{L - s + z}{l^2\left((L - s + z)^2 + l^2\right)^{1/2}}\right] - \frac{zL}{a^2 l^2 (z^2 + l^2)^{1/2}}$$

let $t = L - s + z$

$$dt = -ds \qquad \int_0^L ds = -\int_{L+z}^{z} dt = \int_z^{L+z} dt$$

$$= \frac{1}{a^2}\int_z^{L+z} dt \frac{t}{l^2 (t^2 + l^2)^{1/2}} - \frac{zL}{a^2 l^2 (z^2 + l^2)^{1/2}}$$

$$= \frac{1}{a^2}\left[\frac{(t^2 + l^2)^{1/2}}{l^2}\right]_z^{L+z} - \frac{zL}{a^2 l^2 (z^2 + l^2)^{1/2}}$$

$$= \frac{1}{a^2 l^2}\left[\left((L + z)^2 + l^2\right)^{1/2} - (z^2 + l^2)^{1/2}\right] - \frac{zL}{a^2 l^2 (z^2 + l^2)^{1/2}}$$

Solving for "B2":

$$-\frac{3}{a^2}\int_0^L ds \int_z^{L-s+z} dp \, \frac{p^2}{(P^2 + l^2)^{5/2}}$$

let $u = p$ $\qquad dv = p(p^2 + l^2)^{-5/2}\, dp$

$du = dp$ $\qquad v = -\frac{1}{3}(p^2 + l^2)^{-3/2}$

$$= -\frac{3}{a^2}\int_0^L ds \left[\frac{-p(p^2 + l^2)^{-3/2}}{3} - \int_z^{L-s+z} \frac{-(p^2 + l^2)^{-3/2}}{3}\, dp \right]$$

$$= \frac{1}{a^2}\int_0^L ds \left[p(p^2 + l^2)^{-3/2} \right]_{-z}^{L-s+z} - \frac{1}{a^2}\int_0^L ds \int_{-z}^{L-s+z} dp \, (p^2 + l^2)^{-3/2}$$

$$= \frac{1}{a^2}\int_0^L ds \left[p(p^2 + l^2)^{-3/2} - \frac{p}{l^2(p^2 + l^2)^{1/2}} \right]_z^{L-s+z}$$

$$= \frac{1}{a^2}\int_0^L ds \left[\frac{L-s+z}{\left((L-s+z)^2 + l^2\right)^{3/2}} - \frac{L-s+z}{l^2\left((L-s+z)^2 + l^2\right)^{1/2}} \right.$$

$$\left. - \frac{z}{(z^2 + l^2)^{3/2}} + \frac{1}{l^2(z^2 + l^2)^{1/2}} \right]$$

$$= \frac{1}{a^2}\int_0^L ds \left[\frac{L-s+z}{\left((L-s+z)^2 + l^2\right)^{3/2}} - \frac{L-s+z}{l^2\left((L-s+z)^2 + l^2\right)^{1/2}}\right]$$

$$+ \frac{zL}{a^2}\left[\frac{1}{l^2(z^2+l^2)^{1/2}} - \frac{1}{(z^2+l^2)^{3/2}}\right]$$

let $t = L - s + z$

$$dt = -ds \qquad \int_0^L ds = -\int_{L+z}^{z} dt = \int_z^{L+z} dt$$

$$= \frac{1}{a^2}\int_z^{L+z} dt \left[\frac{t}{(t^2 + l^2)^{3/2}} - \frac{t}{l^2(t^2 + l^2)^{1/2}}\right]$$

$$+ \frac{zL}{a^2}\left[\frac{1}{l^2(z^2 + l^2)^{1/2}} - \frac{1}{(z^2 + l^2)^{3/2}}\right]$$

$$= \frac{1}{a^2}\left[\frac{-1}{(t^2 + l^2)^{1/2}} - \frac{(t^2 + l^2)^{1/2}}{l^2}\right]_z^{L+z}$$

$$+ \frac{zL}{a^2}\left[\frac{1}{l^2(z^2 + l^2)^{1/2}} - \frac{1}{(z^2 + l^2)^{3/2}}\right]$$

$$= -\frac{1}{a^2}\left[\frac{1}{\left((L+z)^2 + l^2\right)^{1/2}} + \frac{\left((L+z)^2 + l^2\right)^{1/2}}{l^2} - \frac{1}{(z^2 + l^2)^{1/2}}\right]$$

$$+ \frac{(z^2 + l^2)^{1/2}}{a^2 l^2} + \frac{zL}{a^2}\left[\frac{1}{l^2(z^2 + l^2)^{1/2}} - \frac{1}{(z^2 + l^2)^{3/2}}\right]$$

$$\frac{4\pi\varepsilon}{\mu^2} E = \frac{zL}{a^2 l^2 (z^2 + l^2)^{1/2}} + \frac{1}{a^2 l^2}\left[\left((L-z)^2 + l^2\right)^{1/2} - (z^2 + l^2)^{1/2}\right]$$

$$- \frac{1}{a^2}\left[\frac{1}{\left((L-z)^2 + l^2\right)^{1/2}} - \frac{1}{(z^2 + l^2)^{1/2}}\right]$$

$$- \frac{1}{a^2 l^2}\left[\left((L-z)^2 + l^2\right)^{1/2} - (z^2 + l^2)^{1/2}\right]$$

$$+ \frac{zL}{a^2}\left[\frac{1}{(z^2+l^2)^{3/2}} - \frac{1}{l^2 (z^2+l^2)^{1/2}}\right]$$

$$- \frac{zL}{a^2 l^2 (z^2 + l^2)^{1/2}} + \frac{zL}{a^2}\left[\frac{1}{l^2 (z^2+l^2)^{1/2}} - \frac{1}{(z^2+l^2)^{3/2}}\right]$$

$$- \frac{1}{a^2}\left[\frac{1}{\left((L+z)^2 + l^2\right)^{1/2}} - \frac{1}{(z^2 + l^2)^{1/2}}\right]$$

$$- \frac{1}{a^2 l^2}\left[\left((L+z)^2 + l^2\right)^{1/2} - (z^2 + l^2)^{1/2}\right]$$

$$+ \frac{(L + a)(l^2 - 2z^2)}{a(z^2 + l^2)^{5/2}}$$

$$\boxed{\frac{4\pi\varepsilon}{\mu^2} E = \frac{(L + a)(l^2 - 2z^2)}{a(z^2 + l^2)^{5/2}} + \frac{2}{a^2 (z^2 + l^2)^{1/2}} - \frac{1}{a^2}\left[\frac{1}{\left((L-z)^2 + l^2\right)^{1/2}} + \frac{1}{\left((L+z)^2 + l^2\right)^{1/2}}\right]}$$

Figure A.3. Derivation of the dipole-dipole interaction energy.

REFERENCES

(1) Lindoy, L. *Nature* **1994**, *368*, 6467.

(2) Lehn, J. *Science* **1993**, *260*, 1762.

(3) Whitesides, G.; Mathias, J.; Seto, C. *Science* **1991**, *254*, 1312.

(4) Lindsey, J. *New J. Chem.* **1991**, *15*, 153.

(5) Kwon, Y.; Chvalun, S.; Schneider, A.; Blackwell, J.; Percec, V.; Heck, J. *Macromolecules* **1994**, *27*, 6129.

(6) Zhang, J.; Pesak, D.; Ludwick, J.; Moore, J. *J. Am. Chem. Soc.* **1994**, *116*, 4227.

(7) Bhattacharya, S.; Smith, C.; Dickstein, W. *Macromolecules* **1992**, *25*, 1373.

(8) Tomalia, D. *Adv. Mat.* **1994**, *6*, 529.

(9) Bissell, B.; Cordova, E.; Kaifer, A.; Stoddart, J. *Nature* **1994**, *369*, 133.

(10) Sun, X.; Ambilino, D.; Ashton, P.; Parsons, I.; Stoddart, J.; Tolley, M. *Macromol. Symp.* **1994**, *77*, 191.

(11) Amabilino, D.; Stoddart, J. *Pure and Appl. Chem* **1993**, *65*, 2351.

(12) Amabilino, D.; Parsons, I.; Stoddart, J. *Trends Polym. Sci.* **1994**, *2*, 146.

(13) Percec, V.; Heck, J.; Johansson, G.; Tomazos, D.; Kawasumi, M.; Ungar, G. *Macromol. Sci. - Pure and Appl. Chem.* **1994**, *A31*, 1031.

(14) Moore, J.; Zhang, J.; Wu, Z.; Venkataraman, D.; Lee, S. *Macromol. Symp.* **1994**, *77*, 295.

(15) McGrath, K. P.; Kaplan, D. L. *Macromol. Symp.* **1994**, *77*, 183.

(16) Mao, G.; Tsao, Y.; Tirrell, M.; Davis, H. *Langmuir* **1993**, *9*, 3461.

(17) Eisenbach, C.; Heinemann, T.; Ribbe, A.; Stadler, E. *Macromol. Symp.* **1994**, *77*, 125.

(18) Ritter, H. *Macromol. Symp.* **1994**, *77*, 73.

(19) Smith, S.; Spontak, R.; Satkowski, M.; Ashraf, A.; Heape, A.; Lin, J. *Polymer* **1994**, *35*, 4527.

(20) Donley, J.; Fredrickson, G. *Macromolecules* **1994**, *27*, 458.

(21) Dhoot, S.; Watanabe, H.; Tirrell, M. *Colloids Surf. A - Phys. Eng. Aspects* **1994**, *86*, 47.

(22) Koklas, S.; Gravalos, K.; Kalfoglou, N. *Polymer* **1994**, *35*, 1425.

(23) Radzilowski, L. H.; Wu, J. L.; Stupp, S. I. *Macromolecules* **1993**, *26*, 879.

(24) Schrauwen, C.; Pakula, T.; Wegner, G. *Macromol. Chem.* **1992**, *193*, 11.

(25) Adams, J.; Gronski, W. *Makromol. Chem. Rapid Commun.* **1989**, *10*, 553.

(26) Perly, B.; Duoy, A.; Gallot, B. *Makromol. Chem.* **1976**, *177*, 2569.

(27) Duoy, A.; Gallot, B. *Polymer* **1982**, *23*, 1039.

(28) Duoy, A.; Gallot, B. *Polymer* **1987**, *28*, 147.

(29) Kodaira, T.; Mori, K. *Makromol. Chem.* **1992**, *193*, 1331.

(30) Joslin, S.; Jackson, W.; Farris, R. *J. Appl. Polym. Sci* **1994**, *54*, 439.

(31) Ignatious, F.; Lenz, R.; Kantor, S. *Macromolecules* **1994**, *27*, 5248.

(32) Tuzar, Z.; Kratochvil, P. In *Surface and Colloid Science*; E. Matijevic, Ed.; Plenum Press: New York, 1993; Vol. 15.

(33) Halperin, A.; Tirrell, M.; Lodge, T. P. *Advances in Polymer Science* **1992**, *100*, 31.

(34) Tuzar, Z.; Kratochvil, P. *Adv. Coll. Interf. Sci.* **1976**, *6*, 201.

(35) Hashimoto, T.; Shibayama, M.; Kawai, H. *Macromolecules* **1980**, *13*, 1237.

(36) Roe, R.; Fishkis, M.; Chay, J. *Macromolecules* **1981**, *14*, 1091.

(37) Helfand, E. *Macromolecules* **1975**, *8*, 552.

(38) Helfand, E.; Wasserman, Z. R. *Macromolecules* **1976**, *9*, 879.

(39) Helfand, E.; Wasserman, Z. R. *Macromolecules* **1978**, *11*, 960.

(40) Helfand, E.; Wasserman, Z. R. *Macromolecules* **1980**, *13*, 994.

(41) Leibler, L. *Macromolecules* **1980**, *13*, 1602.

(42) Parsonage, E.; Tirrell, M.; Watanabe, A.; Nuzzo, R. *Macromolecules* **1991**, *24*, 1987.

(43) Chu, B. *Photon Correlation Spectroscopy: Applications to Polymer Solutions*, Chapter 8, 1989, p. 161.

(44) Young, C.; Missel, P.; Mazer, N.; Benedek, G.; Carey, M. *J. Phys. Chem.* **1978**, *82*, 1375.

(45) Pecora, R. *Dynamic Light Scattering: Applications of Photon Correlation Spectroscopy*; Plenum Press: New York, 1985.

(46) Sivaram, S.; Singh, R. *Adv. Polym. Sci.* **1991**, *101*, 169.

(47) Krause, G.; Hashimoto, T. *J. Appl. Polym. Sci.* **1982**, *27*, 1745.

(48) Majumdar, B.; Keskkula, H.; Paul, D. R. *Polymer* **1994**, *35*, 1386.

(49) Scott, C.; Macosko, C. *J. Polym. Sci., Polym. Phys.* **1994**, *32*, 205.

(50) Gido, S.; Thomas, E. *Macromolecules* **1994**, *27*, 6137.

(51) Hajduk, D.; Harper, P.; Gruner, S.; Honeker, C.; Kim, G.; Thomas, E.; Fetters, L. *Macromolecules* **1994**, *27*, 4063.

(52) Kaelble, D. *Polym. Sci. Tech.* **1975**, *9A*, 199.

(53) Brown, H. *Science* **1994**, *263*, 1411.

(54) Xu, R.; Dunger, G.; Winnik, M.; Martinho, J.; Doliveira, J. *Langmuir* **1994**, *10*, 2977.

(55) Cosgrove, T.; Phipps, J.; Richardson, R.; Hair, M.; Guzonas, D. *Coll. Surf. A - Physiochem. Engr. Aspects* **1994**, *86*, 91.

(56) deGennes, P. G. *Macromolecules* **1980**, *13*, 1069.

(57) Kwon, G.; Naito, M.; Nataoka, K.; Yokoyama, M.; Sakurai, Y.; Okano, T. *Coll. Surf. B - Biointerfaces* **1994**, *2*, 429.

(58) Ulyanova, N. N.; Baranovskaya, I. A.; Liubina, S.; Bezrukova, M. A.; Rudkovskaya, G. D.; M.Shabsels, B.; Vlasov, G. P.; Eskin, V. E. *Macromolecules* **1991**, *24*, 3324.

(59) Reibel, L.; Spach, G.; Dufour, C. *Biopolymer* **1973**, *12*, 2391.

(60) Bianchi, E.; Ciferri, A.; Conio, G.; Marsano, E.; Tealdi, A. *Macromolecules* **1984**, *17*, 1526.

(61) Marsano, E.; Bianchi, E.; Ciferri, A.; Ramis, G.; Tealdi, A. *Macromolecules* **1986**, *19*, 626.

(62) Hwang, W. F.; Wiff, D. R.; Benner, C. L.; Helminiak, T. E. *J. Macromol. Sci. Phys. Ed.* **1983**, *B22*, 231.

(63) Flory, P. J. *Macromolecules* **1978**, *11*, 1138.

(64) Flory, P. J. *Macromolecules* **1978**, *11*, 1141.

(65) Kwolek, S. L.; Morgan, P. W.; Schaefgen, J. R. In *Encyclopedia of Polymer Science and Engineering, 2nd ed.*; J. I. Kroschwitz, Ed.; John Wiley and Sons: New York, 1987; Vol. 9; p. 1.

(66) deGennes, P. G. *The Physics of Liquid Crystals;* Clarendon Press: Oxford, 1975.

(67) Song, M. H.; Price, G. E.; Vakil, U. M.; Dotrong, M. H. *Am. Chem. Soc., Div. Polym. Chem. Preprints* **1992**, *33*, 319.

(68) Jadhav, J. Y.; Krigbaum, W. R.; Ciferri, A.; Preston, J. *J. Polym. Sci, Polym. Lett.* **1989**, *27*, 59.

(69) Halperin, A. *Europhys. Lett.* **1989**, *10*, 549.

(70) Williams, D. R. M.; Fredrickson, G. H. *Macromolecules* **1992**, *25*, 3561.

(71) Machida, S.; Sano, K.; Sasaki, H.; Yoshiki, M.; Mori, Y. *J. Chem. Soc., Chem. Commun.* **1992**, 1626.

(72) Enriquez, E. P.; Samulski, E. T. *Mat. Res. Soc. Symp. Proc.* **1992**, *255*, 423.

(73) Enriquez, E. P.; Gray, K. H.; Guarisco, V. F.; Linton, R. W.; Mar, K. D.; Samulski, E. T. *J. Vac. Sci. Technol.* **1992**, *A10*, 2775.

(74) Halperin, A.; Alexander, S.; Schechter, I. *J. Chem. Phys.* **1987**, *86*, 6550.

(75) Chen, Z. Y.; Talbot, J.; Gelbart, W.; Ben-Shaul, A. *Phys. Rev. Lett.* **1988**, *61*, 1376.

(76) Semenov, A. N.; Vasilenko, S. V. *Sov. Phys. JETP* **1986**, *63*, 70.

(77) Halperin, A. *Macromolecules* **1990**, *23*, 2724.

(78) Raphael, E.; deGennes, P. G. *Makromol. Chem., Macromol. Symp.* **1992**, *62*, 1.

(79) Petschek, R. G.; Wiefling, K. M. *Phys. Rev. Lett.* **1987**, *59*, 343.

(80) Collings, P. J. *Liquid Crystals: Nature's Delicate Phase of Matter*; Princeton Univ. Press: New York, 1990.

(81) *Liquid Crystals and Their Applications*; Kallard, T., Ed.; Optosonic Press: New York, 1973.

(82) Wada, A. In M. A. Stahman, Ed., *Chain Regularity and Dielectric Properties of Poly-a-Amino Acids in Solution*; Univ. Wisconsin Press: 1962; p. 131.

(83) Wada, A. In M.A. Stahman, Ed., *Polyamino Acids, Polypeptides, and Proteins*; Univ. Wisconsin Press: Madison, 1962.

(84) Zhang, G.; Fournier, M.; Mason, T.; Tirrell, D. *Macromolecules* **1992**, *25*, 3601.

(85) Majda, M. ACS Symp. Ser., 1994; Vol. 561; p. 135.

(86) Nuzzo, R.; Allara, D. *J. Am. Chem. Soc.* **1983**, *105*, 4481.

(87) Rabkeclemmer, C.; Leavitt, A.; Beebe, T. *Langmuir* **1994**, *10*, 1796.

(88) Whitesides, G.; Laibinis, P. *Langmuir* **1990**, *6*, 87.

(89) Ulman, A. *Ultrathin Organic Films*; Academic Press: San Diego, 1991.

(90) Marques, C.; Joanny, J.; Leibler, L. *Macromolecules* **1988**, *21*, 1051.

(91) Carey, F. *Organic Chemistry*; McGraw-Hill: New York, 1987.

(92) Atkins, P. W. *Physical Chemistry*; 3rd ed.; W. H. Freeman and Company: 1986.

(93) Wada, A. *Adv. Biophys.* **1976**, *9*, 1.

(94) Bromberg, J. P. *Physical Chemistry*; Second ed.; Allyn and Bacon, Inc.: Boston, 1984.

(95) Israelachvili, J. *Intermolecular and Surface Forces*; 2nd ed.; Academic Press: 1992.

(96) Tracy, M.; Pecora, R. *Macromolecules* **1992**, *25*, 337.

(97) Russo, P.; Karasz, F.; Langley, K. *J. Chem. Phys.* **1984**, *80*, 5312.

(98) Kubota, K.; Chu, B. *Biopolymers* **1983**, *22*, 1461.

(99) Kubota, K.; Tominaga, Y.; Fujime, S. *Macromolecules* **1986**, *19*, 1604.

(100) Schmidt, M. *Macromolecules* **1984**, *17*, 553.

(101) Doty, P.; Bradbury, J. H.; Holtzer, A. M. *J. Am. Chem. Soc.* **1956**, *78*, 947.

(102) *CRC Handbook of Chemistry and Physics*; 72nd ed.; Lide, D., Ed.; CRC Press: Boston, 1991.

(103) Biosym Technologies, Inc.: San Diego, 1993.

(104) Miyazawa, T.; Blout, E. R. *J. Am. Chem. Soc.* **1961**, *83*, 712.

(105) Miyazawa, T. In M. A. Stahman, Ed., *Polyamino Acids, Polypeptides, and Proteinss*; Univ. Wisconsin Press: Madison, 1962.

(106) Tsuboi, M. *J. Polym. Sci.* **1962**, *59*, 139.

(107) Allerhand, A.; Oldfield, E. *Biochemistry* **1973**, *12*, 3428.

(108) Charney, E.; Milstien, J.; Yamaoka, K. *J. Am. Chem. Soc.* **1970**, *92*, 2657.

(109) Aqvist, J.; Luecke, H.; Quiocho, F.; Warshel, A. *Proc. Natl. Acad. Sci.* **1991**, *88*, 2026.

(110) Tsutsumi, A.; Hikichi, K.; Kaneko, M. *Rep. Progr. Polym. Phys. Jpn.* **1970**, *13*, 331.

(111) Saba, R.; Sauer, J.; Woodward, A. *J. Polym. Sci.* **1963**, *A1*, 1483.

(112) Koleske, J.; Lundberg, R. *Macromolecules* **1969**, *2*, 438.

(113) Hilner, A.; Anderson, J.; Borkowski, E. *Macromolecules* **1972**, *5*, 446.

(114) Tschoegel, N.; Ferry, J. *J. Am. Chem. Soc.* **1964**, *86*, 1474.

(115) Iwata, K. *Biopolymers* **1980**, *19*, 125.

(116) *Polymer Liquid Crystals*; Ciferri, A.; Krigbaum, W. R.; Meyer, R. B., Ed.; Academic Press: New York, 1982.

(117) Gilman, H.; Haubein, A. *J. Am. Chem. Soc.* **1944**, *66*, 1515.

(118) Gilman, H.; Cartledge, F. *J. Organomet. Chem.* **1964**, *2*, 447.

(119) Ndoni, S.; Papadakis, C.; Bates, F.; Almdal, K. *Rev. Sci. Instrum.* **1995**, *66*, 1090.

(120) Quirk, R. P.; Chen, W.-C. *Makromol. Chem.* **1982**, *183*, 2071.

(121) Quirk, R. P.; Yin, J.; Fetters, L. J. *Macromolecules* **1989**, *22*, 85.

(122) Quirk, R. P.; Yin, J. *J. Polym. Sci., Part A: Polym. Chem.* **1992**, *30*, 2349.

(123) Daly, W. H.; Poche, D. *Tetrahedron Lett.* **1988**, *29*, 5859.

(124) Fuller, W.; Verlander, M.; Goodman, M. *Biopolymers* **1976**, *15*, 1869.

(125) Block, H. *Poly(γ-Benzyl-L-Glutamate) and Other Glutamic Acid Containing Polymers*; Gordon and Breach Science Publishers: New York, 1983.

(126) Mitchell, J. C.; Woodward, A. E.; Doty, P. *J. Am. Chem. Soc.* **1957**, *79*, 3955.

(127) Lundberg, R. D.; Doty, P. *J. Am. Chem. Soc.* **1957**, *79*, 3961.

(128) Rich, D.; Singh, J. In *The Peptides;* Academic Press: 1979; Vol. 1; p. 241.

(129) Periard, J.; Riess, G. *Kolloid Z.Z. Polym.* **1971**, *248*, 877.

(130) Periard, J.; Banderet, A.; Riess, G. *Polym. Lett.* **1970**, *8*, 109.

(131) Chu, B. *Laser Light Scattering: Basic Principles and Practice;* 2nd ed.; Academic Press: New York, 1991.

(132) Berne, B.; Pecora, R. *Dynamic Light Scattering;* John Wiley and Sons: New York, 1976.

(133) Provencher, S. *Comput. Phys. Commun.* **1982**, *27*, 213.

(134) Provencher, S. *Comput. Phys. Commun.* **1982**, *27*, 229.

(135) *Polymer Handbook*; 3rd ed.; Brandrup, J.; Immergut, E. H., Ed.; John Wiley and Sons, Inc: New York, 1989.

(136) Huglin, M. *Light Scattering from Polymer Solutions;* Academic Press: New York, 1972.

(137) Kerker, M. *Scattering of Light and Other Electromagnetic Radiation;* Academic Press: New York, 1969.

(138) Munk, P. *Introduction to Macromolecular Science;* Wiley: New York, 1989.

(139) Wyatt, P. J. *Anal. Chim. Acta* **1993**, *272*, 1.

(140) J. Ingle, J.; Crouch, S. *Spectrochemical Analysis;* Prentice Hall: Englewood Cliffs, 1988.

(141) Greenler, R. G. *J. Chem. Phys.* **1966**, *44*, 310.

(142) Azzam, R. M.; Bashara, N. M. *Ellipsometry and Polarized Light;* Elsevier Science Publishers: New York, 1988.

(143) Russo, P.; Miller, W. *Macromolecules* **1984**, *17*, 1324.

(144) Perrin, F. *J. Phys. Radium* **1936**, *7*, 1.

(145) Broersma, S. *J. Chem. Phys.* **1960**, *32*, 1626.

(146) Broersma, S. *J. Chem. Phys.* **1960**, *32*, 1632.

(147) Katime, I.; Quintana, J. In *Comprehensive Polymer Sci.*; G. Allen, Ed.; 1989; Vol. I; p. 103.

(148) Halliday, L.; White, J. *Pure Appl. Chem.* **1971**, *26*, 545.

(149) Dickstein, W. Ph.D. Thesis, University of Massachusetts, 1987.

(150) Daoud, M.; Cotton, J. P. *J. Phys. (Paris)* **1982**, *43*, 531.

(151) Birshtein, T. M.; Zhulina, E. B. *Polymer* **1984**, *25*, 1453.

(152) Zhulina, E. B.; Birshtein, T. M. *Polym. Sci. USSR* **1985**, *27*, 570.

(153) Birshtein, T. M.; Borisov, O. V.; Zhulina, E. B.; Khokhlov, A. R.; Yurasova, T. A. *Polymer Sci. USSR* **1987**, *29*, 1293.

(154) Wang, Z.-G.; Safran, S. A. *J. Chem. Phys.* **1988**, *89*, 5323.

(155) Shukla, P.; Muthukumar, M.; Langley, K. *J. Appl. Polym. Sci.* **1992**, *44*, 2115.

(156) Zero, K.; Pecora, R. *Macromolecules* **1982**, *15*, 87.

(157) Goebel, K.; Miller, W. *Macromolecules* **1970**, *3*, 64.

(158) Lodge, T., Personal Communication, May, 1995.

(159) Qin, A.; Tian, M.; Ramireddy, C.; Webber, S.; Munk, P. *Macromolecules* **1994**, *27*, 120.

(160) Hirata, M.; Tsunashima, Y. *Macromolecules* **1989**, *22*, 249.

(161) Tirrell, M.; Torkelson, J. *J. Rheology* **1979**, *23*, 751.

(162) Helfrich, J.; Hentschke, R.; Apel, U. *Macromolecules* **1994**, *27*, 472.

(163) Gerber, J.; Elias, H. *Die Makromol. Chem.* **1968**, *112*, 142.

(164) Daly, W., Personal Communication, August, 1994.

(165) Tirrell, M.; Parsonage, E.; Watanabe, H.; Dhoot, S. *Polymer Journal* **1991**, *23*, 641.

(166) Patel, S.; Hadziioannou, G.; Tirrell, M. *Proc. Nat. Acad. Sci.* **1987**, *84*, 4725.

(167) Watanabe, H.; Tirrell, M. *Macromolecules* **1993**, *26*, 6455.

(168) Alexander, S. *J. Phys (Paris)* **1977**, *38*, 977.

(169) Hirz, S. MS Thesis, University of Minnesota, 1986.

(170) Cosgrove, T.; Heath, T.; vanLent, B.; Leermakers, F.; Scheutjens, J. *Macromolecules* **1987**, *20*, 1692.

(171) Flory, P. J. *Principles of Polymer Chemistry*; Cornell University Press: Ithaca, 1971.

(172) Ansarifar, M. A.; Luckham, P. F. *Polymer* **1988**, *29*, 329.

(173) Hadziioannou, G.; Patel, S.; Granick, S.; Tirrell, M. *J. Am. Chem. Soc.* **1986**, *84*, 4725.

(174) Taunton, H. J.; Toprakeioglu, C.; Fetters, L. J.; Klein, J. *Nature* **1988**, *332*, 712.

(175) Loeb, G. *J. Coll. Interf. Sci.* **1968**, *26*, 236.

(176) Jones, R.; Tredgold, R. *J. Phys. D, Appl. Phys.* **1988**, *21*, 449.

(177) Takenaka, T.; Harada, K.; Matsumoto, M. *J. Coll. Interf. Sci.* **1980**, *73*, 569.